BOSTON UNIVERSITY

GRADUATE SCHOOL OF ARTS AND SCIENCES

Dissertation

DISCERNING THE NEUTRINO MASS ORDERING USING ATMOSPHERIC NEUTRINOS IN SUPER-KAMIOKANDE I–V

by

THOMAS WESTER

B.A., University of Chicago, 2017

Submitted in partial fulfillment of the

requirements for the degree of

Doctor of Philosophy

2023

Approved by

First Reader

Edward T. Kearns, Ph.D.
Professor of Physics

Second Reader

Robert M. Carey, Ph.D.
Professor of Physics

To my Dear Ol' Dad!

Acknowledgments

I have been incredibly fortunate to meet and work with a host of fantastic physicists who, through their combined mentorship, set me on a path to write this dissertation. In approximate chronological order, thanks to Stephen Pordes for giving me my first summer research job at Fermilab, and to Thomas Alexander for helping me destroy my first PMT. Thanks to my University of Chicago mentors, Professor Luca Grandi and Dr. Richard Saldanha, for connecting me to the world of experimental particle physics, for the opportunity to build and run our own detector, and for teaching me to think harder about my plots before I show them at group meetings. Thanks to my mentors at Fermilab and MIT, Professors Janet Conrad, Taritree Wongjirad, and Dr. Daniel Winklehner. I would not have decided to study neutrino physics without your encouragement and support.

I owe so much of my scientific training to my mentors at Boston University, Dr. Linyan Wan, and my advisor, Professor Ed Kearns. Linyan's vast knowledge of Super-K, her ability to find new and interesting analysis techniques using our 27-year-old experiment, and her clear and comprehensive presentations make her an exemplary physicist that I aspire to be like. Ed's emphasis on using basic principles of detectors as the building blocks for complicated analyses has helped me to develop my intuition as an experimental particle physicist. I am also grateful to Ed for his perspectives on past and future experiments, which provided much-needed context when first entering the world of neutrino oscillation analyses. I am further indebted to Ed's keen eye for aesthetics, which has saved me many times from presenting inscrutable plots to our collaborators. Finally, I am most grateful for Ed's guidance in helping me to distill the story of the measurement presented in this dissertation from all its technical aspects.

The analysis presented in this dissertation is only possible thanks to the hard work of so many Super-Kamiokande collaborators. I was fortunate to meet many of

them in person throughout my first two years of grad school during trips to Japan. In 2018, I got to witness the entire collaboration mobilize to refurbish the 10-storey SK detector from head-to-toe—an incredible feat of coordination that highlighted the unique expertise of each collaborator. Through my small roles managing the outer detector PMT high voltages, and tuning the SK outer detector simulation, I learned the fundamentals of SK calibration from Dr. Shunichi Mine, who I hope to accompany on another ski trip one day.

For the analysis presented in this dissertation, I am especially thankful to the oscillation working group members, Pablo Fernández, Seungho Han, and Magda Posiadała-Zezula, for their direct contributions to many aspects of this analysis, and insights during our regular meetings. Thank you for fielding my requests for obscure analysis inputs, and for all your critical work needed to prepare the new expanded fiducial volume and SK V data for analysis.

A special thanks is in order to the `OscMaestro` himself, Professor Roger Wendell. I have learned so much about neutrino oscillations and assembling the myriad components required for this analysis under Roger's guidance. Roger gave me the tools I needed to perform this analysis, and then encouraged me to question conventions and to look for improvements. Roger also fully convinced me that I'd rather know the neutrino mass ordering than the value of δ_{CP}. After this dissertation is submitted, I am excited to continue working with Roger to finish writing the next SK neutrino oscillation paper.

Physics is no fun without friends. I am thankful for all my friends at Boston University, especially Chris Cosby, Brian Dawes, Diana Gooding, Paige Kunkle, and David Long. Aside from being accomplished physicists, they are kind, funny, and insightful colleagues who have made my time at Boston University so enjoyable. No matter if we were working on problem sets, discussing literature[1], or just chatting in

[1] *Spiderlight* doesn't qualify.

the office, their upbeat attitudes and support during our time in grad school have made it a joy to come to campus every day.

I would be remiss to not mention my friends who remind me that there's more to life than neutrinos. From my time at the University of Chicago (UC), Jonathan Gerstell, Isaac Krone, Aidan Lilienfeld, Ted Litchfield, and Avery Robinson have remained the best of friends despite our distance. Our regular calls and perpetual stream-of-consciousness chats are a constant reminder for me to find humor in everyday things, and that the lessons of particle physics only provide one out of many ways to approach complicated problems. I also thank my fellow members of Vacuist, Stavros Aganis, Henry "Mica" Goldsmith, and Iain Standing, for giving me an outlet to focus on music instead of neutrinos for a few hours every week here in Boston.

The people who deserve the most credit are the ones who have sustained me through the marathon that is obtaining a physics Ph.D. Moving to Boston put me on the East Coast for the first time, and I have been so lucky to have another home base here with the Kapadia family. Quaid, Carolyn, Andrew, Alistair, Grandmom, Dadima, and Caesar have always made me feel at home, provided me with delicious homemade Indian food, and, occasionally, a healthy amount of chaos! Back in Chicago, I have had the lifelong support of my parents, Barbara and William, and my brother Stephen. My father, a particle physicist himself, showed me by example what a fulfilling career pursuing interesting questions about the universe can look like. Last but not least, thank you to my partner of 8 years (time flies!), Alex Kapadia. I owe who I am as a person today to her profound thoughtfulness, intellect, and kindness. I am so happy to have built our life together in Chicago and Boston, and can't wait to start our next adventure.

DISCERNING THE NEUTRINO MASS ORDERING USING ATMOSPHERIC NEUTRINOS IN SUPER-KAMIOKANDE I–V

THOMAS WESTER

Boston University, Graduate School of Arts and Sciences, 2023

Major Professor: Edward T. Kearns, Ph.D., Professor of Physics

ABSTRACT

Neutrino oscillation experiments have demonstrated evidence for three distinct neutrino masses. However, whether there are two light neutrinos and one heavy neutrino (normal), or the other way around (inverted), known as the neutrino mass ordering, remains undetermined. This thesis presents a search for indications of the neutrino mass ordering in 6511 live-days (484 kiloton-years) of atmospheric neutrino data collected with the Super-Kamiokande (SK) detector between 1996 and 2020. The data set is a 30 % increase in exposure since the previous published analysis, and the analysis methodology includes improvements to the separation of neutrino and anti-neutrino data. This thesis also presents an analysis of the SK data with constraints on neutrino oscillation parameters from reactor neutrino experiments and the T2K long-baseline experiment. The constraints from the T2K experiment include, for the first time, an anti-neutrino-enhanced data sample. The atmospheric neutrino analysis favors the normal neutrino mass ordering, rejecting the inverted ordering at the 92.3 % (1.43 σ) level. The inclusion of external constraints from T2K data increases the rejection to the 97.9 % (2.03 σ) level.

Contents

List of Tables

List of Figures

List of Abbreviations

1p1h .... One-particle one-hole
2p2h .... Two-particle two-hole
ADC .... Analog-to-digital converter
BDT .... Boosted decision tree
CC .... Charged current
CCQE .... Charged current quasi-elastic
CP .... Charge-parity
DIS .... Deep inelastic scattering
DONUT .... Direct Observation of the Nu Tau
DUNE .... Deep Underground Neutrino Experiment
ES .... Electron scatter
FC .... Fully-contained
FGD .... Fine-grained detector
FHC .... Forward horn current
FSI .... Final state interaction
GALLEX .... Gallium Experiment
GNO .... Gallium Neutrino Observatory
ID .... Inner detector
IMB .... Irvine-Michigan-Brookhaven
K2K .... KEK to Kamioka
KamLAND .... Kamioka Liquid Scintillator Antineutrino Detector
KS .... Kolmogorov-Smirnov
LEP .... Large Electron-Positron Collider
LFG .... Local Fermi gas
MC .... Monte Carlo
MEC .... Meson exchange current

MINOS .... Main Injector Neutrino Oscillation Search
MSW .... Mikheyev–Smirnov–Wolfenstein
NC .... Neutral current
NOvA .... NuMI Off-axis ν_e Appearance
NRE .... Nucleon removal energy
OD .... Outer detector
PC .... Partially-contained
PDF .... Parton distribution function
PID .... Particle identification
PMNS .... Pontecorvo-Maki-Nakagawa-Sakata
PMT .... Photomultiplier tube
POT .... Protons on target
PREM .... Preliminary Reference Earth Model
QAC .... Charge-to-analog converter
QBEE .... QTC-based electronics with ethernet
QTC .... Charge-to-time converter
RENO .... Reactor Experiment for Neutrino Oscillation
RFG .... Relativistic Fermi gas
RHC .... Reverse horn current
RMS .... Root-mean-square
RPA .... Random phase approximation
SAGE .... Soviet–American Gallium Experiment
SI .... Secondary interaction
SK .... Super-Kamiokande
SNO .... Sudbury Neutrino Observatory
SSM .... Standard Solar Model
T2K .... Tokai to Kamioka
TDC .... Time-to-digital converter
TPC .... Time projection chamber
Up-μ .... Upward-going muon
UV .... Ultra-violet

Chapter 1

Introduction

1.1 The Neutrino Mass Ordering

Is there one heavy neutrino and two light neutrinos, or the other way around? This is a simple question to pose in 2023, but its simplicity encodes decades of theoretical and experimental results which have enabled us to ask it. This question presupposes the following statements: There are three neutrinos. Neutrinos have mass. Two of the neutrinos are close in mass, while a third is not. We have strong evidence for these individual statements, but somehow, we ended up short of putting the neutrinos in order. This is the neutrino mass ordering question.

The outlook for resolving this problem is optimistic: New experiments on the horizon will produce, detect, and measure more neutrinos than ever before. Additionally, combined measurements of neutrino properties from multiple, currently-operating experiments have the potential to converge on a single answer—either "normal" for one heavy neutrino, or "inverted" for two—possibly by the end of the decade [1]. In 2023, our current best measurement of the neutrino mass ordering primarily comes from three operating experiments: The Tokai to Kamioka (T2K) experiment, the NuMI Off-axis ν_e Appearance (NOvA) experiment, and the Super-Kamiokande (SK) experiment. Figure 1·1 summarizes recent measurements of the neutrino mass ordering from T2K and NOvA: The horizontal and vertical axes show possible combinations of parameters of nature which, when combined with an assumption about the mass ordering, give better or worse agreement with observed data. Their uncertainties are

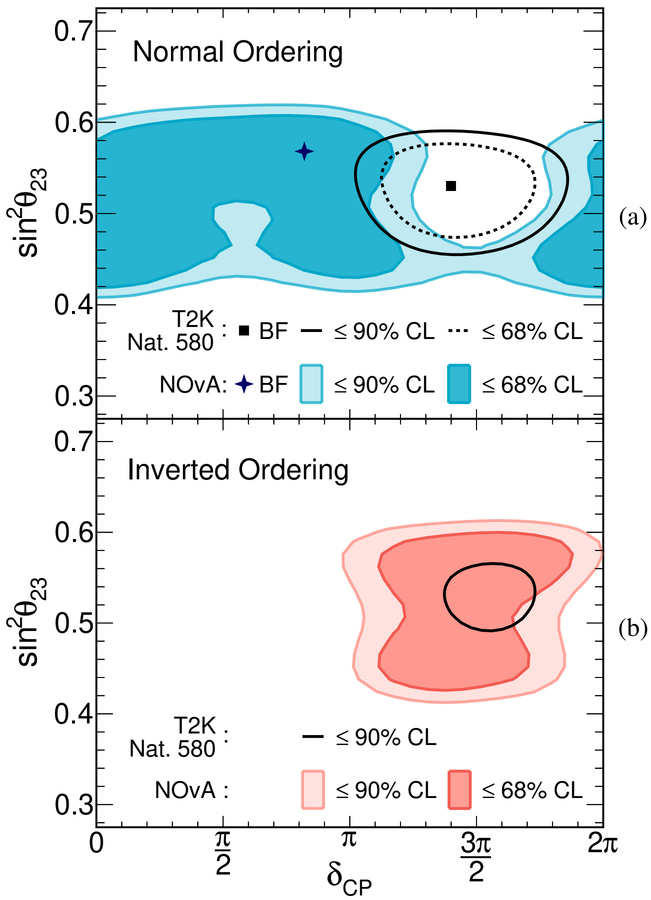

Figure 1·1: NOvA and T2K measurements of neutrino oscillation parameters $\sin^2\theta_{23}$ and δ_{CP} in each of the two neutrino mass ordering scenarios. Figure is reproduced from [2].

shown by the filled regions for NOvA and as black outlines for T2K. The top panel shows the parameter measurements assuming the normal ordering, while the bottom panel shows the same parameters assuming the inverted ordering.

We can make several observations about the figure. First, the normal ordering contains the parameters which best describe both data sets. This is indicated by the black cross and square in the top panel. Second, the parameter regions in the bottom panel are smaller than those in the top panel. This indicates that a larger amount of the parameter space is ruled out in the inverted ordering. Finally, we note that, in the normal ordering, the filled region from NOvA and the outline from T2K do not overlap. This tells us that, at present, their data sets are in tension, and favor different parameters of nature.

The tension between T2K and NOvA creates the following situation for the neutrino mass ordering: Both experiments are better described by the normal ordering, but their preferences for other parameters only overlap in the inverted ordering. Disentangling these conflicting statements will require more data from the T2K and NOvA experiments. In the meantime, we can turn to the other experiment, SK, to weigh in on the mass ordering.

Unlike the T2K and NOvA experiments, which make their measurements using artificial neutrino beams, the SK experiment observes neutrinos produced in the atmosphere. These atmospheric neutrinos offer a unique perspective on the neutrino mass ordering. This thesis will describe the historical context for how we have arrived at the neutrino mass ordering question, how the SK experiment is sensitive to measuring it, and then present the current best measurement of the neutrino mass ordering using atmospheric neutrinos. The thesis will conclude with a combined analysis of the SK and T2K data sets to further improve the measurement.

1.2 Brief History of Neutrinos

Neutrinos were originally proposed by Wolfgang Pauli in 1930 as an explanation for the continuous distribution of electron energies observed from beta decays [3]. In a beta decay, it was known that a neutron at rest decays into an electron and a proton, which, through conservation of momentum and energy, should always result in an electron and proton with fixed energies,

$$n \stackrel{?}{\rightarrow} p + e^{-}. \tag{1.1}$$

While many explanations, including violations of energy conservation [4], were considered to explain this phenomenon, Pauli proposed the presence of a third particle, which carried away part of the energy of the decay, as the solution. The beta decay reaction, including a neutrino, is written as

$$n \rightarrow p + e^- + \nu, \tag{1.2}$$

where ν represents the neutrino. Two properties of the neutrino, that it was extremely light and electrically neutral, were inferred from the beta decay spectrum, and that any charged particles would have been detected.

While the proposed neutrino solved the beta decay issue in theory, experimental detection of a neutrino would not be accomplished until 1956. A neutral particle, perhaps massless, would necessarily have a minuscule chance of interaction. Hans Bethe and Rudolf Peierls, using Enrico Fermi's theory of the weak nuclear force, calculated this chance in 1934, estimating the interaction cross section of a neutrino produced from beta decay as $\sigma < 10^{-44}\,\text{cm}^2$ [5, 6]. Thus, only a large detector and a huge quantity of neutrinos from a known source would suffice to make an observation.

Twenty years later, Arthur Cowan and Frederick Reines devised a plan to observe anti-neutrinos from a nuclear reactor via the *inverse* beta decay process,

$$\bar{\nu}_e + p \rightarrow n + e^+. \tag{1.3}$$

The Cowan-Reines experiment hoped to identify these inverse beta decays using the coincidence of the energy emission from the anti-electron, e^+, annihilation with atomic electrons in the detector, followed by the additional energy release from the capture of the neutron by cadmium molecules. The experiment observed excess coincidences when the nuclear reactor was operational, implying the presence of neutrinos, and also confirmed Bethe and Peierls cross section prediction [7].

More neutrino experiments followed which established three distinct neutrino "flavors." The neutrinos observed by Cowan and Reines always produced an anti-electron, which later became understood as the anti-particle of one of three flavors of charged leptons. In 1962, Leon Lederman, Melvin Schwartz and Jack Steinberger observed neutrinos which produced the next-heaviest charged lepton, the muon, at Brookhaven National Laboratory [8]. In contrast to the Cowan-Reines experiment, the Brookhaven experiment used a source of stopped pions which decayed into muons and neutrinos. When these neutrinos interacted in a downstream detector, muons were detected instead of electrons. The third neutrino associated with the tau lepton was observed by the Direct Observation of the Nu Tau (DONUT) experiment in 2000 [9] using high-resolution emulsion detectors to observe any short-lived tau particles produced in neutrino interactions. Apart from these direct observations, detectors at the Large Electron-Positron Collider (LEP) observed decays of the 91 GeV Z boson at a rate in precise agreement with predictions which assumed exactly three neutrino flavors.

1.3 Neutrinos in the Standard Model

In the 1970s, Sheldon Glashow, Steven Weinberg, and Abdus Salam created a formulation of particle interactions that included the electromagnetic, weak, and strong forces, three generations of quarks and leptons, and a mechanism to explain particle masses, which became known as the Standard Model [10, 11]. In the Standard Model, particles are classified by their quantum spin. Matter consists of spin-1/2 particles called *fermions*, and the interactions between the fermions are mediated by the exchange of spin-1 force-carrying particles called *bosons*. The Standard Model further distinguishes two classes of fermions, quarks and leptons. Quarks interact via all three forces, while the charged leptons interact via the weak and electromagnetic forces. Neutrinos are leptons, but, since they are electrically neutral, do not have electromagnetic interactions. The charges and experimentally-measured masses of the fermions are listed in Table 1.1. The final component of the Standard Model is the Higgs boson, a spin-0 particle which gives rise to the masses of the W and Z bosons, the massless photon, and the masses of the charged fermions.

	Generation			Charge
	I	II	III	
Quarks	**u** 2.3 MeV/c^2	**c** 1270 MeV/c^2	**t** 172700 MeV/c^2	+2/3
	d 4.8 MeV/c^2	**s** 95 MeV/c^2	**b** 4180 MeV/c^2	−1/3
Leptons	**e** 0.51 MeV/c^2	$\boldsymbol{\mu}$ 106 MeV/c^2	$\boldsymbol{\tau}$ 1780 MeV/c^2	−1
	$\boldsymbol{\nu_e}$ $< 10^{-6}$ MeV/c^2	$\boldsymbol{\nu_\mu}$ $< 10^{-6}$ MeV/c^2	$\boldsymbol{\nu_\tau}$ $< 10^{-6}$ MeV/c^2	0

Table 1.1: The masses and electric charges of the three generations of spin-1/2 fermions in the Standard Model. Anti-particles have the opposite charge. The electron neutrino mass is bounded above at 0.9 eV/c^2 by direct measurements from KATRIN in 2022 [12], and the sum of all three neutrino masses is bounded above at ~ 0.2 eV/c^2 by data fits to cosmological models [13].

In the Standard Model, neutrinos only experience the weak interaction. There are two variants of the weak interaction: charged current (CC) and neutral current (NC). In a CC interaction, particles exchange a W boson and change flavor, either from a neutrino into the corresponding charged lepton, or from an “up,” charge +2/3, type quark into a “down,” charge -1/3, type quark. The flavor change means that, for a neutrino to undergo a CC interaction, it must be energetic enough to produce its corresponding charged lepton. In an NC interaction, a particle exchanges a Z boson, and never changes flavor. Example Feynman diagrams depicting weak interaction processes are shown in Figure 1·2. Anti-particle interactions proceed similarly, but with opposite charges.

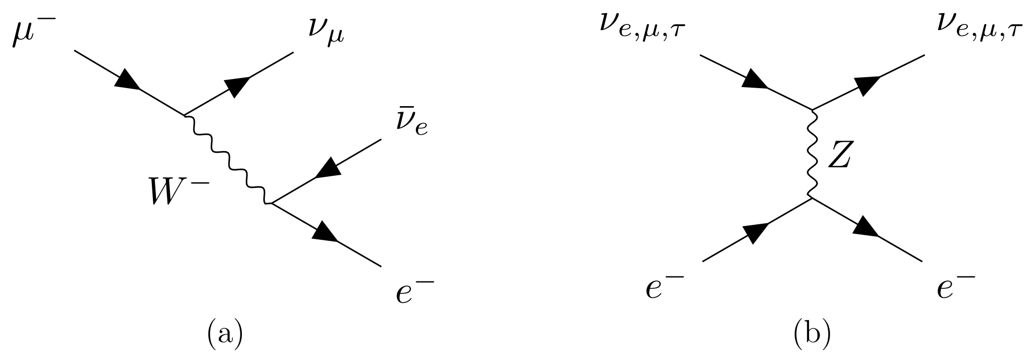

Figure 1·2: Feynman diagrams of example (a) CC and (b) NC processes. In (a), a muon decays weakly into a muon neutrino, electron anti-neutrino and an electron. In (b), a neutrino of any flavor scatters with an electron via the exchange of a Z boson, leaving the final state particles unchanged.

In addition to spin and charge, the quantum fields underlying the particles of the Standard Model also possess either an intrinsic left-handed or right-handed chirality. Weak interactions depend on a particle's chirality, as only left-handed particles or right-handed anti-particles may interact via the weak force. Charged quarks and leptons exist as both left-handed and right-handed variants, however, as neutrinos only have weak interactions, there is no experimental evidence for right-handed neutrinos or left-handed anti-neutrinos.

By extension, neutrino mass is not present in the Standard Model. In the Standard Model, the quarks and charged leptons acquire their masses through interactions of their left- and right-handed chiral variants with the Higgs field. Since neutrinos have no right-handed particle or left-handed anti-particle, this interaction does not occur in a minimal Standard Model, leaving neutrinos as massless particles. While adding a right-handed neutrino with no interactions to the Standard Model would provide a mechanism for neutrino mass, it still leaves open the question of the smallness of neutrino mass relative to the other particles. For this reason, neutrino mass is considered to be an indication of physics processes beyond the Standard Model.

1.4 Neutrino Mass & Oscillations

While neutrinos successfully explained beta decay, experiments observing neutrinos from the Sun in the 1960s, and later using neutrinos produced in the atmosphere in the 1980s, observed deficits compared to the expected rate of neutrino interactions. These became known as the solar and atmospheric neutrino problems. Proposed solutions to these problems varied, and included neutrino decay, or simply that the predicted rate of neutrinos from these sources were incorrect. However, ultimately the phenomenon of neutrino oscillations would successfully explain both issues. Crucially, neutrino oscillations require that the neutrinos have mass.

1.4.1 Neutrino Oscillation Theory

To see how massive neutrinos oscillate, we propose that the three neutrino flavors, ν_e, ν_μ and ν_τ, are mixtures of neutrinos with different masses, ν_1, ν_2 and ν_3. This mixture is represented via a matrix:

$$\begin{pmatrix} \nu_e \\ \nu_\mu \\ \nu_\tau \end{pmatrix} = \begin{pmatrix} \mathbf{U}_{e1} & \mathbf{U}_{e2} & \mathbf{U}_{e3} \\ \mathbf{U}_{\mu 1} & \mathbf{U}_{\mu 2} & \mathbf{U}_{\mu 3} \\ \mathbf{U}_{\tau 1} & \mathbf{U}_{\tau 2} & \mathbf{U}_{\tau 3} \end{pmatrix} \begin{pmatrix} \nu_1 \\ \nu_2 \\ \nu_3 \end{pmatrix}, \tag{1.4}$$

where the matrix $\mathbf{U}$ is called the Pontecorvo-Maki-Nakagawa-Sakata (PMNS) matrix [14, 15]. The elements of $\mathbf{U}$ mix the flavor states and mass states. The mixture of mass states, 1, 2, and 3, for any flavor state, α, can be written compactly as

$$|\nu_\alpha\rangle = \sum_{i=1}^{3} \mathbf{U}_{\alpha i} |\nu_i\rangle. \tag{1.5}$$

In this framework, we can use Equation 1.5 to compute the probability of observing a neutrino created as one flavor as another flavor after some time t. The equation describing the propagation of a neutrino with flavor α is

$$|\nu_\alpha(t)\rangle = \sum_{i=1}^{3} \mathbf{U}_{\alpha i} e^{-iE_i t} |\nu_i(t=0)\rangle \tag{1.6}$$

where E_i is the energy eigenvalue of the ν_i mass state. For a near-massless neutrino with energy, E, traveling in a vacuum, the neutrino momentum, p, may be approximated as E, and so $E_i = \sqrt{m_i^2 + p^2} \approx E + m_i^2/2E$. We compute the probability of observing a neutrino of one flavor, α, as another flavor, β by computing the overlap of Equation 1.6 and squaring. The probability is

$$\begin{aligned} P(\nu_\alpha \to \nu_\beta) &= |\langle \nu_\beta(t)|\nu_\alpha(0)\rangle|^2 \\ &= \left| \left(\sum_{j=1}^{3} \mathbf{U}^*_{\beta j} e^{iE_j t} \langle \nu_j(t)| \right) \left(\sum_{i=1}^{3} \mathbf{U}_{\alpha i} e^{-iE_i t} |\nu_i(0)\rangle \right) \right|^2 \\ &= |\sum_{i=1}^{3} |\mathbf{U}^*_{\beta i} \mathbf{U}_{\alpha i} e^{-iE_i t}|^2 \\ &= \sum_{i=1}^{3} |\mathbf{U}^*_{\beta i} \mathbf{U}_{\alpha i}|^2 + \sum_{i \neq j} \mathbf{U}_{\alpha i} \mathbf{U}^*_{\beta j} \mathbf{U}^*_{\alpha j} \mathbf{U}_{\beta j} e^{-i(E_i - E_j)t} \end{aligned} \tag{1.7}$$

In the third line, we have used $\langle \nu_i|\nu_j\rangle = 0$ for $i \neq j$ and 1 otherwise. Equation 1.7 tells us that the probability of a neutrino switching flavors by the time we observe it is a function of t and $E_i - E_j$. If the neutrinos are massless, then $E_i - E_j \propto m_i^2 - m_j^2 = 0$, and the time-dependent component vanishes. On the other hand, if at least one neutrino has a mass, the time-dependent component is nonzero, predicting that the probability of observing the neutrino as a different flavor changes as it travels. This phenomenon is known as neutrino oscillation.

To see how neutrino oscillations can produce measurable effects, we consider the structure of $\mathbf{U}$. By requiring that $\mathbf{U}$ is unitary, we can express it as a product of three rotation matrices which each mix two out of the three mass states via an angle,

θ_{ij}, and one complex phase, δ. Then $\mathbf{U}$ becomes:

$$\mathbf{U} = \begin{pmatrix} 1 & 0 & 0 \\ 0 & \cos\theta_{23} & \sin\theta_{23} \\ 0 & -\sin\theta_{23} & \cos\theta_{23} \end{pmatrix} \begin{pmatrix} \cos\theta_{13} & 0 & \sin\theta_{13}e^{-i\delta} \\ 0 & 1 & 0 \\ -\sin\theta_{13}e^{i\delta} & 0 & \cos\theta_{13} \end{pmatrix}$$
$$\times \begin{pmatrix} \cos\theta_{12} & \sin\theta_{12} & 0 \\ -\sin\theta_{12} & \cos\theta_{12} & 0 \\ 0 & 0 & 1 \end{pmatrix}. \tag{1.8}$$

To understand how each parameter affects the probability of observing a neutrino of a particular flavor, we consider the simpler case of two-neutrino oscillations. In this case, there are only two flavors, and the mixing matrix only contains a single angle:

$$\begin{pmatrix} \nu_\alpha \\ \nu_\beta \end{pmatrix} = \begin{pmatrix} \cos\theta & \sin\theta \\ -\sin\theta & \cos\theta \end{pmatrix} \begin{pmatrix} \nu_1 \\ \nu_2 \end{pmatrix} \tag{1.9}$$

In this scenario, Equation 1.7 now becomes:

$$\begin{aligned} P(\nu_\alpha \to \nu_\beta) &= 2\cos^2\theta\sin^2\theta - \left(\cos^2\theta\sin^2\theta\right)\left[e^{-i(E_1-E_2)t} + e^{i(E_1-E_2)t}\right] \\ &= \frac{\sin^2 2\theta}{2}\left[1 - \frac{1}{2}\left(e^{-i(E_1-E_2)t} + e^{i(E_1-E_2)t}\right)\right] \\ &= \sin^2 2\theta \sin^2\left[\frac{(E_1-E_2)t}{2}\right]. \end{aligned} \tag{1.10}$$

By substituting $E_i = E + m_i^2/2E$, we obtain:

$$P(\nu_\alpha \to \nu_\beta) = \sin^2 2\theta \sin^2\left(\frac{\Delta m^2 t}{4E}\right), \tag{1.11}$$

in natural units. Here, $\Delta m^2 = m_1^2 - m_2^2$, and is called the squared mass difference or mass splitting. In an experiment, we observe neutrinos traveling from a production point at a distance away from our detector, L. For a near-massless neutrino, we can substitute t for L. Then, using powers of $\hbar$ and c, we can convert L to units of kilometers, Δm^2 to units of eV^2/c^4, and E to units of GeV:

$$\frac{\Delta m^2 t}{4E} \approx \frac{\Delta m^2/c^4 L \cdot c^4}{4E \cdot \hbar c} \approx 1.27 \frac{\Delta m^2(\text{eV}^2) L(\text{km})}{E(\text{GeV})} \tag{1.12}$$

which gives the two-flavor probability formula:

$$P(\nu_\alpha \to \nu_\beta) \approx \sin^2 2\theta \sin^2\left(1.27\frac{\Delta m^2 L}{E}\right). \tag{1.13}$$

It is also straightforward to repeat the above calculation for the two flavor *survival* probability, i.e., the probability of a neutrino remaining as its initial flavor:

$$P(\nu_\alpha \to \nu_\alpha) \approx 1 - \sin^2 2\theta \sin^2\left(1.27\frac{\Delta m^2 L}{E}\right). \tag{1.14}$$

From Equation 1.13 and Equation 1.14, we see that the various components influence the oscillation pattern as follows: The mixing angle, θ, controls the overall amplitude of the oscillation, while the squared mass difference, Δm^2, controls the frequency of the oscillation as a neutrino with energy, E, travels along a baseline, L.

The two flavor approximation is useful to explain the leading-order oscillation effect when the mass of one neutrino state is sufficiently different from the other two. For the three-flavor case, the squared mass differences are expressed as $\Delta m^2_{ij} \equiv m^2_i - m^2_j$. Then the two-flavor approximation holds when $|m^2_1 - m^2_2| \gg |m^2_3 - m^2_2|$ or $|m^2_1 - m^2_2| \ll |m^2_3 - m^2_2|$. Experiments have determined that this condition is satisfied to a good approximation, and have measured $|\Delta m^2_{32}|$ to be approximately 30 times $|\Delta m^2_{21}|$. This also implies that $|\Delta m^2_{32}| \approx |\Delta m^2_{31}|$.

Note that for the oscillation framework we have considered, the sign of Δm^2_{ij} does not play any role for neutrino oscillations; Δm^2_{ij} only appears inside the sine squared term of Equation 1.13 and Equation 1.14. For this reason, the leading-order neutrino oscillation effects only allow us to measure the mixing angles θ_{ij} and the absolute values of the squared mass differences. We can understand the neutrino mass ordering question as the unknown sign of Δm^2_{32} or Δm^2_{31}.

1.4.2 Matter Effects

In matter, electron flavor neutrinos experience a modified potential due to an increased forward scattering amplitude with atomic electrons. Figure 1·3 shows Feynman diagrams of the processes that contribute to this amplitude for electron flavor neutrinos. These processes are not present for muon and tau flavor neutrinos, so the modified potential changes the neutrino oscillation probabilities asymmetrically from the vacuum case. We can compute the modification by adding a potential term to the electron neutrino component of the neutrino Hamiltonian:

$$H_{\text{Matter}} = H_{\text{Vacuum}} + \mathbf{U}^\dagger \begin{pmatrix} a & 0 & 0 \\ 0 & 0 & 0 \\ 0 & 0 & 0 \end{pmatrix} \mathbf{U} \tag{1.15}$$

where we have written the Hamiltonian H_{Matter} in the mass basis, i.e., the eigenvalues of H_{Vacuum} are the E_i from Eq. 1.6. The electron potential is written as a 3×3 matrix in the flavor basis, and $\mathbf{U}$ is the PMNS mixing matrix which rotates this matrix into the mass basis. The potential, a, depends on the material's electron density, N_e, and the energy scale of the weak interaction given by Fermi's constant, G_F: $a = \pm\sqrt{2}G_F N_e$. The sign of a is positive for neutrinos and negative for antineutrinos [16].

We may inspect the general impact of the matter potential on neutrino oscillations by again simplifying to the two-flavor case. Starting with the two-flavor mixing matrix of Equation 1.13, the Hamiltonian for massive neutrinos propagating in matter is now

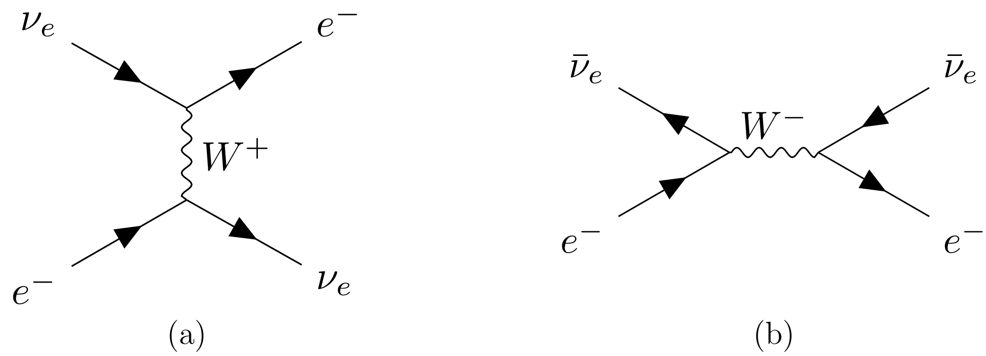

Figure 1·3: Feynman diagrams of the two processes exclusive to (a) electron neutrinos and (b) electron anti-neutrinos when propagating through a medium.

given by:

$$\begin{aligned} H_{\text{Matter}} &= \begin{pmatrix} \frac{m_1^2}{2E} & 0 \\ 0 & \frac{m_2^2}{2E} \end{pmatrix} + \begin{pmatrix} \cos\theta & -\sin\theta \\ \sin\theta & \cos\theta \end{pmatrix} \begin{pmatrix} a & 0 \\ 0 & 0 \end{pmatrix} \begin{pmatrix} \cos\theta & \sin\theta \\ -\sin\theta & \cos\theta \end{pmatrix} \\ &= \begin{pmatrix} \frac{m_1^2}{2E} + a\cos^2\theta & a\sin\theta\cos\theta \\ a\sin\theta\cos\theta & \frac{m_2^2}{2E} + a\sin^2\theta \end{pmatrix}. \end{aligned} \tag{1.16}$$

We can interpret Equation 1.16 as the Hamiltonian for neutrino states with effective masses in a new basis, $\tilde{\nu}_1$ and $\tilde{\nu}_2$. This implies there is an effective mixing angle, $\tilde{\theta}$, which mixes the effective mass states into flavor states ν_e and ν_x (a mixture of ν_μ and ν_τ), such that

$$\begin{pmatrix} \nu_e \\ \nu_x \end{pmatrix} = \begin{pmatrix} \cos\tilde{\theta} & \sin\tilde{\theta} \\ -\sin\tilde{\theta} & \cos\tilde{\theta} \end{pmatrix} \begin{pmatrix} \tilde{\nu}_1 \\ \tilde{\nu}_2 \end{pmatrix} \equiv \tilde{\mathbf{U}} \begin{pmatrix} \tilde{\nu}_1 \\ \tilde{\nu}_2 \end{pmatrix} \tag{1.17}$$

The new mixing matrix $\tilde{\mathbf{U}}$ from Equation 1.17 can be used to diagonalize the matter Hamiltonian and solve for the effective quantities relevant to neutrino oscillations. It can be shown that:

$$\Delta\tilde{m}^2 = \Delta m^2 \sqrt{\sin^2 2\theta + \left(\frac{2aE}{\Delta m^2} - \cos 2\theta\right)^2} \tag{1.18}$$

$$\sin^2 2\tilde{\theta} = \frac{\sin^2 2\theta}{\sin^2 2\theta + \left(\frac{2aE}{\Delta m^2} - \cos 2\theta\right)^2} \tag{1.19}$$

Equation 1.18 and Equation 1.19 imply that the $\nu_e \rightarrow \nu_x$ oscillation probability is modified in matter, and that the modification depends on the amount of mixing in a vacuum, θ, the matter density, a, and the *signed* mass splitting, Δm^2. In contrast, the two-flavor vacuum oscillation probabilities given in Equation 1.13 and Equation 1.14 only depend on the magnitude of the mass splitting, $|\Delta m^2|$. As we will see, this dependence of the modified oscillation probabilities in matter on the sign of the mass splitting provides a way to measure the neutrino mass ordering.

The theoretical results presented in this section have important implications for experimental tests of neutrino oscillations. The next section show how these results successfully describe many neutrino phenomena, and discuss how we can use them to probe remaining questions about neutrino oscillations.

1.5 Neutrino Oscillation Experiments

The goal of neutrino oscillation experiments is to measure the values of the PMNS parameters and the mass splittings by observing neutrino oscillations. While the oscillations proceed as a function of the neutrino travel distance, L, and energy, E, experimental considerations restrict observations to a limited range of L and E combinations. Therefore, different experiments are sensitive to different combinations of oscillation parameters.

Neutrinos observed by oscillation experiments manifest as an excess, *appearance*, or deficit, *disappearance*, of a particular flavor relative to the no-oscillation scenario. This section will describe experimental techniques used to observe neutrino appearance and disappearance from different neutrino sources.

1.5.1 Solar Neutrinos

Electron neutrinos with energies $0.1\,\mathrm{MeV} \sim 10\,\mathrm{MeV}$ are produced in the Sun as part of nuclear fusion and decay processes. Many reactions contribute to the total solar neutrino flux, but the most numerous by several orders of magnitude are from proton-proton fusion, the *pp*-chain,

$$p^+ + p^+ \to {}^2\mathrm{H}^+ + e^+ + \nu_e. \tag{1.20}$$

While these *pp* neutrinos are the most numerous, they are also the lowest energy solar neutrinos, with a maximum energy of $< 0.5\,\mathrm{MeV}$. Neutrinos of higher energies are produced from decays of heavier isotopes which are created from the fusion of hydrogen into helium, then helium into beryllium and lithium. In particular, the ^{7}Be produced in these fusion chains occasionally capture protons, forming boron-8, ^{8}B. The ^{8}B isotopes then decay into neutrinos with energies up to $\sim 15\,\mathrm{MeV}$:

$$^8\mathrm{B} \to {}^8\mathrm{Be} + e^+ + \nu_e \tag{1.21}$$

The first observation of solar neutrinos came from the Homestake experiment [17], led by Ray Davis, using these ^{8}B neutrinos. The Homestake experiment began in 1965, and consisted of a chlorine tank and filtration system. Davis hoped to observe argon atoms produced in the reaction $\nu_e + \mathrm{Cl} \to \mathrm{Ar} + e^-$. This reaction has a threshold energy of $0.81\,\mathrm{MeV}$, low enough to be induced by ^{8}B neutrinos. By 1964, the theoretical prediction of the solar neutrino flux from what would become the Standard Solar Model (SSM) [18–20] had calculated the expected flux of ^{8}B neutrinos [21], thereby directly predicting the number of argon atoms the Homestake experiment should observe. The Homestake experiment eventually reported a measurement of the solar neutrino flux of about 1/3 of the SSM prediction in 1969 [22]. While these results were puzzling, the results were not widely accepted due to doubts around the experiment and the SSM itself.

The Homestake measurements of the solar neutrino flux were corroborated by the Kamiokande-II detector in 1989. Kamiokande-II also observed ^{8}B neutrinos, and, unlike the Homestake experiment, demonstrated the neutrinos it observed came from the Sun by recording the energies and directions of the particles produced in neutrino interactions. Separate efforts by the Soviet–American Gallium Experiment (SAGE) [23] and Gallium Experiment (GALLEX)[1] [24] experiments, which operated from 1990-2007 and 1991-2003 respectively, used gallium detectors with lower detection thresholds to detect *pp* neutrinos. Both the Kamiokande-II and the gallium experiments observed a deficit compared to the SSM. Together with Davis' original measurements, these deficits became collectively known as the *solar neutrino problem*.

Neutrino oscillations proved to be the answer to the solar neutrino problem. The definitive measurement would come from the Sudbury Neutrino Observatory (SNO) experiment in 2001, which utilized heavy water, D_2O, as a detector target. The deuterium in the heavy water allowed SNO to detect both CC and NC solar neutrino interactions. A third interaction type, electron scatters (ES) with atomic electrons, was also observed. The interactions observed by SNO are summarized as:

$$\text{CC}: \quad \nu_e + d^+ \to p^+ + p^+ + e^- \tag{1.22}$$

$$\text{NC}: \quad \nu_{e,\mu,\tau} + d^+ \to p^+ + n + \nu_{e,\mu,\tau} \tag{1.23}$$

$$\text{ES}: \quad \nu_{e,\mu,\tau} + e^- \to \nu_{e,\mu,\tau} + e^- \tag{1.24}$$

While ν_μ and ν_τ neutrinos do not have CC interactions in SNO, all three flavors have NC and ES interactions. By detecting the electron produced in the CC and ES interactions, and the neutron associated with the NC interactions, SNO could effectively measure the CC and NC interactions separately. SNO data showed that the deficit in solar ν_e interactions was only present in the CC interactions, but that the NC and ES channels agreed with the SSM [25, 26]. This result provided direct evidence for solar neutrinos oscillating to different flavors, while also reaffirming the

[1] Later, Gallium Neutrino Observatory (GNO)

flux predictions of the SSM.

Solar neutrino oscillations are sensitive to the θ_{12} mixing angle and the Δm^2_{21} mass splitting through electron neutrino disappearance. The vacuum probability from Equation 1.14 tells us that, for long distances, the survival probability approaches $P(\nu_e \to \nu_e) \to 1 - \frac{1}{2}\sin^2 2\theta$, which is, at minimum, 1/2. This is the leading-order effect in solar neutrino oscillations.

Experimentally, the measured probability is closer to 1/3. We obtain this smaller value of the survival probability by invoking matter effects. Equation 1.19 contains a resonance condition, $2aE/\Delta m^2_{21} = \cos 2\theta_{12}$, which maximizes the effective mixing angle in matter, consequently increasing the probability of ν_e oscillations to other flavors. The resonance condition is satisfied for neutrinos with energies $E \sim 1\,\mathrm{MeV}$, and $\Delta m^2_{21} \sim 10^{-5}\,\mathrm{eV}^2$. Additionally, the resonance condition only occurs if $\Delta m^2_{21} > 0$. Applying this information to the observed solar neutrino deficit of 1/3 the prediction measures the θ_{12} mixing angle, the size of the Δm^2_{21} mass splitting, and the order of two of the neutrino masses, $m_2 > m_1$. The precise treatment of matter effects in solar neutrino oscillations summarized here was developed in the 1970s-1980s, and became known as the Mikheyev–Smirnov–Wolfenstein (MSW) effect [27, 28].

Current measurements from solar neutrino experiments place $\sin^2\theta_{12} \approx 0.31$ and $\Delta m^2_{21} \approx 7.5 \times 10^{-5}$ eV^2[2]. Contemporary solar neutrino experiments aim to more precisely determine the energy dependence of the solar neutrino oscillation pattern, and to observe matter effects of solar neutrinos passing through the Earth, leading to "day-night asymmetry." A thorough treatment of solar neutrino oscillations, including sub-leading effects, may be found in [30].

[2]With input from reactor neutrino experiments. See Section 1.5.2

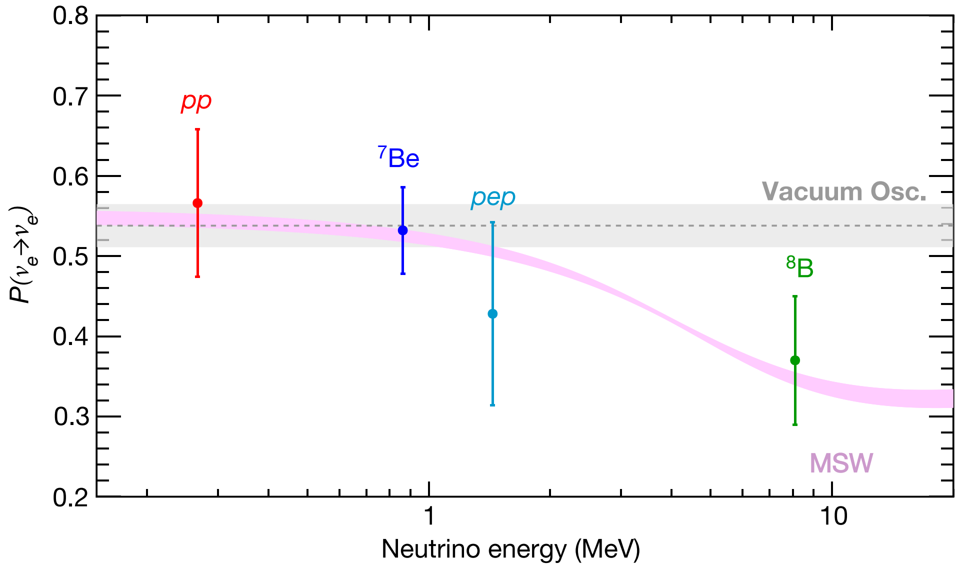

Figure 1·4: Measurements of electron neutrino survival probabilities from the BOREXINO experiment in 2018, adapted from [29]. The dashed grey line shows the expected survival probability with vacuum oscillations, while the pink curve shows the expected oscillations accounting for the MSW effect. BOREXINO is sensitive to *pp*, ^{8}B and other solar neutrinos at intermediate energies.

1.5.2 Reactor Neutrinos

Nuclear reactors provide a source of electron anti-neutrinos with 10s of MeV of energy. In a reactor, a ^{235}U nucleus captures a thermal neutron, either converting it to ^{236}U, or, more frequently, initiating fission into lighter elements and more neutrons. The fission products undergo successive beta decays which produce more neutrons, anti-electrons, and electron anti-neutrinos.

The Kamioka Liquid Scintillator Antineutrino Detector (KamLAND) experiment, which has been operating in Japan since 2002, made subsequent measurements of reactor neutrinos at long baselines. The KamLAND experiment uses a liquid scintillator detector target to precisely measure the energies of particles produced following an inverse beta decay interaction, cf. Equation 1.3). Neutrino interactions in the liquid scintillator create light proportional to the energy of the anti-electron produced, followed by a delayed burst of light from the capture of the neutron, which enables low-background neutrino identification. The energy resolution of KamLAND is approximately 2 % for 10 MeV neutrinos.

KamLAND observes neutrinos from multiple reactors across Japan, at an average baseline of 180 km. At this average baseline and reactor neutrino energy, KamLAND provides sensitivity to, and is an independent measurement of, Δm^2_{21} values $\sim 10^{-5}\,\mathrm{eV}^2$. In 2002, the KamLAND experiment first reported significant electron anti-neutrino disappearance as a function of neutrino energy, consistent with the measured mixing from solar neutrino experiments [31].

While KamLAND is sensitive to Δm^2_{21} and θ_{12}, a detector placed at a much shorter distance from a reactor, ~ 1 km away, can observe neutrino oscillations sensitive to the θ_{13} mixing angle. The dependence on this angle can be seen from the leading-order oscillations given by the form of Equation 1.14:

$$P(\bar{\nu}_e \to \bar{\nu}_e) \approx 1 - \sin^2 2\theta_{13} \sin^2 \left(1.27 \frac{\Delta m^2_{31} L}{E}\right) \tag{1.25}$$

The short baseline reactor experiments Chooz [32] and Palo Verde [33] were among the first to search for evidence of nonzero values of θ_{13}. Both experiments placed upper bounds on the mixing angle, but did not see significant electron anti-neutrino disappearance. Larger reactor experiments followed which could provide higher statistics, and in 2012, the Reactor Experiment for Neutrino Oscillation (RENO) [34], Daya-Bay [35] and Double Chooz [36], a successor experiment to Chooz, published results indicating reactor anti-neutrino disappearance, excluding $\theta_{13} = 0$.

Reactor neutrino experiments offer the most precise measurements of θ_{13}. Current reactor neutrino measurements place $\sin^2\theta_{13} \approx 0.0220$ with ~ 2 % uncertainty. Future reactor experiments, which plan to improve the energy resolution of inverse beta decay events and acquire more statistics, have the potential to probe three flavor, sub-leading effects with electron anti-neutrino disappearance. The next-most sensitive oscillation effects for reactor neutrinos depend on θ_{12} and Δm^2_{21}, and, with high enough energy resolution, modifications in the oscillation pattern due to the small differences between $|\Delta m^2_{32}|$ and $|\Delta m^2_{31}|$ may be observable with reactor neutrinos [37].

1.5.3 Atmospheric Neutrinos

Neutrinos are produced through the interaction of cosmic rays with nuclei in Earth's atmosphere. These interactions result in hadron showers of mostly pions and kaons, which decay into neutrinos and muons. The muons also decay into two neutrinos, i.e.,

$$\pi^+ \to \mu^+ + \nu_\mu, \quad \mu^+ \to e^+ + \bar{\nu}_\mu + \nu_e \tag{1.26}$$

$$\pi^- \to \mu^- + \bar{\nu}_\mu, \quad \mu^- \to e^- + \nu_\mu + \bar{\nu}_e \tag{1.27}$$

Both the positively- and negatively-charged hadrons are produced at approximately equal rates, and the number of neutrinos from Equation 1.26 and Equation 1.27 indicates that the flavor ratio present in the atmospheric neutrino flux is $(\nu_\mu + \bar{\nu}_\mu) : (\nu_e + \bar{\nu}_e) \sim 2 : 1$. Atmospheric neutrinos have energies spanning from a few MeV to several TeV, and travel on baselines to an observer on the Earth's surface ranging from $\sim$ 15 km if they are produced directly overhead, to $\sim$ 13 000 km if they are produced on the opposite side of the Earth and traverse the Earth's interior before arriving at a detector.

A convenient quantity for describing atmospheric neutrino baselines is the *zenith angle* which measures the neutrino angle with respect to the normal vector on Earth's surface. The relationship between zenith angle and baseline is demonstrated in Figure 1·5. The dependence can be derived for a sphere of radius r and a production height h, and is

$$L(\cos\theta_z) = -r\cos\theta_z + \sqrt{2rh + h^2 + r^2\cos^2\theta_z} \tag{1.28}$$

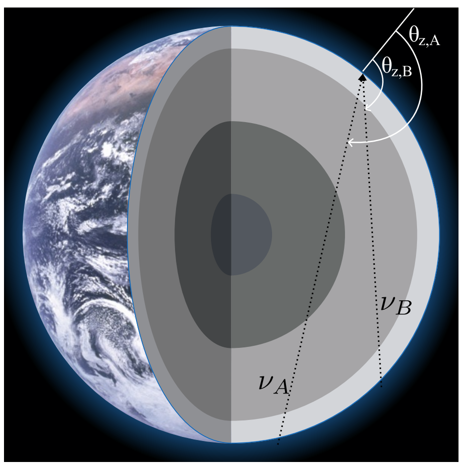

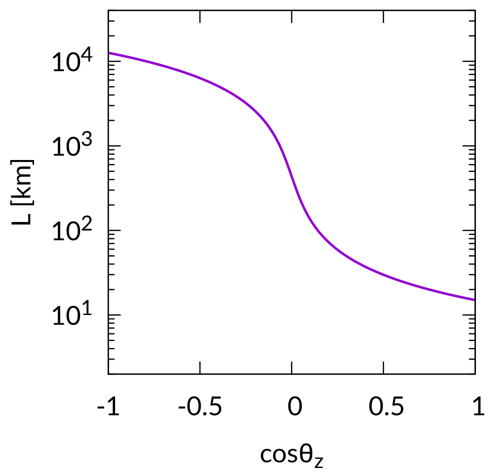

Figure 1·5: Atmospheric neutrino path length correspondence with zenith angle. **Left**: a diagram of atmospheric neutrino paths through the Earth, adapted from [38]. Neutrinos ν_A and ν_B travel on different baselines and pass through different layers of the Earth, e.g., ν_A passes through the crust, mantle, inner core, mantle, and crust before arriving at an exit point on the surface. The zenith angles are indicated as $\theta_{z,\mathrm{A}}$ and $\theta_{z,\mathrm{B}}$ respectively. **Right**: Approximate dependence of the atmospheric neutrino baseline L on the cosine of the zenith angle θ_z from Equation 1.28. Negative values of $\cos\theta_z$ correspond to neutrinos arriving from below the horizon, where their baselines are thousands of kilometers. Positive values of $\cos\theta_z$ correspond to neutrinos arriving from above the horizon, with a minimum baseline of $\sim 15\,\mathrm{km}$. The baseline changes rapidly around the horizon, $\cos\theta_z \sim 0$.

Atmospheric neutrinos were first detected in 1965 [39, 40]. Two decades later, hints of the atmospheric neutrino deficit began to emerge with measurements by the Irvine-Michigan-Brookhaven (IMB) [41] and Kamiokande-II [42] experiments. Kamiokande-II observed a deficit of muon-flavor neutrinos which could not be explained, even with large uncertainties on the atmospheric neutrino flux. The

Kamiokande-II successor experiment, SK, published a definitive observation of a deficit of atmospheric neutrino events in 1998 [43]. The deficit was found to occur for muon neutrinos arriving from below the detector, while muon neutrinos arriving from above, and electron neutrinos from all directions, agreed with the predictions of the atmospheric neutrino flux. Neutrino oscillations could explain both the deficit for upward-going muon neutrinos and lack of deficit elsewhere: the expected leading-order disappearance and survival probabilities for atmospheric neutrinos may be written as

$$P(\nu_e \to \nu_e) \approx 1 - \sin^2 2\theta_{13} \sin^2\left(1.27\frac{\Delta m^2_{31} L}{E}\right) \approx 1 \tag{1.29}$$

$$P(\nu_\mu \to \nu_\tau) \approx \sin^2 2\theta_{23} \sin^2\left(1.27\frac{\Delta m^2_{32} L}{E}\right) \tag{1.30}$$

for a small θ_{13} and $\Delta m^2_{31} \sim 10^{-3}\,\mathrm{eV}^2$. Equation 1.29 predicts minimal disappearance for the electron neutrinos, while Equation 1.30 predicts that muon neutrinos with energies $\sim 1\,\mathrm{GeV}$ traveling along baselines greater than $\sim 100\,\mathrm{km}$ "disappeared" through $\nu_\mu \to \nu_\tau$ oscillations.

Atmospheric neutrinos experience matter effects as they travel through the Earth. Atmospheric neutrinos arriving at a detector from below necessarily cross the dense inner layers near Earth's core, where the electron density can modify neutrino oscillation probabilities through the mechanism described in Section 1.4.2. Following Equation 1.19, the effective mixing angle $\theta_{13,\mathrm{M}}$, which governs $\nu_\mu \to \nu_e$ oscillations in matter, is given by

$$\sin^2 2\theta_{13,\mathrm{M}} = \frac{\sin^2 2\theta_{13}}{\sin^2 2\theta_{13} + \left(\frac{2aE}{\Delta m^2_{31}} - \cos 2\theta_{13}\right)^2} \tag{1.31}$$

Assuming small vacuum mixing such that $\cos 2\theta_{13} \approx 1$, the resonance condition is satisfied for $\Delta m^2_{31}/E \approx a$. This is attainable with atmospheric neutrinos. For example, choosing round numbers, for $\Delta m^2_{31} \sim 10^{-3}\,\mathrm{eV}^2$, $E \sim 1\,\mathrm{GeV}$, and the density near the Earth's core $\rho \sim 10\,\mathrm{g\,cm^{-3}}$ [44], then $\Delta m^2_{31}/E \approx 10^{-21}\,\mathrm{GeV}$ and a is similar:

$$\begin{aligned}
a &= 2\sqrt{2}G_F N_e = 2\sqrt{2}G_F \rho N_A(\hbar c)^3 \\
&\approx (2\sqrt{2}) \cdot 1.17 \times 10^{-5}\,\mathrm{GeV^{-2}} \cdot 10\,\mathrm{g\,cm^{-3}} \cdot 6.02 \times 10^{23} N\,\mathrm{mol^{-1}} \\
&\qquad \times \left(1.97 \times 10^{-14}\,\mathrm{GeV\,cm}\right)^3 \\
&\approx 10^{-21}\,\mathrm{GeV}
\end{aligned}$$

The above calculation applies to neutrinos if $\Delta m^2_{31} > 0$, and equivalently, the resonance condition is also present for anti-neutrinos if $\Delta m^2_{31} < 0$. Therefore, the sign of Δm^2_{31} predicts an enhancement of either $\nu_\mu \to \nu_e$ oscillations or $\bar{\nu}_\mu \to \bar{\nu}_e$ oscillations in atmospheric neutrinos. Thus, current and future atmospheric neutrino experiments can look for excess upward-going electron neutrinos or electron anti-neutrinos to determine the sign of Δm^2_{31}. This is illustrated in Figure 1·6, which shows $\nu_\mu \to \nu_e$ oscillations probabilities for atmospheric neutrinos and anti-neutrinos in the normal and inverted neutrino mass ordering scenarios. The resonant region occurs for $\cos\theta_z < 0$ and $E_\nu \sim 3\,\mathrm{GeV}$ for neutrinos in the normal ordering (top left) and for anti-neutrinos in the inverted ordering (bottom right).

1.5.4 Long Baseline Neutrinos

Beams of neutrinos can be produced artificially by accelerating protons onto fixed targets. The protons interact in the target material, producing hadron showers of mostly pions. The desired negatively- or positively-charged hadrons are then focused by a series of electro-magnets called *horns* which simultaneously deflect hadrons of the wrong charge. The focused hadrons pass into a decay volume where they decay into muons and muon neutrinos, i.e., following Equations 1.26 and 1.27. Any remaining hadrons and most of the muons are absorbed by dense material placed after the decay

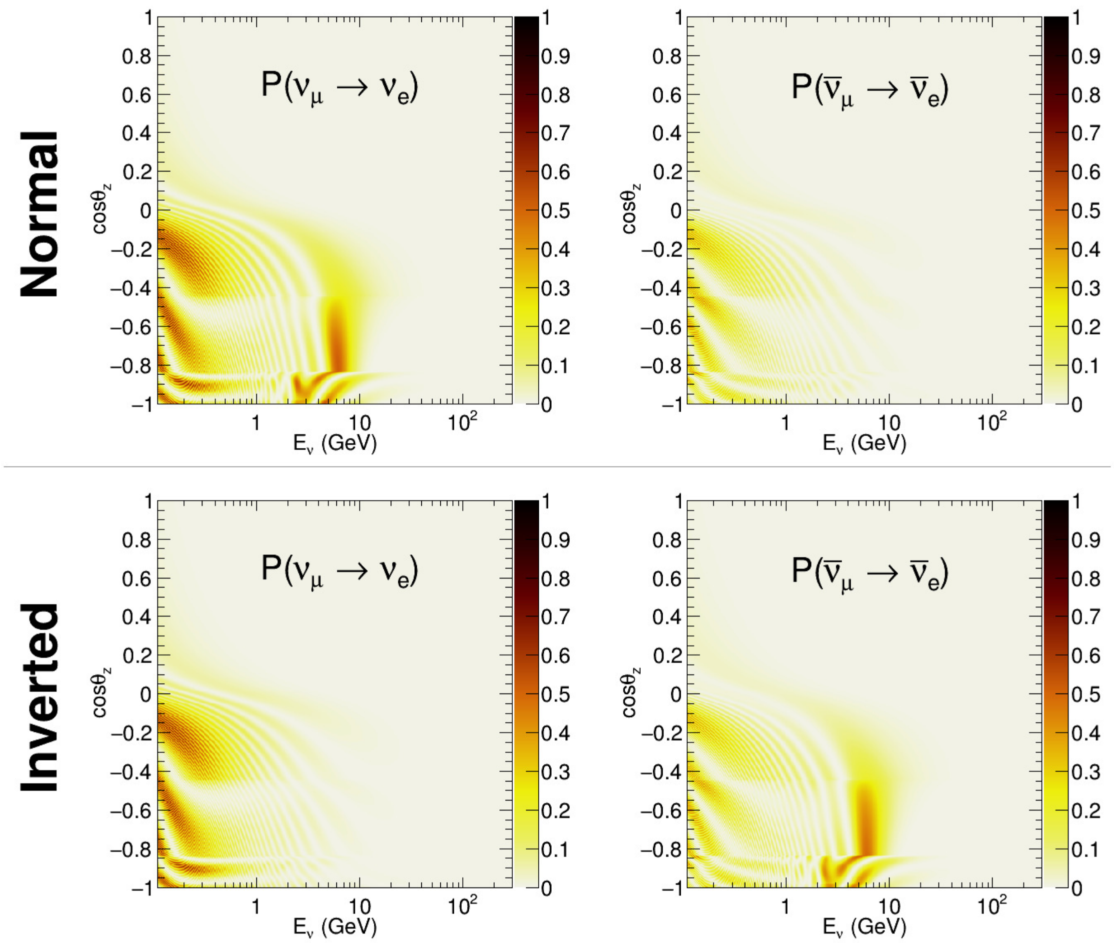

Figure 1·6: Electron neutrino appearance probabilities for atmospheric neutrinos and anti-neutrinos in each neutrino mass ordering scenario. The top row shows the probabilities in the normal ordering while the bottom row shows the probabilities in the inverted ordering. The left column shows the probabilities for neutrinos while the right column shows the probabilities for anti-neutrinos. A resonance region can be seen for $\cos\theta_z < 0$ and $E_\nu \sim 3\,\text{GeV}$ in the top left and bottom right panels.

volume, leaving just the highly-focused, highly-pure ν_μ or $\bar{\nu}_\mu$ neutrinos, to propagate as a beam.

A typical long baseline experiment consists of a neutrino beam with peak energy $\sim$ 1 GeV, a near detector, and a far detector. The near detector is positioned to observe the un-oscillated neutrino beam at a short distance, usually hundreds of meters, while the far detector measures the neutrino beam after oscillations at distances hundreds of kilometers away from the production point. The near and far detector, by observing the same neutrino beam, make simultaneous measurements of the beam that constrain many of the systematic uncertainties in the experiment.

Since long baseline experiments only observe neutrinos at one distance, preliminary measurements of $|\Delta m^2_{32}|$ by atmospheric neutrino experiments were needed to establish likely values of $|\Delta m^2_{32}|$ and $\sin^2\theta_{23}$. The first long baseline experiment, KEK to Kamioka (K2K), sent a beam of neutrinos along a 250 km baseline from the KEK accelerator complex towards the existing SK detector. K2K published its first oscillation results in 2002, in agreement with measurements of θ_{23} and $|\Delta m^2_{32}|$ by SK [45]. Subsequent long baseline experiments followed: The Main Injector Neutrino Oscillation Search (MINOS) experiment [46], which operated at Fermi National Accelerator laboratory from 2005 to 2016, utilized magnetized calorimeters in its far detector to separate particles based on charge, suppressing contamination of neutrinos or anti-neutrinos in the opposite beam configuration, and improving the energy determination of neutrino events. MINOS also confirmed the atmospheric neutrino measurements.

Long baseline experiments are able to probe θ_{13} and δ_{CP} through ν_e appearance. Here, a full three-flavor framework is required. Leading-order oscillations are controlled by combinations of θ_{13} and θ_{23} mixing angles, while the next-largest amplitude involving all three mixing angles and δ_{CP} is approximately 20% of the leading-order term [47]. The maximum ν_e appearance corresponds to the L/E value that predicts a minimum $\nu_\mu \to \nu_\mu$ disappearance. Since L is fixed, long baseline experiments tune their neutrino beams to have the highest flux near this L/E value. The T2K experiment, the successor to K2K, refined the long baseline technique by sending its neutrino beam at an off-axis angle with respect to SK, narrowing the observed energy spectrum [48]. Although at the time, it was unclear if θ_{13} was nonzero, T2K observed hints of electron neutrino appearance in 2011, suggesting a nonzero value of θ_{13} and the possibility of measuring δ_{CP} [49]. The T2K measurement was confirmed and measured precisely by reactor experiments shortly after (see Section 1.5.2). In 2015, the NOvA experiment also observed electron neutrino appearance in a long baseline experiment [50].

The T2K and NOvA long baseline experiments have made the most precise measurements of $|\Delta m^2_{31}|$, $\sin^2\theta_{23}$ and δ_{CP}. Current measurements place $\sin^2\theta_{23} \approx 0.55$, $|\Delta m^2_{31}| \approx 2.45 \times 10^{-3}$ eV^2, and $\delta_{\mathrm{CP}} \approx 1.3\pi$ radians. Future long baseline experiments will employ more powerful neutrino beams, resulting in higher statistics, and higher-resolution detectors to enable better neutrino energy measurements.

1.6 Present Status of Oscillation Measurements

Neutrino experiments using the various sources described in Section 1.5 have measured all PMNS oscillation parameters and mass splittings. The global average of measurements are summarized in Table 1.2. Despite the high precision of many PMNS parameter measurements, the uncertainties still permit several fundamentally different neutrino oscillation scenarios. This section will describe several of the open questions in neutrino oscillation searches.

Parameter	Value	Fractional Uncertainty (%)
$\sin^2\theta_{12}$	0.307 ± 0.013	4
$\sin^2\theta_{13}$	0.0220 ± 0.0007	3
$\sin^2\theta_{23}$	0.546 ± 0.021	4
Δm^2_{21} (eV^2)	$(7.53 \pm 0.18) \times 10^{-5}$	2
Δm^2_{32} (eV^2)	$(2.453 \pm 0.033) \times 10^{-3}$	1
δ_{CP}/π (rad)	1.36 ± 0.20	15

Table 1.2: Listing of averaged PMNS parameters and mass splitting measurements from various experiments [51]. Note that the sign of $\Delta m^2_{31,32}$ is unknown, and results are shown assuming $\Delta m^2_{32} > 0$.

1.6.1 Octant of θ_{23}

It is unknown whether or not θ_{23} is in the upper octant, $\theta_{23} > \pi/4$, or the lower octant, $\theta_{23} < \pi/4$. Maximal 2-3 mixing, $\theta_{23} = \pi/4$, or $\sin^2\theta_{23} = 0.5$, is also allowed. Values of θ_{23} near $\pi/4$ imply an approximate μ-τ lepton flavor symmetry in the PMNS matrix. The symmetry holds exactly, e.g., $|\mathbf{U}_{\tau i}| = |\mathbf{U}_{\mu i}|$, if $\delta_{\text{CP}} = \pm\pi/2$ and $\theta_{23} = \pi/4$, as can be see from Equation 1.8. The typical implication of a symmetry in a physical system is a conserved quantity, so the proximity of θ_{23} to $\pi/4$ could be a hint of a new conservation law. A review of the flavor symmetries in neutrino mixing may be found in [52].

1.6.2 Value of δ_{CP}

Charge-parity (CP) violation is a difference in particle interactions under the simultaneous interchange of a particle for its anti-particle (charge) and its direction (parity). CP violation is a necessary condition for explaining the large matter–anti-matter asymmetry of the universe [53]. While CP violation has been observed for quarks as early as 1964 [54], the amount of CP violation observed in quark interactions is too small to fully account for all of the matter-anti-matter asymmetry in the universe. Neutrinos offer another possible channel for CP violation. The phase δ_{CP} from the PMNS mixing flips sign between neutrinos and anti-neutrinos. Values of δ_{CP} which are non-integer multiples of π, therefore, predict different amounts of mixing for neutrinos and anti-neutrinos, a clear indication of CP violation.

Current neutrino oscillation experiments are in tension over observed values of δ_{CP}. In 2020, T2K reported a rejection of the δ_{CP} scenario at an over 99% confidence level [55], while in 2021, NOvA reported a measurement more consistent with $\delta_{\mathrm{CP}} = \pi$ [56], disfavoring the T2K result and implying minimal CP violation. These results are shown in Figure 1·1.

1.6.3 Neutrino Mass Ordering

Having explored the theory and historical context of neutrino oscillation measurements, we return to the original question of this work: there are two distinct scenarios for the neutrino mass ordering, depicted in Figure 1·7. In the normal ordering, there is one heavy neutrino, ν_3, relative to the ν_1 and ν_2. This implies $\Delta m^2_{32,31} > 0$. The situation is reversed in the inverted ordering, where ν_2 and ν_1 are heavier than ν_3.

The neutrino mass ordering has implications for both neutrino oscillations and other areas of physics. The absolute sum of neutrino masses is an input to cosmological models describing the evolution of large scale structure in the universe [57]. The neutrino masses also control the expected rate of the neutrino-less double beta decay process, with larger masses predicting higher rates [58]. This process, if observed, would have profound implications for our understanding of neutrino masses. Additionally, as the neutrino mass ordering is sensitive to matter effects, the energy spectrum of neutrinos produced in supernova is expected to depend on the mass ordering [59]. Neutrinos are a powerful probe of supernova dynamics, since 99 % of a supernova's energy is radiated in neutrinos.

The neutrino mass ordering remains unknown because the leading-order neutrino

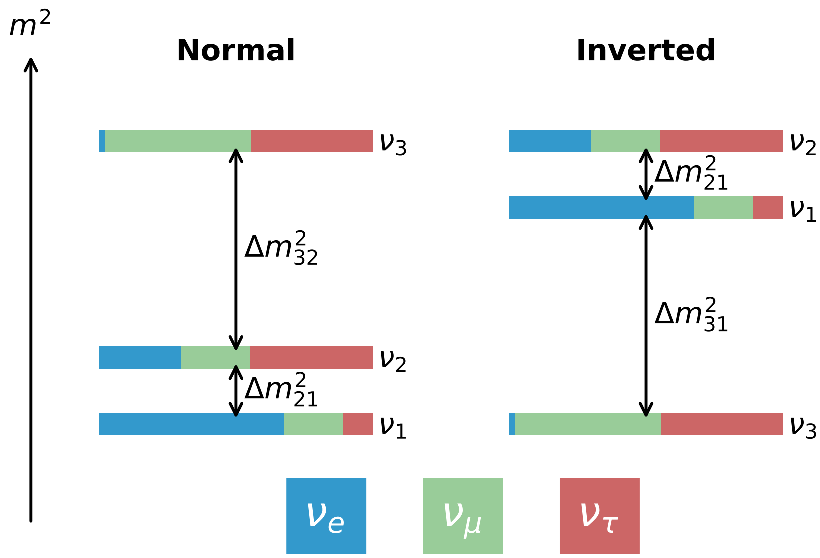

Figure 1·7: Schematic of the unknown neutrino mass ordering. The neutrino mass states, ν_1, ν_2 and ν_3 can be ordered in two distinct ways: with ν_3 as the heaviest (normal) or as the lightest (inverted) neutrino. The flavor content of the mass states, given by the squared row elements of the reciprocal PMNS matrix, are shown as different colors. The PMNS parameters are the central values from Table 1.2, with $\delta_{\mathrm{CP}} = 0$.

oscillation probabilities are independent of the sign of the mass splittings. While matter effects allowed solar neutrino experiments to determine $\Delta m^2_{21} > 0$, the same analysis is more difficult with terrestrial neutrinos whose oscillations are instead governed by Δm^2_{32}. Further, we have seen already seen how the T2K and NOvA experiments have made measurements of the mass ordering that are difficult to reconcile.

Atmospheric neutrinos are sensitive to the mass ordering through resonant oscillations induced by matter effects. However, this approach comes with challenges: Atmospheric neutrino experiments must contend with the intrinsic electron neutrinos already present in the atmospheric neutrino flux. Long baseline experiments do not have this issues, although the matter effect for neutrino beams traveling near Earth's surface is smaller than for atmospheric neutrinos passing near the Earth's core, resulting in less sensitivity to the mass ordering. Future efforts to determine the neutrino mass ordering using detectors with superior energy resolution and reactor neutrinos are also planned [60].

1.7 Thesis Overview

This thesis will present a measurement of the unknown neutrino mass ordering and of neutrino oscillation parameters $\sin^2\theta_{23}$, $|\Delta m^2_{32}|$, and δ_{CP} using atmospheric neutrinos. The atmospheric neutrino data are collected in the Super-Kamiokande detector over 6511.3 live-days, corresponding to a total exposure of 484 kiloton-years. The SK detector is described in Chapter 2, and the simulation of atmospheric neutrino events used in the analysis is described in Chapter 4. Results of an analysis using only SK atmospheric neutrino data are presented in Chapter 5. Chapter 6 then presents an analysis of the SK data using external constraints, namely on $\sin^2\theta_{13}$ from reactor neutrino experiments, and on δ_{CP}, $|\Delta m^2_{31}|$, and $\sin^2\theta_{23}$ using a model of the T2K long baseline experiment.

Chapter 2

The Super-Kamiokande Detector

The Super-Kamiokande (SK) detector [61] is a 41.4 m tall, 39.3 m diameter, cylindrical water tank, containing 50 kt of ultra-pure water, illustrated in Figure 2·1. The SK detector is located in Gifu prefecture, Japan, underneath Mount Ikenoyama. The mountain provides shielding from cosmic rays, approximately equivalent to a water depth of 2700 m. A ground-level, kilometer-long tunnel provides access to the SK site, which includes a network of experimental halls, water circulation systems, and control rooms for monitoring detector operation. Excavation of the SK cavern began in 1991, and construction of the detector finished in 1996. Data taking officially began on April 1, 1996.

The original goals of the SK experiment were to search for nucleon decay and to conclusively resolve the hints of the solar and atmospheric neutrino disappearance observed by the IMB and Kamiokande experiments [62]. Members of both the IMB and Kamiokande collaborations worked together to build SK. The volume of the SK detector is approximately 17 times that of the original Kamiokande detector.

The SK detector has operated nearly continuously since its construction. The SK data-taking periods are divided into phases, SK I-V and SK Gd, summarized in Table 2.1. There were three significant gaps in SK data taking. At the end of the SK I phase, the detector was drained to replace photomultiplier tubes (PMTs) which had failed during its first five years of operation. During re-filling, one of the PMTs imploded, creating a shock wave and chain reaction which destroyed nearly half of all

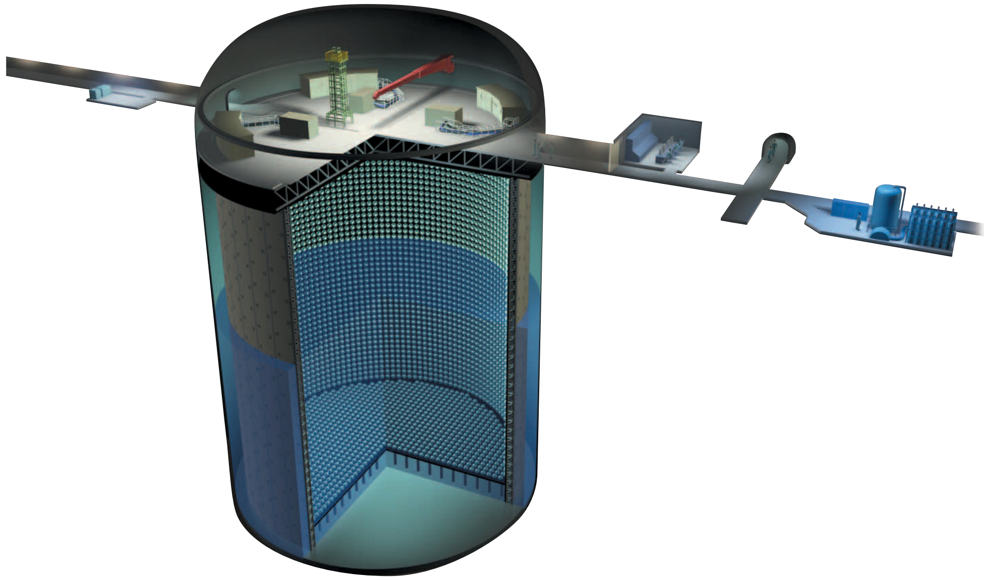

Figure 2·1: Illustration of the SK detector, half-filled with water. The SK detector resides in an excavated pit underneath Mount Ikenoyama, accessed via tunnel. The figure shows the tunnel which connects the control room and top dome areas, which are accessible during operation. The tank is divided into two regions, the inner detector (ID) and outer detector (OD). Both regions are instrumented with photomultiplier tubes (PMTs) See text.

PMTs in the detector. The experiment proceeded: acrylic covers were installed on the remaining PMTs, and the PMTs were re-distributed across the detector. The detector operated in this configuration during the SK II phase until replacement PMTs could be installed. Installation of replacement PMTs occurred in 2006, restoring the detector to full operation for the SK III phase. The detector then operated stably for 12 years. In 2008, SK underwent an electronics upgrade which did not require the tank to be drained. The electronics upgrade marked the beginning of the SK IV phase. In 2018, the detector was drained a third time for major refurbishment work, including the installation of a new water system capable of recirculating gadolinium in the detector's water, PMT replacement, cleaning, and leak repair. Data taking resumed after the work in 2019, initiating the pure-water SK V phase. In 2020, gadolinium was dissolved into the detector's water, marking the beginning of the SK Gd phase. The phases of SK are summarized in Table 2.1.

Phase	Dates	Livetime (Days)	Photo-coverage	Electronics	Target
SK I	1996–2001	1489.2	40%	ATM	H_2O
SK II	2002–2005	798.6	19%	ATM	H_2O
SK III	2006–2008	518.1	40%	ATM	H_2O
SK IV	2008–2018	3244.4	40%	QBEE	H_2O
SK V	2019–2020	461.0	40%	QBEE	H_2O
SK Gd	2020-Present	—	40%	QBEE	$H_2O + Gd$

Table 2.1: Operating conditions for the six data-taking phases of the SK experiment. SK II had reduced photocoverage following the loss of approximately half of the PMTs at the end of SK I. At the time of writing, SK Gd is ongoing. Data from SK Gd is not presented in this thesis.

This chapter will discuss the SK detector concept, outline the different detector systems, and present the different methods for calibrating the response of the detector to neutrino interactions.

2.1 Detection Principles

The SK detector uses Cherenkov radiation [63] to detect charged particles passing through the detector's water. Charged particles moving faster than the speed of light in a medium cause the electric dipoles of molecules in the medium to coherently align, creating an outward emission of radiation. The detection of Cherenkov radiation in SK is shown schematically in Figure 2·2. Cherenkov radiation has several characteristics which depend on the index of refraction n of the medium. The minimum momentum required for particles to emit Cherenkov radiation is given by

$$p_{\text{Thresh.}} = \frac{mc}{\sqrt{n^2 - 1}}, \tag{2.1}$$

and the Cherenkov radiation is emitted at a fixed angle, given by

$$\theta_C = \cos^{-1}(1/\beta n), \tag{2.2}$$

where β is the particle's velocity expressed as a fraction of the speed of light. The emitted Cherenkov photon spectrum per unit length is given by the Frank-Tamm formula [63],

$$\frac{d^2N}{dx d\lambda} = \frac{2\pi\alpha Z^2}{\lambda^2}\left(1 - \frac{1}{n^2\beta^2}\right) \tag{2.3}$$

where λ is the wavelength, Z is the charge of the particle, and α is the fine structure constant. In water, n is wavelength-dependent, but typical values are $n \approx 1.33$ with variations of only a few percent for visible wavelengths. This gives threshold momenta for particles of $p_{\text{Thresh.}} \approx 1.14m$, e.g., about 120 MeV/c for muons. The Cherenkov angle for particles with $\beta \approx 1$ is 42° in water. In water, a charged particle produces about 3000 photons per cm in the 300 nm to 550 nm wavelength range.

Cherenkov photons in SK propagate through the water to the PMTs on the detector walls. Photons can knock out electrons on a PMT's surface via the photoelectric effect. These "photoelectrons" are then accelerated onto a series of conductive plates called dynodes using electric fields inside the PMT, knocking out additional electrons at each dynode. The electrons eventually reach the last dynode, which produces a few-nanosecond wide current pulse with a voltage proportional to the number of electrons. The typical amplification factor, or *gain*, of an SK PMT is 10^7, and the timing resolution is 2 ns. PMTs with pulses above a specified threshold are considered *hit*. In aggregate, the Cherenkov photons form ring patterns of hit PMTs due to the fixed emission angle given by Equation 2.2. The times, charges, and known positions of

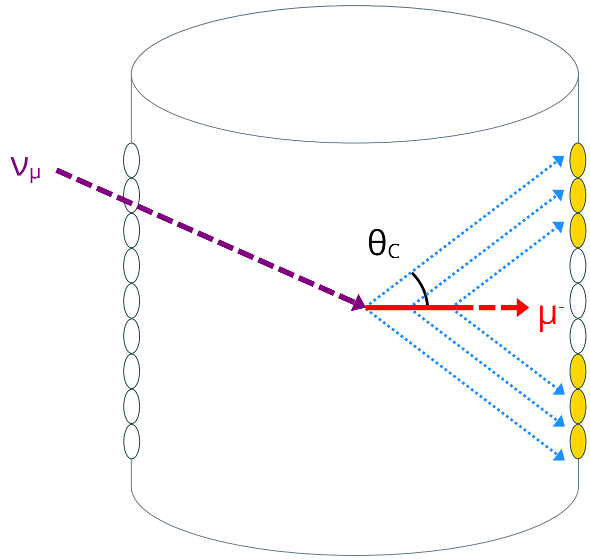

Figure 2·2: Illustration of Cherenkov radiation detection in SK. Charged particles such as muons (μ^-) with momentum greater than the threshold given by Eq. Equation 2.1 emit Cherenkov radiation at an angle, θ_C, given by Eq. Equation 2.2. Note that neutral particles like neutrinos (ν_μ) and particles below the Cherenkov threshold, indicated by dashed tracks, do not emit Cherenkov radiation. The Cherenkov radiation is detected by PMTs on the detector walls (yellow ellipses).

each hit PMT are used to determine properties of the particle, including its energy, direction, and type.

2.2 Detector Systems

2.2.1 Inner Detector

While the total volume of the SK tank is 50 kt, particles are reconstructed within the 32 kt inner detector (ID), an optically-isolated region within the main tank. The ID contains over 11 000 20-inch PMTs, mounted to a steel structure situated between 2 to 3 m from the tank walls. The PMTs are arranged orthogonally, providing an average photocoverage of 40 %.

A schematic view of the Hamamatsu R3600 20-inch ID PMT is shown in Figure 2·3. Following the accident in 2001, acrylic covers were installed around all 20-inch

ID PMTs to prevent future chain reactions in the event of another PMT implosion. The installation of a 20-inch PMT in a cover during 2018 is also shown in Figure 2·3. The cover is not water-tight, but, in the event of an implosion, reduces the flow rate of water able to enter the PMT. The photocathode is hemispherical bialkali glass, chosen for its high quantum efficiency for Cherenkov radiation wavelengths and low chance of spontaneous photoelectron emission. The typical quantum efficiency for a 20-inch PMT is shown versus the Cherenkov emission spectrum, from Equation 2.3, in Figure 2·4. The light collection of the 20-inch PMTs also depends on the incident angles of photons on the photocathode. This dependence is measured using dedicated calibration sources.

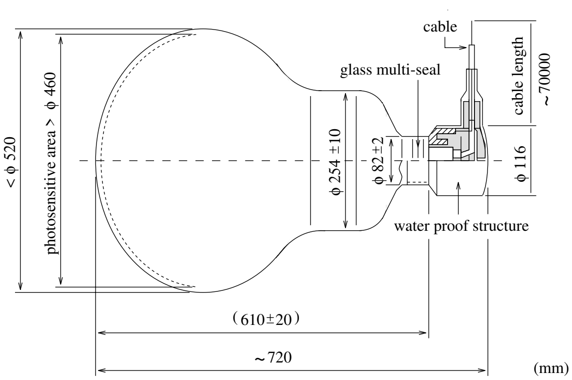

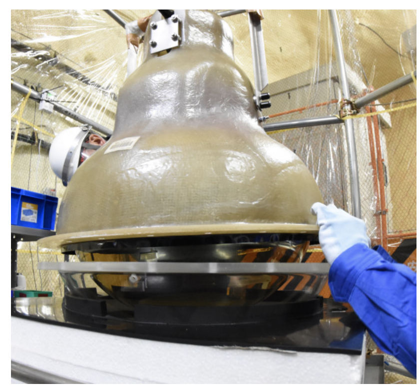

Figure 2·3: The 20-inch ID PMT. **Left**: Schematic diagram of a 20-inch ID PMT from [61]. **Right**: Installation of a 20-inch PMT in the acrylic shock-proof cover.

2.2.2 Outer Detector

The 2.2 m region between the tank walls and the steel support structure of the ID PMTs defines the 18 kt cylindrical outer detector (OD) volume. The OD primarily enables SK to separate cosmic muons from neutrino events: Cosmic muons entering the detector deposit light in both the ID and OD, while neutrinos may interact in the ID without leaving a visible signature in the OD. The OD is also used to determine

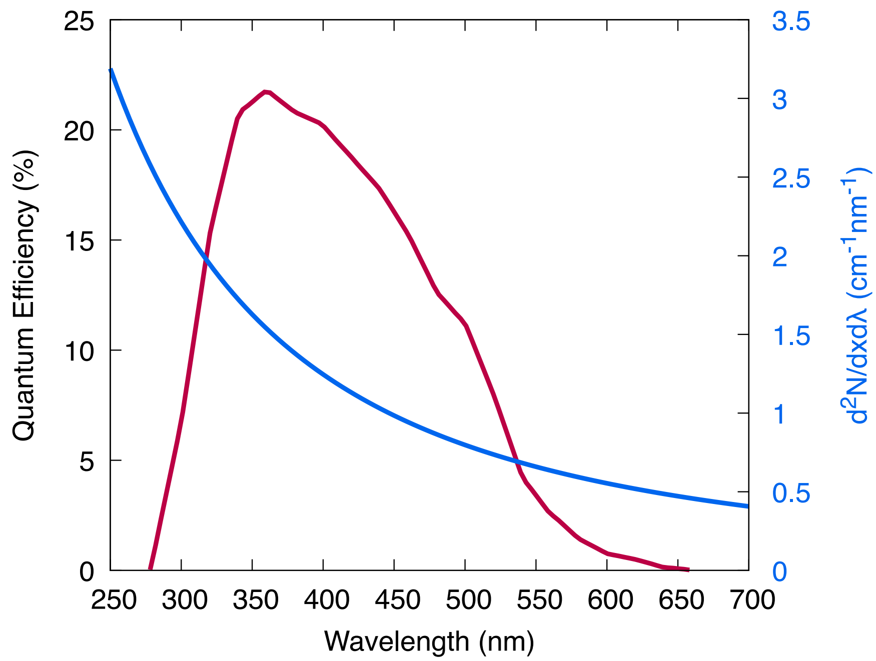

Figure 2·4: The quantum efficiency of a 20-inch PMT as a function of wavelength. The spectrum of photos produced per cm from Equation 2.3 is also shown using the right vertical axis. The quantum efficiency curve is taken from [61].

if a particle stopped within the ID or exited the ID. Particles which are visible in the ID and then exit into the OD create hits in both regions, with OD hits occurring later in time. Due to the steel support structure, there is a 55 cm un-instrumented region between the ID and OD.

Because the OD's primary role is to veto events rather than reconstruct them, light collection is its highest priority over precise timing and charge determination. Approximately 1800 8-inch PMTs are mounted to the inner wall of OD. Each PMT has a $60 \times 60\,\mathrm{cm}^2$ wavelength-shifting acrylic plate optically coupled to its photocathode, which guides light into the PMT, effectively increasing its area. The walls of the OD are covered in reflective white Tyvek sheets which increase the chance of any light being detected. Several OD PMTs are shown in-situ in the OD in Figure 2·5. The top and bottom end-cap regions of the OD also contain the steel beams used to support

Figure 2·5: Pictures of the SK OD. **Left**: The outer detector, viewed from below & looking up. The OD PMT mounting configuration is shown. PMTs are approximately 2 m apart. The semi-transparent square plates around each PMT are the wavelength-shifting plates. The white material is the reflective Tyvek. **Right**: The OD top end-cap region. The segmentation Tyvek forming the wall optically separates the top end-cap region from the rest of the OD. The steel support beams and the water system plumbing in the top end-cap region are also visible.

the ID[1]. After the SK II phase, additional Tyvek, extending from the steel structure sides to the top and bottom of the SK tank, was installed to optically separate the top and bottom OD volumes from the barrel volume. This Tyvek is called *segmentation Tyvek*. Both the steel support structure and the segmentation Tyvek in the top OD regions can be seen in Figure 2·5.

While the OD PMTs all share similar geometries, they are comprised of different models. The oldest OD PMTs are Hamamatsu R1408s recycled from the IMB experiment, which operated between 1981 and 1991. At the end of the SK IV phase, approximately 30% of the OD PMTs were IMB type. In 2018, many were replaced, lowering the number to 20% IMB type starting with SK V. The remaining OD PMTs are a newer Hamamatsu R5912 model, which were installed after the SK I, SK II,

[1] The steel structure's impact on light collection in these regions was studied, and found to reduce the travel distance of light in the outer detector. In simulations of the detector, this is accounted for as a penalty term to each photon's chance of absorption. See Chapter 4.

and SK IV phases.

2.2.3 Water System

The SK detector uses ultra-pure water as its detection target. The water's purity affects the attenuation length of light, so regular purification of the water is essential to detector operation. The SK I-IV phases all operated with the water system described in [61]. Starting with the SK V phase, the water system was upgraded to allow Gadolinium to be recirculated into the water. A detailed description of the new water system may be found in [64], and a summary is provided here.

The purpose of the water system is to continuously re-circulate and purify the water. The SK I-IV water system processed 30 t to 60 t of water per hour during SK IV, fully re-circulating the water approximately every month. In both the SK I-IV and present water systems, the water passes through a series of filters and purifiers which remove particulate matter. If not removed, the particulate matter can reduce the transparency of the water to Cherenkov light, or emit radioactive backgrounds such as radon.

For the SK I-IV water system, the water was filtered though a passive 1 µm mesh to remove larger particulates. Then, the water was cooled to 13 °C. The cooling helps both to maintain a uniform level of dark noise in the PMTs and also to prevent bacterial growths. The water then passed through a cartridge polisher which removed ion contaminants, and an ultra-violet (UV) light which killed any remaining bacteria. Radon-reduced air was then dissolved into the water to improve the efficiency of the next step, passage through a vacuum de-gassifier, used to remove any dissolved gasses in the water. Finally the water passed into an ultra-filter and membrane de-gassifier which removed sub-µm particulates and any remaining radon gas, respectively. The number of particulates $< 0.2\,\mu\text{m}$ in size entering the ultra-filter was estimated to be $1000\,\text{cm}^{-3}$, which was reduced to $6\,\text{cm}^{-3}$ after. Radon concentration for water returning to the SK tank after filtration was estimated to be $0.4\,\mathrm{mBq\,m^{-3}}$.

This thesis will not describe the gadolinium loading of SK, however, the water system designed for use with gadolinium was implemented starting with the SK V pure-water phase. Data from the SK V phase is included in the analysis presented in this thesis. The main differences of the SK V water system compared with the SK I-IV system are the installation of various resin-based purifiers which remove heavier ion contaminants associated with gadolinium sulfate, heat exchangers, which allow more precise control of the water temperature, buffer tanks to prevent water losses, and a redundant system capable of recirculating an additional 60 t of water per hour, for a total of 120 t per hour. Figure 2·6 shows a schematic view of the present SK V+ water system. In the new system, water from the SK tank passes through UV filters and a passive mesh filter, similarly to the SK I-IV system. The water then passes through new cation- and anion-exchange resins which remove positive and negative ion contaminants. The water then passes through ultra-filters and membrane degassifiers, as in the SK I-IV system. Water is not lost from the SK V water system: Any water rejected by a filtration process is re-circulated into secondary buffer tanks which can then pass through the filtration system again.

2.2.4 Electronics & Data Acquisition

Dedicated electronics enable the readout of precise charge and timing information from the PMTs. The SK electronics are also responsible for using the quantity and time distribution of PMT hits to trigger the detector to record data during particle interactions.

High voltage and PMT signals from the approximately 11 000 ID PMTs and 1800 OD PMTs are carried by cables between the inside of the tank and the top of the detector. Cables from each quadrant of the detector enter one of four electronics *huts*, small rooms which house high voltage supplies and readout electronics for each set

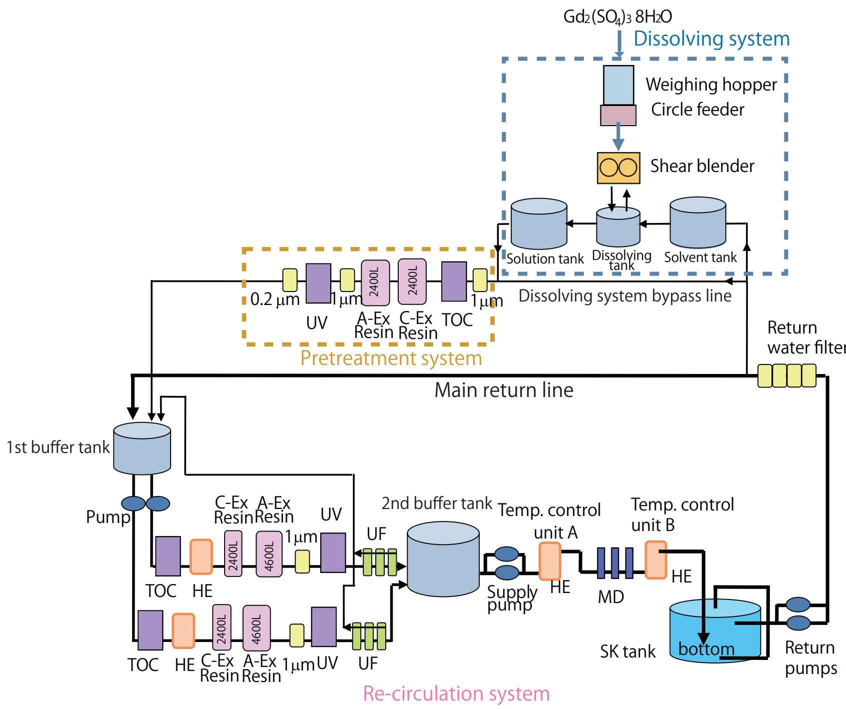

Figure 2·6: The water system used beginning with the SK V period in 2018, reproduced from [64]. Gadolinium was not present during SK V, so the only elements relevant to this thesis are the re-circulation loop beneath the bold black line, i.e., excluding the dissolving and pretreatment systems. The cation- and anion- exchange resins (C-Ex and A-Ex) were not present in the original SK I-IV water system, and remove contaminants associated with gadolinium sulfate. The TOC (total organic carbon reduction) and UV represent types of UV filters, the UF represents an ultra-filter, the HE represents a heat-exchanger, and the MD represents a membrane de-gassifier.

of PMTs. The primary difference between the high voltage systems between the ID and OD is the per-PMT adjustable high voltage for each ID PMT provided by CAEN SY527 high voltage main frames. In contrast, the high voltage for the OD PMTs is distributed across custom “paddle cards”, which send one high voltage to 12 PMTs at once. The OD PMTs also use a combination cable which carries both high voltage and the light detection signal.

The SK detector has used two distinct sets of readout electronics. The first set was in use for the SK I-III phases, and was subsequently replaced beginning with SK IV.

SK I-III Electronics

For SK I-III, PMT signals were processed by 12-channel ATM boards, which recorded the total charge and arrival time of each PMT pulse via a combined analog-to-digital converter (ADC) and time-to-digital converter (TDC) circuit. The charge signal was then split into several other readout systems. One signal was sent to a global trigger system, which tracked the total integrated charge of all PMTs above a specified threshold. One of the other split PMT signals was sent to a charge-to-analog converter (QAC), and another was used to start a constant current integrator. When the global trigger system crossed a total charge threshold, it output a signal to the QAC and current integrator. The signal height of the integrated constant current was converted to the PMT's timing offset relative to the trigger, and the PMT charge and time information from the QAC was converted and stored digitally. A redundant integration and charge readout system was in place for each PMT so that triggers in rapid succession could be stored without dead time. The QACs had to be read out after accumulating 1.3 µs of data, so ID PMT data was stored in 1.3 µs segments. For a comprehensive review of SK I-III ID electronics, see [61, 65].

The OD readout electronics for SK I-III were fundamentally similar to the ID, but used different hardware. The OD PMT signals were read out via custom charge-to-time converter (QTC) chips which converted the signal into a fixed-width pulse for easier digitization. The rising edge of this signal could be interpreted as the hit time, and the width was proportional to the total charge. The OD PMT signals were similarly fed into the global trigger system, and, in the event of a trigger, were digitized and saved into memory buffers for offline processing. A larger window, 16 µs, of OD hits could be stored than ID hits, which was useful for vetoing triggers when activity in the ID was preceded by background-like activity in the OD.

The global trigger system issued different triggers based on the number of hit PMTs. Separate low-energy and high-energy trigger thresholds were set to select physics events for different analyses. The number of hits from the outer detector PMTs could also be used as an independent trigger. The triggers used for SK I-III are summarized in Table 2.2.

SK IV+ Electronics

The SK I-III electronics were replaced in 2008 with both new physical readout circuit boards for both the ID and OD PMTs and a software trigger [66, 67]. The new boards are QTC-based electronics with ethernet (QBEEs), which, similar to the OD electronics of SK I-III, output a single pulse, encoding the time and total charge of each signal. The QBEEs have several advantages over the ATM boards of SK I-III. First, QBEEs have multiple gain settings, set in a ratio of $1 : \frac{1}{7} : \frac{1}{49}$. Each QBEE can process a signal with the three gain settings simultaneously, and return only the lowest setting which is not saturated. Thus, higher-charge PMT signals can be recorded along side lower-charge signals while still retaining acceptable charge resolution. The dynamic range of PMT signals recorded by QBEEs in an event is five times that of the ATM system. Another advantage is the length of the readout: ATM boards were cleared of their charges after 1.3 µs, but QBEEs can record 40 µs of data before needing to be read out. Each QBEE receives signals from 20 PMTs. The PMT signals from each QBEE are then sent to merger computers which apply trigger logic in software.

A major goal of the SK IV hardware upgrade was to enable a variable-length event time window using a software trigger. Longer event windows help to contain delayed particle processes, such as muon or charged pion decays and neutron captures, following the primary interaction (see Section 3.2). In particular, the AFT, or "after," trigger was implemented to save several hundreds of microseconds of data following activity in the ID with no activity in the OD. A summary of the triggers used during SK data taking is presented in Table 2.2.

Trigger	SK I-III		SK IV+	
	Logic	Event Window (μs)	Logic	Event Window (μs)
SLE	5.7 $\rightarrow$ 3.5 MeV equivalent ID hits, and vertex fit within ID	1.3	34 $\rightarrow$ 31 ID hits in 200 ns	$[-0.5, 1.0]$
LE	29 ID hits in 200 ns	1.3	47 ID hits in 200 ns	$[-5, 35]$
HE	31 ID hits in 200 ns	1.3	50 ID hits in 200 ns	$[-5, 35]$
SHE	—	—	70 $\rightarrow$ 58 ID hits in 200 ns	$[-5, 35]$
OD	19 OD hits in 200 ns	16	22 OD hits in 200 ns	$[-5, 35]$
AFT	—	—	SHE, no OD	$[35, 535]$

Table 2.2: Triggers used in the different SK data-taking phases. Hit requirements reflect the approximate numbers used, because the definitions were updated throughout data taking in response to changes in PMT dark rates and failed PMTs. SLE refers to "super low energy," and was implemented in the SK I-III periods using a dedicated external computer to filter events based on the charge in units of MeV and fit event vertices in real time. LE refers to "low energy," HE refers to "high energy," SHE refers to "super high energy," and "AFT" refers to "after." AFT triggers were introduced by means of a software trigger implemented at the start of the SK IV phase.

For all SK phases, digitized PMT hit charge and time information in a time window around each trigger is assembled into "events" on dedicated computers inside the mine. Event data is periodically transferred out of the SK detector area via optical fiber to nearby off-site computers for offline processing and storage. Events are stored in the ZEBRA file format [68], and also as ROOT [69] files.

2.3 Calibration

The response of each SK PMT is tuned to controlled calibration sources to ensure an accurate and uniform response to physics events. In addition, the SK water is studied to characterize the light propagation within the detector.

2.3.1 ID PMT Calibration

The calibration of the ID PMTs begins with high voltage tuning for a subset of 420 ID PMTs designated as "reference" PMTs before installation in the detector. The high voltages of the reference PMTs are tuned to light from a xenon lamp connected to a scintillator ball via optical fiber, so that each PMT's charge output is identical. These reference PMTs are then installed in the SK tank in four vertical strip patterns, one along each quadrant of the detector. The scintillator ball, connected to the same xenon lamp, is then lowered into the tank center, and serves as an isotropic light source, illuminating all PMTs. Since the charge output of the reference PMTs to the light intensity is known in advance, the high voltages of the other, non-reference, PMTs can be adjusted to match the charge response of reference PMTs at the equivalent distance from the scintillator ball. The geometric pattern of the reference PMTs and the scintillator ball tuning method is demonstrated in Figure 2·7.

The high voltage tuning results in a coarse calibration of PMT response, so following the tuning, the relative gain of each PMT is precisely determined. The relative gains are assessed using separate high- and low-intensity light sources. The high-intensity source sends multiple photons to each PMT, such that the charge response of each PMT, Q_i, may be written as:

$$Q_i \propto I_{\text{High}} \times a_i \times \text{QE}_i \times G_i, \tag{2.4}$$

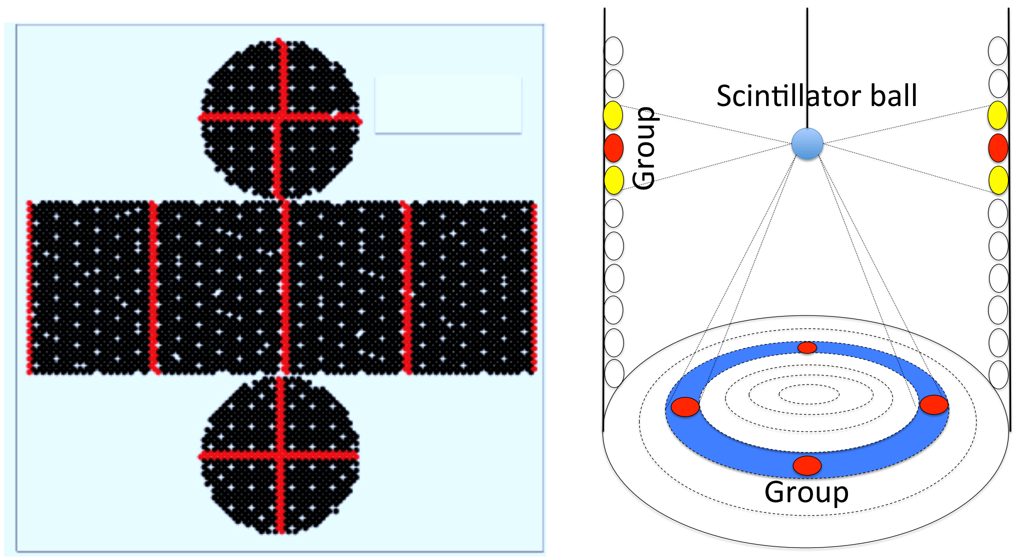

Figure 2·7: Overview of the high voltage tuning using the reference PMT. **Left**: Location of the reference (red circles) PMTs in the SK detector, shown in an unrolled cylinder view. **Right**: Illustration of gain setting using a scintillator ball for the non-reference PMTs. Both figures are reproduced from [70].

where i indexes each PMT, a is the geometric acceptance factor, QE is the quantum efficiency, and G is the gain. The low-intensity source is then used so that any hits are likely to be due to single photoelectrons. The number of hits for the low-intensity source is:

$$N_i \propto I_{\text{Low}} \times a_i \times \text{QE}_i. \tag{2.5}$$

The relative gain is set for each PMT using that G_i is proportional to Q_i/N_i. Because the geometric factor and quantum efficiency cancel in the ratio, the proportionality is the same for all PMTs.

Once the relative gains are known, another calibration method measures the average gain of the entire detector. A nickel source, which isotropically emits 9 MeV photons, is placed at the center of the detector. The photons from the nickel source are sufficiently low-energy such that virtually any hit can be attributed to a single photoelectron emission. The nickel-induced single-photoelectron distribution of each PMT, corrected by each PMT's relative gain, is then added into a single distribution, shown in Figure 2·8. A fit to this whole-detector single-photoelectron distribution establishes a single picocoulombs-to-photoelectrons conversion factor.

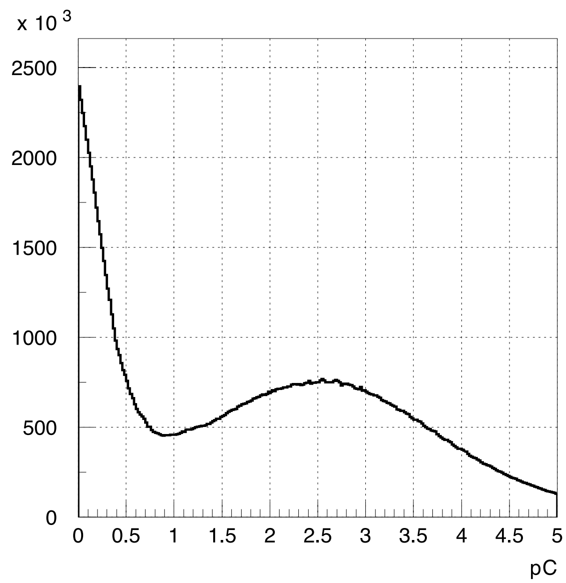

Figure 2·8: Sum of relative gain-corrected ID PMT single-photoelectron distributions. The peak shows the average charge, in picocoulombs, corresponding to one photoelectron.

PMT signal times are calibrated to account for differences in the photoelectron transit times within each PMT, and the differences in signal transit time due to each PMT's cable length. The timing calibration uses a fast-pulsing nitrogen laser, fed into a diffuser ball at the center of the SK detector. The times of the hits induced by the laser are time-of-flight subtracted based on the PMT's distance to the light source, so that each PMT hit is expected to arrive at the same time. Any nonzero "residual times" then correspond to the offsets which need to be added to each PMT's signal times for proper calibration. Another consideration for the timing calibration is that larger signals tend to arrive earlier than small signals, a phenomenon known as *time walk*. To address time walk, the timing offsets are calculated as a function of charge. The resulting table of offsets for a given PMT charge is referred to as a *TQ-map*. A TQ-map is created for each PMT, and fits to these maps are applied as a correction function to all raw data hits prior to any other offline processing. An example of a TQ-map is shown in Figure 2·9.

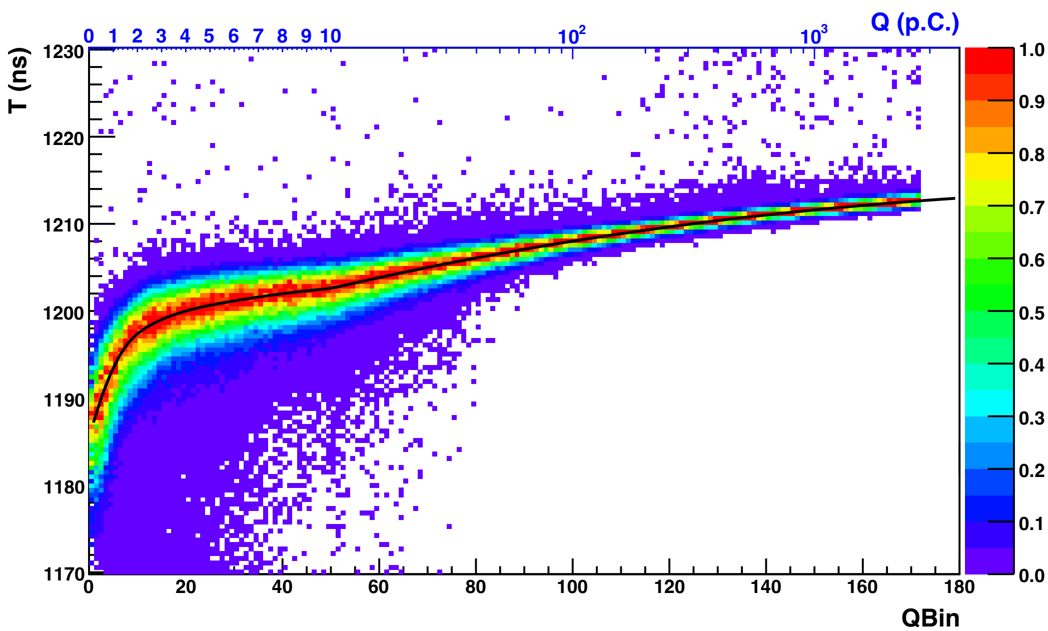

Figure 2·9: The TQ-map of one ID PMT. Each entry of the histogram is a time-of-flight subtracted hit on this PMT induced by a calibration laser. The lower x-axis shows the charge in units of an internal binning scheme, while the upper x-axis shows the charge converted to pico-coulombs. The y-axis shows earlier times as larger values and later times as smaller values, so the time-walk effect, with higher-charge hits arriving earlier, is visible. The black line represents a polynomial fit to the data. Figure is adapted from [70].

2.3.2 OD PMT Calibration

The outer detector PMTs do not have per-channel control of high voltage settings, and, due to the amount of reflected light in the OD, do not have as precise timing information as the ID PMTs. Still, OD PMTs can be coarsely calibrated. First, dark hits, i.e., noise, observed in the window before an event trigger are collected. Dark hits are nearly all due to single-photon detections, so they form single-photoelectron distributions for each OD PMTs. The relationship between high voltage and the charge response from a single-photoelectron is roughly known for each PMT type, so an ideal target high voltage can be calculated. The high voltage for each OD PMTs can then be lowered by adding a zener diode jumper directly to the paddle card.

Timing calibration of the OD PMTs is performed using cosmic muons. The trajectories of cosmic muons which pass through the OD and ID can be fit with ID PMTs to establish an entry point and direction in the ID. Then, the muon's path can be extrapolated backwards into the OD region. The distance of each hit OD PMT to the muon track is calculated assuming fixed-angle Cherenkov emission, allowing for a time-of-flight subtraction. The time-of-flight subtracted hits are used to calculate offsets which correct for any observed timing bias.

2.3.3 Water Parameter Measurements

Light intensity due to water transparency in SK is modeled with an exponential function,

$$I(l, \lambda) = I_0(\lambda) \exp\left[-l/L(\lambda)\right], \tag{2.6}$$

where I is the intensity, l is the distance from the source, λ is the wavelength of the light, and $I_0(\lambda)$, is the source intensity. Equation 2.6 also include a wavelength-dependent scattering coefficient, $L(\lambda)$, which is decomposed into three components:

$$L(\lambda) = (\alpha_{\text{abs.}} + \alpha_{\text{sym.}} + \alpha_{\text{asym.}})^{-1} \, . \tag{2.7}$$

Equation 2.7 contains an absorption term, $\alpha_{\text{abs.}}$, a symmetric scattering term, $\alpha_{\text{sym.}}$, which includes Rayleigh and symmetric Mie scattering, and an asymmetric term, $\alpha_{\text{asym.}}$, which includes the asymmetric component of Mie scattering. Each component is measured using a multi-wavelength laser placed at different locations in the SK tank. Measurements of scattered light from the laser constrain $\alpha_{\text{sym.}}$ and $\alpha_{\text{asym.}}$, while the drop in intensity, measured using PMTs near the laser location and at the opposite side of the tank, establishes $\alpha_{\text{abs.}}$. Figure 2·10 illustrates the water transparency measurement.

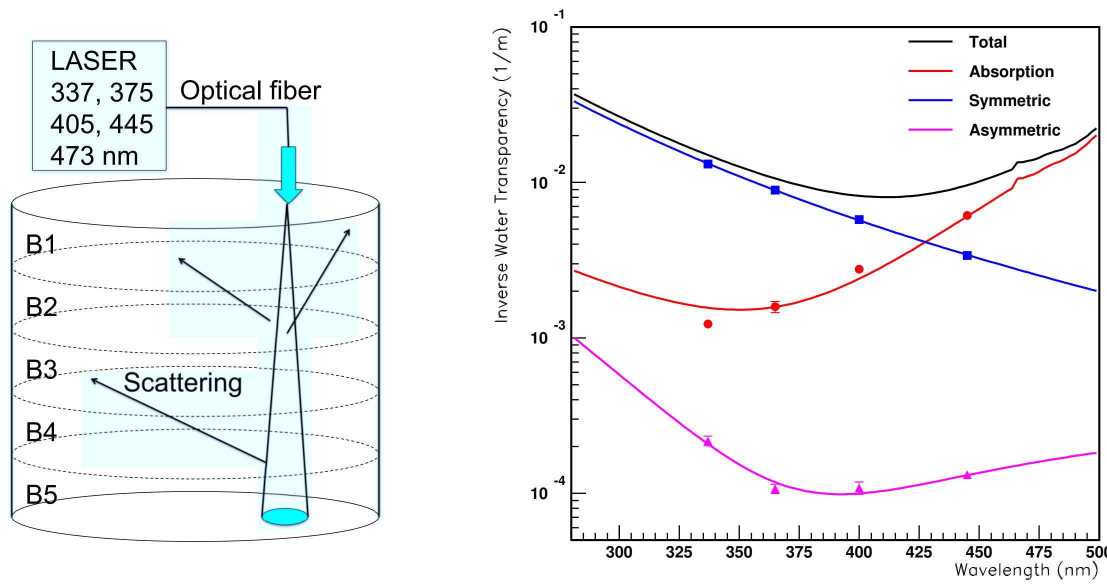

Figure 2·10: Overview of the water transparency measurement. **Left**: Setup of the water transparency measurement with a laser. The labels B1-B5 indicate regions at different depths within in the ID. **Right**: Example results of the laser calibration. Data are shown as points, while the intensity predicted by a tuned simulation is shown as solid lines. Both figures are reproduced from [70].

The water transparency can be measured separately by cosmic muons. Most cosmic ray muons deposit a near-constant 2 MeV/cm of energy in water, corresponding to a fixed amount of Cherenkov radiation per unit track length as they traverse the detector. The ID PMTs are used to reconstruct the muon track through the detector so that the expected hits on each PMT due to the muon's trajectory may be calculated. The ratio of observed charge to the expected charge on each PMT determines the rate of scattering and absorption. The transparency measurement with muons is insensitive to wavelength, but has the advantage that it can be continuously performed during normal detector operation.

2.4 Account of SK V Open Tank Work

In 2018, the SK IV data-taking phase was ended in order to conduct maintenance work. The main goals of the work were:

- Install a new water system, capable of recirculating gadolinium in the detector water. This is described in Section 2.2.3.
- Fix a leak, to prevent any future Gadolinium-loaded water from leaking into the environment.
- Replace PMTs which had failed during the SK III and SK IV phases, a period of 12 years.
- Clean the detector, including removing rust which was thought to potentially react with gadolinium, affecting the water transparency.

The SK "open tank work" involved draining the detector in stages, so that work could be conducted on detector components at varying depths. When open, workers entered the SK detector via gondola, which lowered them and their equipment onto “floating floors” resting at the current water level. In the ID, additional rafts were deployed from the floating floor for traversal away from a primary platform, while in the OD, a floating floor was deployed in a ring, allowing workers to access all sides.

Planning the open tank work involved an assessment of which PMTs and water system components would be accessible on each day, given the water level. Replacing PMTs in both the ID and OD involved cutting PMT cables, splicing new connectors, and covering the splices with heat-shrink tubing to create water-tight connections. Approximately 150 ID and 220 OD PMTs throughout the detector were replaced during the open tank work.

Concurrent with the PMT replacement, workers cleaned the steel structure of the SK tank. Because the steel structure and the tank walls are nominally wrapped in Tyvek (see Figure 2·5), the Tyvek in the outer detector was removed at each layer. This was also necessary for accessing the cables for the ID PMT replacement work. Cleaning the steel structure involved removing rust with electrodes, vacuuming, and retrieving any remaining pieces of PMT glass leftover from the 2001 accident.

To address the leak, workers painted the weld joints and bolt anchors connecting the SK water tank to the cavern walls with MineGuard, a polyurea-silica paste developed for moisture protection in industrial settings. First, the area was cleaned of any rust or debris. Then, MineGuard was applied in two coats with a 24-hour set-in time after the first coat.

After work was finished on an 2 m tall section of the detector, new Tyvek was wrapped around the steel structure, and the water level of the tank was drained an additional 2 m so that work could proceed on the next layer. Figure 2·11 shows the water level as a function of time. The step pattern corresponds to the three days of work on each layer can be seen as the water level decreases. Refilling the detector up to the top level occurred continuously. Additional work was required near the top to re-seal the tank before filling to the full capacity. Figure 2·13 shows scenes from the open tank work. The images show work in the ID and OD at various water levels.

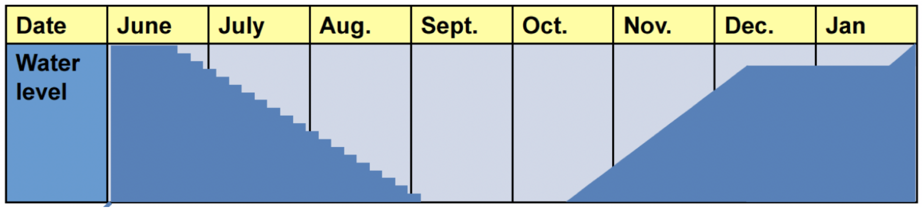

Figure 2·11: The water level during the SK V open tank work. The step pattern reflects times where workers performed various tasks inside the tank.

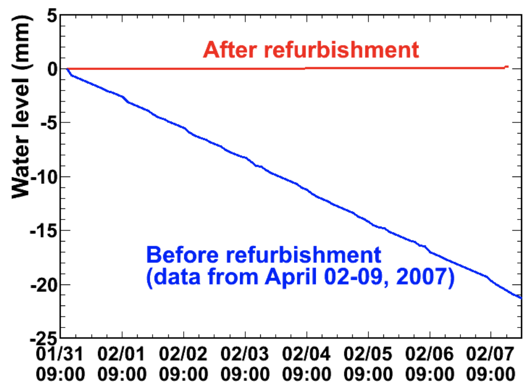

Figure 2·12: The leak assessment after the refurbishment work. Data from SK V is compared to an equivalent period from SK IV, showing no decreases in the water level after the tank open work.

Once the tank open work had completed, the detector water system and water level was monitored precisely. Figure 2·12 shows a measurement of a week-long period from SK IV and at the beginning of SK V. The figure shows that the decrease in water level from the original leak was no longer observed following the open tank work.

Calibrations of PMT hit charge and timing, similar to those described in Section 2.3, were carried out at the beginning of the SK V data-taking phase. In particular, new PMTs installed were calibrated, and the OD high voltages were re-adjusted to improve the consistency of OD PMT single photoelectron responses.

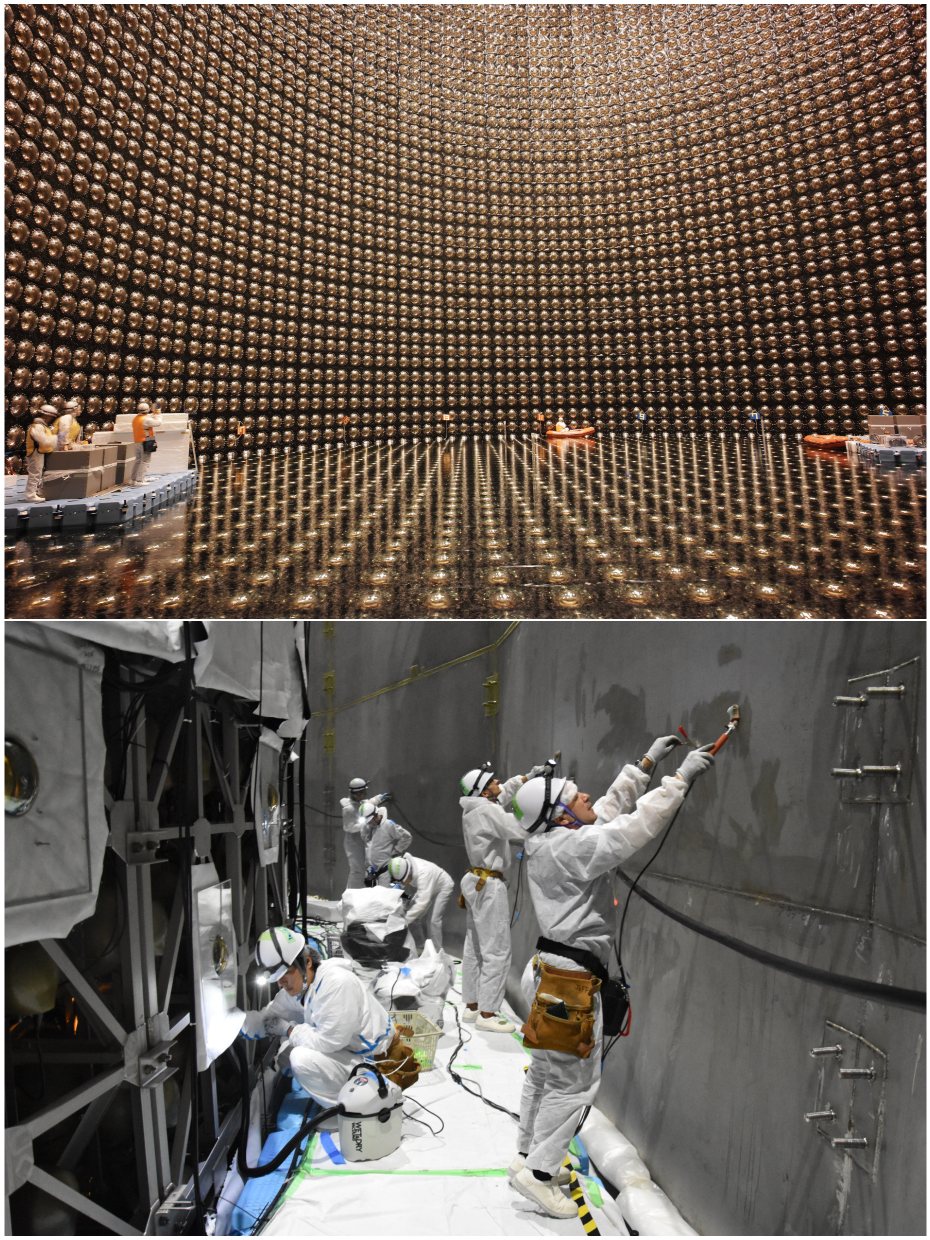

Figure 2·13: Scenes from SK V open tank work. **Top**: Interior view of the ID floating floors during the SK V open tank work. Workers can be seen with replacement PMTs in boxes on one floating floor, while another worker takes measurements from a raft. **Bottom**: Cleaning work in the OD. In the foreground, a worker removes rust using an electrode, while another worker vacuums the steel structure behind an OD PMT. MineGuard from the previous layer can be seen along the joints of the tank wall at the top of the frame.

Chapter 3

Data Reduction & Reconstruction

The SK detector records approximately one million triggers per day, primarily from low-energy radioactive backgrounds at a rate of $\sim 11\,\text{Hz}$, and from cosmic muons at a rate of $\sim 3\,\text{Hz}$. Only about 10 of these triggers per day correspond to atmospheric neutrino interactions. The process of selecting likely neutrino interactions from background triggers is called *reduction*.

Once atmospheric neutrino candidates are identified in data, properties about the particles observed in the time window around the trigger are inferred from patterns of hit PMTs. This process is called *event reconstruction*.

3.1 Data Reduction

Atmospheric neutrino candidates have three broad classifications at SK: fully-contained (FC), partially-contained (PC), and upward-going muon (Up-μ). The distinguishing characteristics between these classifications are:

- FC events have an interaction vertex reconstructed within the ID, and no OD activity. Hence, all final state particles are fully contained.
- PC events have an interaction vertex reconstructed within the ID, and no entry point in the OD, but do have an exit point in the OD. The exiting particle is typically a muon produced by a CC ν_μ interaction.
- Up-μ events are induced by neutrinos interacting in the rock around SK or in

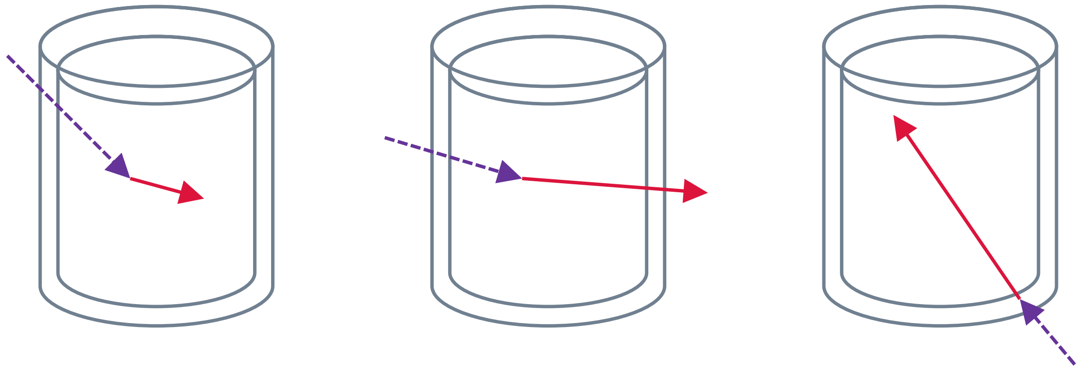

Figure 3·1: The three neutrino event toplogies at SK. The cylinders represent the ID within the SK tank. FC and PC events have a vertex within the ID. PC events have a particle that exits the ID, creating an exit point in the OD. Up-μ events have a vertex outside the ID and an upward-going muon track.

the OD water. These events look like cosmic muons, but pointed upward, i.e., coming from below the horizon. Up-μ neutrino events well-below the horizon have a low contamination from cosmic muons, since the Earth acts as a shield against cosmic muons coming from below.

The three neutrino classifications are shown in Figure 3·1. The SK reduction procedure identifies neutrinos of each class by applying a series of successive cuts. The cuts either remove or accept *events*, collection of PMT hit charges and times recorded within a time window around a trigger. Earlier cuts remove obvious non-neutrino events using simple calibrated detector information, while later cuts, which remove more uncommon backgrounds, tend to be more computationally expensive. This section describes the selection process for neutrino events in each of the three classes. Timing information used in the cuts is relative to the event trigger, defined to be at 0 ns. Additional details of the reduction process may be found in other theses [71, 72].

3.1.1 FC Reduction

The FC reduction consists of five steps, FC1-FC5.

FC1

The first step of FC reduction removes obvious radioactive backgrounds and other low-energy triggers, and cosmic muons, which produce many hits in the OD. FC1 requires that:

- ➔ The number of ID photoelectrons in a 300 ns sliding window must exceed 200 (100 for SK II)
- ➔ The number of hits in the OD between -500 ns and $+300$ ns around the event time must not exceed 50 (SK I-III) or 55 (SK IV+)

This cut is almost 100 % efficient for selecting neutrinos. Approximately 3500 events pass FC1 per day, a 99 % reduction from the initial one million triggers. Note that events which fail the second cut of FC1 may still be classified as PC or Up-μ events.

FC2

FC2 removes high-charge noise events coming from a single ID PMT, and applies a stricter cut to remove additional lower-energy events which may have passed FC1. The cuts are:

- ➔ No single ID PMT may account for more than 50 % of the charge in the event
- ➔ If the number of photoelectrons is less then 100 000 (50 000 for SK II), then the number of OD hits between -500 ns and $+300$ ns around the estimated event time must not exceed 25 (30 for SK IV+)

After FC2, approximately 900 events remain per day.

FC3

FC3 removes cosmic ray muons with certain characteristics not covered by FC1 and FC2, particular configurations of low-energy events, and for removing "flasher" events caused by spontaneous discharge of light from PMTs. The two types of muons addressed by FC3 are

- High-energy muons which lose energy due to bremsstrahlung and pair production, instead of ionization. These energy loss processes result in short bursts of light in the OD, which sometimes evade the FC1 and FC2 cuts.
- Muons which produce concentrated hits in the OD. These muons do not produce enough OD hits to be cut by FC1 and FC2, but produce a cluster of hits in the OD around an entry or exit point.

FC3 addresses the high-energy muons with the following cut:

➔ There must be fewer than 40 OD hits in a 500 ns sliding window

Muons with visible entry points in the OD are found via a dedicated muon track fitting procedure. The fit assumes the earliest saturated ID PMT to be the muon entry point. If the muon passes through the detector and exits the ID, an exit point, and therefore direction, is found using the center of all saturated ID PMTs. Otherwise, the fit calculates the muon direction such that it maximize the expected charge in the ID. The fit also computes a goodness score, i.e., the likelihood that the time of each PMT hit originated from a Cherenkov cone along the muon's track. The entry and exit point are used in the following cuts to identify and remove muons:

➔ (Entry & exit point): The event must not match the following conditions: The maximum charge on a single PMT exceeds 230 photoelectrons, there are more than 1000 ID PMT hits, and the number of OD hits within an 8 m radius of the entry or exit point is 10 or more.

- ➔ (Entry point only): The event must not match the following conditions: The number of OD hits within an 8 m radius of the entry point is 10 or more, or (SK I only) the number of OD hits within an 8 m radius of the entry point is more than four, and the muon's fitted goodness score is more than 0.5.

Next, due to gaps in the OD PMT coverage from cables and plumbing, scintillator paddles are installed as vetoes at four positions around the detector. FC3 requires

- ➔ There must be no scintillator veto activity within 4 m of the fitted entry point.

FC3 also attempts to remove additional low-energy events that can evade the FC1 step due to multiple random coincidences. For a true neutrino event, a single vertex should be present, while multiple coincident low energy events will not have a single best-fit vertex. FC3 chooses a vertex as the point which gives the smallest residuals for time-of-flight subtracted hits. This time-of-flight vertex is used for the following cut, and in subsequent cuts:

- ➔ The number of time-of-flight subtracted hits in a 50 ns sliding window must exceed 50 (25 for SK II)

This cut alone is not sufficient to remove all low-energy events. If a cosmic muon arrives after the low energy event triggers the detector, it can still pass this and the preceding cuts. Therefore, another cut is applied to search for these late-arriving muons:

- ➔ If the number of photoelectrons in the ID is greater than 5000 (2500 for SK II), then there must be fewer than 20 OD hits in a +300 ns to +800 ns window.

Finally, FC3 removes flasher events, where a single PMT undergoes electrical discharge which produces light detectable by neighboring PMTs. A characteristic of flasher events are PMT hits occurring at later times after a trigger than in true particle interactions, which motivates the following cuts:

- ➔ (SK I only) The minimum number of ID hits within a 100 ns residual time sliding window between +100 ns and +700 ns must be less than 10. If there are more than 800 ID hits, the number of ID hits in found by the sliding window must be less than 15.

- ➔ (SK II+) The minimum number of ID hits within a 100 ns sliding window between +100 ns and +700 ns must be less than 20.

- ➔ The goodness score of the time-of-flight vertex must be greater than 0.4.

Approximately 80 events per day remain after FC3. Events which pass FC3 are fully reconstructed, with a much more sophisticated algorithm, described in Section 3.2.

FC4

FC4 implements a data-driven cut to remove additional flasher events. Experts select flasher candidates for inclusion in a database of reference events, and new events are compared to these references. FC4 implements a likelihood function consisting of two variables constructed using the hit patterns of the events: a correlation, and the Kolmogorov-Smirnov (KS) test statistic. The correlation, r, between two events, A and B, is defined as:

$$r = \frac{1}{N}\sum_{i}^{N}\frac{1}{\sigma_A\sigma_B}\left[(Q_i^A - \langle Q^A\rangle)(Q_i^B - \langle Q^B\rangle)\right] \tag{3.1}$$

where i indexes groups of nearby ID PMTs (about $4\,\mathrm{m}^2$), Q_i is the summed charge of the i^{th} region, $\langle Q\rangle$ is the average change of the event, and σ is the root-mean-square (RMS) of the distribution of charges in the event. Similar events will have large values of r. The KS statistic is computed using the distributions of charges within each ID PMT region. Smaller values of the KS statistic indicate better agreement. The 10 patches with the highest r values and 10 smallest KS values are used to compute the likelihood. Events which produce a high likelihood when compared to known flasher patterns are cut by FC4.

FC5

A final set of quality cuts are applied to events passing FC4 to remove remaining flashers, low-energy backgrounds, and muons which pass near additional gaps in the OD which are un-instrumented.

First, flashers are addressed by applying a more sophisticated vertex fit, using the method described in Section 3.2. Hit times are newly time-of-flight subtracted from this fitted vertex, resulting in new residual times. FC5 applies two flasher cuts using the new vertex and residual times:

➔ If the minimum number of hits in a 100 ns residual time sliding window is six or more, the vertex goodness score must be greater than 0.4.

➔ (SK II+ only) If the minimum number of hits in a 100 ns residual time sliding window is less than six, the vertex goodness score must be greater than 0.3.

FC5 attempts to remove low-energy backgrounds caused by invisible muons, i.e., muons with momentum below the Cherenkov threshold. An invisible muon may not produce enough hits in the OD to be removed by earlier reduction steps, but can still trigger the detector when it decays into an electron. FC5 introduces a cut based on the maximum energy of an electron from a muon decay at rest, estimated to be 1000 photoelectrons (500 for SK II). Events below this maximum energy are searched for using time-clustered hits in the OD inside a 200 ns sliding window from -9000 ns to -200 ns. A second cluster is searched for from -200 ns to 200 ns. The goal of these clusters is to detect entering activity from the OD, e.g., an energetic muon in the

OD which produces a secondary muon below Cherenkov threshold that subsequently enters the ID. Based on these OD clusters, two cuts are introduced:

- ➔ If the OD hit cluster locations are 500 cm apart, the number of hits in the first cluster must be less than five, and the number of hits in both clusters must be less than 10.

- ➔ Otherwise, the number of hits in the first OD cluster must be less than 10.

While FC3 addressed gaps in the OD using scintillator paddles, FC5 addresses several remaining un-instrumented gaps. The following cut is applied:

- ➔ If the muon fitter's goodness score is greater than 0.4, there are more than 1000 photoelectrons in the ID, and the fitted muon direction is larger than 37° above the horizon, the distance between the OD entry point and the nearest gap must be larger than 2.5 m.

Finally, FC5 applies one cut based on the reconstructed vertex (see Section 3.2) to further remove entering muons:

- ➔ There must be fewer than 4 OD hits within 8 m of the reconstructed entry point in a 200 ns sliding window between −500 ns and +300 ns.

3.1.2 PC Reduction

PC events are less common than FC events, occurring at a rate of 0.6 per day. Due to the segmentation Tyvek installed at the start of SK III (see Section 2.2.2 and Figure 3·2), the PC reduction was overhauled for SK III onward. This thesis will describe the current method for selecting PC events. The SK I-II PC reduction technique is documented in other theses [73].

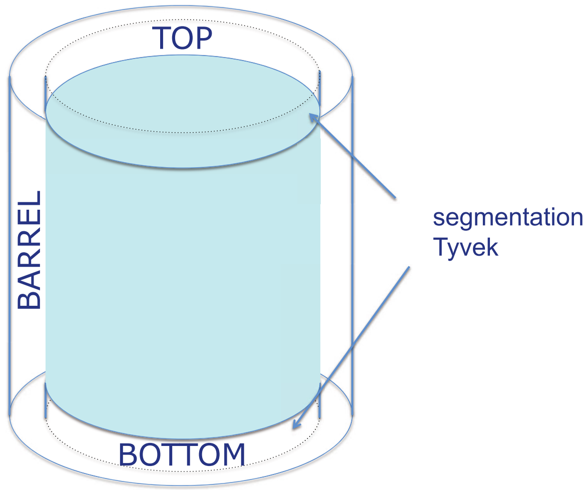

Figure 3·2: Labeled regions of the OD, and the segmentation Tyvek, which are referenced in several parts of the PC reduction. The top and bottom of the OD cylinder are collectively called the end-cap regions, and are optically separated from the barrel region by the segmentation Tyvek. Figure is adapted from [70].

PC1

PC events ideally have one exit cluster of hits in a single OD region. PC1 enforces that no two OD regions, top end-cap, barrel, and bottom end-cap, illustrated in Figure 3·2, have obvious OD clusters. PC1 also ensures that the energy deposition in the ID is consistent with a particle exiting into the OD. The first quality cuts are

- ➔ There must be at least 1000 photoelectrons in the ID.
- ➔ There must be fewer than 11 OD hits in the top end-cap region or fewer than 10 hits in the bottom end-cap region.
- ➔ There must be fewer than 84 OD hits in the barrel region or fewer than 29 hits total in the top end-cap and bottom end-cap regions.

PC1 also calculates the average distance between pairs of hit OD PMTs, a quantity called $\mathrm{ODR}_{\mathrm{Mean}}$, defined as

$$\mathrm{ODR}_{\mathrm{Mean}} = \frac{1}{N_{\mathrm{Pair}}} \sum_i \sum_{j \neq i} |\vec{x}_i - \vec{x}_j| \tag{3.2}$$

where N_{Pair} is the number of pairs of hits, and $\vec{x}_i$ is the position of the i^{th} PMT. $\mathrm{ODR}_{\mathrm{Mean}}$ is large for events with multiple OD clusters, and small for events with only a single cluster. PC1 also requires

➔ $\mathrm{ODR}_{\mathrm{Mean}}$ must be less than 2140 cm.

PC2

PC2 implements a more sophisticated algorithm to identify OD hit clusters than in the FC reduction. The algorithm used for PC reduction divides the OD into regions, then merges hits in each region into the neighboring region with the most hits. PC2 requires

➔ There must be at most one region with more than 10 OD hits found by the clustering algorithm.

PC2 also excludes events based on the number of hits in the end-cap regions as a function of the number of hits in the barrel region. This function, $f(N_{\mathrm{Barrel}})$, plotted in Figure 3·3, is a piecewise exponential which decreases in the number of OD barrel hits, N_{Barrel}. PC2 requires that

➔ The number of OD end-cap hits must be less than $f(N_{\mathrm{Barrel}})$.

PC3

PC3, similarly to FC3, removes flasher events by searching for ID hits arriving after the primary event trigger. PC3 applies a sliding window cut:

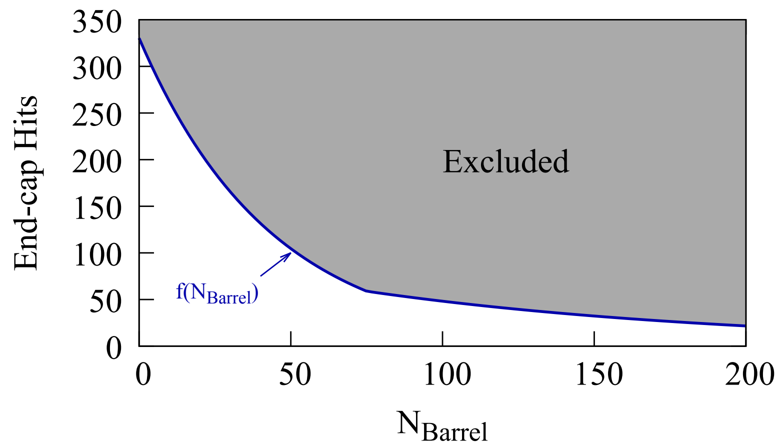

Figure 3·3: The cut applied based on the number of OD hits in each region as part of the PC2 reduction step.

➔ The minimum number of ID hits within a 100 ns residual time sliding window between +200 ns and +700 ns must be less than 10 if there are fewer than 800 ID hits, otherwise the number must be less than 15.

PC4

PC4 removes events with improbable vertices. As in the FC reduction, PC4 estimates a vertex using time-of-flight subtracted hits. PC4 also applies a dedicated fitter, `muboy`, which classifies muons in one of four categories

- *Stopping*: The muon enters the ID and stops
- *Through-going*: The muon enters the ID, then exits the ID
- *Multi-muon*: There are multiple muons with different entry points in the same event
- *Corner clipper*: The muon entered and exited through the corner of the end-cap region, resulting in a thin Cherenkov ring in the ID.

`muboy` also assigns an overall goodness score based on an event's likelihood of being a true cosmic muon. The `muboy` algorithm assumes the vertex of any event is outside the ID, so true PC events will have low goodness scores according to `muboy`.

With the two vertices, and direction and classification information from `muboy`, PC4 creates several optional conditions. Depending on the `muboy` classification, a subset of these conditions must be passed. The conditions are

- The difference between the angle from the `muboy` vertex and the angle from the time-of-flight vertex to the highest-charge OD hit cluster (calculated as part of PC2) must be less than 90°.

- The difference between the angle from the `muboy` vertex and the angle from the time-of-flight vertex to the earliest saturated ID PMT must be less than 143.13°.

- The length of the fitted muon track from `muboy` must be less than 1750 cm.

- The goodness of the `muboy` fit must be less than 0.52.

- The distance from the `muboy` vertex to the corner of the tank must be larger than 300 cm.

PC4 assumes that Multi-muon and corner-clipper events are more difficult to reconstruct, and so applies looser cuts than for stopping and through-going muons. PC4 applies the conditions

➔ If the `muboy` class is stopping or through-going, the event must not fail more than one of the five PC4 optional conditions

➔ If the `muboy` class is Multi-muon or corner-clipper, the event must not fail more than three of the five PC4 optional conditions

Finally, PC4 places additional restrictions on events identified as stopping muons by `muboy`:

- If the `muboy` class is stopping, the goodness of the `muboy` fit must be less than 0.5, or there must be fewer than 10 OD hits within 8 m of the `muboy` entrance point in a -200 ns to $+300$ ns window.

There are approximately 900 events per day that which pass PC4.

PC5

PC5 further removes muon backgrounds from the PC sample. Muons which enter near the top edge of the detector and exit through the bottom edge can produce a single large cluster of hits in OD, and, depending on the proximity to the detector wall, a small cluster of hits in the ID. Such events can evade PC1-PC4. PC5 applies a cut using OD PMTs contained by 8 m spheres along the top and bottom detector edges. The spheres on the top and bottom which contain the maximum charge are used for the following cut:

- At least one sphere must contain fewer than seven OD hits, or at least one sphere must contain fewer than 10 photoelectrons, or the average hit times in the spheres must be outside the interval given by $[0.75c/40\,\mathrm{m}, 1.5c/40\,\mathrm{m}]$, i.e., a range of plausible transit times across the SK tank.

The final check of this cut ensures that the distance between hits in the selected spheres is consistent with a muon traversing the height of the detector.

Events which pass PC4 are fit to identify a Cherenkov ring and vertex using the algorithms described in Section 3.2. PC5 applies a series of cuts to further mitigate stopping muons, corner clippers, and events near the OD gaps using the information from this fit. These are

- ➔ The angle between the fitted Cherenkov ring and the center of the largest OD hit cluster must be less than 90°.
- ➔ The fitted vertex must be greater than 150 cm away from the ID top and bottom edges.
- ➔ If a scintillator veto paddle is triggered, the angle between the line from the veto paddle to the fitted vertex and the line from the fitted vertex to the fitted ring direction must be greater than 37°.

As in PC4, PC5 implements a cut which requires events to satisfy a subsets of optional conditions. Each condition addresses a specific background category. The conditions are listed below with the intended background they address in parentheses:

- (Through-going muons) If the fitted entrance point and exit point, determined by extrapolating the vertex and fitted ring direction, contain OD hits which are separated in time by $[0.75c/d, 1.5c/d]$, where d is the distance between the points, there must be fewer than five OD hits within an 8 m radius of either point.
- (Through-going muons) There must not be a cluster of OD PMT hits containing 17 hits, and a second cluster containing 10 or more hits.
- (Stopping muons) There must not be 10 or more hits within 8 m of the fitted entrance point.
- (Stopping muons) A fit assuming the entrance point is the earliest hit ID cluster must not contain more than 60 % of the photoelectrons in a 42° cone around the fitted track, and there must not be more than six OD hits within 8 m of the assumed entrance point.

- (Stopping muons) The angle between the fitted Cherenkov ring and the largest OD hit cluster must be less than 90°.

- (Corner-clippers) The track length determined from the vertex cannot be more than 15 m longer than the track length estimated from the total ID charge divided by 2 MeV/cm. Corner clipper muons typically have short tracks in the ID, so there can be large disparities in track length estimated from the ring and from the charge.

- (Non-neutrino) There must be 1 decay electron in the event.

The final optional condition targets muons which pass through the detector without producing hadrons. Such muons would create events with no decay electrons, while neutrino events at PC energies are likely to produce hadrons which decay into visible electrons near the vertex. This is discussed in Chapter 4. The corresponding PC5 cut based on the above optional conditions is:

➔ Events must not fail more than one of the PC5 optional conditions.

3.1.3 Up-μ Reduction

Up-μ events constitute about 1.5 atmospheric neutrino events per day. Backgrounds for Up-μ events well-below the horizon are much less than for FC and PC due to the shielding of cosmic muons by the earth. However, events with fitted directions near the horizon can result from downward-going cosmic rays just above the horizon which produce upward-scattered muons, creating an irreducible background for the Up-μ sample. The reduction steps presented here involve quality checks for muon-like events and comparisons of fit directions using different methods. Since the Up-μ selection relies on the direction of the events, requirements on zenith angle, $\cos\theta_z \lesssim 0$, appears in the selection. See Section 1.5.3.

First Reduction

The first Up-μ reduction cut corresponds to a minimum momentum cut for a 1 GeV/c muon, and a maximum momentum cut, above which muon reconstruction is not feasible.

- ➔ The number of ID photoelectrons in a 300 ns sliding window must be between 6000 and 1 750 000 (3000 and 800 000 for SK II)

Second Reduction

This step successively applies seven different muon vertex and direction fitting routines optimized for different types of muons, e.g., through-going, stopping, or muons which lose energy due to radiative losses instead of ionization. While high goodness scores according to various muon fitters were used to remove backgrounds in the FC and PC reductions, they are used here to accept neutrino events. The conditions for the second reduction step are

- ➔ The muon must be fit as upward-going or horizontal with a goodness score above a threshold by at least one fitter
- ➔ The muon must not be fit as downward-going with a goodness score above a threshold by any of the fitters

A full list of the fitters and the associated thresholds, as well as additional logic about the fitting order, is presented in other theses [74].

Third Reduction

Events which pass second reduction are fit by a computationally-intensive fitted called `precisefit`. Using the `precisefit` information, a cut is applied on the direction and on minimum allowed momentum:

- ➔ The fitted direction must be upward-going
- ➔ If the muon is classified as stopping, the momentum must be greater than 1.6 GeV/c.
- ➔ If the muon is classified as through-going, the fitted track length must be greater than 7 m.

Fourth Reduction

The Up-μ fourth reduction step was implemented beginning with SK IV, and utilized the segmentation Tyvek in the OD (see Section 2.2.2). As with PC events, the fourth step uses the number of OD PMT clusters, calculated via a clustering algorithm.

- ➔ The number of OD hit clusters must be exactly one, or the direction between the two clusters with the most hits must be upward-going or horizontal with $\cos\theta_z < 0.035$.

Fifth Reduction

In 2019, and enacted starting with the SK V data set, the Up-μ reduction was further automated with a fifth reduction step. The new step places additional cuts which were previously evaluated manually by experts manually on an event-by-event basis.

- ➔ The angle between the `muboy` (see Section 3.1.2) fitted direction and the dedicated Up-μ muon fitter fitted direction must be less than 20°.
- ➔ The `muboy` goodness score must be > 0.25.
- ➔ The `muboy` fitted direction must be $\cos\theta_z < 0.02$.

3.1.4 Post-reduction Eye-scanning

Because SK observes $\sim$ 10 atmospheric neutrino events per day, it is feasible for experts to visually inspect all events, known as *eye-scanning*. The purpose of eye-scanning is not to remove events, rather, it is to estimate the background contamination after the final reduction steps in each sample. Each sample, FC, PC, and Up-μ, is eye-scanned following the sample's final reduction step.

3.1.5 ID-OD Cross Talk

In 2018, it was discovered that large amounts of charge deposited on ID PMTs could induce small amounts of charge on nearby OD PMTs, which could then register as hits, known as *cross talk*. In 2019, a new preprocessing step was implemented to remove OD hits induced by cross talk. All SK data was re-processed using the above reduction steps, but excluding any OD hits with times greater than 50 ns after the trigger and charges less than 0.2 photoelectrons. The development of this cut is documented in the thesis by C. Kachulis [75].

Figure 3·4 shows the average number of FC, PC, and Up-μ events remaining after all reduction steps per day during the SK I-V data-taking phases. The figure shows the stability of these reduction criteria over the lifetime of the experiment.

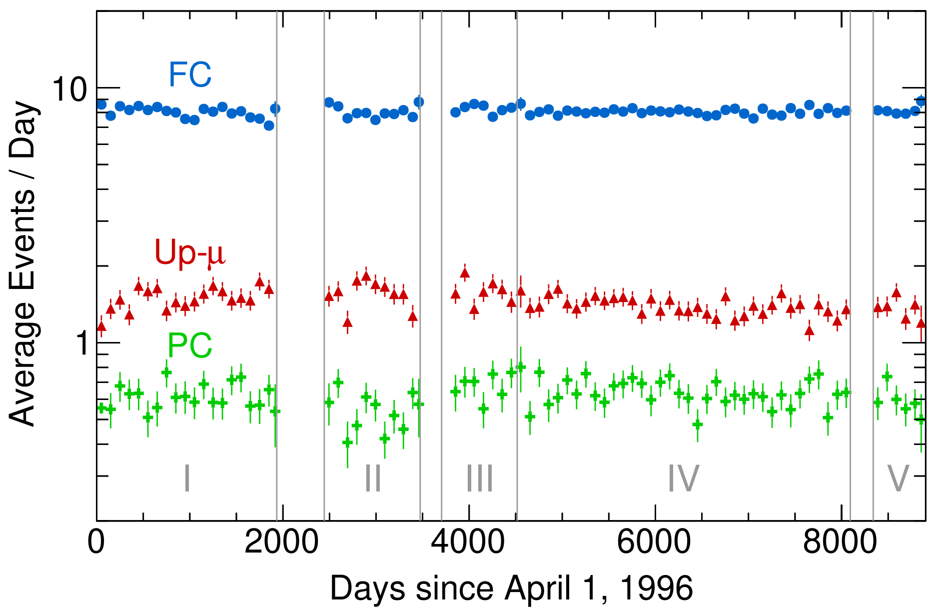

Figure 3·4: Average number of FC, PC, and Up-μ events per day during the SK I-V data-taking phases. The events shown are the final sample used in this analysis, and have passed all reduction steps, including additional criteria described in Section 5.1.

3.2 Reconstruction

Reconstruction involves counting and classifying the particles in each event which passes the reduction stage for physics analyses. The primary reconstructed object at SK is a Cherenkov ring, which contains information about the particle's vertex, direction, and type. SK uses a set of algorithms to identify, count, and categorize Cherenkov rings, collectively called APFIT. This section will provide an overview of APFIT functionality. Further documentation is also available in [76].

A separate algorithm, FITQUN, has also been used to reconstruct SK events [77]. FITQUN will be discussed in Chapter 6 as part of the analysis with external constraints from T2K.

3.2.1 Event Vertex

When reconstructing neutrinos events, assuming a single vertex is a powerful constraint on the expected timing distribution of PMTs. Reconstruction for FC and PC events begins with a preliminary vertex fit in the ID based on the residual hit times after subtracting the time-of-flight to the vertex. APFIT refines this time-of-flight vertex later using additional information. The residual times from a trial vertex, $\vec{x}$, are computed as

$$t_i^{\text{Resid.}}(\vec{x}) = t_i - \frac{n}{c}|\vec{x} - \vec{x}_i^{\text{PMT}}| \tag{3.3}$$

where n is the index of refraction in water, t_i represents the calibrated hit time relative to the trigger, and $\vec{x}_i^{\text{PMT}}$ is the position, of the i^{th} PMT. The best vertex is taken as the point which minimizes the width of the distribution of $t_i^{\text{Resid.}}$. This is accomplished using a goodness of fit parameter, G, based on a Gaussian likelihood,

$$G(\vec{x}) = \sum_i \frac{1}{\sigma(q_i)} \exp\left\{-\frac{(t_i^{\text{Resid.}} - t_0)^2}{2[1.5\sigma(\langle q\rangle)]^2}\right\} \tag{3.4}$$

where q_i is the charge of the i^{th} hit PMT, $\sigma(q)$ is the timing resolution of the readout electronics for a pulse of charge q, and t_0 is a free parameter for the residual time distribution peak position. The vertex which minimizes G becomes the starting point for the next step.

The time-of-flight vertex can be improved by considering just the hits produced by a single Cherenkov ring. While an event might contain multiple rings, the brightest ring contains the most information for finding a vertex. This ring can be identified by charge-weighting each hit, correcting for water attenuation and the incident angle. The corrected charge is defined as

$$q_i^{\text{Corr.}}(\vec{x}) = q_i \exp\left(-\frac{|\vec{x} - \vec{x}_i^{\text{PMT}}|}{L}\right) \frac{\cos\theta}{f(\theta)} \tag{3.5}$$

where, the vertex, position, and charge are the same as in Equation 3.4, L is the attenuation length of the water, θ is the angle of incidence from the vertex to the hit PMT, and f is the acceptance of the PMT as a function of θ. The vector sum of hit PMTs, weighted by the corrected charge, establishes a preliminary ring direction, $\vec{d}$.

The ring direction is refined by testing various Cherenkov angles. The Cherenkov angle (see Equation 2.2) for a particle moving close to the speed of light in water is 42°, but this can be smaller for particles with lower momenta. A new goodness of fit parameter is defined which attempts to accomplish three goals: (i) penalize small, non-Cherenkov-like angles, (ii) match the opening angle to the expected opening angle from a particle which would produce the contained charge, and (iii) maximize the charge contained in a ring of the assumed angle. The measure is

$$G(\vec{d}, \theta_c) = \frac{1}{\sin\theta_c} \times \exp\left[-\frac{(\theta_c - \theta_{\text{Exp.}})^2}{2\sigma_\theta^2}\right] \times \left(\frac{dq^{\text{Corr.}}}{d\theta}|_{\theta=\theta_c}\right)^2 \int_0^{\theta_c} q^{\text{Corr.}}(\theta) d\theta \qquad (3.6)$$

where $\theta_{\text{Exp.}}$ is one of three angles: 42°, or the angle assuming a muon, or the angle assuming an electron, produced the observed charge. σ_θ is the angular resolution, and the differential term gives the change in the total corrected charge contained versus opening angle of the ring, i.e., to measure how suddenly the charge changes outside the ring edge. The first term addresses goal (i), the second term addresses goal (ii), and the third term addresses goal (iii).

Minimizing Equation 3.6 establishes a refined ring direction and Cherenkov angle. The initial time-of-flight vertex from Equation 3.3 may now be refined by shifting the residual times of hits within the Cherenkov ring by the difference from the initial vertex, $\vec{x}$, to a vertex, $\vec{y}$, constrained to be on the line given by the fitted angle and the fitted ring direction:

$$t_i^{\text{Resid.}}(\vec{x}, \vec{y}) = t_i - \frac{n}{c}|\vec{y} - \vec{x}_i^{\text{PMT}}| - \frac{1}{c}|\vec{y} - \vec{x}| \qquad (3.7)$$

The vertex goodness is once again calculated via Equation 3.4, and separate goodness scores are constructed for hits inside and outside the Cherenkov ring. A minimization routine finds the new best-fit vertex based on the new residual time distribution.

3.2.2 Ring Counting

For events containing multiple rings, APFIT transforms the ring fitting problem into a peak-finding problem using the method of Hough transformations [78]. The method is illustrated in Figure 3·5. In the figure, circles of the same radius are drawn around each hit PMT position, white dots in the left panel. For a true circular arrangement of PMT hits, the rings drawn around each PMT will overlap at a single point, creating a region of highest intensity, shown in the right panel. APFIT refines the Hough transformation technique by applying the transformation to the expected charge from rings at a particular angle, weighted by the observed charge. The hit positions of PMTs are mapped from Cartesian coordinates into the altitudinal and azimuthal directions within the SK ID cylinder for performing the transformation. The positions of any peaks found in the transformation space then correspond to a ring direction.

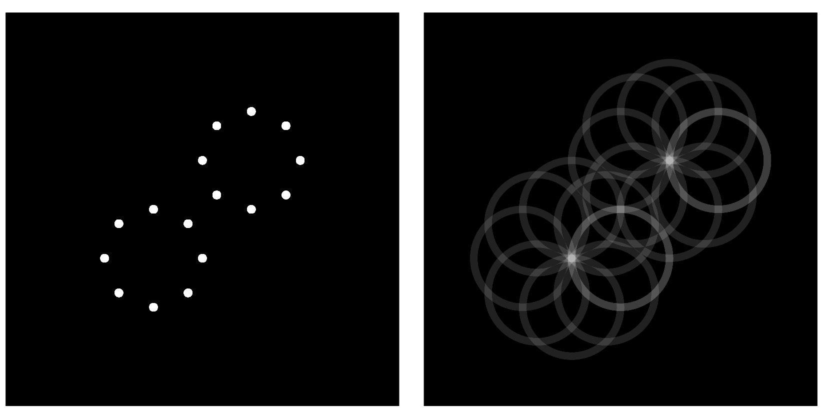

Figure 3·5: Graphical demonstration of a Hough transform. **Left**: Points are arranged in rings. **Right**: Rings are drawn around each point from the left panel. Due to the ring arrangement of the points, the drawn rings overlap, forming bright points in the Hough space.

Rings are added to the event iteratively. APFIT implements a likelihood variable for N rings. Additional rings are added only if they cause the likelihood to increase over the hypothesis for the original number of rings. The likelihood is

$$L_{N_{\text{Ring}}} = \sum_{i}^{N_{\text{PMT}}} \log\left[P\left(q_i, \sum_{j}^{N_{\text{Ring}}} \alpha_j q_{i,j}^{\text{Exp.}}\right)\right] \tag{3.8}$$

where $P(q_1, q_2)$ is the Poisson (if $q_i^{\text{Exp.}} < 20$ photoelectrons) or Gaussian probability of observing a charge q_1 given an expected charge q_2, α_j is a weight applied to the j^{th} ring, and $q_{i,j}^{\text{Exp.}}$ is the expected charge contribution to the i^{th} PMT from the j^{th} ring. APFIT will add up to five rings per event. Figure 3·6 demonstrates how Equation 3.8 may be used to separate single and multi-ring events. The difference between the single ring hypothesis, L_1, and the hypothesis with more than one ring, L_2, for atmospheric neutrino data from the SK IV-V phases and simulation (see Chapter 4) is shown. The distributions reflect the expectation that lower-energy neutrino interactions are more likely to produce only one ring.

3.2.3 Particle Identification

Particle identification (PID) in APFIT involves classifying ring candidates as originating from electromagnetic showers, e-*like* or muons, μ-*like*. Electrons tend to radiate energy via bremsstrahlung, or through Compton scattering, producing energetic photons. These photos then undergo pair production, producing additional electrons and positrons which produce their own Cherenkov rings. These processes tend to deflect the direction of electrons, resulting in ring patterns with blurred edges. In contrast, muons, which are heavier than electrons, tend to travel without significant deflection, resulting in sharp ring edges. Figure 3·7 shows example e-like and μ-like rings from candidate neutrino interactions in SK.

APFIT constructs a likelihood function based on the expected distribution of hits

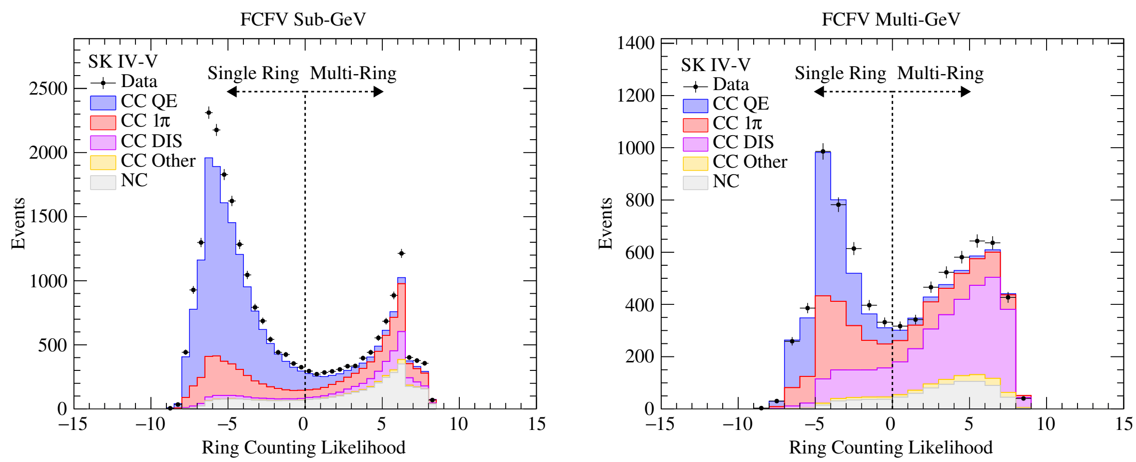

(a) (b)

Figure 3·6: Ring counting likelihood, $L_2 - L_1$, from Equation 3.8, for atmospheric neutrino data and simulation for the SK IV-V phases. Positive values indicate that the hypothesis with at least two rings was preferred over the single-ring hypothesis. The case for sub-GeV events (visible energy less than 1330 MeV) is shown in (a), and multi-GeV events (visible energy greater than 1330 MeV) is shown in (b).

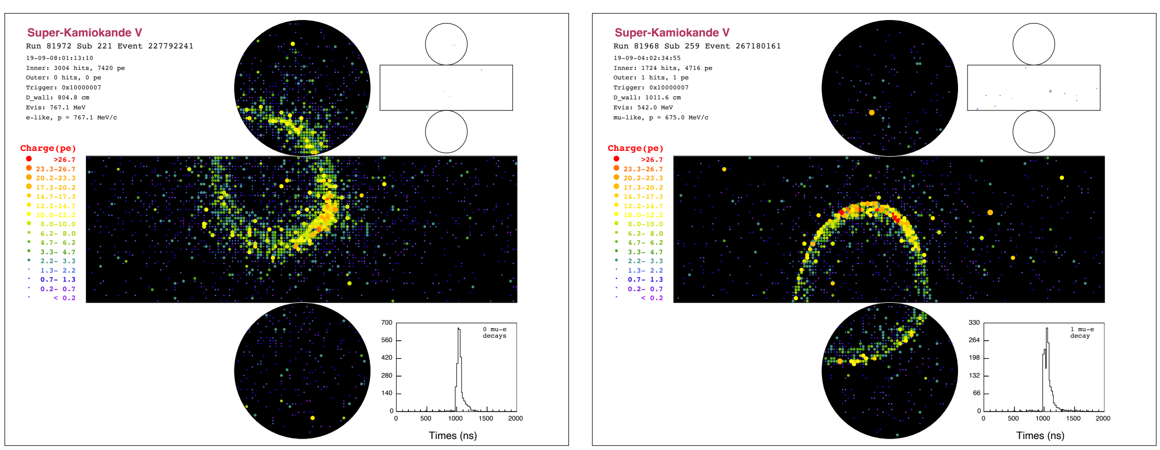

(a) (b)

Figure 3·7: Neutrino candidate events from SK V data. Bright dots represent hit PMTs, with color and radius corresponding to the observed charge. (a) shows an e-like event with blurred ring edges, while (b) shows a μ-like event with sharp ring edges.

and charges assuming a muon or electron parent particle for the ring. This pattern likelihood for the n^{th} ring is

$$L_n^{\text{Pattern}}(e,\mu) = \prod_{\theta_i<1.5\theta_c}^{N_{\text{PMT}}} P\left[q_i, q_{i,n}^{\text{Exp.}}(e,\mu) + \sum_{j\neq n} q_{i,j}^{\text{Exp.}}\right] \tag{3.9}$$

where the product is taken over all PMTs contained within a ring with opening angle given by 1.5 times the Cherenkov angle, θ_C, and the probability $P(q_1, q_2)$ has the same definition as in Equation 3.8. The contribution to the total charge from other rings in the event is added via the summation term within the probability, without assuming a particle type. For this likelihood, the expected charge from the n^{th} ring, $q_i^{\text{Exp.}}(e,\mu)$, is calculated from a combination of already-fitted quantities and pre-computed simulations. Both the e and μ scenarios account for the fitted vertex and ring direction, and use the average light produced in simulations of probable particle trajectories produce estimates for the expected charge. The key differences between the muon and electron expectations are that the photon emission points are constrained to be on the muon's estimated track, and that the muon may also produce extra light from energetic electrons knocked out as it ionizes the water. A full description of the expected charge distributions for this step is presented in [79].

APFIT applies an additional correction to events with a single ring, based on the expected Cherenkov angle for an electron or muon with a specified momentum, $\theta_{\text{Exp.}}(e,\mu)$:

$$P^{\text{Angle}}(e,\mu) = \begin{cases} \exp\left[-\frac{(\theta-\theta_{\text{Exp.}}(e,\mu))^2}{2\sigma_\theta}\right] & N_{\text{Ring}} = 1 \\ 1 & N_{\text{Ring}} > 1 \end{cases}, \tag{3.10}$$

where θ is the reconstructed Cherenkov angle, and σ_θ is the estimated Cherenkov angle fitting resolution. Using Equation 3.9 and Equation 3.10, APFIT outputs a single number to indicate e- or μ-like PID preference. First, the pattern likelihood is converted to a probability assuming a χ^2 distribution,

$$\chi_n^2(e,\mu) = -2\log L_n^{\text{Pattern}}(e,\mu)$$
$$\implies P_n^{\text{Pattern}}(e,\mu) = \exp\left\{-\frac{[\chi_n^2(e,\mu) - \min(\chi_n^2(e),\chi_n^2(\mu))]^2}{4N_{\text{PMT}}}\right\} \tag{3.11}$$

Such that $P_n(e,\mu) = P_n^{\text{Pattern}}(e,\mu) \times P^{\text{Angle}}(e,\mu)$. Then the preference for e- or μ-like for the n^{th} ring may be expressed as

$$L_n^{\text{PID}} = \sqrt{-\log P_n(\mu)} - \sqrt{-\log P_n(e)} \tag{3.12}$$

The distributions of Equation 3.12 for SK IV-V data and simulation (see Chapter 4) are shown in Figure 3·8.

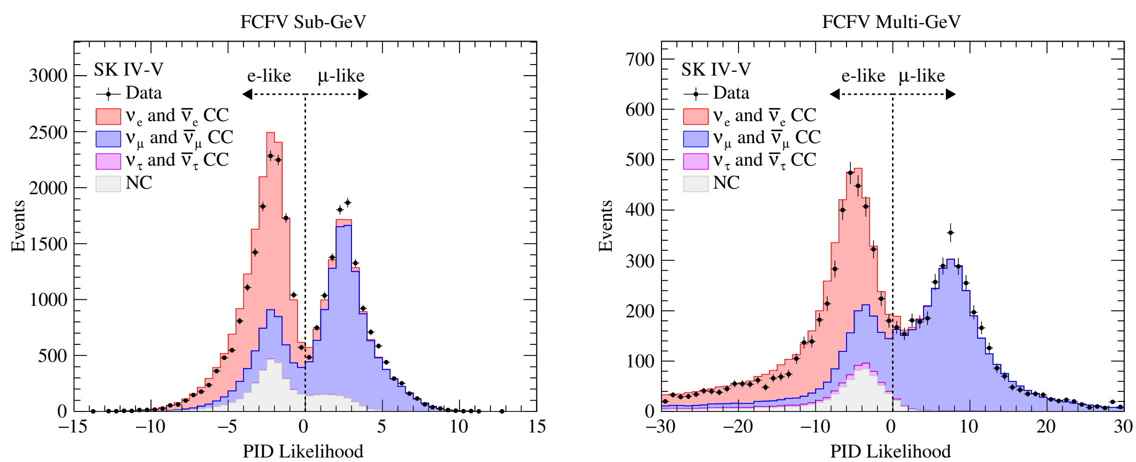

(a) (b)

Figure 3·8: PID likelihood from Equation 3.12 for atmospheric neutrino data and simulation for the SK IV-V phases. Positive values indicate that the leading ring is μ-like, while negative values indicate e-like. The case for Sub-GeV events (visible energy less than 1330 MeV) is shown in (a), and Multi-GeV events (visible energy greater than 1330 MeV) is shown in (b).

3.2.4 Event Vertex, Revisited

For single-ring events, APFIT re-integrates the PID information from the previous reconstruction step to improve the vertex fit. In an iterative process, the vertex and direction are moved in small steps to maximize the pattern likelihood from Equation 3.9. The procedure is repeated for seven iterations, or until the vertex is stable to within 5 cm and the direction is stable to within 0.5° between subsequent iterations.

3.2.5 Momentum Reconstruction

Each Cherenkov ring corresponds to a particle with a particular momentum. In the case of single-ring events, the momentum may be computed from the sum of the observed charge within the Cherenkov ring. In the case of multi-ring events, rings may overlap, and so the observed charge on must be divided among each ring. The observed charge on the i^{th} PMT from the n^{th} ring is defined using the fraction of the expected charge from the n^{th} ring,

$$q_{i,n} = q_i \left(\frac{q_{i,n}^{\text{Exp.}}}{\sum_j^{N_{\text{Ring}}} q_{i,j}^{\text{Exp.}}} \right) \tag{3.13}$$

APFIT uses the divided charges (with acceptance corrections from Equation 3.5) to compute an intermediate quantity for each ring, $R_n^{\text{Tot.}}$,

$$\begin{aligned} R_n^{\text{Tot.}} &= \frac{G_{\text{MC}}}{G_{\text{Data}}} \left(\sum_i q_{i,n}^{\text{Corr.}} - \sum_j q_j^{\text{Scatter}} \right) \\ & i \in (\theta_{i,n} < 70^\circ \text{ and } -50\,\text{ns} < t_i^{\text{Resid.}} < 250\,\text{ns}) \\ & j \in (\theta_{j,n} < 70^\circ) \end{aligned} \tag{3.14}$$

where G_{MC} and G_{Data} are the relative gains in the simulation and data respectively, i and j index PMT hits satisfying the listed angular and residual time conditions, $\theta_{i,n}$ is the angle of the i^{th} PMT relative to the n^{th} ring vertex and direction, and q_j^{Scatter} is the expected charge scattered onto the j^{th} PMT not originating from the Cherenkov ring. $R_n^{\mathrm{Tot.}}$ is converted to a momentum for each ring using a lookup table which matches $R_n^{\mathrm{Tot.}}$ values for each ring to simulated particles with known momenta.

3.2.6 Ring Counting, Revisited

APFIT uses the momentum of each ring, p_i, to merge lower-energy rings into higher-energy ones, and remove spurious rings. The two conditions are

- Two rings i and j are merged if $\theta_{i,j} < 30^\circ$ and $p_i \cos\theta_{i,j} < 60\,\mathrm{MeV/c}$.
- A ring i is removed if $p_i < 50\,\mathrm{MeV/c}$ and $p_i / \sum_j p_j < 0.05$.

3.2.7 Decay Electron Tagging

In addition to Cherenkov rings, SK also sees electrons from the decay of muons following the primary interaction. The observation of decay electrons provides information about the parent muon track and the charge, positive or negative, of the muon. The charge information is statistical: negatively-charged muons, and pions, which decay into negatively-charged muons (see Equation 1.27), are more likely to be absorbed in the water before decaying. Therefore, decay electrons are most often observed associated with positively-charged muons. The usefulness of this fact for distinguishing between neutrino and anti-neutrino interactions will be discussed in Chapter 5.

The mean lifetime of the muon is 2.2 µs, so many of these electrons are contained within the primary SK I-III event windows, and all are contained within the SK IV+ event windows, listed in Table 2.2. In the case of SK I-III, decay electrons appearing after the primary event window may trigger the detector again, resulting in a second "sub-event."

The simplest decay electrons to search for in SK I-III are decay electrons within sub-events, and, in SK IV+, decay electrons 450 ns after the primary trigger. A dedicated algorithm searches for signatures of these decay electrons. While energetic decay electrons can have enough momentum to produce Cherenkov rings, the number of hits is often too low to attempt a full reconstruction. Instead, decay electrons are found with timing information. The algorithm scans for peaks in a 30 ns residual time window above background. Here, the background, N_{Bkg}, is estimated from the number of hits in a small window before the peak. A decay electron must satisfy the following conditions:

- $N_{\mathrm{Peak}} - N_{\mathrm{Bkg}} \geq 50$ (25 for SK II)
- $(N_{\mathrm{Peak}} - N_{\mathrm{Bkg}})/\sqrt{N_{\mathrm{Bkg}}} > 6.63$ (5.17 for SK II)

Following the identification of a peak, the hits in the peak are used to estimate a vertex, once again by minimizing Equation 3.4. The fitted t_0 parameter from the vertex fit estimates the decay time. The decay electron is counted if the number of hits in a 50 ns window around t_0 is greater than 50 (25 for SK II) and the goodness parameter $G > 0.5$.

In some cases, a decay electron can be identified, but its vertex cannot be reliably established. One such case is when a decay happens too soon after the primary event, such that a hit peak is visible but the decay electron hits are too difficult to distinguish from the primary event hits. Decay electron tagging in SK I-III was further complicated by an impedance mismatch which occasionally caused spurious hits due to reflected signals. Decay electrons were not searched for in the reflected hit region. Additionally, due to the shorter event window during SK I-III, decay electrons could be split between multiple events if not all hits were contained within the same event window. The identification of these decay electrons is described in [80]. For the SK I-III data used in this thesis, these split decay electrons are counted, but their vertex is considered unreliable. This is relevant to the Multi-Ring event classification discussed in Section 5.1.1.

3.2.8 Neutron Tagging

Neutrons produced following a neutrino interaction may be captured by hydrogen in the detector's water. The captures create excited deuterium, which decays, emitting photons with an average combined energy of 2.2 MeV,

$$n + p^+ \rightarrow d^+ + \gamma \tag{3.15}$$

The 2.2 MeV energy deposition corresponds to approximately seven ID PMT hits. This is enough to be detected in SK. Observing neutrons has several benefits for SK physics: The energy of neutrino interactions correlates with the number of neutrons produced, the presence or absence of neutrons can be used to identify particle interaction processes, and the average number of neutrons produced for neutrino and anti-neutrino interactions of the same energy differs. This last consideration will be discussed in relation to distinguishing between neutrino and anti-neutrino interactions in Chapter 5.

The average neutron capture time on hydrogen is $\tau = 204.8 \pm 0.4\,\mu\text{s}$, so detecting neutrons using the SK I-III electronics was not feasible. As described in Section 2.2.4, the software trigger implemented for SK IV allowed variable event time windows extending out to 535 µs after the trigger, enabling the detection of neutron captures for the SK IV phase and later.

A dedicated neutron tagging algorithm was developed for SK IV based on a two step process [75, 81]. First, clusters of hits were identified as possible candidates, and these hits were fit to find a capture vertex. Next, the hits in the clusters and the vertex were used to define variables which were input into a neural network. The neural network classified the event as either a neutron capture or background based on weighted combinations of each variable.

Beginning with SK V, the neutron tagging algorithm was modified to disregard the fitted neutron capture vertex[1]. The present algorithm uses a modified set of variables calculated assuming the primary event vertex is the neutron capture vertex, and uses a different neural network structure from the original SK IV algorithm. This thesis will provide a summary of the SK IV approach and note the differences with the SK V method.

Step 1: Candidate Selection

Neutron capture candidates are found using a sliding 10 ns residual time window, where the residual times are calculated assuming the primary event vertex[2]. Candidate selection is based on the number of hits in, and around, the window:

- The number of hits in the 10 ns sliding window must be seven or more and less than 50.
- The number of hits in a 200 ns window around the time of the first hit of the candidate hit cluster must be less than 200

The first requirement bounds the expected hit count from a true neutron capture to reduce spurious coincidences from both PMT noise and higher-energy radioactive backgrounds or decay electrons. The second requirement ensures the neutron captures are not coincident with, e.g., a muon passing through the detector. This candidate selection also establishes a capture time, t_0, taken to be the time of the first hit in the candidate window.

For SK IV only, once the candidates are selected, three fits for the neutron capture vertex were performed using the hits within the 10 ns window. The first fit, `BONSAI`

[1] Seungho Han, *NTag software and analysis for SK-V*. Super-Kamiokande Collaboration Meeting, December 2, 2022

[2] This first step is the same for SK IV and SK V, except for the hit threshold, changed to five, and time window, extended to 14 ns. The prompt vertex assumption follows from simulation studies showing that 70 % of neutron captures occur within 200 cm of the primary event vertex, so the residual times are minimally affected by the assumption.

[82], checks for vertices at points which produce near-zero residual times for subsets of hit PMTs, then successively adds additional hits. Vertices which decline in goodness as more hits are added are dropped from consideration. The second fit searches for a vertex on a fixed grid within a sphere centered at the primary event vertex and with a radius of 2 m. The third fit is a re-application of the previous fit, but considers the whole SK detector. The results of the fits are used as inputs in the next section.

Step 2: Neural Network Classification

Neural network classifiers add weighted combinations of information from an event, and output a score reflecting the similarity of the event to pre-classified, "labeled" events. The neural network weights are obtained through a training process. Training consists of applying the neural network to labeled events, assessing the classification decision as correct or incorrect, and adjusting the network weights based on the assessment. For sufficiently realistic training data, the network will eventually optimize the event information to make statistically accurate classification decisions.

In order for a neural network to classify neutron captures, it must be trained on true neutron capture signals and realistic backgrounds. Simulated neutron captures within a realistic description for the SK detector (see Section 4.3) are used as training set for the neutron tagging neural network. However, not all true neutron captures will make an observable signal within the SK detector. For training the neural network, "true" neutron captures are defined as captures identified using the initial candidate selection step, and have a t_0 within 100 ns of the true capture time from simulation. This requirement produces $\sim 1\,\%$ fake events labeled as "true" and $\sim 0.1\,\%$ true events labeled as background in the simulated training data. The candidate selection step also produces false positives, leading to a flat background which has no correlation with true neutron captures. The distribution of differences between the calculated t_0 and the nearest true simulated neutron capture is shown in Figure 3·9. A peak of

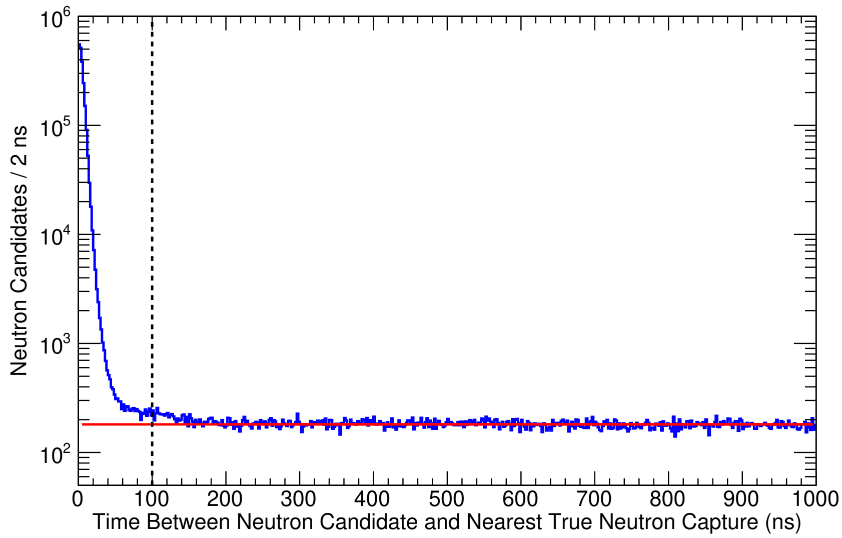

Figure 3·9: Distribution of the time differences between the first hit in a candidate residual time PMT hit cluster and the true neutron capture time for simulated neutron captures. The capture is labeled as "true" if the difference is less than 100 ns, i.e., events to the left of the dashed line. The flat background, red line, is extended to the left of the 100 ns line as an estimate of the background rate for this labeling process. Reproduced from [81].

true neutron captures is visible below 100 ns. The flat background component can be seen extending to large time differences. This component has been extrapolated into the "true" region below 100 ns as an estimate of the background.

Once simulated true candidates and background events have been labeled, measurable quantities of potential neutron captures which are statistically different for true neutron captures and backgrounds must be chosen. The variables used and a brief description for SK IV are listed in Table 3.1. Each variable's inclusion in the network is motivated by physical characteristics of neutron captures. For example, radioactive backgrounds occur most frequently near the detector walls, due to contaminants present in the detector components. Therefore, backgrounds are more likely to occur near a wall than true neutron captures. Additionally, PMT hits from

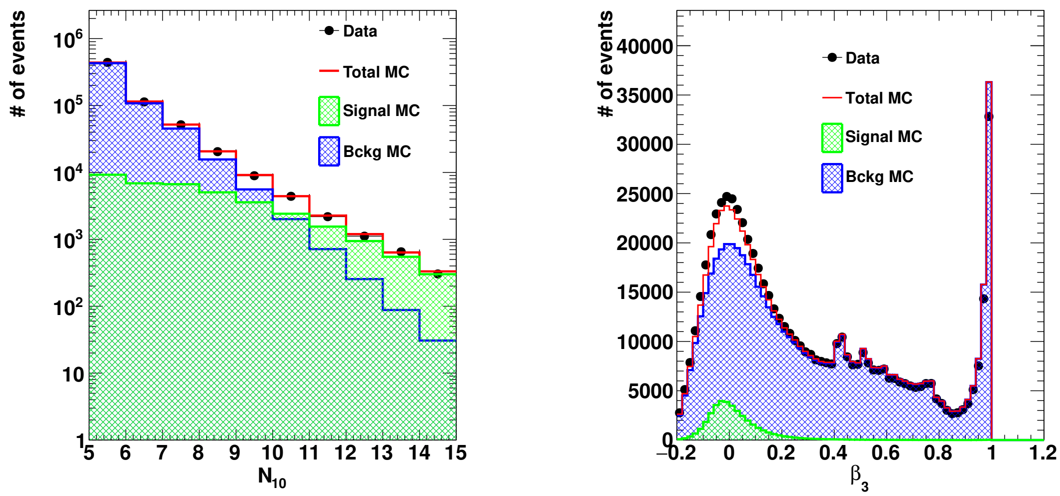

Figure 3·10: Two example variable distributions used as input to the neutron tagging neural network. **Left**: N_{10} distribution for simulated signal and background events versus SK IV data. Signal events tend to have higher N_{10} than background events, as can be seen from the green histogram extending to higher values. **Right**: Isotropy parameter, β_3, distribution for simulated signal and background events, versus SK IV data. Signal events tend to have lower isotropy than background events, as can be seen from the narrow distribution of signal events near 0. Both figures are reproduced from [81]

.

true neutron captures tend to have narrow residual time distributions, small isotropy (they are spatially clustered), and have high consistency with Cherenkov patterns. Background events may be different in one or more of these areas. Two variables used in both the SK IV and SK V selection, N_{10} and β_l for $l = 3$, are shown in Figure 3·10. Distributions for the other variables may be found in [81].

For SK V, the following variables from Table 3.1 are kept: N_{10}, N_{300}, t_{RMS}, ϕ_{RMS}, β_l, NF_{Wall} and L_{towall}. The exact values of the window sizes for several variables, in ns, were also adjusted. All other variables were removed. Two new variables were also added: a data-driven likelihood of each hit originating from PMT dark noise, and the ratio between the number of hit PMTs with a preceding hit within 10 µs to

Variable	Description
N_{10}	The number of hits within a 10 ns residual time window
N_{300}	The number of hits within a 300 ns time window
t_{RMS}	The RMS of the residual times of hits
$\min(t_{\mathrm{RMS}})$	The smallest RMS of residual time hits for combinations of three hits within the 10 ns residual time window
ΔN_{10}	The difference of N_{10} using the primary event vertex and the reconstructed neutron vertex
Δt_{RMS}	The difference of t_{RMS} using the primary event vertex and the reconstructed vertex
θ_{Mean}	Average opening angle from the reconstructed vertex to hit PMTs
ϕ_{RMS}	The RMS of the azimuthal angles of PMT hits
N_C	The number of clustered hits found by merging hits in 14° cones centered at the fitted vertex
$P_{\mathrm{Accept.}}$	Calculated probability of hits based on PMT geometrical acceptance for the fitted vertex.
L_C	Likelihood of hits originating from a single Cherenkov cone
β_l	Isotropy of the hits viewed from the residual time fitted vertex (5 parameters)
N_{Low}	Number of hits on low-probability PMTs.
BS_E	Reconstructed energy from `BONSAI` fit
$\mathrm{BS}_{\mathrm{Wall}}$	Distance from `BONSAI` vertex to the nearest wall
$\mathrm{NF}_{\mathrm{Wall}}$	Distance from residual time fitted vertex to the nearest wall
$(\mathrm{NF}-\mathrm{AP})_{\mathrm{Dist.}}$	Distance from the residual time fitted vertex to the APFIT primary vertex
$(\mathrm{NF}-\mathrm{BS})_{\mathrm{Dist.}}$	Distance from the residual time fitted vertex to the `BONSAI` vertex
L_{towall}	Distance from the residual time fitted vertex to the wall in the direction of the hits from the neutron capture

Table 3.1: Variables used in the SK IV neutron tagging neural network selection. The variables are grouped into three qualitative categories: hit counts & times, hit spatial distribution, and vertex information. Table is adapted from [81].

the total number of hit PMTs in the residual window, N_{10}.

Figure 3·11 shows the performance of the neural network algorithm for identifying neutrons in SK IV data. The neural network outputs a classification score based on the degree of similarity between an event and trained signal and background events. Cutoff scores for different values of the N_{10} variable were chosen to accept or reject neutron capture candidates based on the estimated contamination rate of false neutron captures. For neutron capture candidates with $N_{10} \geq 7$, the chosen cutoff values corresponds to an average false tagging rate of 0.016 neutrons per event, and an efficiency of selecting true neutron captures of 26 %.

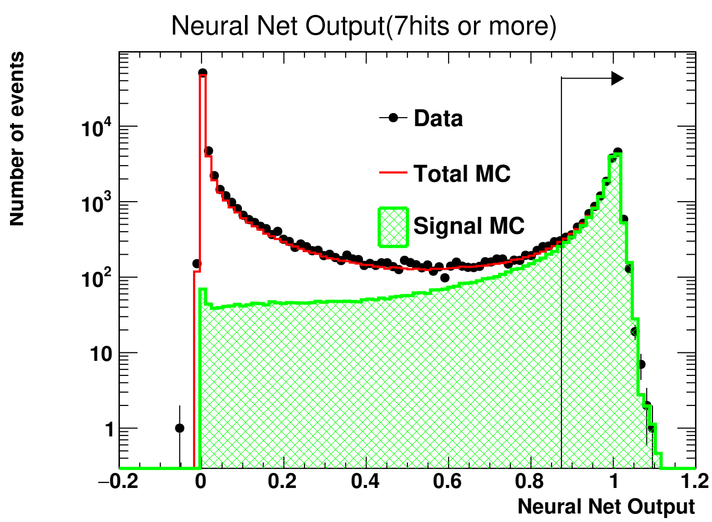

Figure 3·11: Neural network performance in SK IV for neutron candidates with $N_{10} \geq 7$. The green histogram shows the distribution of neural network scores for simulated "true" neutron captures (see text), while the red line shows the distribution for all simulated candidates. The black points show the neural network score distribution for neutron capture candidates following neutrino interactions in SK IV data. The vertical line represents the cutoff value on the neural network output for accepting neutron candidates. Reproduced from [81].

.

Chapter 4

Simulation of Atmospheric Neutrinos

Extracting neutrino oscillation parameters from SK atmospheric neutrino data requires a robust prediction of atmospheric neutrino interactions at SK. Due to the complexities of the atmospheric neutrino flux, neutrino cross sections, and detector effects, an analytic prediction is not feasible. Instead, simulated neutrino interactions drive the prediction.

Simulated neutrino interactions are generated by first assigning each neutrino a direction, energy, and flavor based on the predicted flux of atmospheric neutrinos. The particles produced from the possible interaction processes involving a neutrino of a particular energy are then generated according to a set of cross section models. These secondary particles are stepped through a realistic simulation of the SK detector to produce simulated events. Simulated events are reconstructed with the same algorithms as data events, so that properties of the simulation and data may be compared directly.

The analysis in this thesis uses the flux model of Honda et al. [83], and the cross section models of the NEUT [84] version 5.4.0 neutrino interaction generator. Propagation of particles within the SK detector is performed using the SKDETSIM program, developed internally by the SK collaboration.

4.1 Atmospheric Neutrino Flux Calculation

The first step of simulating atmospheric neutrinos is to estimate the energy- and direction-dependent atmospheric neutrino flux observed at SK. The necessary components of the atmospheric neutrino flux calculation are explained in detail in [85]. Calculating the atmospheric neutrino flux begins with measurements of the primary cosmic ray flux. Cosmic rays with energies relevant for atmospheric neutrinos are measured directly at heights of $\sim$ 30 km by balloon experiments [86], or at even higher altitudes, $\gtrsim$ 100 km, by experiments on spacecraft [87]. These measurements are performed at multiple sites around the world and during different seasons to capture the variations due to atmospheric conditions.

Next, the primary cosmic ray flux measurements are convolved with models of proton-nuclei interactions to generate the number and energy distributions of secondary hadrons. The primary hadrons relevant to neutrino production are pions and kaons. While pions nearly always decay into muon neutrinos, kaons decay into different neutrino flavor combinations, e.g., listed with branching ratios,

$$K_L^0 \rightarrow \pi^{\pm} + e^{\mp} + \nu_e \qquad (41\,\%) \tag{4.1}$$

$$K_L^0 \rightarrow \pi^{\pm} + \mu^{\mp} + \nu_\mu \qquad (27\,\%) \tag{4.2}$$

There are more secondary pions than kaons produced per primary cosmic ray interaction, but at high energies, pions tend to interact before decaying, increasing the contribution to the neutrino flux from kaons. Further, high-energy muons from pion and kaon decays tend to reach the Earth's surface before decaying, leaving kaons as the primary source of electron neutrinos at the highest energies. These effects result in an increase of the muon-to-electron neutrino flavor ratio, discussed in Section 1.5.3, from about 2 : 1 below a few GeV to 4 : 1 to near 10 GeV. The dependence of the flavor ratio as a function of neutrino energy is visualized in Figure 4·1.

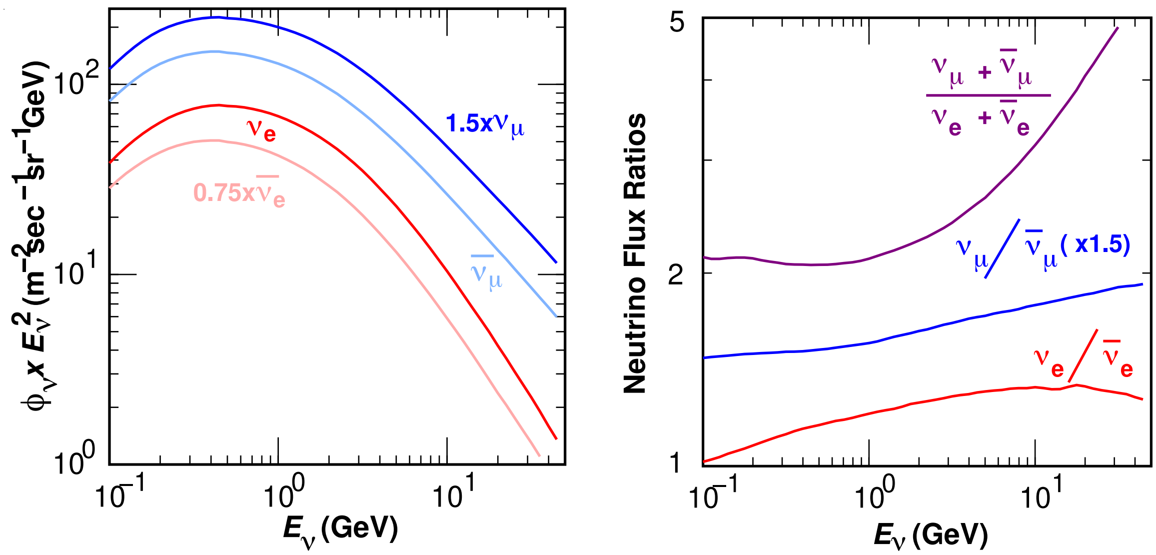

Figure 4·1: Atmospheric neutrino fluxes for different neutrino flavors. **Left**: 1D Atmospheric neutrino fluxes calculated for the Kamioka site. **Right**: 1D atmospheric neutrino flavor ratios calculated for the Kamioka site. Both figures are adapted from [83].

The most precise inputs for the hadron production models come from experiments which accelerate protons on to fixed targets [88]. However, these experiments do not cover the entire phase-space of incident proton energies and outgoing hadron kinematics required to fully predict the atmospheric neutrino flux. Instead, measurements of secondary cosmic muons are used as an estimate for the hadron production model inputs where no direct measurements are available.

4.1.1 Corrections to the Atmospheric Neutrino Flux

The atmospheric neutrino flux calculation has time-varying and anisotropic corrections due to additional effects. These effects mean that the flux must be calculated in "4D": as a function of neutrino energy, zenith angle, azimuth angle, and for different time conditions. The fluxes provided by Honda et al. are also calculated using the terrain profiles of different detector sites, e.g., for SK underneath Mt. Ikenoyama, to reflect the mediation of the cosmic ray flux based on the shape of the overburden.

Because primary cosmic rays are positively charged, the Earth's magnetic field preferentially deflects cosmic rays in an anisotropic way. The deflection additionally implies that cosmic rays below certain energies cannot enter the atmosphere and interact, since they would have had to travel on nonphysical trajectories to enter the atmosphere. This is known as the *East-West Effect* [89], and produces an azimuthal dependence in the atmospheric neutrino flux. The East-West effect results in a deficit of neutrinos arriving from the eastern direction. This is accounted for in the atmospheric neutrino flux calculation by computing the negative-time trajectories of each primary cosmic ray in the presence of the Earth's magnetic field. If the trajectory intersects the Earth in the past, i.e., the cosmic ray was not of astrophysical origin, the ray is rejected.

Cosmic rays entering Earth's atmosphere also must pass through the solar wind, the magnetized plasma emitted by the Sun. The solar wind prevents low-energy, $\sim 1\,\text{GeV}$, cosmic rays from entering into the solar system, while higher-energy cosmic rays enter diffusely as they lose energy [90]. During periods of high solar activity, or *solar maximum*, the turbulence of the solar wind suppresses the lower-energy cosmic rays. On the other hand, during periods of *solar minimum*, more of these lower-energy cosmic rays can pass into the solar system. The solar wind has modulations due to solar activity every 11 years, and therefore produces differences in the atmospheric neutrino flux during SK data taking. The solar modulation effect can change the flux of the lowest-energy neutrinos used in the present analysis by up to 10 %. The size of this effect decreases rapidly with increasing neutrino energy.

The atmospheric neutrino fluxes used for simulating events in this analysis are calculated for three levels of solar activity: minimum, maximum, and "middle." The simulated neutrino events are generated assuming the flux of primary cosmic rays at solar middle, then re-weighted by the fraction of live time spent in solar minimum

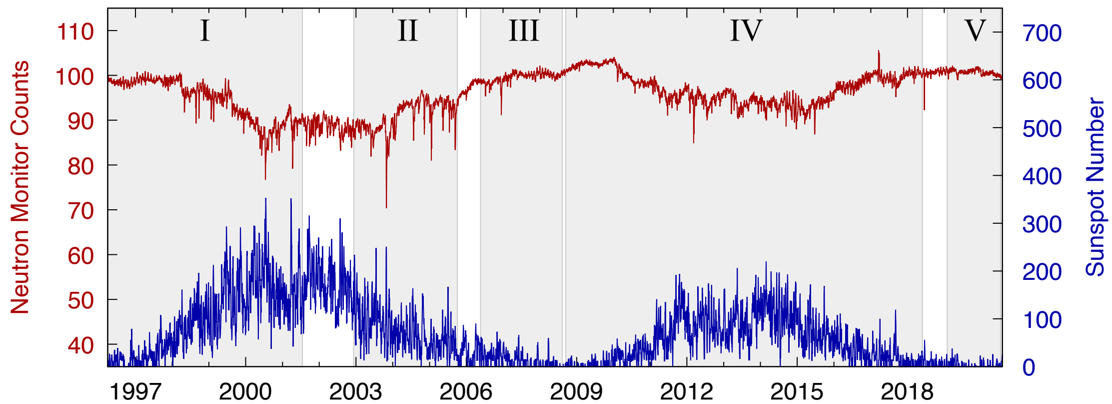

Figure 4·2: Neutron monitor counts during the SK I-V data-taking phases. The neutron monitor data is from [92]. Each SK phase is indicated by a filled grey region. The solar minimum and maximum fractions for each SK phase are calculated as the neutron count ratio during periods of solar minimum and maximum activity. The calculated fractions are tabulated in Table 4.1.

and solar maximum conditions. These fractions are calculated using counts from a neutron monitor [91], which counts the number of cosmic neutrons as a proxy for the number of primary cosmic rays. The fractions are formed by linearly extrapolating the average neutron monitor counts over the each SK phase between the counts during the nearest solar minimum and solar maximum, as defined by the nearest local minimum and maximum sunspot number. The neutron monitor data from [92] and sunspot numbers are visualized in Figure 4·2. Table 4.1 lists the computed maximum and minimum fractions used for the flux re-weighting.

4.2 Neutrino Interaction Models

Neutrino interactions can be broadly categorized based on the final state particles produced. The relevant processes for the analysis presented in this thesis are quasi-elastic, single pion production, and deep inelastic scattering (DIS). NEUT implements several models which predict the interaction cross sections and the kinematics of the

Phase	Solar Activity (%)	
	Min.	Max.
SK I	70	30
SK II	30	70
SK III	100	0
SK IV	44	56
SK V	94	6

Table 4.1: Solar minimum and maximum fractions used for the simulation of atmospheric neutrinos in each phase of SK data taking in this analysis.

outgoing particles in each process.

At atmospheric and beam neutrino energies, neutrinos primarily interact with the protons and neutrons (nucleons) bound within nuclei. For interactions in water, relevant for SK physics, neutrino interactions are separately modeled for interactions with the hydrogen nuclei, nearly free of nuclear effects, and the bound nucleons within the oxygen nucleus.

4.2.1 Quasi-elastic

Quasi-elastic processes are the primary interaction process for neutrinos with energies between $\sim 100\,\text{MeV} - 1\,\text{GeV}$. Quasi-elastic processes in nuclei involve a neutrino interacting with a nucleon to produce an outgoing particle and ejected nucleons, and can be charged current (CC) or neutral current (NC), e.g.,

$$\text{(CC):}\ \nu_l + n \to p + l^- \tag{4.3}$$

$$\text{(CC):}\ \bar{\nu}_l + p \to n + l^+ \tag{4.4}$$

$$\text{(NC):}\ \nu_l + p, n \to \nu_l + p, n \tag{4.5}$$

$$\text{(NC):}\ \bar{\nu}_l + p, n \to \bar{\nu}_l + p, n \tag{4.6}$$

These interactions are *quasi*-elastic because there is only one outgoing lepton which carries away a majority of the momentum compared to the ejected nucleon, and the nucleus has a negligible recoil. A Feynman diagram of the most relevant quasi-elastic process for this analysis, charged current quasi-elastic (CCQE), is shown in Figure 4·3. The figure depicts a neutrino interacting with one of the valence down quarks in a neutron, converting it to an up-quark, and producing an outgoing lepton. Quasi-elastic processes are further categorized into one-particle one-hole (1p1h) and two-particle two-hole (2p2h) processes, referring to the number of nucleons ejected from the nucleus. Illustrations of the 1p1h and 2p2h processes are shown in Figure 4·4.

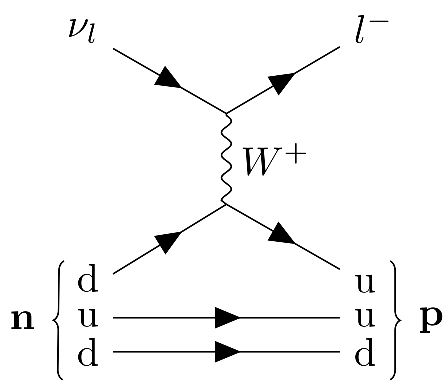

Figure 4·3: A Feynman diagram for the CCQE process. The neutrino with lepton flavor l interacts with a quark inside a nucleon, changing its flavor. An outgoing lepton is produced, and the nucleon remains in-tact after the interaction.

1p1h

The 1p1h interaction refers to both the CC and NC variants of the quasi-elastic process involving a neutrino interaction freeing a single nucleon. Because the ejected nucleon is often invisible, e.g., below Cherenkov threshold, or electrically-neutral if it is a neutron, the double-differential cross section in outgoing lepton energy and angle

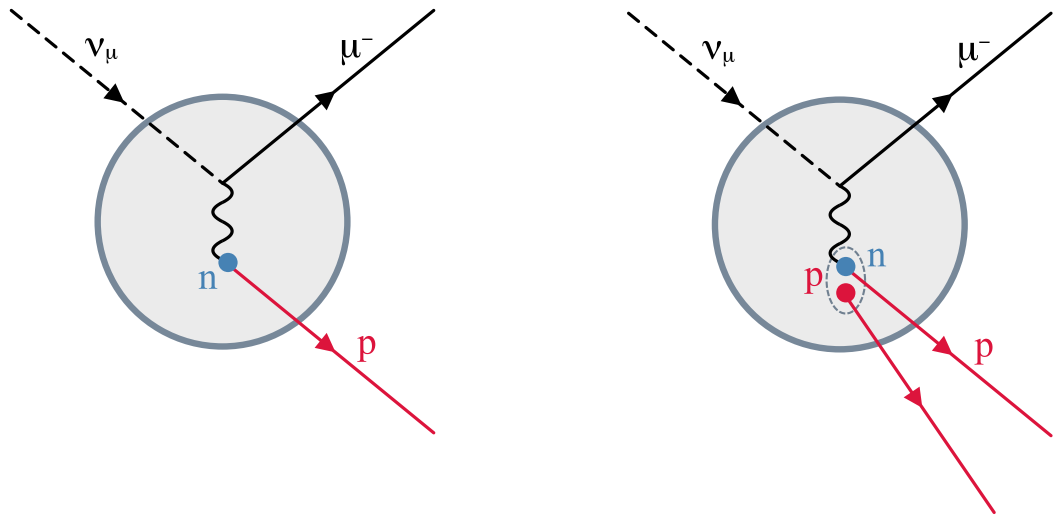

Figure 4·4: Drawings of 1p1h and 2p2h processes. **Left**: An example 1p1h process in a nucleus, in which a muon neutrino converts a neutron into a proton and ejects it from the nucleus. **Right:** An example 2p2h process, in which a muon neutrino interacts with a neutron in a strongly correlated nucleon pair, ejecting both nucleons from the nucleus.

is used:

$$\frac{d^2\sigma}{dE_{\mathrm{Lep}}d\cos\theta_{\mathrm{Lep}}} = \frac{|\vec{k}_{\mathrm{Lep}}|}{|\vec{k}_{\nu}|}\frac{G^2}{4\pi^2}L_{\mu\sigma}W^{\mu\sigma} \tag{4.7}$$

where θ_{Lep} is the angle of the outgoing lepton in the lab frame, E_{Lep} is the lepton energy, $\vec{k}$ are the four momenta of the particles in the lab frame. The final two terms, $L_{\mu\sigma}$ and $W^{\mu\sigma}$, are the leptonic and hadronic tensors which encode the relativistic kinematics of the process. The leptonic tensor is calculated as

$$L_{\mu\sigma} = k_{\mathrm{Lep},\mu}k_{\nu,\sigma} + k_{\mathrm{Lep},\sigma}k_{\nu,\mu} - g_{\mu\sigma}\left(k_{\nu}\cdot k_{\mathrm{Lep}}\right) \mp i\epsilon_{\mu\sigma\alpha\beta}k^{\alpha}_{\mathrm{Lep}}k^{\beta}_{\nu} \tag{4.8}$$

where ϵ_{ijkl} is the Levi-Civita tensor, and $g_{\mu\sigma}$ is the Minkowski metric. The sign for the final term is negative for neutrinos and positive for anti-neutrinos. The exchange of the W or Z boson, and the momentum transfer to the recoiling hadronic system is then encapsulated in the hadronic tensor. The hadronic tensor is not easily computed; it is typically an effective function of nucleon masses, nuclear effects, quark distribution functions, and various corrections.

The authors of [93] calculate the hadronic tensor of Equation 4.7 for the quasi-elastic process. In the calculation, the key contribution comes from the combination of vector and axial-vector current terms, $V^\alpha - A^\alpha$, characteristic of the weak interaction,

$$V^\alpha = 2\cos\theta_C \left[F_1^V(q^2)\gamma^\alpha + i\sigma^{\alpha\beta} q_\beta \frac{F_2^V(q^2)}{2M} \right] \tag{4.9}$$

$$A^\alpha = \cos\theta_C G_A(q^2) \left[\gamma^\alpha\gamma_5 + q^\alpha\gamma_5 \frac{2M}{m_\pi^2 - q^2} \right] \tag{4.10}$$

where θ_C is the Cabibbo angle from quark mixing, γ are the Dirac gamma matrices, M is the nucleon mass, m_π is the pion mass, and q is the four-momentum transfer, $\vec{k}_\nu - \vec{k}_{\mathrm{Lep}}$. Equation 4.9 contains three form factors, F_1^V, F_2^V and G_A. Of these, F_1^V and F_2^V are measured via electron-nucleon scattering experiments, and are considered well-constrained. However, the G_A form factor is only present for neutrino-nucleus scattering, making external measurements difficult. G_A has an assumed dipole form:

$$G_A(q^2) = g_A \left(1 - \frac{q^2}{M_A^{\mathrm{QE}\,2}} \right)^{-2}, \tag{4.11}$$

where the proportionality, $g_A \equiv G_A(q^2 = 0)$, is measured precisely to be ~ 1.27 from beta decay [94]. Equation 4.11 contains a parameter, the axial mass, M_A^{QE}, which is considered experimentally uncertain. Measured values of M_A^{QE} differ by as much as $\sim 25\,\%$ [95]. In addition to modifying the q^2 dependence of the quasi-elastic cross section, larger values of M_A^{QE} increase the total cross section while smaller values decrease the total cross section.

For interactions with nucleons bound within a nucleus, inter-nuclear effects can modify the momentum of a nucleon within a nucleus, as well as the energy required to free it, known as the *nucleon removal energy.* An example of one such nuclear effect is Fermi Motion, referring to the non-zero momentum of each nucleon within the nucleus. This, and other effects, change the total phase-space available for neutrino interactions to produce outgoing particles with particular kinematics. As a result, the description of the nucleons bound within a nucleus affects the interaction cross section.

There is currently no one universally accepted model for bound nucleon momentum distributions and nucleon removal energies. NEUT implements several models, but for this thesis, two are relevant: relativistic Fermi gas (RFG) and local Fermi gas (LFG). The RFG treatment in NEUT follows the LLewellyn-Smith formalism [96], and assumes a single nucleon momentum distribution and nucleon removal energy for all nucleons in the nucleus. Nucleons in the RFG model occupy momentum states up to the Fermi Momentum of the nucleus, p_F, adhering to the Pauli exclusion principle. The LFG model implements the momentum distributions of the RFG model, but postulates radially-dependent p_F and nucleon removal energies. The LFG model tends to predict broader distributions of outgoing lepton energies and angles than the RFG model. The differences between the RFG and LFG models will be further discussed in Section 6.3.3.

NEUT implements the random phase approximation (RPA) correction, an additional effect for 1p1h process due to weak-charge screening effects from other nucleons within the nucleus [97]. In NEUT, RPA corrections are pre-tabulated as a function of the four-momentum transfer, q^2, and can be applied to both RFG and LFG cross sections. In general, the RPA correction decreases the cross section at smaller values of q^2. RPA corrections are not applicable to neutrino interactions with free nucleons.

For the analysis presented in this thesis, simulated bound 1p1h interactions use the default NEUT 5.4.0 configuration, including the "BBBA05" [98] vector form factor parametrization and the LFG model with RPA corrections based on the Valencia model [99]. The axial mass is also set to the NEUT 5.4.0 default value, M_A^{QE} =

$1.05\,\mathrm{GeV/c^2}$.

2p2h

2p2h, and, more broadly, multi-nucleon interactions, involve a neutrino interacting with a strongly-correlated nucleon pair, such that more than one nucleon is freed from the nucleus. The 2p2h contribution to quasi-elastic processes has been estimated to be as high as 20 % [99], although no direct measurements are available for a water target. Models of 2p2h-like interactions include nucleon-nucleon correlations and meson exchange currents (MECs). Nucleon-nucleon correlations refer to short-range strong and electromagnetic forces between the quarks in the nucleons, while MEC refers the longer-range forces due to multi-quark (meson) exchange. The kinematics of the outgoing particle can differ between the different 2p2h mechanisms: MEC-like 2p2h often results in a Δ baryon resonance excitation of one of the nucleons, without decay to a pion. Thus, the cross section for 2p2h is thought to be higher for momentum transfers q near the Δ baryon mass. The implications of this effect on the analysis presented in this thesis is mentioned in Section 6.3.5.

In SK, 1p1h and 2p2h have identical experimental final states, since the ejected nucleons are not observed, leaving the outgoing lepton (if CC) as the only visible particle. Since 1p1h and 2p2h processes have different distributions of lepton kinematics, a realistic neutrino interaction simulation needs to separately account for the 2p2h contribution.

The analysis presented in this thesis uses the NEUT 5.4.0 default implementation of 2p2h cross sections based on the Valencia model [99]. This model is an extension of the 1p1h model from the previous section, but includes multi-nucleon potentials in the hadronic tensor calculation. The model also applies RPA corrections to the 2p2h cross section.

4.2.2 Single Pion Production

Processes producing a lepton, recoiling nucleus, and single pion in the final state constitute a significant portion of the total neutrino cross section at intermediate energies, $\sim$1 GeV to 3 GeV. This energy range is especially relevant for atmospheric and beam neutrinos. There are two main mechanisms for single pion production, resonant and coherent.

Resonant Pion Production

Resonant pion production refers to single pion production from the decays of excited baryon resonances. Resonant pion production is estimated to account for $\gtrsim 90\,\%$ of the single pion production process. The resonant pion production processes include CC channels,

$$\nu_l + p \to l^- + p + \pi^+, \qquad \bar{\nu}_l + p \to l^+ + p + \pi^- \tag{4.12}$$

$$\nu_l + n \to l^- + n + \pi^+, \qquad \bar{\nu}_l + n \to l^+ + n + \pi^- \tag{4.13}$$

$$\nu_l + n \to l^- + p + \pi^0, \qquad \bar{\nu}_l + p \to l^+ + n + \pi^0 \tag{4.14}$$

and NC channels,

$$\nu_l + p \to \nu_l + p + \pi^0, \qquad \bar{\nu}_l + p \to \bar{\nu}_l + p + \pi^0 \tag{4.15}$$

$$\nu_l + p \to \nu_l + n + \pi^+, \qquad \bar{\nu}_l + p \to \bar{\nu}_l + n + \pi^+ \tag{4.16}$$

$$\nu_l + n \to \nu_l + p + \pi^-, \qquad \bar{\nu}_l + n \to \bar{\nu}_l + p + \pi^- \tag{4.17}$$

$$\nu_l + n \to \nu_l + n + \pi^0, \qquad \bar{\nu}_l + n \to \bar{\nu}_l + n + \pi^0 \tag{4.18}$$

A Feynman diagram for an example CC resonant pion production process is shown in Figure 4·5.

To calculate the resonant pion production cross section, one needs to add the

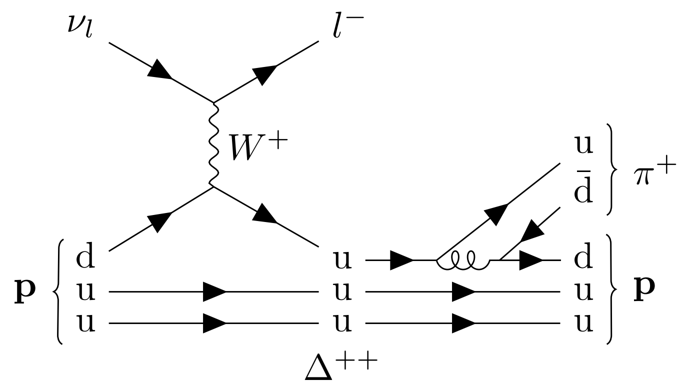

Figure 4·5: A Feynman diagram for a resonant pion production process. A neutrino with lepton flavor l interacts with a nucleus, changing the flavor of one of the quarks. A Δ^{++} baryon is temporarily created in an excited state, which then radiates a gluon, producing a proton and pion.

contributions from each baryon resonance that produces the desired final state. The largest contribution to these resonances at few-GeV energies is the $\Delta(1232)$, which is the lowest-mass resonance above the pion production threshold. However, there are 18 such resonances below 2 GeV. NEUT simulates resonant single pion processes in two steps. In the first step, NEUT calculates the cross section for producing a baryon resonance, accounting for interference between the multiple possible resonance states up to $q < 2\,\text{GeV}$. In the second step, NEUT computes decays of the excited baryon into pions, considering branching fractions and the kinematic dependence on angular momentum of the parent baryon state.

NEUT uses the Rein-Sehgal model [100] for resonant pion production. As in the case of quasi-elastic cross sections, the resonant pion production cross sections contains an axial form factor,

$$C_A^5(q^2) = C_A^5(0)\left(1 - \frac{q^2}{M_A^{\text{Res }2}}\right)^{-2} \tag{4.19}$$

In Equation 4.19, both the resonant pion production axial mass, M_A^{Res}, and the coefficient, $C_A^5(0)$ (simply referred to as C_A^5), are considered unconstrained by experiments.

Resonant single pion production also produces identical final states as some non-resonant channels, e.g., excited protons and neutrons. The authors of [100] note that a contribution from these isospin-1/2 states, added incoherently, is both theoretically motivated and better describes data. The size of this contribution is a free parameter in NEUT, referred to as the *isospin-1/2 background*, $I_{\frac{1}{2}}$.

Resonant single pion processes are simulated for the present analysis using the Rein-Sehgal [100] model, which is the default model in NEUT 5.4.0. The value of the axial mass for resonant single pion production, M_A^{Res}, is set to $0.95\,\mathrm{GeV/c^2}$, the C_A^5 form factor coefficient is set to 1.01, and the isospin-1/2 background scaling parameter, $I_{\frac{1}{2}}$, is set to 1.3.

Coherent Pion Production

Coherent pion production refers to neutrino interactions with the whole nucleus instead of a nucleon. The cross section for this process is much smaller than for resonant production, but cannot be distinguished from resonant pion production at SK. Because coherent pion production only occurs at low q^2, the nuclear recoil is small, such that the outgoing pion is forward-scattered.

Coherent single pion processes are simulated for this analysis using two different models in NEUT. Below 10 GeV, the Berger-Sehgal model [101] is used, while above 10 GeV, the Rein-Sehgal [100] model is used. The main difference between the models is the inclusion of non-zero lepton mass in the Berger-Sehgal calculation. The use of the two models was newly introduced as the default configuration for NEUT 5.4.0 to reflect recent scattering experiment data [102].

4.2.3 Deep Inelastic Scattering

Deep inelastic scattering (DIS) becomes the dominant interaction process for neutrinos with energies $\gtrsim 5\,\mathrm{GeV}$. DIS interactions are characterized by a neutrino interacting with a quark directly, breaking apart the nucleon, and creating multiple hadrons in the final state. In NEUT, an interaction which produces two or more hadrons in the final state is considered to be DIS. DIS is especially relevant for atmospheric neutrinos, as a large fraction of the atmospheric neutrino flux extends into the DIS-dominated energy region.

Due to the potentially high multiplicity of outgoing particles, the DIS cross section is most conveniently calculated in terms of the Bjorken scattering variables x and y. Here, x represents the fraction of the initial nucleon momentum carried by the struck quark, and y represents the fraction of momentum transferred from the neutrino to the hadronic system. Higher values of x correspond to more elastic-like collisions, and higher values of y imply more energy available for the hadronic system. Following [103], the double-differential CC DIS cross section in terms of x and y is

$$\frac{d^2\sigma}{dxdy} = \frac{G_F^2 ME}{\pi}\left\{\left(1 - y + \frac{y^2}{2} + C_1\right) F_2(x) \mp \left[y\left(1 - \frac{y}{2}\right) + C_2\right] xF_3(x)\right\} \tag{4.20}$$
$$C_1 = \frac{m^2}{4E^2} - \frac{M}{2E}xy + \frac{m^2 y}{4MEx} - \frac{m^2}{2MEx}$$
$$C_2 = -\frac{m^2}{4MEx}$$

where M is the nucleon mass, m is the outgoing lepton mass, E is the neutrino energy, and F_2 and F_3 are parton distribution functions. The sign of Equation 4.20 is negative for neutrinos and positive for anti-neutrinos. The sign difference implies that neutrino and anti-neutrino interactions will produce differing amounts of hadrons for the same incident neutrino energy. This will be discussed later in Section 5.1.

NEUT simulates DIS events based on the calculated invariant mass of the hadronic system, W. For $W < 2\,\mathrm{GeV/c^2}$, NEUT uses a custom multi-pion production model tuned to hadron multiplicities measured from bubble chamber data [104, 105]. For $W > 2\,\mathrm{GeV/c^2}$, `PYTHIA` v5.72 [106] is used. `PYTHIA` implements its own hadron multiplicity models, which sometimes result in single pion production. To avoid overlap with the single pion production cross sections separately computed by NEUT, these are discarded.

The analysis presented in this thesis uses the default DIS model of NEUT. This includes GRV98 parton distribution functions (PDFs) [107] with corrections in the low-q^2 region from Bodek and Yang [108].

4.2.4 Final State Interactions

Final state interactions (FSIs) refer to nuclear effects that modify the outgoing hadrons produced in neutrino interactions. In NEUT, four such processes are considered,

- Scattering: A hadron produced in an interaction scatters, changing its momentum and direction.
- Absorption: A hadron produced in an interaction is absorbed before being detected.
- Production: An additional hadron is produced through inelastic interactions with other nucleons.
- Charge exchange: A hadron interaction results in the conversion of a hadron to one with a different charge, e.g. $\pi^+ + n \to \pi^0 + p$.

A related class of effects are secondary interactions (SIs), which refer to the same FSI processes occurring in the detector medium instead of within a nucleus.

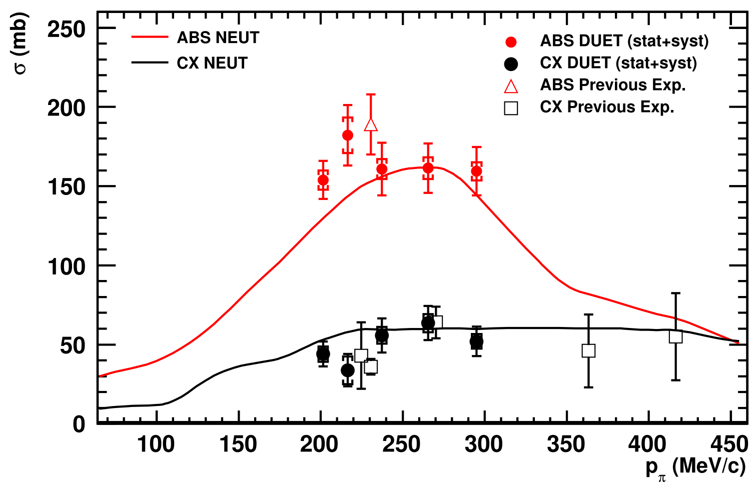

Figure 4·6: Comparison of NEUT predicted $\pi^+ - \mathrm{C}$ cross sections for the absorption (ABS) and charge exchange (CX) FSI processes to those measured by the DUET pion scattering experiment. Figure is adapted from [110].

FSI and SI processes are implemented in a statistical way in NEUT. For FSI, each pion is stepped through the nuclear medium according to estimates of the mean free path. At each step, the pion may randomly undergo one of the FSI processes. NEUT has six parameters which scale the probabilities of each FSI process: The charge exchange and scattering without additional hadron production processes have separate scale parameters for pions with momentum above and below 500 MeV/c. These parameters are tuned to pion scattering data, see Figure 4·6, [109]. The values of the parameters used for simulated interactions in this thesis are listed in Table 4.2.

The total cross sections as a function of incident neutrino energy, calculated with NEUT 5.4.0, for the processes described in this section are shown in Figure 4·7 for electron neutrinos. The cross sections for muon and tau-flavored neutrinos behave similarly, except for the different threshold energies for CC interactions.

FSI Process	NEUT Name	Value
Elastic scattering, $p_\pi < 500\,\mathrm{MeV/c}$	`FEFQE`	1.069
Elastic scattering, $p_\pi > 500\,\mathrm{MeV/c}$	`FEFQEH`	1.824
Charge exchange, $p_\pi < 500\,\mathrm{MeV/c}$	`FEFCX`	0.697
Charge exchange, $p_\pi > 500\,\mathrm{MeV/c}$	`FEFCXH`	1.800
Absorption	`FEFABS`	1.404
Production	`FEFINEL`	1.002

Table 4.2: Probability scaling factors applied to the NEUT FSI processes used in the simulation of atmospheric neutrino interactions. The values are the default values of NEUT 5.4.0.

4.3 Detector Simulation

Neutrino interactions simulated by NEUT ultimately produce lists of final state particles and their momenta. To be compared with SK data, these particles still need to be simulated within the SK detector. This is accomplished with the SKDETSIM program, based on `GEANT3` software [111]. SKDETSIM is responsible for simulating particle traversal through the SK water and the detection of photons by SK hardware.

Particles produced in neutrino interactions must propagate in the detector water, where they can be affected by SIs. SKDETSIM uses a combination of hadronic interaction models to simulate SIs: For hadrons with momenta below 500 MeV/c, SKDETSIM uses the interaction simulation from the NEUT FSI model (see Section 4.2.4). Above 500 MeV/c, SKDETSIM uses the `GEANT3` library `GCALOR` [112].

SKDETSIM simulates Cherenkov radiation emission for charged particles using a combination of `GEANT` models with additional custom features. Among these are the Rayleigh and Mie scattering components of the water transparency model (see Section 2.3.3). SKDETSIM also implements an additional "top-bottom asymmetry" parameter which corrects for differences in the water quality at the bottom versus top of the SK tank.

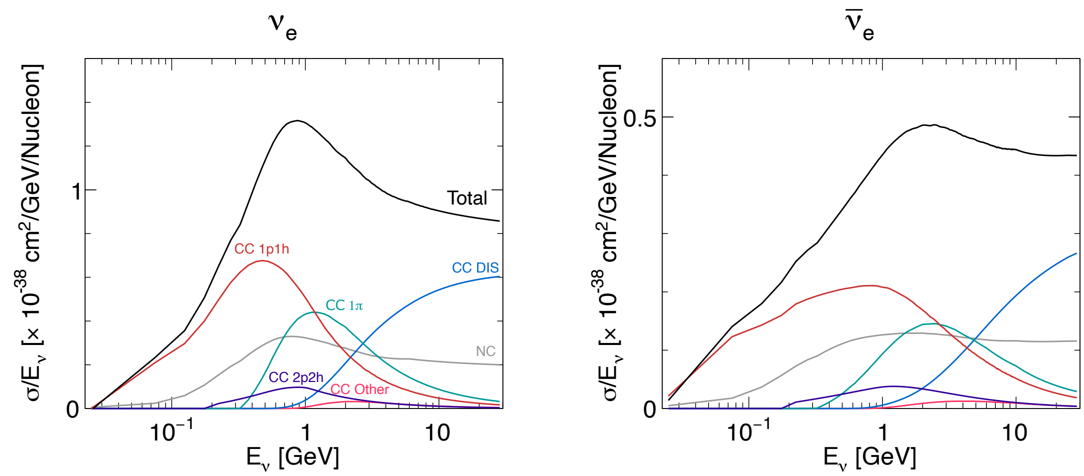

Figure 4·7: Total electron neutrino cross sections divided by neutrino energy, versus neutrino energy, for a water target. The cross sections are calculated with NEUT 5.4.0. The different lines show the contribution to the total cross section for each interaction mode. "CC Other" refers to single, non-pion hadron production. **Left**: Cross sections for neutrinos. **Right:** Cross sections for anti-neutrinos, including the anti-neutrino CC contribution with free protons in water. The line colors match the labels in the left plot.

Cherenkov photons are propagated by SKDETSIM within an approximate geometry of the SK tank. SKDETSIM also contains tuning parameters which adjust the effective reflectivity of Tyvek (see Section 2.2). For photons reaching SK PMTs, SKDETSIM implements a data-driven model of PMT responses and dark noise. The PMT response model in SKDETSIM considers the incident angle and wavelength of incident photons, and the relative quantum efficiency of each PMT. Each photon which reaches the PMT photocathode may additionally reflect, absorb, or transmit through the photocathode without producing a photoelectron. An overall quantum efficiency correction, `COREPMT`, is applied to all PMTs. `COREPMT` is determined from studies of through-going cosmic ray muons for analyses using neutrinos with energies > 100 MeV. Additional details on the detector simulation, and details relevant to analyses with neutrino energies < 100 MeV, may be found in [113].

For the analysis presented in this thesis, 500 years of atmospheric neutrino events

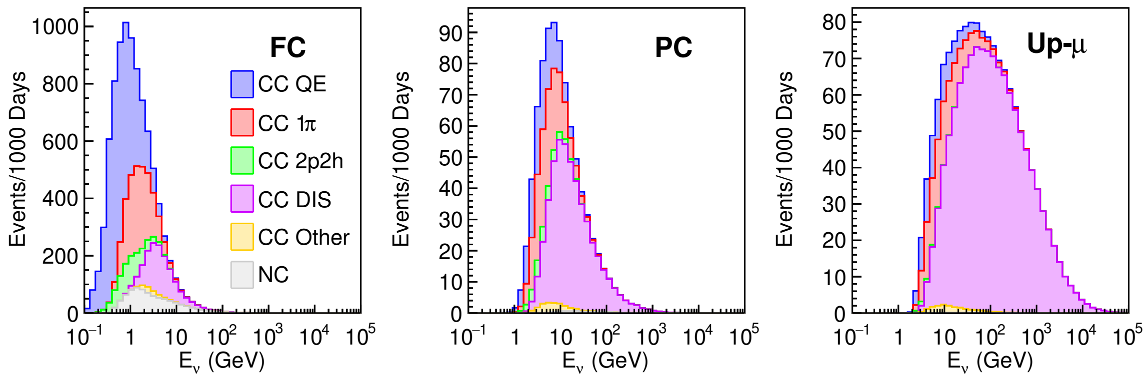

Figure 4·8: True neutrino energy distributions of simulated atmospheric neutrino MC events by interaction mode. "CC Other" refers to single, non-pion hadron production. Distributions are shown for **Left**: FC events, **Center**: PC events, and **Right**: Up-μ events.

are simulated according to the detector conditions in each phase of SK data taking. By using Monte Carlo (MC) events from each phase, the MC accounts for the average detector conditions, e.g., the number of failed PMTs and average PMT gains. The true neutrino energy distributions for the SK IV atmospheric neutrino MC events are shown in Figure 4·8. The distributions are separated by true interaction process to show the energy dependence of the interaction cross sections. The panels in the figure correspond to the distribution for events selected as FC, PC and Up-μ.

Chapter 5

Atmospheric Neutrino Oscillation Analysis

This chapter describes the analysis procedure to determine neutrino oscillation parameters from SK atmospheric neutrino data. Neutrino events identified in the SK data by the procedure in Section 3.1, and simulated MC neutrino events, are separated by reconstruction information into sub-samples which are sensitive to different oscillation effects. Neutrino oscillations are then applied to the MC events to produce a prediction for the data. In addition to oscillation parameters, systematic uncertainties on the flux and cross section models, and on reconstruction efficiency, vary the MC prediction. Oscillation parameters are measured by quantifying the degree of data-MC agreement for a set of oscillation parameters, after accounting for variations in systematic uncertainties.

SK has performed several atmospheric neutrino oscillation analyses in the past [38, 114, 115]; the analysis presented here is a continuation of these analyses utilizing new data and new techniques. The major updates for this analysis are the inclusion of data from an expanded fiducial volume, neutron tagging information used in the event selection, a Multi-Ring classification scheme using a boosted decision tree (BDT), and the inclusion of SK V data.

5.1 Neutrino Sample Selection

As discussed in Chapter 1, the most relevant parameters for atmospheric neutrinos oscillations are θ_{23}, $|\Delta m^2_{32,31}|$, θ_{13}, δ_{CP}, and the neutrino mass ordering. Of these, atmospheric neutrinos are uniquely sensitive to the neutrino mass ordering through matter effects, resulting in an excess of either upward-going ν_e or $\bar{\nu}_e$ events with several GeV of energy. Consequently, identifying these events within all the atmospheric neutrino candidates is a major first step for the analysis. At the same time, other types of atmospheric neutrinos which are not as sensitive to the neutrino mass ordering constrain other oscillation parameters and systematic uncertainties. As described in Chapter 3 atmospheric neutrino candidates are classified as either FC, PC, or Up-μ. For this oscillation analysis, these neutrino candidates are further separated into different sub-samples based on their likely flavors and energies.

Atmospheric neutrino events with large uncertainties on reconstructed quantities do not provide useful oscillation information, and tend to introduce backgrounds. For this reason, FC, PC, and Up-μ neutrino candidates are subject to additional quality cuts. These cuts, and later selections, use the reconstructed visible energy, E_{Vis}, defined as the sum of the reconstructed momenta from all reconstructed rings in an event assuming the ring was produced by an electron. The cuts are:

- ➔ (FC): E_{Vis} must be greater than 30 MeV, the number of OD hits must be less than 16 (10 for SK I), and the reconstructed vertex must be greater than 100 cm from the detector walls.

- ➔ (PC): The ID charge must be greater than 3000 photoelectrons (1500 photoelectrons for SK II), the number of OD hits must be less than 16 (10 for SK I), and the reconstructed vertex must be greater than 200 cm from the detector walls.

➔ (Up-μ Stopping): The reconstructed muon momentum p_μ must be greater than 1.6 GeV/c.

➔ (Up-μ Through-going): The fitted track length must be greater than 700 cm.

These cuts suppress any remaining low-energy events, entering cosmic muon backgrounds, and events with poor reconstructed fit information.

5.1.1 FC Samples

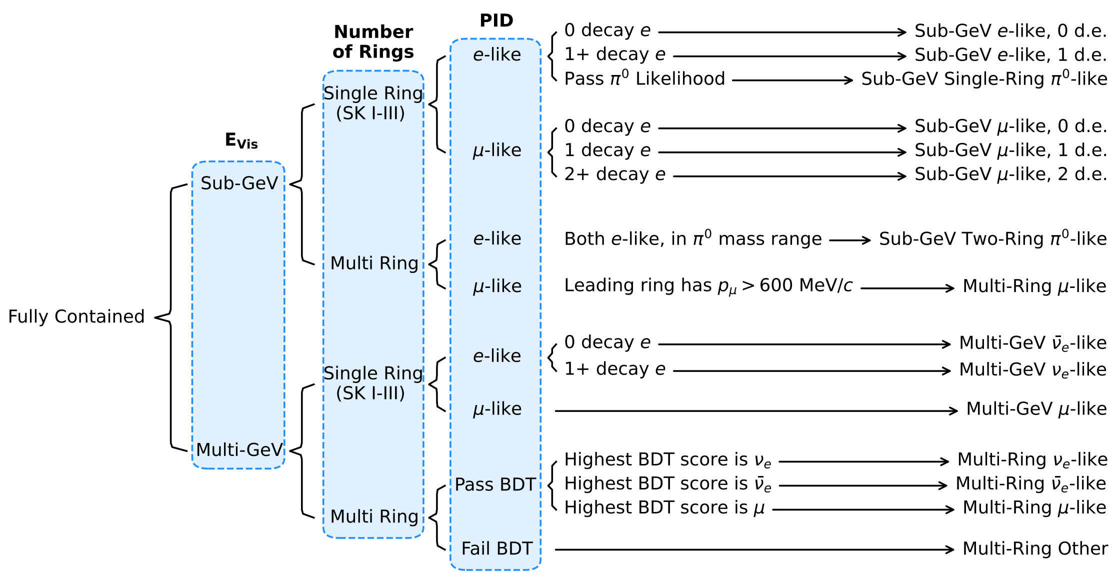

Figure 5·1: Overview of FC event selection. For this analysis, sub-GeV and multi-GeV single ring events from the SK IV-V phases are separated out into additional samples. Note that the Multi-Ring μ-like sample contains both sub-GeV and multi-GeV events. Figure is inspired by Figure 7.1 from [116].

FC events are divided into 14 sub-samples for SK I-III, and 16 sub-samples for SK IV-V. The sub-samples are based on E_{Vis}, the number of rings, PID information, and the numbers of decay electrons and neutrons. Figure 5·1 shows an overview of the FC sub-sample selection. The first step categorizes FC events as either sub-GeV or multi-GeV using E_{Vis}, either below or above 1330 MeV[1]. Then, sub-GeV and multi-GeV events are separated further based on the number of rings, either single or multiple, and into likely e- and μ-like samples.

This analysis uses the numbers of decay electrons and neutrons to enhance the purity of neutrinos and anti-neutrinos in the FC sub-samples. Because decay electrons are more likely to be observed with positively-charged muons, the following neutrino and anti-neutrino interactions can be statistically separated based on the number of decay electrons,

$$\nu_\mu + n \to \mu^- + p, \qquad \bar{\nu}_\mu + p \to \mu^+ + n(\to e) \tag{5.1}$$

$$\nu_l + p \to l^- + p + \pi^+(\to e), \qquad \bar{\nu}_l + p \to l^+ + p + \pi^- \tag{5.2}$$

$$\nu_l + n \to l^- + n + \pi^+(\to e), \qquad \bar{\nu}_l + n \to l^+ + n + \pi^- \tag{5.3}$$

and similarly, the number of neutrons produced can help separate neutrinos from anti-neutrinos: At low energies, the CCQE interaction produces free neutrons for anti-neutrino events but not for neutrino events,

$$\nu_l + n \to l^- + p, \qquad \bar{\nu}_l + p \to l^+ + n \tag{5.4}$$

and at high energies, anti-neutrino interactions are also more likely to produce multiple neutrons than neutrinos due to the structure of the DIS cross section, discussed in Section 4.2.3.

Since neutron tagging was not possible until the SK IV phase, the event selection for neutrinos observed during the SK I-III phases only uses the number of decay electrons. Section 5.1.1 and Section 5.1.1 will discuss the event selection without neutron tagging, then Section 5.1.1 will discuss the incorporation of tagged neutron

[1]The division at 1330 MeV has historical origins in SK analyses searching for proton decay, where the expected signal is $E_{\text{Vis}} \sim m_p \approx 931$ MeV, and atmospheric neutrinos are the main background.

information for the event selection used for data collected during the SK IV-V phases.

Sub-GeV Samples

Sub-GeV events are more numerous than multi-GeV events due to the exponentially-falling flux of atmospheric neutrinos with neutrino energy. However, sub-GeV events also have worse direction and energy resolution compared to multi-GeV events, resulting in smeared oscillation effects. To remove poorly-reconstructed events, sub-GeV events must also pass a minimum momentum cut based on the PID classification of the most energetic ring:

- ➔ (e-like): $p_e > 100\,\mathrm{MeV}$
- ➔ (μ-like): $p_\mu > 200\,\mathrm{MeV}$

Sub-GeV events which pass the minimum momentum requirements are classified by the number of rings and PID information. For sub-GeV events with a single e-like ring, three sub-samples are defined. Two samples are formed based on the number of decay electrons, one or more. A third sample was introduced to separate NC interactions where a π^0 is produced, but only one of the rings from its decay is reconstructed. Sub-GeV single-ring e-like events are passed through a dedicated fitter which forces two e-like rings to be reconstructed. If the dedicated fitter result better agrees with the observed light pattern than the original single-ring hypothesis, the event is categorized as single-ring π^0-like.

Sub-GeV events with a single μ-like ring are separated based on the number of decay electrons. There are separate categories for zero, one, and two or more decay electrons. CCQE interactions are expected to produce up to a single decay electron, so the zero and one decay electron categories are purer in true CCQE interactions. Events with two decay electrons are separated from the CCQE-enhanced samples since these likely result from additional pions produced below Cherenkov threshold, leading to a larger reconstructed momentum bias than for CCQE interactions.

Sub-GeV events with multiple rings are only included in two instances: First, if there are exactly two e-like rings, and the reconstructed momentum is consistent with the π^0 mass, the event is classified as two-ring π^0-like. Next, if there are multiple rings, and the most energetic ring is μ-like, the event is only kept if the reconstructed momentum is $> 600\,\mathrm{MeV/c}$, and it is classified as multi-ring μ-like. Other sub-GeV multi-ring events are not used in this analysis, as the neutrino flavor determination is typically less reliable, adding minimal sensitivity to oscillation effects.

Multi-GeV Samples

Multi-GeV events with a single e-like ring are separated into sub-samples with zero and one or more decay electrons corresponding to $\bar{\nu}_e$-like and ν_e-like, respectively. No decay electron separation is performed for multi-GeV single-ring μ-like events.

In previous analyses, multi-GeV events with multiple rings were classified according to a likelihood-based selection. The likelihood of an event being e-like or μ-like was computed as the likelihood ratio for four reconstruction input variables,

$$\mathcal{L} = \sum_i^4 \log\left[\frac{\Gamma_i^{\mathrm{S}}(x_i)}{\Gamma_i^{\mathrm{B}}(x_i)}\right] \tag{5.5}$$

where i indexes each variable, x_i is the observed value of the variable, and $\Gamma_i^{\mathrm{S,B}}$ is the MC distribution of each variable using true signal and background events, respectively. Here, the signal is defined as true ν_e and $\bar{\nu}_e$ CC events, while other events are considered to be background. The four variables used in the likelihood calculation were: the number of decay electrons, the distance of the furthest decay electron from the primary event vertex, $L_{\mathrm{Decay}\ e}$[2], the PID likelihood of the most

[2]The calculation of $L_{\mathrm{Decay}\ e}$ for SK I-III events excludes decay electrons with unreliable vertices. See Section 3.2.7.

energetic ring, and the fraction of momentum carried by the most energetic ring, F_{mom}. This approach was able to improve the separation of e-like from μ-like multi-ring events versus simply using the PID likelihood of the most energetic ring from $\sim 50\,\%$ to $\sim 70\,\%$.

The likelihood methodology was extended to a two-stage process in [38]. A second likelihood, designed to separate ν_e from $\bar{\nu}_e$, was applied to the e-like candidates. This likelihood used three variables: the number of decay electrons, the transverse momentum of the most energetic ring, T_{mom}, and the number of rings.

This analysis replaces the multi-ring likelihood-based classification with a BDT classifier based on the same input variables used in both likelihood steps. The development of the BDT is documented in [117]. Compared to the likelihood selection, the BDT has the advantage of weighting each input variable's importance for the classification decision based on learned outcomes from training data. MC events with true, known interactions channels are used to train the multi-ring BDT. Each MC event is classified into one of four samples: ν_e-like CC, $\bar{\nu}_e$-like CC, μ-like (for both ν_μ and $\bar{\nu}_\mu$ CC), or "other." The "other" category removes NC and ν_τ CC events from the CC samples which increases the purity of the CC samples.

The BDT performance is sensitive to the number of true events of each sample. For example, because there are fewer true $\bar{\nu}_e$ events than ν_e in the atmospheric neutrino MC, the BDT can correctly classify more events overall by classifying all $\bar{\nu}_e$ events as ν_e. To circumvent this problem, the events used for training are weighted such that the correctly classifying a $\bar{\nu}_e$ event counts more towards the BDT's classification performance.

The distributions of the input variables used for the Multi-Ring BDT are shown for the SK IV-V phases in Figure 5·2, and the output classification decision, "BDT score" is compared for ν_e-live and $\bar{\nu}_e$ like in Figure 5·3.

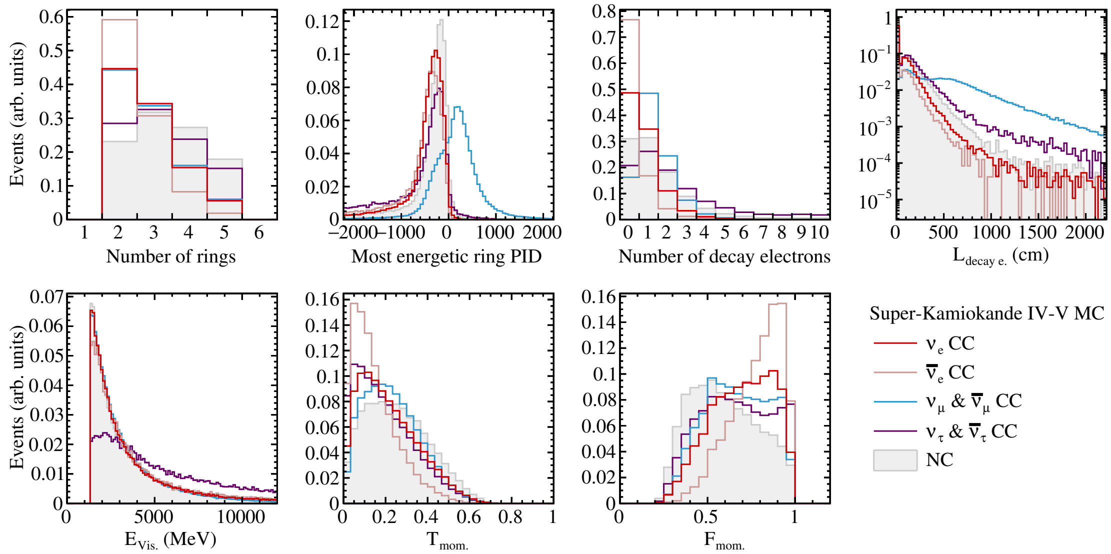

Figure 5·2: Area-normalized SK IV-V MC distributions of the different input variables used for the Multi-Ring BDT selection. True CC neutrino interactions are shown as solid lines while the NC contribution is shown as a filled area. T_{mom} is the transverse momentum of the most energetic ring, and F_{mom} is the fraction of the energy carried by the most energetic ring.

Neutron Tagged Samples

The number of tagged neutrons is used as an additional handle when classifying FC, single-ring events from the SK IV-V phases. Figure 5·4 shows an overview of the modified selection compared to the SK I-III selection. The modification is the same for both sub-GeV and multi-GeV events based on the following principles:

- ν_e CC interactions will produce decay electrons more often than $\bar{\nu}_e$ interactions due to π^+ production.
- ν_μ CC interactions will produce exactly one decay electron less often than $\bar{\nu}_\mu$ CC interactions, due to μ^- capture.
- Neutrino CC interactions will produce fewer neutrons than anti-neutrino CC

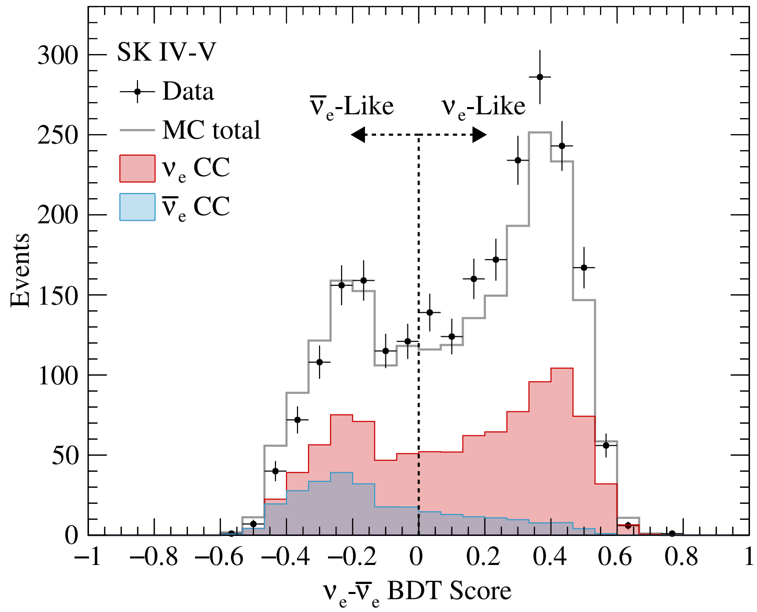

Figure 5·3: ν_e and $\bar{\nu}_e$ separation using the Multi-Ring BDT score for SK IV-V data and MC events. The events shown have a maximum score for either the ν_e or $\bar{\nu}_e$-like category, and the final classification decision is the maximum score of any category. The distributions of ν_e and $\bar{\nu}_e$ scores are preferentially peaked to the right and left of 0 respectively, indicating that the BDT is able to statistically separate these events. The contribution of ν_μ, ν_τ, and NC backgrounds to the ν_e and $\bar{\nu}_e$-like samples is reflected in the MC total line.

interactions.

The corresponding event selection criteria correspond to five sub-samples each for sub-GeV and multi-GeV:

- For e-like events, there are three sub-samples:
  - If the event has at least one decay electron, it is classified as ν_e-like.
  - If the event has no decay electrons and no tagged neutrons, it is classified as a ν_e-$\bar{\nu}_e$-like mixture.

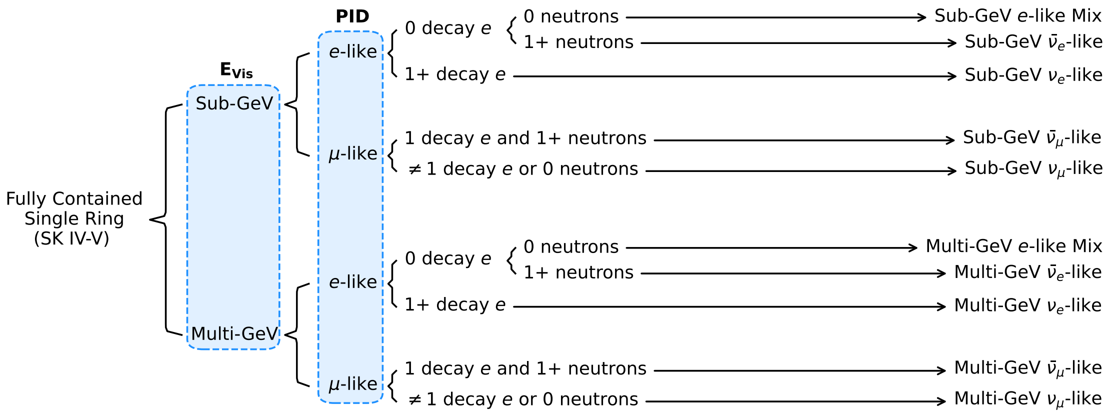

Figure 5·4: The modified FC single-ring event selection for the SK IV-V phases, using the number of tagged neutrons. The motivations for the selection criteria for each sub-sample are described in the text.

  - If the event has no decay electrons at least one tagged neutron, it is classified as $\bar{\nu}_e$-like.

- For μ-like events, there are two sub-samples:

  - If the event has exactly one decay electron, and at least one tagged neutron, it is classified as $\bar{\nu}_\mu$-like.

  - Otherwise, it is classified as a ν_μ-like.

5.1.2 PC Samples

PC events are further divided into two sub-samples based on the estimated stopping point of the produced muon, either in the OD, "PC stopping," or completely outside the SK tank, "PC Through-going." Since PC stopping events have an end point of the OD, their energies may be estimated using the total muon track length, i.e., using the portion of the track in the ID extrapolated to a stopping point in the OD. For PC Through-going events, the momentum of the muon can only be estimated using the portion of the track inside the tank, so the total energy is unknown.

The separation between PC stopping and Through-going sub-samples is performed using the ratio of observed charge to expected charge for a muon with the observed track length. The observed charge consists of the charge of the primary ring reconstructed in the ID, and the maximum charge in a 500 ns sliding window from -500 ns to 500 ns in the OD. The expected charge is the dE/dx for a relativistic muon with a path length equal to the ID path length extrapolated to the SK tank wall, accounting for the un-instrumented region between the ID and OD.

Two additional corrections are applied to the expected charge: For PC events, the high interaction energies often result in multiple outgoing particles with similar directions, which can appear as a single ring. A correction is applied if the charge estimated from the ID track length is greater than the expected dE/dx energy loss of a single particle. The expected charge calculation also applies a correction factor for the different configurations of the OD Tyvek and PMTs during the different SK phases. The factor is determined from the agreement between cosmic muon data and MC, and is applied to the expected charge based on the exit point region in the OD, i.e., top, barrel, or bottom.

5.1.3 Up-μ Samples

Up-μ events are divided into three sub-samples based on each event's expected energy. From lowest to highest average energy, Up-μ events which stop within the ID are categorized as "Up-μ stopping," while Up-μ through-going events are separated into non-showering and showering. The non-showering and showering sub-samples are distinguished based on whether or not the reconstructed muon track is consistent with the expected charge from dE/dx. Showering muons typically have a catastrophic interaction with a nucleus as they travel, creating additional particle showers at one or more sites along the track. The full algorithm which performs the non-showering/showering separation is described in [74].

The event selections described above for FC, PC, and Up-μ events results in 19 sub-samples for SK I-III data and 21 sub-samples for SK IV-V data.

5.1.4 Zenith & Momentum Binning

Because neutrino oscillations depend on the neutrino oscillation baseline, L, and neutrino energy, E, events in each sub-sample are binned into a 2D binning scheme based on their reconstructed zenith angle and observed momentum as correlates of L and E, respectively. FC and PC events are divided into 10 zenith angle bins spanning $-1 \leq \cos\theta_z \leq 1$. There are four exceptions for FC samples, which are only assigned a single zenith angle bin due to limited statistics and poor directional information: single- and two-ring π^0-like, sub-GeV e-like with one decay electron, and sub-GeV μ-like with two decay electrons. Up-μ events, which, by definition, come from below the horizon, are divided into 10 evenly-spaced zenith angle bins spanning $-1 \leq \cos\theta_z \leq 0$.

This analysis updates the zenith angle bins for FC and PC events compared to past SK oscillation analyses. In previous SK analyses, the 10 zenith angle bins were evenly-spaced on the $[-1, 1]$ interval, i.e., with a constant width of 0.2 [38]. However, these bin edges do not align with the mass ordering signal region, defined by the zenith angles where the matter-induced resonant oscillations are expected to occur. This can lead to a potential ambiguity when assessing the data counts in the bins nearest to the signal region. This analysis has updated the zenith angle bin definitions to better capture the resonance region using variable-width zenith angle bins. The comparison of the bins used in this analysis with the evenly-spaced bins is shown in Figure 5·5. The zenith angle bins for the Up-μ samples are not updated for this analysis; they remain evenly-spaced on the interval $[-1, 0]$.

The second axis of the 2D bins separates events by momentum information. This analysis does not attempt to reconstruct the neutrino energy, rather, the observed

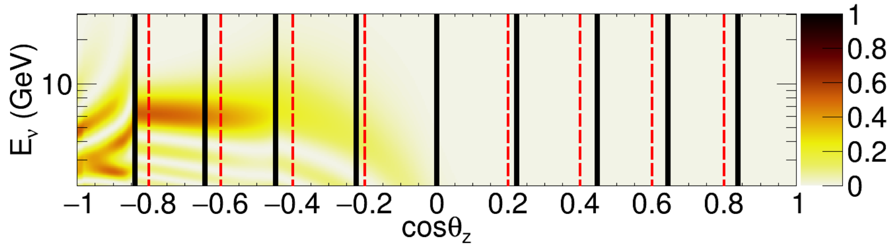

Figure 5·5: Comparison between the zenith angle bins used in this analysis (solid black lines) with the evenly-spaced bins used in previous SK oscillation analyses. The updated bins are symmetric about $\cos\theta_z = 0$. The color scale shows the $\nu_\mu \to \nu_e$ oscillation probability calculated for the normal mass ordering. Using the evenly-spaced bin scheme, the resonance region is partially divided between two bins which include significant fractions of non-resonance regions. In the updated scheme, the resonance region near $\cos\theta_z \approx -0.8$ is better separated from the non-resonance region at smaller zenith angles.

momenta of reconstructed rings for FC events, or of muon tracks for PC and Up-μ events, is used as a correlated quantity. The atmospheric neutrino sub-samples utilize up to five momentum bins, listed in Table 5.1. The definition of "momentum" changes for each sub-sample based on the assumed best correlate of the neutrino energy.

The bin definitions result in 140 FC multi-ring bins, 10 FC π^0-like bins, 60 PC bins, and 50 Up-μ bins, which are used for all SK phases. The remaining FC single-ring events are binned into 260 bins for SK I-III and 410 bins for SK IV-V. The grand total is 930 bins used for the atmospheric neutrino events in this analysis.

5.1.5 Expanded Fiducial Volume

Previous SK atmospheric neutrino analyses only included FC events with a reconstructed vertex at least 200 cm away from any ID wall which defined a 22.5 kt fiducial volume. This atmospheric neutrino oscillation analysis includes, for the first time, FC events with reconstructed vertices between 100 cm to 200 cm from the detector walls for all SK phases, adding a 4.7 kt additional volume. The conventional and additional volumes are collectively called the expanded fiducial volume which contains 27.2 kt

Sample	Number of Bins	Edges, $\log_{10}[p\,(\text{MeV})]$
FC		
Sub-GeV single-ring and single-ring π^0-like	5 $e^{\pm}$ momentum	$2.0, 2.4, 2.6, 2.8, 3.0, 3.2$
Sub-GeV two-ring π^0-like	5 π^0 momentum	$2.0, 2.2, 2.4, 2.6, 2.8, 3.2$
Multi-GeV single-ring e-like	4 $e^{\pm}$ momentum	$3.0, 3.4, 3.7, 4.0, 5.0$
Multi-GeV single ring μ-like	2 $\mu^{\pm}$ momentum	$3.0, 3.4, 5.0$
Multi-Ring ν_e-like and $\bar{\nu}_e$-like	3 visible energy	$3.0, 3.4, 3.7, 5.0$
Multi-Ring μ-like	4 visible energy	$2.0, 3.12, 3.4, 3.7, 5.0$
Multi-Ring Other	4 visible energy	$3.0, 3.4, 3.7, 4.0, 5.0$
PC		
Stopping	2 visible energy	$2.0, 3.4, 5.0$
Through-going	4 visible energy	$2.0, 3.12, 3.4, 3.7, 5.0$
Up-μ		
Stopping	3 visible energy	$3.2, 3.4, 3.7, 8.0$
Through-going non-showering & showering	Single bin	$2.0, 8.0$

Table 5.1: Momentum bin definitions for atmospheric neutrino sub-samples in this analysis. Each row in the Edges column lists the lower bin edges and the upper edge of the highest-momentum bin. The edges labeled 3.12 are evaluated as exactly $\log_{10}(1330\,\text{MeV/c})$.

of water, a 20 % increase over previous analyses.

To expand the fiducial volume, several aspects of the reconstruction were updated, first reported in [118]. Notably, the expected charge distributions from simulated neutrino interactions, used in the calculation of the ring counting and PID likelihoods (see Section 3.2), were separately re-computed using events within the additional region. The updated charge tables account for the decreased number of hits for events closer to the detector walls. Using these new tables in the reconstruction process reduces the bias in reconstructed quantities versus using the same charge tables as in the conventional fiducial volume.

Accepting events closer to the detector walls also means accepting more non-neutrino backgrounds. Close to the walls, the reduction steps which remove flasher PMTs and cosmic muons are less efficient. Experts eye-scanned events in the additional fiducial volume region to newly estimate the non-neutrino backgrounds separately from the conventional region. The distribution of non-neutrino backgrounds estimated for the SK I-IV phases is shown in Figure 5·6. While the non-neutrino backgrounds are higher, they are still tolerable. As demonstrated in the figure, the number of non-neutrino background events increase from approximately 0.1 % to only 0.5 % in the additional region, which is still deemed acceptable. Extending the fiducial volume even closer to the walls is prohibited by the sharp increase in backgrounds.

Figure 5·7 and Figure 5·8 show the atmospheric neutrino data and MC events, including FC events from the expanded fiducial volume, categorized into the different analysis sub-samples. Table 5.2 lists the total number of data and MC events for each sub-sample. The table also shows the MC purity, i.e., the fraction of the true neutrino flavor of MC events in each sub-sample. Note that the SK IV-V multi-GeV $\bar{\nu}_e$ sample, which uses neutron tagging information, has a higher purity of true $\bar{\nu}_e$ CC events than the equivalent SK I-III sample.

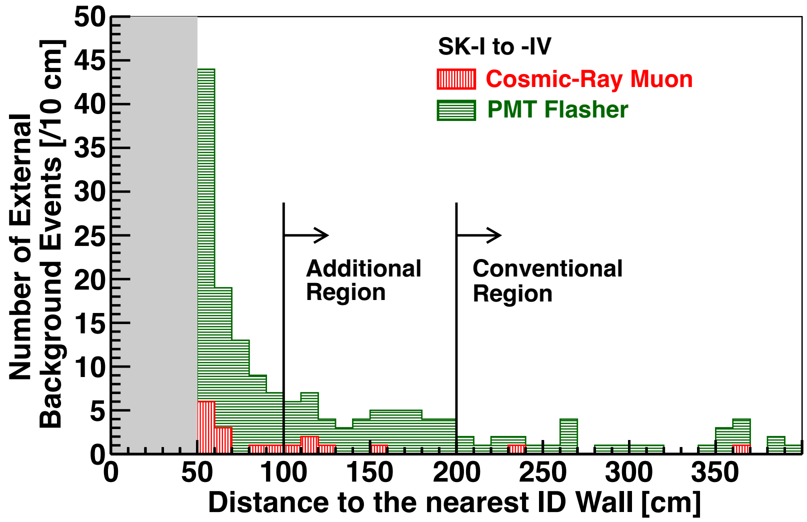

Figure 5·6: Non-neutrino backgrounds determined by eye-scanning during the SK I-IV phases in the conventional and additional fiducial volume regions. Figure is adapted from [118].

Sample	MC Purity (%)					Events	
	ν_e	$\bar{\nu}_e$	$\nu_\mu + \bar{\nu}_\mu$	$\nu_\tau + \bar{\nu}_\tau$	NC	MC	Data
Fully contained (FC), single ring, Sub-GeV							
SK I-III							
e-like							
0 decay-e	73.3	22.7	0.4	0.0	3.6	6399.6	6647
1 decay-e	79.6	1.6	10.6	0.1	8.1	612.0	682
μ-like							
0 decay-e	2.7	0.8	85.3	0.1	11.2	2153.6	2419
1 decay-e	0.1	0.0	96.8	0.0	3.0	4241.1	4476
2 decay-e	0.1	0.0	97.7	0.1	2.2	330.6	336
SK IV-V							
ν_e-like	79.4	1.6	11.5	0.1	7.4	943.7	1093
ν_e or $\bar{\nu}_e$-like	78.9	17.6	0.4	0.0	3.1	5951.4	6669
$\bar{\nu}_e$-like	58.2	36.7	0.5	0.1	4.4	2264.8	1668
ν_μ-like	1.1	0.3	92.9	0.0	5.7	6595.6	7879
$\bar{\nu}_\mu$-like	0.1	0.0	95.0	0.1	4.9	2150.0	1793

Continued on next page

Table 5.2 – Continued from previous page

Sample	MC Purity (%)					Events	
	ν_e	$\bar{\nu}_e$	$\nu_\mu + \bar{\nu}_\mu$	$\nu_\tau + \bar{\nu}_\tau$	NC	MC	Data
Fully contained (FC), single ring, Multi-GeV							
SK I-III							
ν_e-like	56.9	8.6	11.5	3.9	19.0	360.1	383
$\bar{\nu}_e$-like	55.6	34.1	1.6	1.2	7.5	1361.6	1339
ν_μ-like	0.2	0.1	99.2	0.3	0.2	1587.3	1564
SK IV-V							
ν_e-like	60.8	8.7	11.3	3.3	15.9	584.9	643
ν_e or $\bar{\nu}_e$-like	63.8	28.7	1.0	0.7	5.8	867.6	986
$\bar{\nu}_e$-like	43.5	46.0	1.1	1.5	7.9	737.0	616
ν_μ-like	0.2	0.1	99.2	0.3	0.1	1462.9	1619
$\bar{\nu}_\mu$-like	0.1	0.0	99.4	0.4	0.2	592.7	503
SK I-V common samples							
Fully contained (FC) Sub-GeV NC π^0-like							
Single-ring	21.9	6.4	2.0	0.1	69.6	747.9	868
Two-ring	9.6	2.8	1.6	0.0	86.0	2095.2	2494
Fully contained (FC) Multi-GeV, multi-ring							
ν_e-like	49.5	6.6	18.8	3.5	21.5	2152.3	2411
$\bar{\nu}_e$-like	52.0	26.0	5.8	2.5	13.8	1211.6	1131
μ-like	2.8	0.3	91.4	0.6	5.0	3255.2	3427
Other	20.4	2.3	27.1	7.4	42.9	838.0	982
Partially-contained (PC)							
Stopping	8.9	3.4	82.1	1.1	4.5	641.3	689
Through-going	0.6	0.2	97.9	0.7	0.6	3308.0	3397
Upward-going muons (Up-μ)							
Stopping	0.8	0.3	98.6	0.0	0.3	1571.8	1753.8
Non-showering	0.2	0.1	99.7	0.0	0.1	5314.7	6423.9
Showering	0.1	0.0	99.8	0.0	0.1	1051.4	1110.6

Table 5.2: Nominal MC and data events in each sub-sample for this analysis. Columns two to six list the fractions of true neutrino flavor in the MC. The MC events are computed with neutrino oscillations and without fitted systematic uncertainties. Oscillations are calculated assuming the normal mass ordering and $\Delta m^2_{32} = 2.4 \times 10^{-3}\,\mathrm{eV}^2$, $\sin^2\theta_{23} = 0.5$, $\sin^2\theta_{13} = 0.0220$, and $\delta_{\mathrm{CP}} = 4.71$. Up-$\mu$ data events are shown after background subtraction.

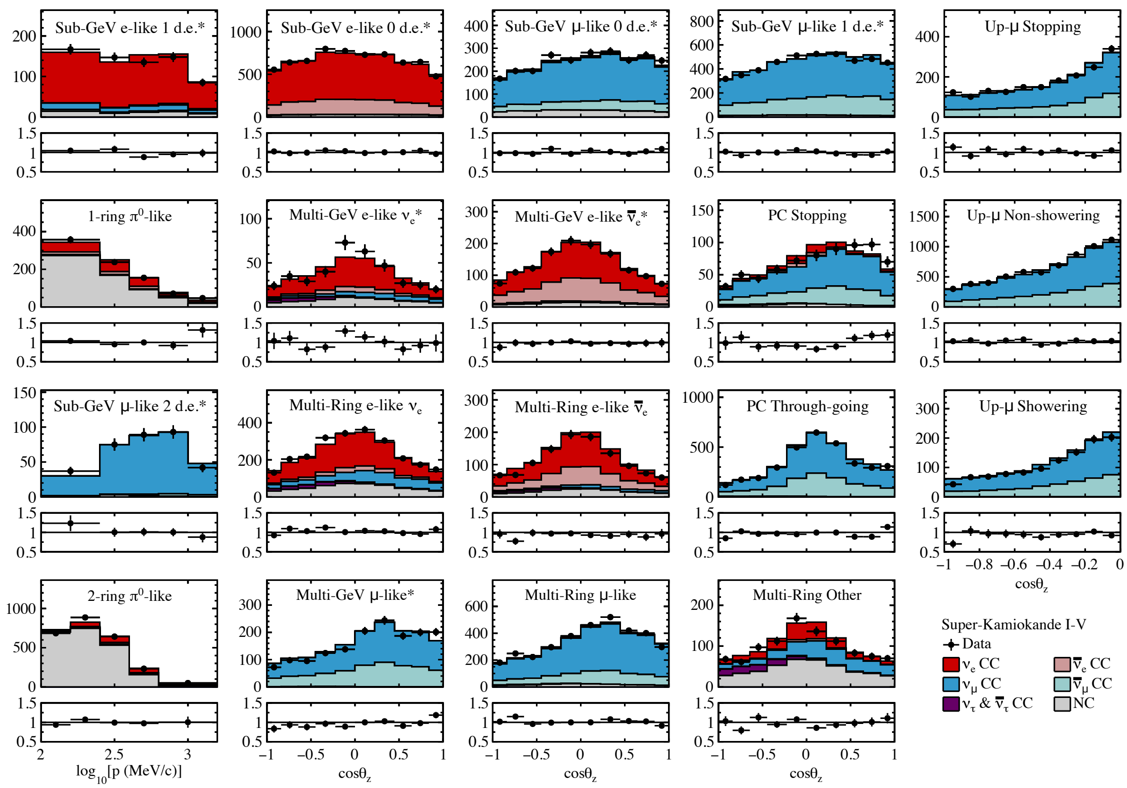

Figure 5·7: Zenith angle or $\log_{10}[p\,(\mathrm{MeV})]$ distributions for atmospheric neutrino events used in this analysis, including events from an expanded fiducial volume. The 19 samples without tagged neutron information are shown. Black data points show the observed number of counts in each bin, while the filled histograms show the contribution to the expected number of counts from the MC prediction. The MC includes neutrino oscillations. The data-to-MC ratio is plotted beneath each sub-sample. All error bars are statistical. Asterisks represent samples containing only SK I-III FC single ring events, i.e., where the SK IV-V events have been separated out.

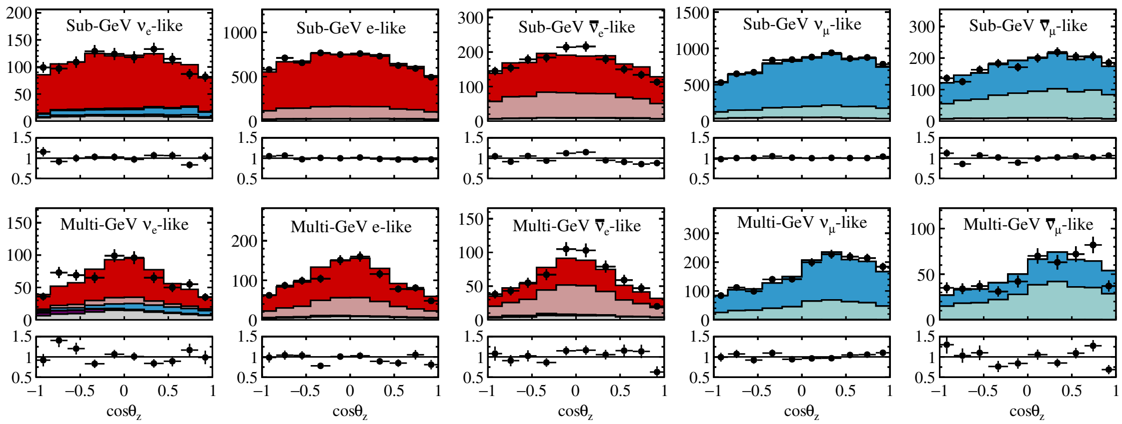

Figure 5·8: Zenith angle distributions for the 10 SK IV-V FC single-ring samples using the number of tagged neutrons. The meaning of the data points, error bars, and filled histograms is identical to what is shown in Figure 5·7.

5.2 Systematic Uncertainties

This analysis considers multiple sources of systematic uncertainties which affect the oscillation parameters extracted from the MC fit to data. Systematic uncertainties are treated as Gaussian fluctuations in the nominal flux, cross section, and detector response parameters which alter the nominal MC prediction. This section lists the corresponding change in the nominal MC prediction for a 1σ fluctuation in each systematic uncertainty source. The largest uncertainties, and those with the largest effect on the fitted oscillation parameters, are related to the flux and cross section inputs to the simulation. However, the detector performance can induce some non-negligible bias on certain oscillation parameters, discussed below.

This atmospheric neutrino oscillation analysis includes a total of 193 independent sources of systematic uncertainties. Of these, 48 account for effects common to all SK phases, e.g., inputs to flux and cross section models. The remaining 145 uncertainties result from 29 $\times$ 5 sources of detector and temporal effects relevant to individual SK phases, e.g., the performance of the detector reconstruction during a particular data-taking phase.

Many of the systematic errors are identical to those documented in detail in [71]. However, several uncertainty sources have been updated or removed entirely, and several new uncertainty sources have been added. This thesis will provide an overview of each source used in the present analysis.

5.2.1 Atmospheric Neutrino Flux Uncertainties

The atmospheric neutrino flux uncertainties are described briefly here. Several of the uncertainties are provided by [119], and compare the predictions of the Honda atmospheric neutrino flux model with two models produced by other groups [120, 121], referred to as "the three flux models" below.

Flux normalization: An overall flux normalization uncertainty, estimated from the combined uncertainties on the hadron production models, air density, and hadron interaction models used as inputs to the atmospheric neutrino flux calculation, varies the event rate of all samples as a function of the true neutrino energy. There are independent errors for neutrinos with energies above and below 1 GeV. Fluctuations in this uncertainty correspond to changes in the normalization of the MC events, visualized in Figure 5·9.

Flavor ratios: There are three sets of uncertainties on the overall muon-to-electron flavor ratio, $(\nu_\mu + \bar{\nu}_\mu)/(\nu_e + \bar{\nu}_e)$, and the individual neutrino-anti-neutrino ratios for $\nu_e/\bar{\nu}_e$ and $\nu_\mu/\bar{\nu}_\mu$. The overall muon-to-electron flavor ratio uncertainty is calculated as the percent difference in flavor ratio between the three flux models, averaged over all directions. The neutrino-anti-neutrino ratios are calculated by comparing the ratios of π^+/π^- and K^+/K^- production in the three flux models, also averaged over all directions. Each uncertainty has three independent errors for energy ranges: $E_\nu < 1\,\mathrm{GeV}$, $1\,\mathrm{GeV} < E_\nu < 10\,\mathrm{GeV}$, and $E_\nu > 10\,\mathrm{GeV}$. For these uncertainties, a 1σ change corresponds to an increase in the weight by $+1/2$ of the percent difference for the numerator neutrino type, and a simultaneous $-1/2$ change by the percent difference for the denominator neutrino type. The change in event weight as a function of neutrino energy for the flux uncertainties is visualized in Figure 5·9.

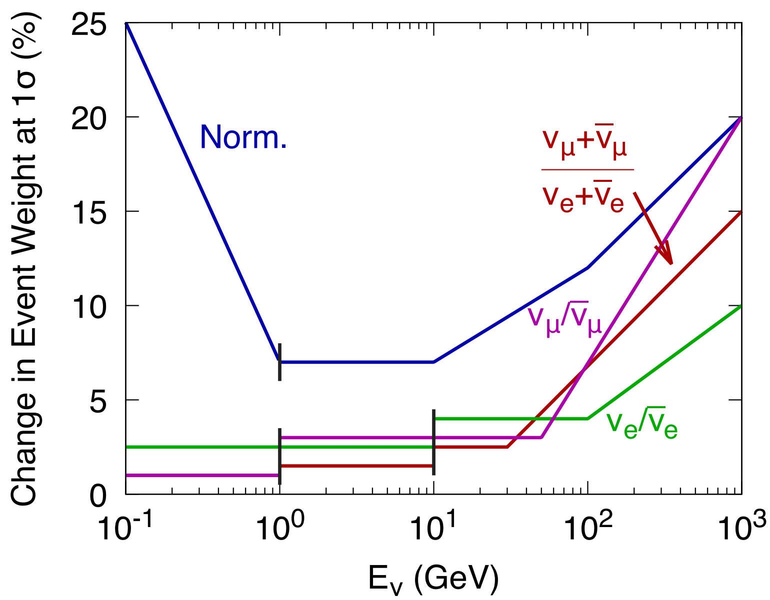

Figure 5·9: Change in event weight for a 1σ change in the absolute flux normalization and flux flavor ratio systematics. The weights are computed as linear functions of $\log_{10}[E_\nu\,(\mathrm{GeV})]$. The absolute flux normalization has two independent systematics in the analysis, which are split at the vertical bar at 1 GeV. The flavor ratio uncertainties have three separate components, split at the vertical bars at 1 GeV and 10 GeV. The normalization uncertainty affects all neutrinos in the MC, while the flavor ratio uncertainties only apply to neutrinos of the specified flavor. Note that the change in event weight for the flavor in the denominator of the flavor ratios has the opposite sign.

K/π ratio: Above 10 GeV, kaons become an appreciable fraction of the neutrino-producing particles in the atmospheric neutrino flux. Uncertainty on the ratio of

pions to kaons translates to uncertainty on the atmospheric neutrino flux prediction. To estimate the uncertainty, the Honda flux model is computed assuming an alternate ratio of kaons and pions. The energy-dependent ratio between the alternate calculation and the nominal model is taken as the 1σ effect. The effect is largest for the highest energies; it is approximately 3 % for the FC and PC samples, and extends up to 10 % for the Up-μ samples.

Neutrino path length: Variations in the atmospheric density can change the average atmospheric neutrino production height, and therefore the oscillation baseline. This has a few-percent effect on the path length of neutrinos coming from above the horizon, and is negligible for neutrinos coming from below the horizon. The 1σ variation is taken as a change in the atmospheric density by 10 %, estimated from the comparison of two atmospheric density models [122, 123]. The corresponding event weights are computed as the ratio of oscillation probabilities after this change to the nominal oscillation probabilities.

Up/Down Ratio: Earth's magnetic field produces an asymmetry in the zenith angle distributions for low-energy atmospheric neutrinos. The uncertainty on this effect is calculated by comparing the zenith angle, θ_z, distributions predicted by the three flux models. The change in event weight for a 1σ fluctuation of this uncertainty ranges from 0.02 % to 3.4 % depending on the neutrino direction, energy, and sub-sample.

Horizontal/Vertical Ratio: Near the horizon, the distance traveled by atmospheric pions and muons increases, allowing for more time to interact or decay. This makes the flux near the horizon sensitive to atmospheric neutrino flux model inputs not assessed by the up/down ratio uncertainty. The horizontal/vertical ratio systematic quantifies the variation in the flux predictions in the horizontal ($0 < \cos\theta_z < 0.1$) and vertical ($0.9 < \cos\theta_z < 1.0$) directions from the three flux models. The change in event rate from a 1σ fluctuation of this uncertainty is approximately 1 % to 3 %.

Solar Activity: This uncertainty modifies the dependence of the low-energy atmospheric neutrino flux due to the solar wind time variation, discussed in Section 4.1.1. The $\pm 1\sigma$ effect is found by re-calculating the minimum and maximum solar activity fractions (see Table 4.1) for a shift in the dates of each SK phase by ± 1 year. Events are re-weighted by the ratio of the flux after the shift to the nominal flux. The change in event rate from this uncertainty is $< 1\,\%$ for all bins in the analysis, and is largest for low-energy neutrinos. The largest effect among the SK phases is for the SK II phase, which occurred mostly in-between a solar minimum and maximum.

Relative Normalizations: While the absolute flux normalization accounts for the uncertainty on the Honda flux inputs, differences in the absolute flux normalization between the three flux models are not accounted elsewhere. These differences primarily occur above 10 GeV, which is the energy range most relevant for the multi-GeV FC, PC, and Up-μ stopping samples. Separate 5 % uncertainties on the normalizations of the multi-GeV FC and PC+Up-μ samples are introduced to cover these differences.

5.2.2 Neutrino Interaction Model Uncertainties

This analysis implements 26 uncertainties for various aspects of the cross section models in NEUT.

Quasi-elastic Uncertainties

Quasi-elasitc uncertainties modify aspects of the 1p1h and 2p2h cross section models. These uncertainties primarily affect CC 1p1h, i.e., CCQE, events. For these, the NEUT default model, LFG with RPA corrections and $M_A^{\mathrm{QE}} = 1.05\,\mathrm{GeV/c^2}$, is compared to an alternative RFG model without RPA corrections, and $M_A^{\mathrm{QE}} = 1.21\,\mathrm{GeV/c^2}$. These are referred to as the "nominal LFG model" and "RFG model" below.

Quasi-elastic Axial Mass: The uncertainty on M_A^{QE} from Equation 4.11 modifies the axial form factor, which in turn affects the total cross section and q^2 dependence of the CCQE cross section model. This uncertainty re-weights CCQE events by the double-differential cross section ratio $d^2\sigma/dE_{\mathrm{Lep}}d\cos\theta_{\mathrm{Lep}}$ between a 1σ fluctuation in M_A^{QE} and the nominal value. The 1σ fluctuation is set to $M_A^{\mathrm{QE}} = 1.21\,\mathrm{GeV/c^2}$. Currently, the double-differential cross section ratio is computed assuming the simpler RFG model for both the fluctuated and nominal double-differential cross section. The next set of uncertainties compare the differences between the LFG and RFG models.

CCQE Shape: This uncertainty compares the relative differences in neutrino energy dependence between the RFG and LFG model. The 1σ change is taken to be the fractional difference in the normalized total cross sections, as a function of E_ν, between the RFG model and the nominal LFG model.

CCQE Normalizations: This uncertainty compares the total cross section prediction between the RFG and LFG model. The 1σ change is taken to be the fractional difference in the total cross section between the RFG model and the nominal LFG model. Two independent uncertainties are implemented for the normalizations above and below 1330 MeV. For sub-GeV ν_e and ν_μ CCQE events, the uncertainties are 5 % and 1 %, respectively. For multi-GeV CCQE events, the uncertainties for ν_e and ν_μ flavors are 25 %.

CCQE Flavor Ratios: Additional uncertainties are placed on ratio of neutrino and anti-neutrino CCQE total cross sections, $(\nu_e+\nu_\mu)/(\bar{\nu}_e+\bar{\nu}_\mu)$, and the ratio of electron-to-muon flavor CCQE cross sections, $(\nu_\mu+\bar{\nu}_\mu)/(\nu_e+\bar{\nu}_e)$, as a function of neutrino energy. In each case, the 1σ uncertainty re-weights CCQE events by the fractional change in the total cross section ratio between the RFG model and the nominal LFG model.

2p2h: This analysis assigns a 100 % uncertainty on the 2p2h process, due to the absence of direct measurements.

Single Pion Production Uncertainties

M_A^{Res}, C_A^5, $I_{\frac{1}{2}}$: Independent uncertainties vary the three primary inputs to the Rein-Sehgal resonant pion production model. In each case, the input parameter is shifted by its $+1\sigma$ uncertainty, and the ratio of the double-differential cross section, $d^2\sigma/dq^2dW$, with respect to the nominal values is taken as the 1σ effect. Here, q^2 is the squared 4-momentum transfer, and W is the invariant mass of the pion-nucleon system. The uncertainties for each parameter are $M_A^{\mathrm{Res}} = 0.95 \pm 0.15\,\mathrm{GeV/c^2}$, $C_A^5 = 1.01 \pm 0.12$, and $I_{\frac{1}{2}} = 1.30 \pm 0.20$.

Neutrino/Anti-neutrino Ratio in Single Pion Production: This uncertainty accounts for differences in the neutrino and anti-neutrino resonant pion production cross sections between the nominal Rein-Sehgal model and the Hernández model [124]. The 1σ effect re-weights resonant pion events by the energy-dependent total cross section ratio between the two models. The weights are separately computed for the three CC modes and the four NC modes listed in Equations 4.12–4.18.

Charged/Uncharged Ratio in Single Pion Production: This uncertainty compares the ratio of charged pion, $\pi^\pm$, production to neutral pion, π^0, production between the Hernández model and the nominal Rein-Sehgal model. The 1σ effect increases the weight of the resonant π^0 production modes by 20 % and decreases the weights of the resonant $\pi^\pm$ modes by 20 %.

Coherent Pion Production Normalization: This uncertainty produces a 100 % change in the normalization of the CC ν_μ coherent pion production modes, and a 50 % change in the normalizations of the CC ν_e and NC modes at 1σ.

DIS Uncertainties

DIS Normalization: This uncertainty compares the NEUT nominal DIS total cross section to the world-average DIS total cross section [51]. The uncertainty is calculated from the difference in the total cross section for neutrino energies ranging from 30 GeV to 200 GeV. The 1σ variation corresponds to a 3.5 % change for DIS neutrino interactions and a 6.5 % difference for DIS anti-neutrino interactions.

PDF Difference Below 10 GeV: While NEUT computes the DIS cross section using the GRV PDFs, other PDFs are available. This systematic treats the DIS total cross section ratio between the total DIS cross section computed with PDFs from [125] and the nominal NEUT DIS total cross section as a 1σ effect. The ratio is computed as a function of energy, and for neutrinos and anti-neutrinos. The corresponding change for DIS events is listed in Table 5.3.

Energy (GeV)	Change at 1σ (%)	
	ν	$\bar{\nu}$
< 2	30	50
2–3	10	40
3–5	5	20
5–10	5	10

Table 5.3: Fractional change for DIS events due to a 1σ change in the PDF Difference uncertainty.

DIS q^2 Dependence: There are four independent uncertainties implemented to capture variations of the Bodek-Yang corrections applied to the NEUT DIS cross section models. The first handles cases where the invariant mass of the hadronic system, W, is above $2\,\mathrm{GeV/c^2}$. This uncertainty uses the change in DIS cross section with and without the Bodek-Yang corrections applied, as a function of q^2, as the 1σ uncertainty.

For $W < 2\,\mathrm{GeV/c^2}$, three independent uncertainties vary the vector and axial components, and overall normalization, of the Bodek-Yang correction. For the vector and axial component uncertainties, the 1σ change re-weights events by the ratio of the cross section with and without additional features described by the authors in [126]. The vector uncertainty considers the effect of computing the next-to-leading-order QCD contribution to the F_2 and xF_3 form factors. The axial uncertainty considers the effect of allowing the axial form factors to diverge from the vector components, which are, in the nominal Bodek-Yang correction, assumed to be the same. The normalization uncertainty uniformly scales the size of the correction by $\pm 3\,\%$.

DIS Hadron Multiplicity: This uncertainty considers the uncertainty in the number of hadrons produced in DIS interactions for a given invariant mass of the hadronic system, W. The calculation involves computing the ratio of cross sections as a function of W between the GENIE [127] event generator and NEUT, multiplied by the change in hadron multiplicity at the specified W value. The 1σ effect of this uncertainty does not modify the total number of DIS events; rather, it increases and decreases the frequency of DIS events with particular numbers of outgoing hadrons, before accounting for FSI effects.

Final State Interaction Uncertainties

FSI+SI: Different FSI and SI processes can result in final states that are difficult or impossible to distinguish. As a result, the six FSI and SI parameters in NEUT, listed in Table 4.2, tend to have high correlations when fit to charged pion scattering data. While these correlated fluctuations are not implemented in the fit, this analysis applies a conservative uncertainty on FSI and SI processes: The six FSI+SI parameters are varied based on their uncertainties, taking into account correlations, to produce sets of possible parameter combinations. The two parameter sets which produce the largest increase and largest decrease in total event rate are taken as the 1σ uncertainty. The parameter sets used are listed in Table 5.4. Note that the minimum set has the highest scaling of the pion absorption process, while the maximum set has the lowest.

NEUT Name	Min. Set	Max. Set
`FEFQE`	1.6	1.4
`FEFQEH`	1.1	2.3
`FEFCX`	1.6	0.6
`FEFCXH`	2.3	1.3
`FEFABS`	1.6	0.6
`FEFINEL`	1.5	0.5

Table 5.4: Parameter sets used for computing the change in event weights due to uncertainty in FSI processes.

Neutron Production Uncertainties

Neutron Multiplicity Generator Comparison: This uncertainty takes the probability ratio of producing a given number of neutrons between the GENIE event generator and the nominal NEUT neutron multiplicity model as the 1σ effect. The change in event weight based on this ratio is calculated as a function of the neutrino energy.

Neutron Multiplicity versus Transverse Momentum: Studies of neutron multiplicities in T2K data from [128] revealed a difference in the number of neutrons predicted by the MC versus data, shown in Figure 5·10. The difference was measured for ν_μ and $\bar{\nu}_\mu$ interactions, and has a dependence on the transverse momentum of the outgoing muon. The 1σ effect of this uncertainty changes the number of neutrons by the fractional difference between the MC and data on average, then re-classifies the event according to the procedure in Section 5.1.1.

Previous versions of this uncertainty calculated the change in the number of neutrons by multiplying the number of tagged neutrons by the fractional difference be-

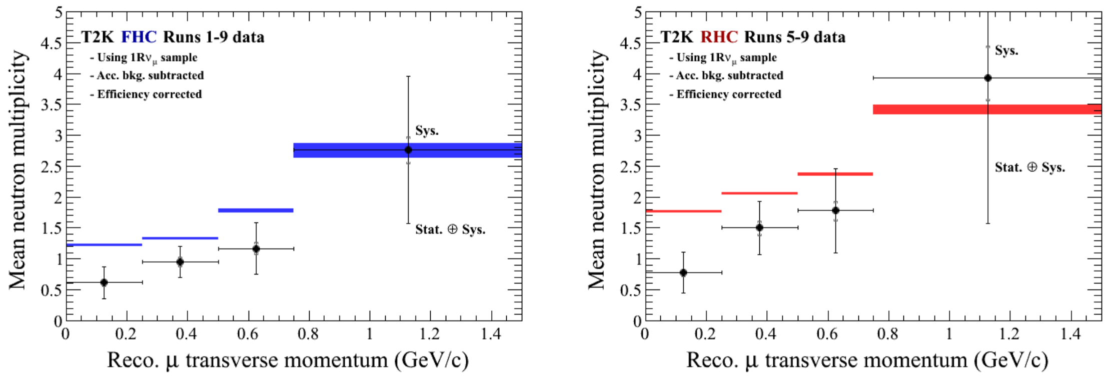

Figure 5·10: Neutron multiplicity measurement with T2K data versus NEUT MC prediction for neutrinos (left) and anti-neutrinos (right). The uncertainty values used in this analysis are the fractional differences between the MC and data points as a function of the lepton transverse momentum. Figures are reproduced from [128].

tween MC and data as the 1σ effect. However, because the event selection procedure in this analysis only relies on the difference between zero and one tagged neutron, simply applying a multiplicative factor to the number of tagged neutrons may not accurately reflect the average change in classification outcome. For example, if the fractional difference for an event is 50 %, an event with two neutrons would move to 1 tagged neutron at -1σ, and leave the event classification unaffected. Thus, the change at 1σ for the event is 0, and scaling the effect would not reflect a larger fluctuation as expected.

Instead, this analysis calculates the change in the number of neutrons by dividing the total event weight into multiple events with any possible shift in the number of neutrons. The probability of increasing or decreasing the number of tagged neutrons by k is calculated from a one-sided Gaussian distribution with a width set such that the expected value of the number of neutrons after the shift is $n \times (1 \pm r)$, where n is the original number of tagged neutrons in the event, and r is the fractional difference between MC and data. If $n = 0$, the width is set to r. In the original example, the -1σ decrease in this systematic splits the weight of the event with two tagged neutrons between three events with zero, one or two tagged neutrons, such that the expected value is $2 \times 0.5 = 1$ tagged neutron. This method then accounts for shifts from $2 \rightarrow 0$ and $2 \rightarrow 2$ tagged neutrons.

Other Interaction Uncertainties

Tau Neutrino Cross Section: This uncertainty changes the rate of CC ν_τ interactions by 25 % as a 1σ effect. The number is estimated from direct measurements of the ν_τ cross section. In 2018, SK published its own measurement with a 20 % uncertainty [129]. It is a future effort to incorporate this measurement, or the ν_τ identification techniques used in that measurement, into this oscillation analysis.

CC/NC Ratio: The 1σ effect of this uncertainty scales the weight of all NC events by 20 %. The size of this error is a conservative estimate from a synthesis of world NC measurements in comparison with theoretical predictions [130].

5.2.3 Detector Performance & Reconstruction Uncertainties

Detector systematic uncertainties are evaluated separately for each SK phase. While, in principle, the uncertainty on various aspects of the reconstruction performance is not fully independent between SK phases, treating them as independent is a conservative estimate of an ultimately minor source of uncertainty, and vastly simplifies the treatment of these sources in the analysis.

Reduction Uncertainties

FC, PC, and Up-μ Reduction Efficiencies: Separate uncertainties are estimated based on MC studies of the various cuts described in Section 3.1. For FC events, the reduction uncertainty primarily comes from data versus MC disagreement in the flasher probability distribution used in FC4, and is highest for the SK V phase. The uncertainty on the efficiency of the cuts is estimated to be $< 1\,\%$ for the Up-μ sample during all SK phases. The values are listed in Table 5.5.

SK Phase	Reduction Uncertainty (%)			
	FC	PC	Up-μ Stopping	Up-μ Through-going
SK I	0.2	2.4	0.7	0.5
SK II	0.2	4.8	0.7	0.5
SK III	0.8	0.5	0.7	0.5
SK IV	1.3	1.0	0.5	0.3
SK V	1.7	1.0	0.7	0.5

Table 5.5: Reduction uncertainties for the different neutrino samples used in this analysis. Uncertainties are separately estimated for Up-μ stopping and through-going events, but a single uncertainty varies the normalization of both samples simultaneously.

FC/PC Separation: A small number of FC and PC events are estimated to be wrongly classified in the alternative sample. The uncertainty on this estimate is calculated for each SK period, and increases the normalization of FC multi-GeV μ-like events while decreasing the normalization of PC events. The change in FC and PC normalizations from this uncertainty at 1σ is $\lesssim 1\,\%$ for all SK periods.

Fiducial Volume/Vertex Resolution: Due to the vertex resolution of APFIT, FC and PC events can be incorrectly reconstructed inside or outside the fiducial volume. A $2\,\%$ uncertainty on the normalization of FC and PC events is assumed from this effect at 1σ. This uncertainty does not apply to Up-μ events since these do not have event vertices within the fiducial volume.

Reconstruction Uncertainties

Many detector systematic uncertainties are estimated using a "scale-and-shift" procedure. The procedure fits the MC distribution of a reconstruction quantity, x, used to separate signal and background in the event selection process, to atmospheric neutrino data. First, MC events are labeled as true signal or background events. Next, the signal and background distributions of x are fit to data by applying a linear transformation to each MC event's x: $x' = \beta_1 x + \beta_0$. The signal and background distributions are transformed independently, so there are four β parameters. Once the best-fit β parameters are found, they are randomly varied assuming Gaussian fluctuations around their best-fit values, where the fluctuations have widths given by the fitted uncertainties. These variations produce a distribution of signal and background event rates, since different β combinations move events above or below the x value used to select signal events. The maximum observed variation in signal event rate from this process is taken as the 1σ uncertainty.

Uncertainties in the ring counting likelihood, ring PID likelihood, and π^0 likelihood variables are estimated with the scale-and-shift procedure. For this analysis, these reconstruction-related uncertainties were separately estimated for events inside the conventional fiducial volume and for events in the additional fiducial volume region. A demonstration of the scale-and-shift fit to the ring counting likelihood distribution using SK V data in each fiducial volume region is shown in Figure 5·11.

Ring Separation: The number of rings is a basic handle for separating neutrinos events into the different analysis sub-samples. The level of disagreement in the distribution of ring counting likelihood (Equation 3.8) between data and MC is used as an estimate of the uncertainty on the ring counting reconstruction. The maximum fractional change in the number of true single- or multi-ring events using the scale-and-shift procedure is taken as the 1σ effect. For this analysis, this systematic is computed

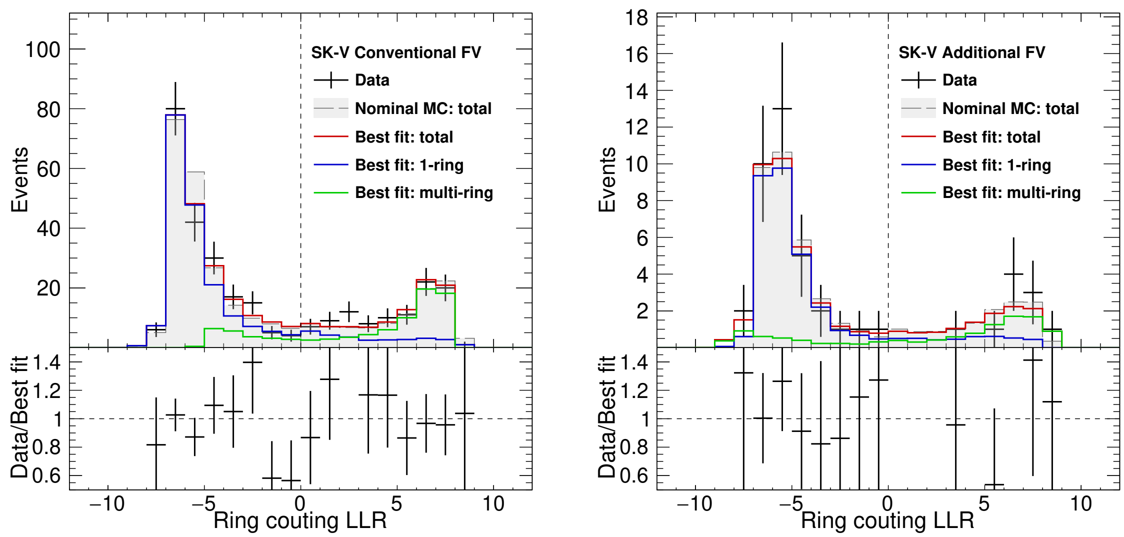

Figure 5·11: Ring counting systematic uncertainty estimation via the "scale-and-shift" method. The figures show the ring counting likelihood for SK V data and MC events classified as sub-GeV μ-like, with fitted muon momentum between 200 MeV/c to 400 MeV/c. The uncertainty estimation is performed in each fiducial volume region, **Left**: conventional and **Right**: additional. Before fitting, the data (black points) and nominal MC distribution (grey histogram) have some degree of disagreement. True single-ring (blue histogram) and multi-ring (green histogram) events are identified as signal and background in the MC, then both distributions are varied to fit the data points, resulting in an improved total fit (red histogram). The vertical dashed line shows the cut value used to classify the event as single- or multi-ring.

for each SK phase and each fiducial volume region. In each case, separate signal and background distributions are fit for six event types: Sub-GeV events are split into 4 types based on the PID of the most energetic ring, electron- or muon-like, and the reconstructed momentum, above or below 400 MeV/c. Multi-GeV events are split into 2 types based on the PID of the most energetic ring.

Particle Identification: Similar to the ring counting uncertainty, an uncertainty on the PID likelihood (Equation 3.12) used to identify the ring-producing particles in an event is estimated through a scale-and-shift procedure. The uncertainty is estimated for each SK phase and separately using data in the conventional and additional fiducial volume regions. In each case, 4 signal classes are used: sub-GeV and multi-GeV, with either a single e- or μ-like ring. An equivalent, independent uncertainty is also implemented for multi-ring events, using the PID of the most energetic ring to define the signal.

Non-ν_e Contamination: The multi-GeV e-like samples receive an additional uncertainty to account for the normalization of the ν_μ contamination. The uncertainty is estimated using the scale-and-shift procedure between data and MC for the ring counting likelihood, as in the ring separation uncertainty. Then, the uncertainty is taken as the ratio between the fitted and nominal fraction of ν_μ events classified as e-like.

NC Contamination in Single-Ring μ-like[3]: Because NC events which produce a charged pion cannot typically be distinguished from muons, a background of NC events is expected in the muon-like samples. This uncertainty places a 10 % uncertainty on NC events which are classified as single-ring μ-like.

Two-Ring π^0: Uncertainty on the likelihood quantity used to select NC π^0 events is similarly implemented to the ring separation and PID likelihood uncertainties. Here, the signal event category used in the scale-and-shift procedure is true NC π^0 events with two visible e-like rings.

Non-ν Background: The uncertainty in the non-neutrino background contamination is estimated using the counts of flasher and cosmic ray muon events found via eye-scan after all reduction steps. The uncertainty is separately estimated in each SK phase for sub-GeV, multi-GeV single-ring, and multi-GeV multi-ring events. Independent systematic uncertainties are implemented for e-like and μ-like events. The contamination of these backgrounds in the PC samples is also included in the uncertainty

[3]This is referred to as the "Hadron Simulation" uncertainty in other SK references.

for μ-like events. This uncertainty modifies the normalization of the corresponding event type, and the 1σ effect changes the normalizations by $< 1\,\%$ for all SK phases and event types.

PC Uncertainties

PC Stopping/Through-Going Separation: This analysis places an uncertainty on the efficiency of the expected charge ratio cut used to separate PC stopping and through-going events. This uncertainty increases the normalization of PC stopping events and proportionally decreases the normalization of PC through-going events, such that the total PC event counts remain the same. There are three independent uncertainties implemented for PC events based on their exit point, either through the ID cylinder side, top, or bottom. The 1σ effect of this uncertainty corresponds to a typically $\sim 20\,\%$ change in the number of PC stopping events.

Up-μ Uncertainties

Energy & Path Cut Efficiencies: The minimum energy requirement for Up-μ stopping events and the minimum path requirement for Up-μ through-going events both have uncertainties on their efficiencies. The uncertainties for each cut are independent, and the estimated change in the normalization of the corresponding sub-samples is estimated to be $1\,\%$ to $3\,\%$ for all SK phases.

Up-μ Stopping/Through-Going Separation: Up-μ events are separated into stopping and through-going sub-samples based on the number of hits within 8 m of the projected exit point in the OD. The separation uses a simple hit-based cut, and is estimated to have an $\sim 1\,\%$ uncertainty, depending on the SK phase. The 1σ effect of this uncertainty proportionally increases the normalization of the Up-μ stopping sub-sample and decreases the normalization of the Up-μ through going sub-samples, both non-showering and showering.

Up-μ Showering/Non-showering Separation: The algorithm used to separate showering and non-showering Up-μ events is based on the ratio of expected charge from simulation to measured charge. The degree of disagreement in this distribution between simulation and data is propagated to a total uncertainty on the showering/non-showering separation. This uncertainty changes the relative normalization of non-showering and showering events, such that the total number of events is preserved. At 1σ, the non-showering event rate changes by 3 % to 4 %, depending on the SK phase.

Up-μ Background Subtraction: The irreducible cosmic muon background in the Up-μ sample due to the up-scattering of cosmic muons from downward-going cosmic rays is not simulated in the MC. Therefore, to compare Up-μ data and MC events, the estimated cosmic muon background must be subtracted from SK data. The subtraction removes the estimated number of background events from the two zenith angle bins nearest to the horizon, and as a function of momentum, for the Up-μ stopping sample, and in single zenith angle bin nearest to the horizon for the Up-μ through-going samples. The uncertainty on the background rate is taken as the 1σ effect; typically 10 to 20 events are subtracted. More details on the estimation of the background rate and uncertainty may be found in [74].

Energy Scale Uncertainties

Absolute Energy Scale: SK uses several standard sources to estimate its reconstruction performance at energies relevant to atmospheric neutrino oscillations: Below 100 MeV, stopping cosmic muons which decay at rest produce decay electrons with a measurable energy distribution. Around 100 MeV, the momenta of the two e-like rings from NC π^0 decays can be summed to reconstruct the π^0 invariant mass. At several GeV, stopping cosmic muons, with a path length determined by the ID entrance point and the vertex of a subsequent decay electron, leave calculable energy depositions. Each of these three sources is simulated and compared to data. The maximum fractional difference between MC and data between any of the three sources is taken as an overall uncertainty on the reconstructed momenta of fitted particles. The energy scale uncertainty is estimated for each SK phase, shown in Figure 5·12. For this analysis, the energy scale uncertainty is also estimated for the decay electron spectrum and π^0 invariant mass sources using only events in the additional fiducial volume region.

While other systematic uncertainties modify the normalization of different event types, the absolute energy scale systematic, for a 1σ change, shifts the reconstructed momentum of all events by the estimated uncertainty. This means that this uncertainty can cause events to move between different momentum bins within their own samples.

Up/Down Energy Scale: The decay electrons from stopped cosmic muons, if energetic enough to produce a Cherenkov ring, can be further separated based on the ring directions. The deviation of the fitted decay electron energy peak between MC and data, binned according to ring direction, provides an estimate of the energy scale uniformity throughout the detector. This uncertainty varies the normalization of upward-going and downward-going FC and PC events by the largest observed deviation. Both the absolute and up/down energy scale uncertainties used in this analysis are listed in Table 5.6.

Other Detector Uncertainties

Decay-e Tagging: The decay electron efficiency uncertainty proportionally changes the normalization of events in the FC sub-GeV and multi-GeV samples which utilize the number of decay electrons as part of their sample selection. The estimated uncertainty

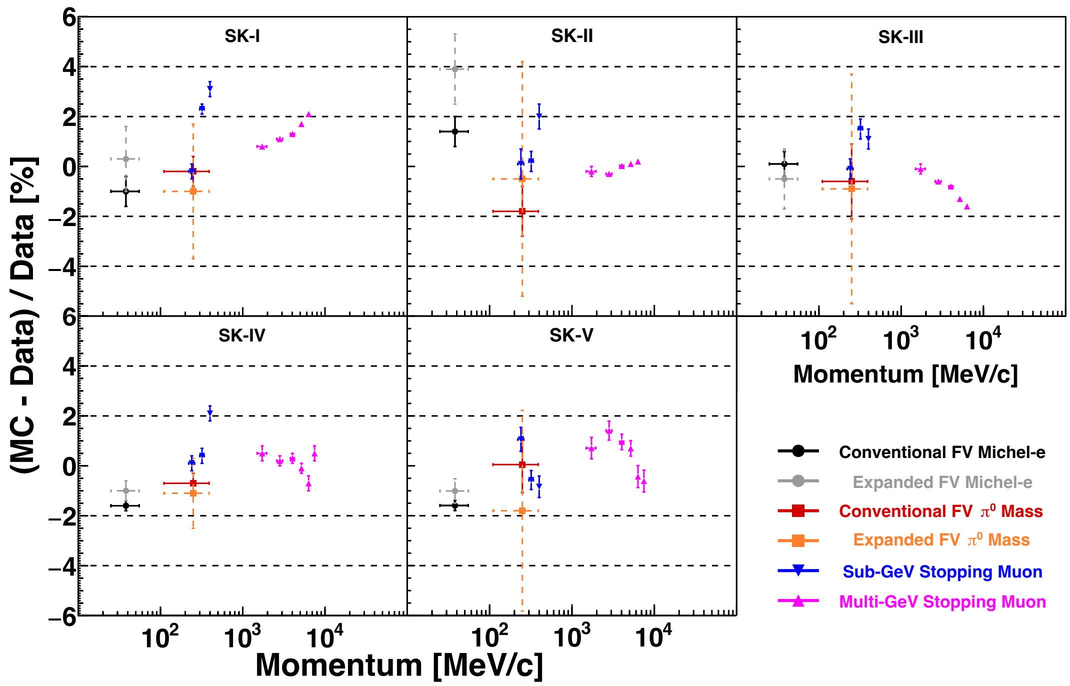

Figure 5·12: Absolute energy scale measurements for all SK phases and separately measured in the conventional (solid lines) and additional (dashed lines) fiducial volume regions. The measurements span a range of energies relevant to atmospheric neutrinos, and are found to be within a few percent for all SK phases & regions.

on the efficiency is 1.5 % for SK I-III and 0.8 % for SK IV-V, and corresponds to a few-percent change in the decay-electron-selected samples for a 1σ variation.

Neutron Tagging: The uncertainty on the neutron tagging algorithm's efficiency is estimated from a combination of two smaller systematic effects: the dependence of the algorithm's efficiency on the neutron's distance from the primary event vertex, and on changing detector conditions. An overall data versus MC neural network efficiency uncertainty is also included. The estimated overall uncertainty is 8 % to 16 %, and is separately estimated for sub-GeV and multi-GeV e-like and μ-like single-ring samples. A 1σ variation in this uncertainty increases the normalization of the samples with no tagged neutrons, and decreases the normalization of the samples

SK Phase	Energy Scale Uncertainty (%) Absolute		Up/Down	
	Conv.	Add.	Conv.	Add.
SK I	3.3	3.3	0.6	1.4
SK II	2.0	3.9	1.1	1.5
SK III	2.4	2.4	0.6	1.3
SK IV	2.1	2.2	0.5	0.5
SK V	1.8	2.0	0.7	0.1

Table 5.6: Energy scale uncertainties for each SK phase and fiducial volume region. "Conv." refers to the conventional fiducial volume while "Add." refers to the additional fiducial volume.

with one tagged neutron proportionally. This systematic is assumed to be correlated between the SK IV-V phases.

Multi-Ring BDT Efficiency & Sample Migration: Uncertainties related to the Multi-Ring BDT selection are calculated using a scale-and-shift procedure. The seven input variables are scaled-and-shifted to fit the MC distributions to the data. Next, pseudo-events, i.e., combinations of the seven input variables, are drawn from the fitted distributions and classified according to the BDT. This procedure is repeated for different values of the fitted β parameters to form a distribution of efficiencies for combinations of β parameters. The change in the average efficiency for events drawn from the post-fit distribution from the nominal efficiency, added in quadrature with the width of the post-fit efficiency distribution, is taken as the systematic uncertainty.

An additional systematic uncertainty is computed using the scale-and-shift procedure on the distribution of BDT scores themselves. The BDT score distribution for each event type is fit to data assuming a true signal component, e.g., "true ν_e CC", and a background component. The change in signal event rate for each event type for variations of the fitted β parameters, added in quadrature with the width of the distribution of signal event rates, is taken as an additional uncertainty.

Of the two Multi-Ring BDT uncertainties, the uncertainty computed by varying the input variable distributions is the larger effect, and is approximately 2 % to 10 %, depending on the SK phase and event type.

5.2.4 Oscillation Uncertainties

1–2 Mixing Parameters: Atmospheric neutrinos are relatively insensitive to the θ_{12} and Δm^2_{21} oscillation parameters. In this analysis, these are taken to be fixed to the global best fit point, with 1σ uncertainties listed in Table 1.2. The corresponding change in event weight is calculated from a full three-flavor oscillation probability framework, in which the numerator is the probability after the $\pm 1\sigma$ change and the denominator is the oscillation probability assuming the central value. Chapter 6 will discuss the impact of constraining θ_{13} in a similar way.

Matter Effect: A conservative 6.8 % uncertainty is assumed on the Earth matter electron density, corresponding to the difference between the electron-to-proton ratio of a pure iron core, $N_e/N_p \approx 0.467$, and a core of lighter elements, $N_e/N_p \approx 0.5$. A $+1\sigma$ change in this uncertainty weights events by the ratio of oscillation probabilities calculated with +6.8 % electron density and the nominal density.

5.3 Analysis Procedure

Neutrino oscillation parameters are extracted from a fit of binned oscillated MC events to atmospheric neutrino data. The fit involves two steps: First, oscillation probabilities are calculated for each MC event given a set of oscillation parameters. Next, the oscillated MC events are fit to the SK data by varying systematic uncertainties to minimize a χ^2 statistic. Neutrino oscillation parameters are scanned over a fixed grid, and the resulting map of best-fit χ^2 values at each grid point establishes a global

Layer	$R_{\text{Min.}}$ (km)	$R_{\text{Max.}}$ (km)	Density ($\text{g}\,\text{cm}^{-3}$)
Atmosphere	6371	–	0
Crust	5701	6371	3.3
Mantle	3480	5701	5.0
Outer core	1220	3480	11.3
Inner core	0	1220	13.0

Table 5.7: Neutrino propagation layers and corresponding densities used for calculating neutrino oscillation probabilities in this analysis, based on a simplified PREM [44]. $R_{\text{Min.}}$ and $R_{\text{Max.}}$ refer to the radii of the spherically-symmetric Earth model.

best-fit point and allowed regions of neutrino oscillation parameter space.

5.3.1 Oscillation Probability Calculation

Section 1.4.1 discussed the theoretical treatment for calculating neutrino oscillation probabilities, both in a vacuum and in constant-density matter. These techniques form the basis of calculating the oscillation probabilities of atmospheric neutrinos.

First, atmospheric neutrinos do not, in general, traverse constant-density matter; they pass through layers of varying density, with the highest densities being near the Earth's core. The extension of oscillations along non-constant density baselines is presented in [131]. The authors compute the oscillation probability along the entire baseline by multiplying the oscillation probabilities for constant-density steps. This can be written in a computationally-tractable form using the general matrix form of the propagated mass eigenvectors, $\mathbf{X}$, for neutrinos passing through a fixed matter density,

$$\mathbf{X} = \sum_k \left[\prod_{j \neq k} \frac{2EH_{\text{Matter}} - M_j^2 \mathbf{I}}{M_k^2 - M_j^2} \right] \exp\left(-i \frac{M_k^2 L}{2E} \right) \tag{5.6}$$

where H_{Matter} is given by Equation 1.15, and $M_i^2/2E$ are its eigenvalues. This definition allows the neutrino probability along a path of changing matter density to be written as

$$P(\nu_\alpha \to \nu_\beta) = \left| \left(\mathbf{U} \prod_i \mathbf{X}(E, \rho_i, L_i) \mathbf{U}^\dagger \right)_{\alpha\beta} \right|^2 , \tag{5.7}$$

where $\mathbf{U}$ is the PMNS matrix, and L_i and ρ_i are the baseline and density of the i^{th} step respectively. This analysis assumes a spherically-symmetric Earth, such that the neutrino oscillation baseline, L, only depends on the zenith angle and production height, i.e., it does not depend on the azimuth angle. The matter densities assumed for each Earth layer are taken from a simplified Preliminary Reference Earth Model (PREM), listed in Table 5.7. Neutrinos with zenith angles above the horizon propagate in air, with negligible density.

The contribution of an individual muon or electron neutrino MC event to the total number of predicted events after oscillations is calculated as the sum of the event's survival probability and the probability for a neutrino of the other flavor, either electron or muon, to to oscillate to the event's original flavor. Note that the flavor ratio of muon and electron neutrinos in the atmospheric neutrino flux differs. The flux difference must be corrected when computing the total oscillation probability for an individual event, e.g.,

$$P(\nu_x \to \nu_e) = P(\nu_e \to \nu_e) + \frac{\Phi_{\nu_\mu}}{\Phi_{\nu_e}} P(\nu_\mu \to \nu_e) \tag{5.8}$$

where Φ_ν is the atmospheric neutrino flux, evaluated for each neutrino's energy and direction. Tau neutrinos are not intrinsic to the atmospheric neutrino flux; they are simulated assuming the same flux as muon neutrinos and their contribution is calculated as purely due to $\nu_\mu \to \nu_\tau$ and $\nu_e \to \nu_\tau$ oscillations.

Path Length and Nearest-Neighbor Averaging

The oscillation probability calculated for low-energy neutrinos can change significantly for small changes in path length and energy due to the L/E dependence of neutrino oscillations. Such rapid oscillation effects are not visible to SK due to the finite energy and direction resolution of the reconstruction. However, if oscillation probabilities are computed assuming exact knowledge of an event's L and E, these rapid oscillations can still be visible in the MC due to limited MC statistics. This can create artifacts in the fitted allowed oscillation parameter regions where the MC does not change smoothly, or even bias the fit result. While producing larger MC sets is one solution, it is not computationally efficient. Instead, an averaging scheme is developed to smooth out oscillation effects for low-energy neutrinos.

The averaging method considers both neutrino path length and energy averaging. First, "neighbor" events are defined as MC events with the same neutrino flavor, within the same analysis sub-sample, and with the same zenith angle bin. For each event, the 20 neighbors with the nearest true neutrino energies are used to compute an RMS energy, E_{RMS}. The RMS energy defines five energy sampling points: $E - E_{\mathrm{RMS}}, E - E_{\mathrm{RMS}}/2, E, E + E_{\mathrm{RMS}}/2, E + E_{\mathrm{RMS}}$. Next, because the neutrino production height in the atmosphere depends on the neutrino energy, for each of the five energies, 20 production heights are calculated and averaged over to determine an average production height. Finally, each event's oscillation probability is calculated as the average of the five probabilities computed using the averaged energies and corresponding averaged path lengths. More details are discussed in the thesis by R. Wendell [132].

5.3.2 F_{ij} Method

The F_{ij} method incorporates the effect of systematic uncertainties by computing a scale factor for the fractional change in the i^{th} bin for a 1σ change in the j^{th} systematic uncertainty source, referred to as an F_{ij}. To calculate the F_{ij}s, MC events are rebinned after applying the $+1\sigma$ and -1σ effect of each systematic uncertainty, then the F_{ij} for each bin i is computed as:

$$F_{ij} = \frac{N_i^{+1\sigma_j} - N_i^{-1\sigma_j}}{2N_i^0}, \tag{5.9}$$

where $N_i^{\pm1\sigma_j}$ is the number of events in the i^{th} bin after a $\pm1\sigma$ change in the j^{th} systematic, and N_i^0 is the nominal number of events in the i^{th} bin. Except for few systematic uncertainty sources, the number of events after the change is found by applying a weight to each MC event, then summing the weights in each bin. The weights are calculated as:

$$\text{Weight} = 1 \pm g(E_\nu, \cos\theta_z, \dots), \tag{5.10}$$

where $g(\dots)$ is the fractional increase or decrease due to a 1σ change in the systematic. Each systematic uncertainty described in Section 5.2 implements a different g depending on the true neutrino kinematics, interaction mode, reconstructed quantities, or analysis sample. The F_{ij}'s impact on the number of events is linear, e.g., a 2σ change in the j^{th} systematic uncertainty will change the number of events in the i^{th} bin by $(2F_{ij})\,\%$. F_{ij}s may not decrease a bin's event count below zero.

Regardless of the how the systematic uncertainty modifies the events, the F_{ij} is calculated using Equation 5.9. Figure 5·13 shows an example of the ν_τ CC cross section uncertainty F_{ij} calculation and its application. True ν_τ events in the MC are re-weighted based on the $\pm1\sigma$ values of the uncertainty, $g = 25\,\%$ for ν_τ, and 0 otherwise. The MC event counts in each bin are re-calculated after the re-weighting to evaluate the F_{ij}. The F_{ij} can then be used to scale the counts in each analysis bin, visualized for one analysis sub-sample in the right panel. Thus, the F_{ij}s can modify the number and distribution of the nominal MC events.

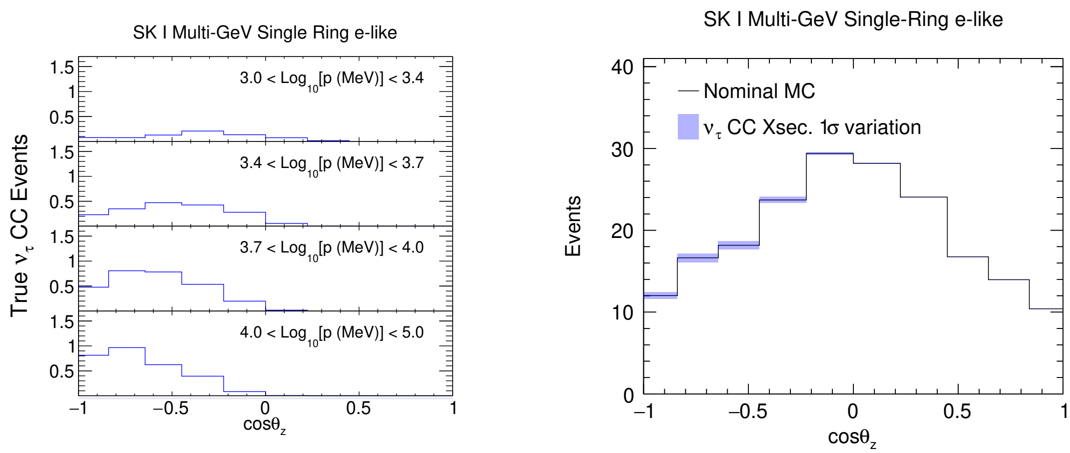

Figure 5·13: Demonstration of the ν_τ CC cross section uncertainty, applied to the multi-GeV single-ring e-like sample. **Left**: The systematic uncertainty varies the number of true ν_τ CC events, which populate the various reconstructed momenta and zenith angle bin in the sample. **Right**: The corresponding change in event rate in the whole sample for a $\pm 1\sigma$ variation in the ν_τ CC component is shown as a function of zenith angle, summing over all momentum bins.

5.3.3 χ^2 Calculation

The χ^2 statistic for comparing MC and data is derived assuming Poisson fluctuations in the number of events in each bin. The probability of observing $\mathcal{O}$ counts from a Poisson distribution with mean E is

$$P(\mathcal{O}|E) = \frac{e^{-E}E^{\mathcal{O}}}{\mathcal{O}!} \tag{5.11}$$

The likelihood for observing a particular configuration of counts, $\mathcal{O}_i$, in n bins, each with expected values, E_i, is therefore

$$\mathcal{L}(E|\mathcal{O}) = \prod_{i=1}^{n} \frac{e^{-E_i}E_i^{\mathcal{O}_i}}{\mathcal{O}_i!} \tag{5.12}$$

The χ^2 statistic may then be formed from the log-likelihood ratio between a particular configuration of E_i and the maximum-likelihood estimator, the $\mathcal{O}_i$ themselves, using

Equation 5.12:

$$\chi^2 = -2\log\frac{\mathcal{L}(E|\mathcal{O})}{\mathcal{L}(\mathcal{O}|\mathcal{O})} = 2\sum_i^n \left(E_i - \mathcal{O}_i + \mathcal{O}_i \log\frac{\mathcal{O}_i}{E_i}\right) \tag{5.13}$$

To incorporate systematic uncertainties, the F_{ij}s from each systematic uncertainty are used to modify the expected counts in each bin,

$$E_i \to E_i\left(1 + \sum_j^{n_{\text{Syst.}}} \epsilon_j F_{ij}\right) \tag{5.14}$$

where j indexes each systematic uncertainty parameter, and ϵ_j (with units of σ) scales the 1σ effect of the j^{th} systematic uncertainty. The ϵ_js are added as penalty terms to Equation 5.13 to form the complete χ^2 statistic:

$$\chi^2 = 2\sum_i^n \left[E_i\left(1 + \sum_j^{n_{\text{Syst.}}} \epsilon_j F_{ij}\right) - \mathcal{O}_i + \mathcal{O}_i \log\frac{\mathcal{O}_i}{E_i\left(1 + \sum_j^{n_{\text{Syst.}}} \epsilon_j F_{ij}\right)}\right] + \sum_j^{n_{\text{Syst.}}} \epsilon_j^2 \tag{5.15}$$

Equation 5.15 may be minimized by observing that $\partial\chi^2/\partial\epsilon_j = 0$ for all ϵ_js at the best fit point. This creates a system of equations which is solved numerically. More details may be found in [133]. For this analysis, the χ^2 statistic is minimized at each point in a grid of neutrino oscillation parameters, listed in Table 5.8. At each point, the E_is in Equation 5.15 are the number of MC events in each bin after applying oscillation probabilities.

5.4 Atmospheric Neutrino Oscillation Results

Fit results are presented using the $\Delta\chi^2$ with respect to the global best fit across all oscillation parameters in both mass orderings. Figure 5·14 shows the 1D $\Delta\chi^2$ profiles of each fitted oscillation parameter, where the value at each point is the minimum $\Delta\chi^2$ among all other oscillation parameters. The solid lines indicate the data fit result, while the dashed lines show the sensitivity at the best-fit oscillation point, i.e., the

Parameter	Min.	Max.	Steps
$\sin^2\theta_{13}$	0.0	0.075	16
$\sin^2\theta_{23}$	0.3	0.775	20
Δm^2_{32} or Δm^2_{31} ($10^{-3}\,\mathrm{eV}^2$)	1.2	3.6	25
δ_{CP}	0	2π	21

Table 5.8: The oscillation point grid used for the atmospheric neutrino analysis. Oscillation parameters are scanned in equally spaced steps, including the minimum and maximum points listed in the table. The grid is scanned twice, once for each mass ordering.

Ordering	$\Delta m^2_{32,31}$ ($10^{-3}\,\mathrm{eV}^2$)	$\sin^2\theta_{23}$	$\sin^2\theta_{13}$	δ_{CP} $(-\pi,\pi)$	χ^2 930 bins	χ^2 Syst.
Normal	$2.40^{+0.07}_{-0.09}$	$0.45^{+0.06}_{-0.03}$	$0.020^{+0.016}_{-0.011}$	$-1.89^{+0.87}_{-1.18}$	1022.06	53.50
Inverted	$2.40^{+0.05}_{-0.33}$	$0.48^{+0.07}_{-0.05}$	$0.010^{+0.021}_{-0.008}$	$-1.89^{+1.32}_{-1.97}$	1027.29	53.57

Table 5.9: Best-fit neutrino oscillation parameters from the atmospheric neutrino oscillation analysis. The uncertainties on each oscillation parameter are the $\pm 1\sigma$ allowed regions assuming a χ^2 distribution with one degree of freedom. The second-to-last column shows the total χ^2, while the last column shows the contribution to the χ^2 from the 193.00 systematic pull terms, cf. the final summation in Equation 5.15.

expected result from a fit to the nominal MC expectation. The dotted lines indicate the critical values of the χ^2 distribution for one degree of freedom, corresponding to the probability of obtaining a particular result.

The mass ordering preference is expressed as the $\Delta\chi^2$ between the best fits in the inverted and normal orderings, $\Delta\chi^2_{\mathrm{I.O.-N.O.}}$. For this atmospheric neutrino analysis, the data fit prefers the normal ordering, with $\Delta\chi^2_{\mathrm{I.O.-N.O.}} = 5.23$.

5.5 Discussion

The oscillation parameters measured using atmospheric neutrinos are in good agreement with existing measurements from other experiments. The value of $\sin^2\theta_{23}$ is in

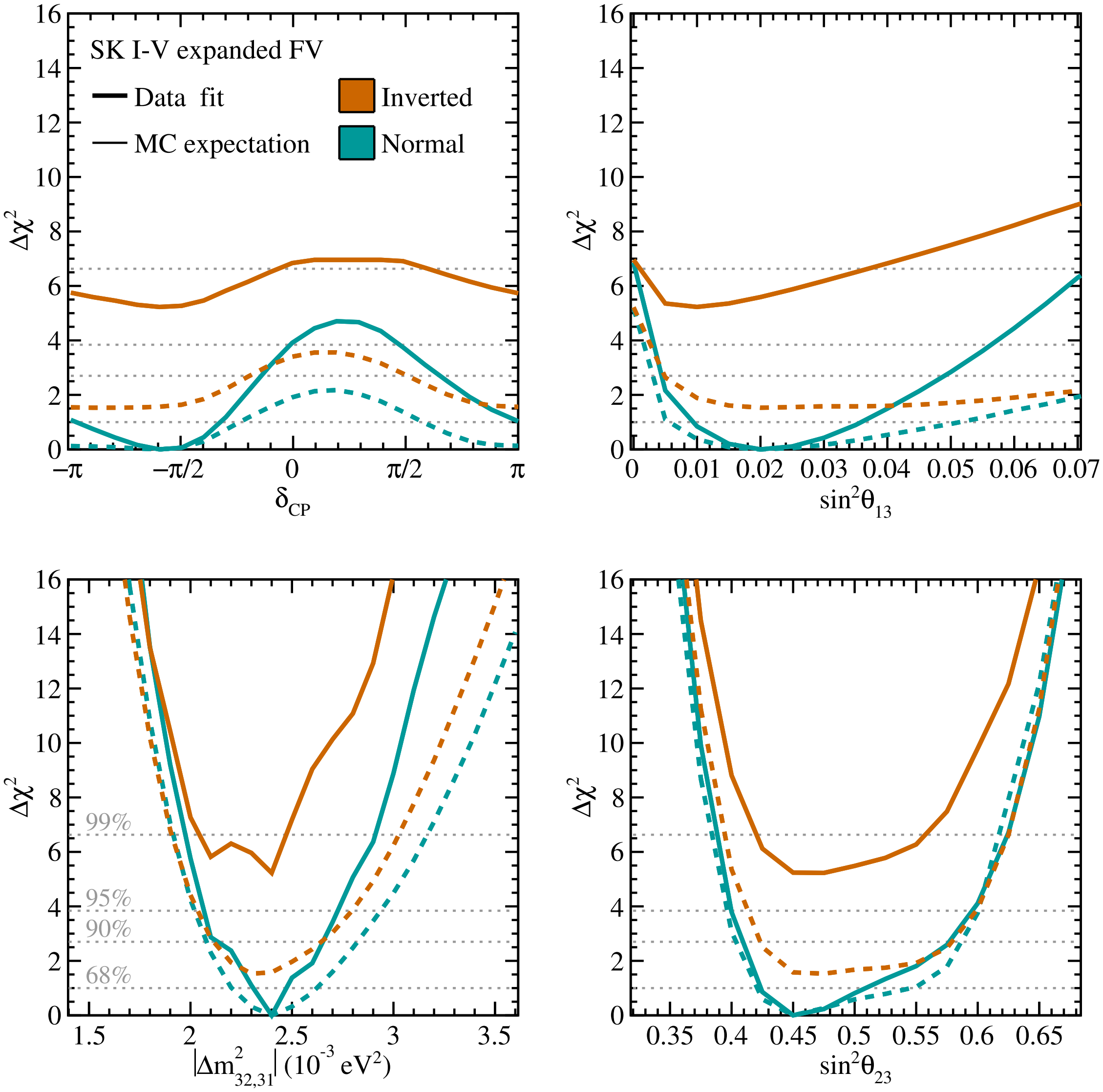

Figure 5·14: 1D $\Delta\chi^2$ profiles of the fitted oscillation parameters for the atmospheric neutrino oscillation analysis. The $\Delta\chi^2$ values are taken with respect to the best-fit in the normal ordering, listed in Table 5.9. For each parameter profile, the value of $\Delta\chi^2$ is minimized over all other oscillation parameters. Solid line shows the result of the fit to SK data, while the dashed lines show the fit to the nominal MC, assuming the best-fit oscillation parameters. The dotted lines correspond to the critical values of the χ^2 distribution with one degree of freedom, as a measure of the probability of obtaining a particular result.

the lower octant, $\sin^2\theta_{23} < 0.5$, while the global average value is in the upper-octant. However, upper-octant values are allowed at the 1σ level, indicating no strong preference. The fitted value of $\sin^2\theta_{13}$ in the normal ordering agrees well with the global measurement, which is dominated by reactor neutrino experiments. In the inverted ordering, $\sin^2\theta_{13}$ is fit somewhat smaller. Both fits exclude $\sin^2\theta_{13} = 0$ at the 1σ level. Recall that large values of $\sin^2\theta_{13}$ enhance the matter effect, which, in the normal ordering, causes an increase ν_e appearance at multi-GeV energies. In the inverted ordering large values of $\sin^2\theta_{13}$ predict an increase of $\bar{\nu}_e$. Therefore, the SK data fit indicates ν_e appearance and relatively suppressed $\bar{\nu}_e$ appearance.

The SK measured value of δ_{CP} is near $-\pi/2$ in both orderings, implying an excess of ν_e appearance relative to $\bar{\nu}_e$ appearance for neutrinos at both sub-GeV and multi-GeV energies. However, $\delta_{\mathrm{CP}} = \pi$ is allowed at the 1σ level, which is consistent with no vacuum neutrino-anti-neutrino oscillation differences. Note that the constraints on δ_{CP} are weaker in the inverted ordering than in the normal ordering, as can be seen in the top left panel of Figure 5·14. This is consistent with fewer anti-neutrinos in the atmospheric neutrino sample: δ_{CP} induces smaller changes in the predicted event rate by modulating $\bar{\nu}_e$ appearance than ν_e appearance, so constraints on this parameter are weaker.

The expected sensitivity to the neutrino mass ordering at the best-fit oscillation parameters in the normal ordering is $\Delta\chi^2_{\mathrm{I.O.-N.O.}} = 1.8$, visible as the height difference at the smallest-$\Delta\chi^2$ points between the dashed normal and inverted lines in any of the panels in Figure 5·14. That the SK data result is in excess of the sensitivity calls for additional interpretation. Several considerations to contextualize the results are described below.

Mass ordering sensitivity for other parameters: The mass ordering sensitivity is highly dependent on the values of $\sin^2\theta_{23}$, $\sin^2\theta_{13}$, and δ_{CP}. Figure 5·15 shows the sensitivity for the mass ordering calculated assuming different values of oscillation parameters allowed by the fit at 1σ. Higher values of $\sin^2\theta_{23}$, higher values of $\sin^2\theta_{13}$, and values of δ_{CP} near $-\pi/2$ predict the largest ν_e appearance signal, and therefore the highest sensitivity to rejecting the inverted mass ordering. Conversely, small values of $\sin^2\theta_{23}$ imply a small ν_e appearance signal, and values of δ_{CP} near $+\pi/2$ enhance the $\bar{\nu}_\mu \to \bar{\nu}_e$ independent of the mass ordering, further suppressing the normal ordering signal.

The range of sensitivity values includes the SK result for values of $\sin^2\theta_{23}$ allowed at the 90 % level, indicating that the difference from fitted data and sensitivity, while in tension, could be resolved through better constraints on $\sin^2\theta_{23}$.

Normal mass ordering preference in the data: Recall that the mass ordering signature is expected to be an excess of upward-going ν_e or $\bar{\nu}_e$ events with a few GeV of energy. For a true mass ordering signature, this pattern should be visible in the data. The flux of multi-GeV ν_e and $\bar{\nu}_e$ atmospheric neutrinos is approximately symmetric above and below the horizon, which motivates defining an asymmetry parameter to quantify any excesses from upward-going events. Define:

$$\text{Asymmetry} = \frac{\text{Up} - \text{Down}}{\text{Up} + \text{Down}}, \tag{5.16}$$

where "Up" and "Down" refer to the counts in each zenith angle bin below $\cos\theta_z \leq -0.4$ and above $\cos\theta_z \geq 0.4$, respectively. Figure 5·16 shows the asymmetry parameter for the eight FC multi-GeV e-like samples, plotted as a function of the momentum estimator for each sample. It can be seen that, in nearly all bins where the MC predicts a higher asymmetry in the normal ordering, the SK data agrees with or is in excess of the prediction. The full zenith angle distributions for each momentum bin are provided in Appendix A. In summary, the excess mass ordering preference compared to the expectation originates from an unlikely configuration of observed counts in the signal bins of this analysis.

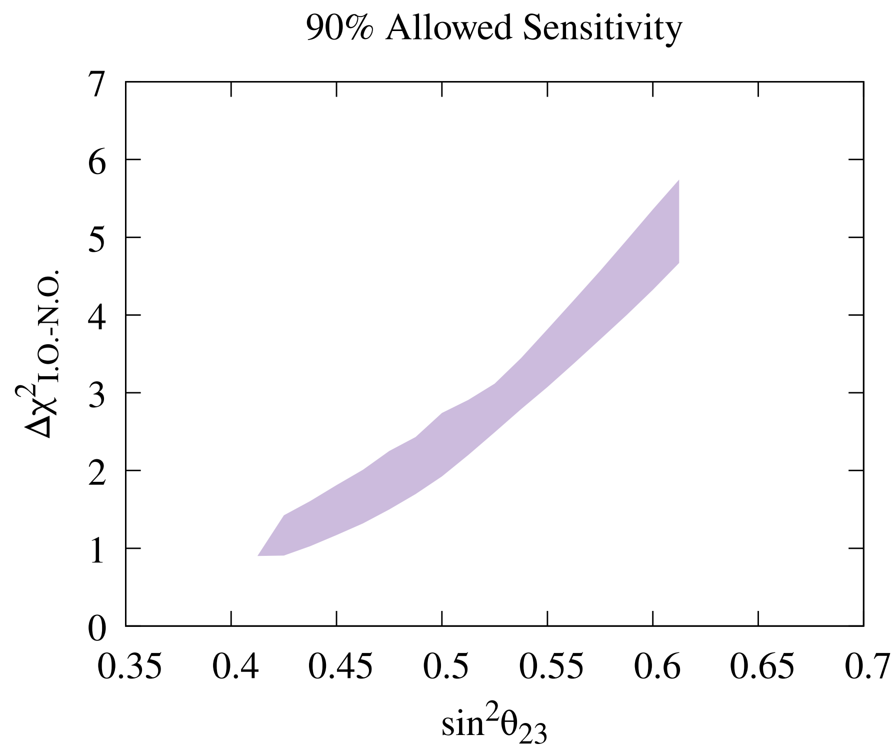

Figure 5·15: Sensitivity to the mass ordering, $\Delta\chi^2_{\mathrm{I.O.-N.O.}}$, as a function of $\sin^2\theta_{23}$. The width of the band corresponds to the minimum and maximum sensitivity for different combinations of the δ_{CP} and Δm^2_{32} oscillation parameters contained at the 90 % confidence level for the nominal sensitivity with θ_{13} constrained, cf. Section 6.1. The width of the band is primarily set by variations in δ_{CP}.

Note that the $\bar{\nu}_e$-enhanced samples still contain a background of ν_e events. This is noticeable where, for example, in the SK I-III multi-GeV $\bar{\nu}_e$ sample, the normal ordering predicts a larger asymmetry than in the inverted ordering. The equivalent SK IV-V sample, which has a smaller background of ν_e contamination due to utilizing neutron tagging information, does not show this feature as strongly. This is an additional verification that the neutron tagging information is improving the purity in those samples.

Distribution of $\Delta\chi^2_{I.O.-N.O.}$: When comparing two hypotheses, the significance of a

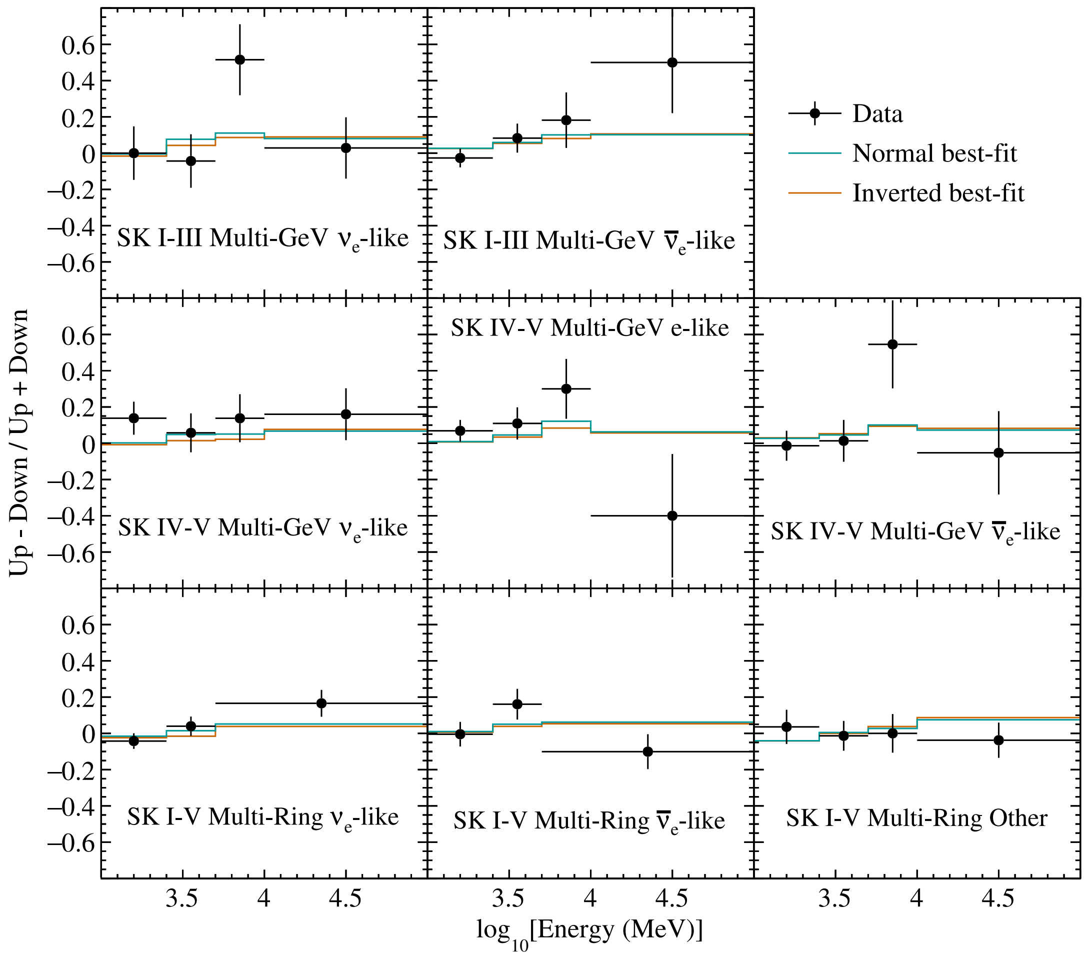

Figure 5·16: The Up/Down asymmetry parameter for the eight multi-GeV e-like samples, where the sensitivity to the neutrino mass ordering is expected. The asymmetry is calculated as a function of energy bin, defined in Table 5.1. The black points are the observed counts from SK data, while the solid lines show the predicted asymmetry from the best-fit normal and inverted oscillation parameters.

$\Delta\chi^2$ statistic can be estimated by taking its square root, i.e., the number of standard deviations is $\sigma \approx \sqrt{\Delta\chi^2}$. This originates from Wilks' Theorem [134] which postulates that, for large sample sizes, the log-likelihood ratio between two hypotheses approaches a χ^2 distribution, with degrees of freedom equal to the difference in degrees of freedom between the hypotheses. Crucially, this theorem only applies to hypotheses which are "nested," i.e., one hypothesis contains additional parameters relative to the other. A naïve application of Wilks' Theorem to the atmospheric neutrino fit results in $\sqrt{5.23} = 2.29\,\sigma$, but this is generally not valid because the normal and inverted mass orderings are not nested hypotheses.

A more robust method for estimating the significance of the observed $\Delta\chi^2_{\text{I.O.}-\text{N.O.}}$ is to simulate its distribution directly by randomly fluctuating the bin counts, known as "toy" data sets. This approach has the following steps:

1. Generate toy data sets by fluctuating the statistics in each bin and fluctuating the nominal values of the systematic uncertainties.
2. Fit each data set to the normal and inverted mass ordering scenarios to generate a distribution of $\Delta\chi^2_{\text{I.O.}-\text{N.O.}}$ statistics.
3. Compute the p-value of the SK data, assuming the measured $\Delta\chi^2_{\text{I.O.}-\text{N.O.}}$ is drawn from this distribution.

While the above procedure is straightforward, it is also computationally-intensive. In general, if the p-value is expected to be small, which is likely for a data result which exceeds its median sensitivity, it will depend on the tails of its underlying distribution. This is the case for the mass ordering analysis: A previous SK analysis [38] used several thousand toy data sets to estimate the mass ordering p-value from a toy data $\Delta\chi^2_{\text{I.O.}-\text{N.O.}}$ distribution. Further, for each data set, the SK analysis software calculates a χ^2 at each point in the full multi-dimensional oscillation parameter space. The number of points is further multiplied by a factor of two when computing $\Delta\chi^2_{\text{I.O.}-\text{N.O.}}$, since oscillation parameters in both mass ordering scenarios need to be scanned. Fitting thousands of toy data sets at each point on a multi-dimensional parameter grid quickly becomes infeasible.

To speed up the calculation of $\Delta\chi^2_{\text{I.O.}-\text{N.O.}}$, toy data sets are fit using a procedure which utilizes that the $\Delta\chi^2_{\text{I.O.}-\text{N.O.}}$ calculation only requires knowledge of the best-fit point in each ordering and not the fit result at every point in the oscillation grid. The fitting procedure calculates the χ^2 at several points on the oscillation grid as before, then extrapolates to estimate which point will have a smaller χ^2 value based on the gradient (slope) of the $\Delta\chi^2$ values between the fitted points and the points' distances in the grid. This algorithm converges on the best-fit point much faster than the exhaustive search of the entire grid. To avoid cases where the gradient estimation leads to a local minimum best fit, the algorithm employs a stochastic annealing [135] routine which re-tries the fit at a randomly-selected nearby point after finding a minimum. A stop condition ensures a finite number of re-tries. This approach is found to be 20 to 30 times faster than the full oscillation parameter grid scan for computing $\Delta\chi^2_{\text{I.O.}-\text{N.O.}}$.

Figure 5·17 shows the distribution of $\Delta\chi^2_{\text{I.O.}-\text{N.O.}}$ from the fitted toy data sets generated assuming a true normal and true inverted mass ordering[4]. The SK data fit result is shown as a solid line at $\Delta\chi^2_{\text{I.O.}-\text{N.O.}} = -5.69$. The probability that the observed SK data fit result would be more extreme, given the distribution of $\Delta\chi^2_{\text{I.O.}-\text{N.O.}}$ from the toy data fits, is the p-value: For the normal ordering, the p-value is the area to the right of the data result, i.e., the fraction of toy data sets with larger $\Delta\chi^2_{\text{I.O.}-\text{N.O.}}$ values. Similarly, for the inverted ordering, the p-value is the area to the left of the data result. The data result corresponds to a p-value of $p = 9.1 \times 10^{-3} \approx 2.36\,\sigma$ assuming the inverted ordering, while the p-value calculated

[4]This toy study was performed for the analysis with θ_{13} constrained, see Section 6.1.

from the measured $\Delta\chi^2_{\text{I.O.}-\text{N.O.}}$ value assuming Wilks' Theorem is $\sqrt{5.69} \approx 2.39\,\sigma$.

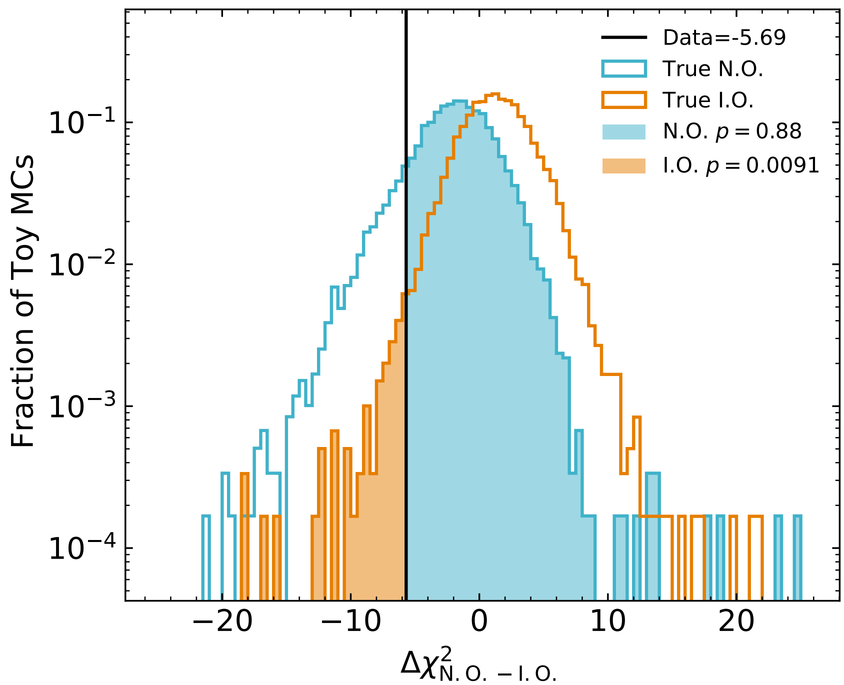

Figure 5·17: Distribution of $\Delta\chi^2_{\text{I.O.}-\text{N.O.}}$ from toy data sets and p-values in the SK atmospheric neutrino oscillation analysis with θ_{13} constrained. The blue and orange histograms represent the distributions of $\Delta\chi^2_{\text{I.O.}-\text{N.O.}}$ extracted from fits to toy data sets generated assuming the normal and inverted mass orderings, respectively. The filled area to the right of the blue histogram, and to the left of the orange histogram, represent the probability of obtaining a less likely result than the data in each ordering.

Once the p-value is obtained from the simulated $\Delta\chi^2_{\text{I.O.}-\text{N.O.}}$ distribution, there is one additional correction which is relevant when testing mutually-exclusive hypotheses such as the neutrino mass ordering. Even though the $\Delta\chi^2_{\text{I.O.}-\text{N.O.}}$ statistic indicates a preference for the normal mass ordering over the inverted ordering in the SK data, the excess preference over the expected sensitivity indicates that it does not necessarily agree with the normal ordering either. One way of incorporating the level of agreement from both hypotheses is to correct the p-value used to reject the inverted ordering by the p-value of accepting the normal ordering, known as the CL_s statistic [136],

$$\mathrm{CL}_s = \frac{p_{\mathrm{I.O.}}}{1 - p_{\mathrm{N.O}}} \tag{5.17}$$

The CL_s statistic is widely used throughout particle physics experiments to ensure that results are not overstated when comparing two hypotheses. The CL_s value from the p-values shown in Figure 5·17 is $\mathrm{CL}_s = 0.077$, i.e., a rejection of the inverted mass ordering at $92.3\,\% \approx 1.43\,\sigma$. This result is better aligned with the expected sensitivity of the experiment than the significances obtained from Wilks' Theorem and the uncorrected p-value.

Chapter 6

Adding External Constraints

The neutrino mass ordering measurement presented in Chapter 5 is inherently limited by SK's ability to simultaneously determine all neutrino oscillation parameters. This chapter considers two extensions to the atmospheric-only analysis: constraints from reactor neutrino experiments on the value of $\sin^2\theta_{13}$, and constraints on $\sin^2\theta_{23}$, Δm^2_{32}, δ_{CP}, and the mass ordering itself, from T2K data.

6.1 Constraints on θ_{13}

As discussed in Section 1.5.2, reactor neutrinos experiments measure θ_{13} by observing $\bar{\nu}_e$ disappearance. The stringent constraint on $\sin^2\theta_{13}$ from reactor experiments stems from high statistics, pure $\bar{\nu}_e$ fluxes, and minimal dependence on other oscillation effects. The current best measurements are provided by the Daya Bay [137], RENO [138], and Double-Chooz [139] experiments, and give an average measurement of $\sin^2\theta_{13} = 0.0220 \pm 0.0007$ [51].

To incorporate the measurement of $\sin^2\theta_{13}$ into the SK atmospheric neutrino oscillation analysis, oscillation probabilities are computed assuming $\sin^2\theta_{13} = 0.0220$, and a new systematic uncertainty is introduced. The systematic uncertainty varies $\sin^2\theta_{13}$ at its $\pm 1\sigma$ value, and calculates the corresponding change in oscillation probabilities for all MC events. The change in event rate is then used to form an F_{ij} (see Section 5.3.2) which can be varied in the fit in the same way as the other systematic uncertainties.

Parameter	Min.	Max.	Steps
$\sin^2\theta_{23}$	0.3	0.725	35
Δm^2_{32} or Δm^2_{31} ($10^{-3}\,\mathrm{eV}^2$)	1.0	4.9	40
δ_{CP}	0	2π	37

Table 6.1: The oscillation point grid used for the SK analysis with $\sin^2\theta_{13}$ constrained. Oscillation parameters are scanned in equally spaced steps, including the minimum and maximum points listed in the table. The grid is scanned twice, once for each mass ordering.

The θ_{13}-constrained analysis analysis uses a new oscillation parameter grid when fitting to increase the number of points scanned for Δm^2_{32}, $\sin^2\theta_{23}$, and δ_{CP}. The new grid definition is shown in Table 6.1. All other aspects of the analysis remain unchanged.

6.1.1 Results

The 1D profiles of the fitted oscillation parameters in the θ_{13}-constrained analysis are shown in Figure 6·1. The 2D profiles of Δm^2_{32} or Δm^2_{31} versus $\sin^2\theta_{23}$ are shown in Figure 6·2. The best-fit oscillation parameters are listed in Table 6.2. The normal mass ordering preference is $\Delta\chi^2_{\mathrm{I.O.}-\mathrm{N.O.}} = 5.69$, an increase of 0.46 compared to the atmospheric-only analysis. The constraint on δ_{CP} has improved, and unlike in the atmospheric-only analysis, δ_{CP} has similar constraints in both orderings, due to the removed degree of freedom. Constraints on both $\sin^2\theta_{23}$ and Δm^2_{32} are unchanged, since the constraints on these parameters are largely driven by ν_μ disappearance, which is not as sensitive to $\sin^2\theta_{13}$ as ν_e appearance.

An increase is mass ordering preference is expected, given that the atmospheric-only best-fit in the inverted ordering preferred a smaller value of $\sin^2\theta_{13}$ than 0.0220. The same caveats discussed in Section 5.5 apply to the $\Delta\chi^2_{\mathrm{I.O.}-\mathrm{N.O.}}$ value obtained in the θ_{13}-constrained analysis: The number of standard deviations estimated from Wilks' Theorem, $\sqrt{5.69} \approx 2.39\,\sigma$, is generally an overestimate of the significance, and

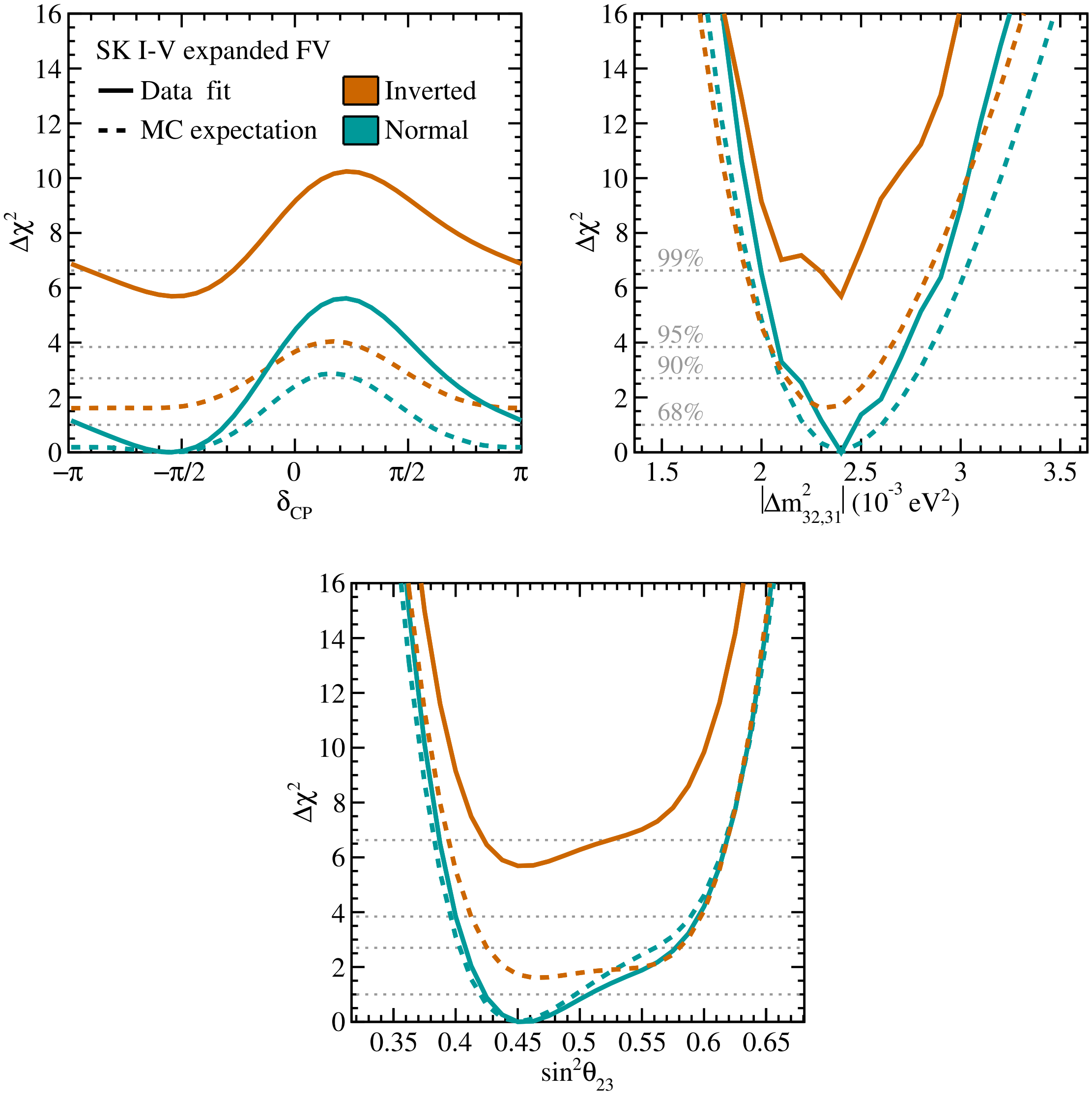

Figure 6·1: 1D $\Delta\chi^2$ profiles of the fitted oscillation parameters for the SK analysis with $\sin^2\theta_{13}$ constrained. The $\Delta\chi^2$ values are taken with respect to the best-fit in the normal ordering, listed in Table 6.2. The meaning of the colors, solid and dashed curves, and dotted lines is the same as in Figure 5·14.

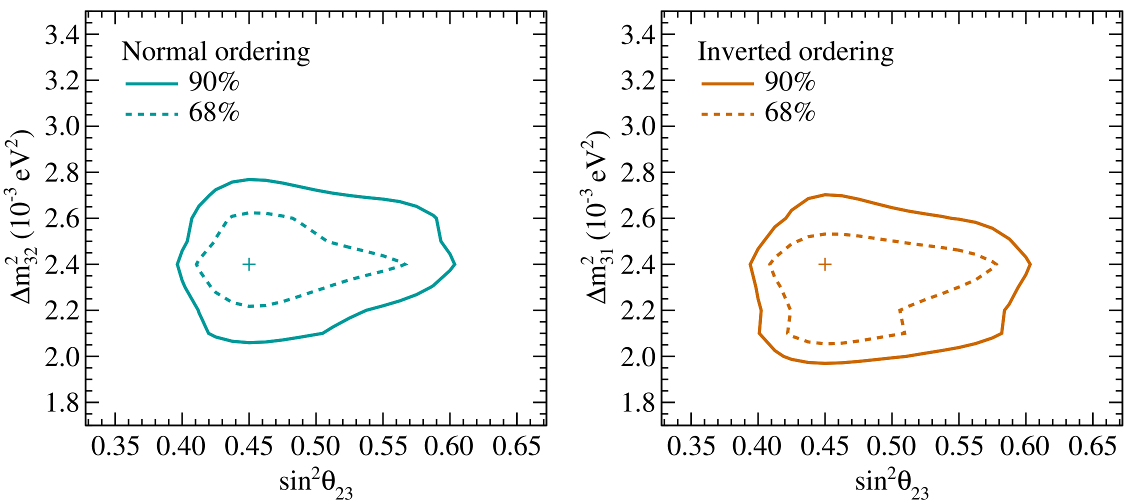

Figure 6·2: 68 % and 90 % confidence level allowed regions of Δm^2_{32} or Δm^2_{31} and $\sin^2\theta_{23}$ for the SK analysis with $\sin^2\theta_{13}$ constrained. The regions are drawn assuming a χ^2 distribution with two degrees of freedom for the **Left**: normal and **Right**: inverted mass ordering scenarios. The $\Delta\chi^2$ values are taken with respect to the best-fit in each ordering, indicated by a cross, and listed in Table 6.2. Note that no values of the oscillation parameters in the inverted ordering are allowed at the 90 % confidence level with respect to the best-fit in the normal ordering.

Ordering	$\Delta m^2_{32,31}$ $(10^{-3}\,\mathrm{eV}^2)$	$\sin^2\theta_{23}$	δ_{CP} $(-\pi,\pi)$	χ^2 930 bins	χ^2 Syst.
Normal	$2.40^{+0.07}_{-0.09}$	$0.45^{+0.06}_{-0.03}$	$-1.75^{+0.76}_{-1.25}$	1022.06	53.55
Inverted	$2.40^{+0.06}_{-0.12}$	$0.45^{+0.08}_{-0.03}$	$-1.75^{+0.89}_{-1.22}$	1027.75	53.54

Table 6.2: Best-fit neutrino oscillation parameters from the SK analysis with $\sin^2\theta_{13}$ constrained. The uncertainties on each oscillation parameter are the $\pm1\sigma$ allowed regions assuming a χ^2 distribution with one degree of freedom.

neglects the mutual exclusivity of the two mass ordering scenarios. Recalling the results of Section 5.5, the CL_s value obtained from the p-values shown in Figure 5·17 is $\mathrm{CL}_s = 0.077$, corresponding to a rejection of the inverted mass ordering at $92.3\,\% \approx 1.43\,\sigma$.

Figure 6·3 shows a comparison of the measurements of Δm^2_{32} and $\sin^2\theta_{23}$ from the θ_{13}-constrained analysis with measurements from other oscillation experiments. The figure compares contemporary neutrino oscillation experiments which are sensitive to ν_μ disappearance with similar L/E combinations as SK. Of the experiments shown, both SK and IceCube use atmospheric neutrinos, although IceCube reconstructs neutrinos with higher average energies than SK, $\sim 10\,\mathrm{GeV}$ to $300\,\mathrm{GeV}$. The NOvA and T2K experiments measure Δm^2_{32}, $\sin^2\theta_{23}$, and δ_{CP} using neutrino beams, where the neutrino baseline is known exactly, and the energy spectrum is much narrower than for atmospheric neutrinos. These features allow NOvA and T2K to set more precise measurements on Δm^2_{32} than SK and IceCube. Measurements of these two parameters are consistent between the various experiments. Notably, all experiments have a best-fit oscillation in the normal ordering, although the other experiments are not as sensitive as SK to the mass ordering. Of the four experiments, only SK has a best-fit value of $\sin^2\theta_{23}$ in the lower octant ($\sin^2\theta_{23} < 0.5$), but its 90 % allowed region spans both octants, and contains all other best-fit points.

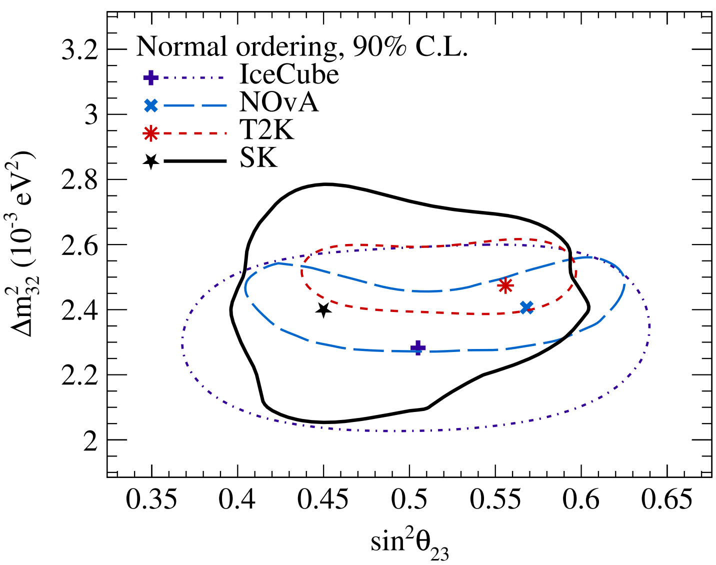

Figure 6·3: 2D 90 % allowed regions of $\sin^2\theta_{23}$ and Δm^2_{32} neutrino oscillation parameters from contemporary neutrino oscillation experiments, analyzed assuming $\sin^2\theta_{13}$ is constrained. The best-fit values of $\sin^2\theta_{23}$ and Δm^2_{32} are indicated with markers. The IceCube contours are from [140], the NOvA contours are from [141], and the T2K contours are from [142].

6.2 Constraints from T2K

As demonstrated by the θ_{13}-constrained analysis, we can improve the SK mass ordering measurement further by introducing constraints on other oscillation parameters. The oscillation parameters $\sin^2\theta_{23}$, Δm^2_{32}, and δ_{CP} have all been measured more precisely by the NOvA and T2K experiments than by SK, suggesting possible improvements. While additional systematic uncertainties could be introduced to implement these constraints, similarly to the θ_{13}-constrained fit, the T2K experiment provides a unique opportunity to obtain an even better measurement. Because T2K records neutrino interactions within the SK detector, variations in the neutrino interaction uncertainties produce a simultaneous effect in both the atmospheric neutrino prediction and in the T2K beam neutrino prediction. This means that a combined analysis of SK and T2K data has the added benefit of improved constraints on neutrino interaction uncertainties, in additional to complementary sensitivity to oscillation effects.

The SK and T2K collaborations have historically analyzed their data independently, with each choosing simulation tools, cross section models, and fitting techniques to best suit their experimental signatures. This thesis will discuss the implementation of T2K data into the atmospheric neutrino analysis using SK software and simulation tools, and publicly-available information from T2K publications only. This has the advantage of using the most recent SK analysis techniques and data, but also has limitations which will be discussed in Section 6.3.5. Separately from the work presented in this thesis, collaborators from both SK and T2K are working to formally analyze SK and T2K data using the resources of both collaborations. The formal SK-T2K joint analysis will unify the reconstruction software, interaction models used in simulation, and perform its fit using the full reconstruction information of both SK and T2K data events, all of which are beyond the scope of this thesis.

6.2.1 The T2K Experiment

This section will discuss the T2K experiment's sensitivity to neutrino oscillation effects and the components of the T2K experiment. An overview of the T2K experiment is shown in Figure 6·4. There are three main components: the neutrino beam production site at the J-PARC accelerator complex in Tokai, Japan, a series of near detectors which monitor the beam and perform cross section measurements, and the far detector, SK, described in detail in Chapter 2.

Neutrino Oscillations with T2K

The T2K experiment uses a 99 %-pure muon neutrino beam to precisely measure Δm^2_{32} and θ_{23} through muon neutrino disappearance, and θ_{13} and δ_{CP} through electron neutrino appearance. The neutrino beam travels along a 295.3 km baseline near

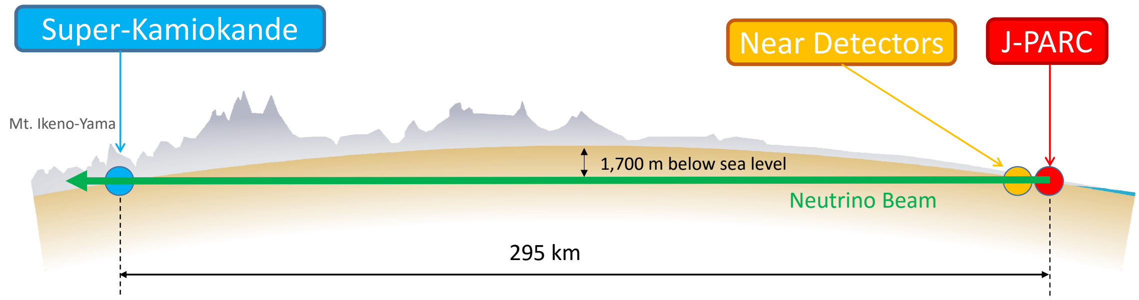

Figure 6·4: Overview of the T2K experiment. The neutrino beam produced at J-PARC passes through a series of near detectors, then propagates through the Earth towards Super-Kamiokande (SK). Figure is adapted from [143].

Earth's surface. Neglecting matter effects, which are small for T2K, the muon neutrino survival probability, including the sub-leading effects of nonzero θ_{13}, is approximately

$$P(\nu_\mu \to \nu_\mu) \approx 1 - \left(\cos^4\theta_{13}\sin^2 2\theta_{23} + \sin^2 2\theta_{13}\sin^2\theta_{23}\right)\sin^2\left(1.27\frac{\Delta m^2_{32}L}{E}\right) \quad (6.1)$$

and is equivalent for anti-neutrinos. The electron neutrino appearance probability, including the effects of δ_{CP}, is approximately[144]:

$$P(\nu_\mu \to \nu_e) \approx 4|\mathcal{T}_3^{\mu e}|^2 \sin^2\Delta_{31} + 8|\mathcal{T}_2^{\mu e}||\mathcal{T}_3^{\mu e}| \sin\Delta_{31}\sin\Delta_{21}\cos\left(\Delta_{32} + \delta_{\mathrm{CP}}\right), \quad (6.2)$$

where $\mathcal{T}_3^{\mu e} = \frac{1}{2}\sin 2\theta_{13}\sin\theta_{23}e^{i\delta_{\mathrm{CP}}}$, $\mathcal{T}_2^{\mu e} \approx \frac{1}{2}\sin 2\theta_{12}\cos\theta_{13}\cos\theta_{23}$. The squared mass differences are absorbed into $\Delta_{ij} \equiv 1.27\Delta m^2_{ij}L/E$. For T2K baseline and typical neutrino energies, oscillation effects due to $\sin^2\Delta_{21}$ are small, and have been neglected.

The largest effect is given by the $\sin^2\Delta_{31}$ term. The second term, referred to as the "interference" term, has a relative amplitude of $\sim 20\,\%$. The interference term crucially depends on δ_{CP} and the sign of Δ_{31}. Because $|\Delta m^2_{32}| \approx |\Delta m^2_{31}|$, there is a degeneracy in the interference term under interchange of $\delta_{\mathrm{CP}} \to \pi - \delta_{\mathrm{CP}}$ and the normal, $\Delta_{31} > 0$, and inverted, $\Delta_{31} < 0$, mass orderings. The degeneracy is lifted for certain values of δ_{CP} by invoking matter effects: Although the T2K neutrino beam experiences smaller matter effects than atmospheric neutrinos passing near the Earth's core, the matter effects can enhance the neutrino appearance probability further than through δ_{CP} alone. In particular, the combination of $\delta_{\mathrm{CP}} = -\pi/2$ and the normal ordering increases the electron neutrino appearance probability higher than for any value of δ_{CP} in the inverted ordering.

Examples of the electron neutrino appearance probabilities, calculated as a function of neutrino energy for the fixed T2K baseline and matter density, are shown in Figure 6·5. The curves are drawn with matter effects which, while small, allow T2K to probe different combinations of δ_{CP} and the neutrino mass ordering. Some combinations of δ_{CP} and the mass ordering are easier to distinguish than others: The left panel shows a pessimistic case, where the effect of different values of δ_{CP} is degenerate with the mass ordering. The right panel shows a best-case scenario, where, if $\delta_{\mathrm{CP}} = -\pi/2$, the normal and inverted mass ordering predict a few-percent difference in the electron neutrino oscillation probability at the peak T2K beam energy.

Both the muon neutrino disappearance and the electron neutrino appearance channels are crucial for T2K's ability to constrain neutrino oscillation parameters. The muon neutrino disappearance channel is largely unaffected by matter effects and the effects of δ_{CP}, and so helps to constrain flux and cross section uncertainties somewhat independently of the electron neutrino appearance channel. In addition, the muon neutrino disappearance constrains Δm^2_{32} and $\sin^2\theta_{23}$ better than the electron neutrino appearance channel due to increased statistics.

Neutrino Beam

The T2K neutrino beam begins at the J-PARC accelerator complex which accelerates 31 GeV protons onto a carbon target. Proton interactions in the target produce showers of pions and hadrons, which are focused through a series of three electromagnetic

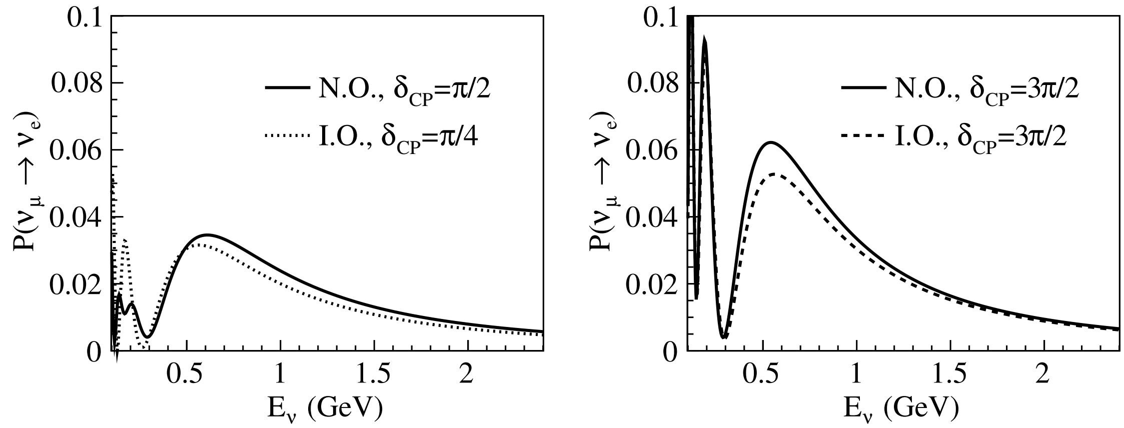

Figure 6·5: Electron neutrino appearance probabilities versus neutrino energy for the T2K baseline. **Left**: If δ_{CP} is near $\pi/2$, the effect of the mass ordering is degenerate with similar values of δ_{CP}. **Right**: For $\delta_{\text{CP}} = 3\pi/2$, the appearance probability is maximized in both orderings, but the normal ordering further enhances the probability.

horns. The direction of the current in the horns determines whether positively- or negatively-charged hadrons are focused, referred to as forward horn current (FHC) for positively-charged hadrons, or reverse horn current (RHC) for negatively-charged hadrons. The hadrons then propagate in 96 m decay volume where they decay into neutrinos. The most numerous hadrons are pions, which decay into muon neutrinos and muons in FHC mode, or anti-neutrinos and anti-muons, in RHC mode. The secondary muons are absorbed by a beam dump placed after the decay volume, resulting in a 99 % pure muon neutrino or anti-neutrino beam which propagates towards SK.

The T2K beam is directed 2.5° off-axis from the SK detector. The off-axis angle reduces the overall neutrino flux, but enhances the flux in the narrow energy range most sensitive to oscillation effects for T2K's baseline. The neutrino energy as a

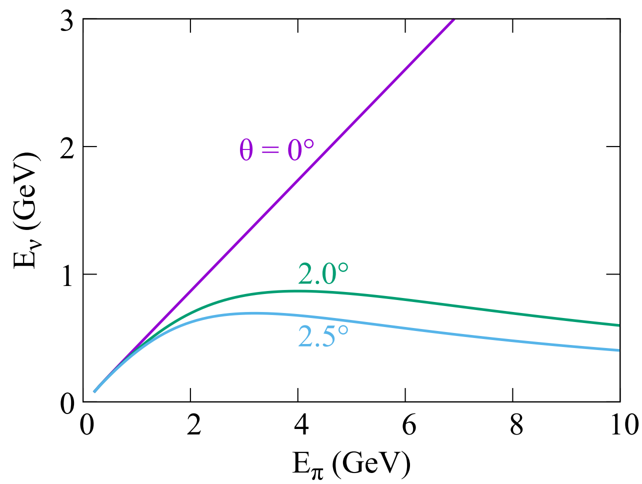

Figure 6·6: Neutrino energy spectrum from pion decay in flight from Equation 6.3. At off-axis angles ($\theta \neq 0°$), a large range of pion energies produce similar neutrino energies.

function of off-axis angle can be calculated from relativistic kinematics:

$$\begin{aligned} [(E_\pi, \vec{p}_\pi) - (E_\nu, \vec{p}_\nu)]^2 &= (E_\mu, \vec{p}_\mu)^2 \\ \implies m_\pi^2 - 2E_\pi E_\nu + 2|\vec{p}_\pi||\vec{p}_\nu|\cos\theta &= m_\mu^2 \\ \implies E_\nu = \frac{m_\pi^2 - m_\mu^2}{2(E_\pi - 2|\vec{p}_\pi|\cos\theta)}, \end{aligned} \tag{6.3}$$

where θ is the angle between the pion and neutrino in the lab frame, and $|\vec{p}_\nu| \approx E_\nu$. The neutrino energy dependence on the pion energy is plotted for different angles in Figure 6·6. At off-axis angles, the outgoing neutrino energy spectrum is much narrower than the on-axis case.

The unoscillated T2K neutrino flux observed at SK is shown for both FHC and RHC modes in Figure 6·7, per 10^{21} protons on target (POT). The contamination of "wrong-sign" neutrinos, e.g., anti-neutrinos in FHC mode and neutrinos in RHC mode, is larger for the RHC flux due to the smaller anti-neutrino cross section. Electron neutrino contamination is also present due to kaons produced from proton in-

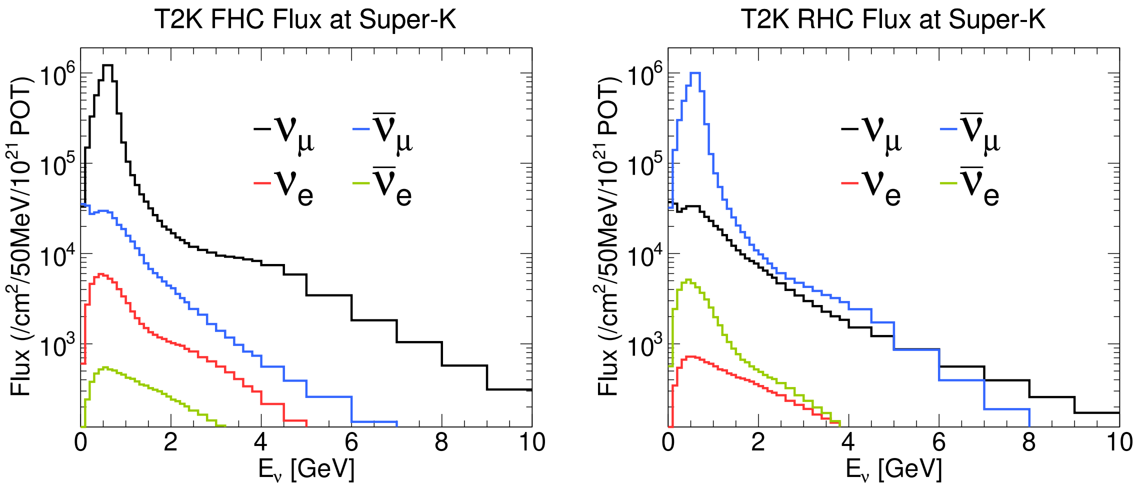

Figure 6·7: Neutrino flux prediction at SK from the T2K neutrino beam, before oscillations. **Left**: FHC, neutrino mode and **Right**: RHC, anti-neutrino mode.

teractions in the target.

Near Detectors

The T2K neutrino beam passes through a detector complex 280 m downstream of the T2K target before arriving at SK. These near detectors monitor properties of the beam and measure neutrino interaction cross sections with higher statistics than is available at SK. A key feature of the near detectors is that they observe an unoscillated neutrino flux: Neutrinos observed at the near detectors have not traveled a sufficient distance to have appreciable oscillation effects. The combination of unoscillated near detector data and oscillated far detector data helps to resolve the effects of flux and cross section models from oscillation parameters. The two primary near detectors are INGRID, an on-axis beam line monitor, and ND280, an off-axis high-resolution tracking detector. These detectors are described in detail in [143] and are summarized here.

INGRID monitors CC ν_μ interactions to characterize the T2K beam profile and intensity. INGRID consists of 14 detector modules arranged in a cross, which view sections of the beam within a $10\,\mathrm{m} \times 10\,\mathrm{m}$ transverse area. The T2K beam center passes through two modules placed at the center of the cross. Each detector module consists of alternating iron plates and scintillator panels. Muon neutrino interactions in the iron plates create muons which leave tracks in the scintillator panels, which can be reconstructed. Veto panels installed on the outside of each module ensure cosmic muons entering from outside the modules are rejected. INGRID observes a sufficient number of interactions to monitor the beam center with a precision of 10 cm each day.

ND280 is a multi-purpose detector which monitors the flavor composition, energies, and interaction rates of neutrinos from the T2K beam. The ND280 detector is placed on the same off-axis angle as SK, such that it observes the same flux of neutrinos as SK. The ND280 detector is surrounded by a magnet and consists of several sub-systems within. First, the T2K beam passes through a detector optimized for observing NC processes which produce π^0s, i.e., $\nu + N \rightarrow \nu + N + \pi^0 + X$. The π^0 detector consists of alternating water targets and scintillator panels. Next, the beam passes through two alternating combinations of fine-grained detectors (FGDs) and time projection chambers (TPCs). This section of the detector identifies the flavor and energy of neutrino interactions using high-resolution tracking information and the magnetic field to separate particles based on electric charge and calculate their momenta. The FGDs provide the interaction target and vertex information, while the TPCs are used for PID and momentum reconstruction. The TPCs contain argon gas, and ionization charge from particle traversals is drifted towards wire planes which produce an image of the track.

The ND280 data is analyzed as additional samples as part of the T2K experiment's neutrino oscillation measurement. ND280 events are selected based on the number of pions in FHC mode, or the number of tracks in RHC mode. The different samples are enhanced for different interaction modes, e.g., the zero-pion sample in FHC mode, and one-track sample in RHC mode, are pure in CCQE interactions.

T2K Event Selection & Reconstruction at SK

T2K events at SK must pass a series of reduction cuts to ensure reliable event reconstruction and remove NC events which are backgrounds to the oscillation analysis. Beam timing information is used to trigger SK at the time of arriving T2K events, which significantly reduces the number of cosmic muon and low-energy contamination. T2K events must fall within a $[-2, 10]$ µs window of the beam signal, and beam signals must not occur within 100 µs of cosmic muon triggers at SK.

Selected T2K events are reconstructed using the FITQUN algorithm, described in detail in [77]. Like APFIT, described in Section 3.2, FITQUN reconstructs the number, momenta, and PID of Cherenkov rings, and counts the number of decay electrons. Unlike APFIT, FITQUN reconstructs events by iteratively updating a likelihood function using trial combinations of particle types and kinematics which produce expected configurations of hit PMTs. The likelihood function is expressed as:

$$\mathcal{L}(\Gamma, \theta) = \prod_{j}^{\text{Unhit}} P_j(\text{Unhit}|\mu_j) \prod_{i}^{\text{Hit}} [1 - P_i(\text{Unhit}|\mu_i)] \times f_q(q_i|\mu_i) f_t(t_i|\Gamma, \theta), \tag{6.4}$$

where Γ represents a particular particle hypothesis, e.g. "single ring e-like", and θ is a set of the particle's kinematic variables. The products compare the light pattern using the probabilities of registering a hit, P_i, of both "unhit" and "hit" PMTs. For hit PMTs, the probability also includes the charge likelihood, $f_q(q_i, \mu_i)$, where q_i is the observed charge and μ_i is the expected charge, and a likelihood for the observed hit time, $f_t(t_i|\Gamma, \theta)$, where t_i is the observed hit time.

Unlike the SK analysis, T2K uses the reconstructed particle information to estimate the energy of the neutrino. The neutrino energy estimation relies on two features of T2K beam neutrinos which are not present for atmospheric neutrinos: First, the direction of T2K neutrinos is known exactly, since all neutrinos arrive from the direction of the beam. Second, the T2K flux has a sharp peak for neutrino energies near 600 MeV, where the CCQE process has the largest cross section. By knowing the beam direction and assuming CCQE interactions, the neutrino energy can be estimated using the outgoing lepton kinematics as

$$E_\nu^{\mathrm{Rec.}} = \frac{2m_{N,i}E_l - m_l^2 + m_{N,f}^2 - m_{N,i}^2}{2(m_{N,i} - E_l + |\vec{p}_l|\cos\theta_l)}, \tag{6.5}$$

where $m_{N,i}$ and $m_{N,f}$ are the initial and final nucleon masses, E_l is the lepton energy, $\vec{p}_l$ is the lepton momentum, and θ_l is the angle of the lepton with respect to the neutrino direction. $m_{N,i}$ is typically the effective nucleon mass after subtracting the nucleon removal energy (NRE), i.e., the average energy required to free the nucleon from the nucleus.

The distribution of true neutrino energy bias due to $E_\nu^{\mathrm{Rec.}}$, computed using the true lepton direction and energy, is shown in Figure 6·8. The bias distribution for CCQE events is peaked around zero, while non-CCQE interactions have broader distributions with longer tails at negative values. This tails reflect that Equation 6.5 does not account for additional particles in the event.

6.3 T2K Model

This thesis presents a combined SK and T2K analysis using an effective description the T2K experiment's flux, cross section models, event selections, and systematic uncertainties, referred to as the "T2K model". The T2K model presented in this thesis is an upgrade to the previous T2K model described in [38], and is based on a description of the more recent T2K Runs 1–9 analysis presented in [144]. The T2K Runs 1–9 analysis uses data collected with 1.494×10^{21} POT in FHC mode, and

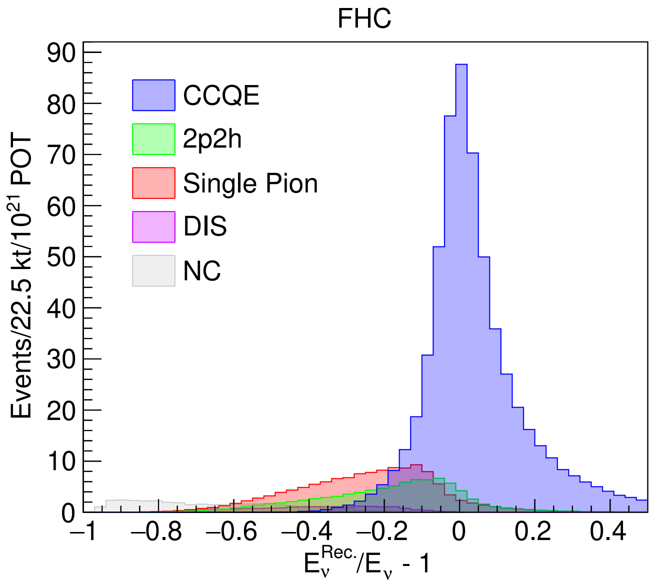

Figure 6·8: Expected $E_\nu^{\text{Rec.}}$ bias for the different neutrino interactions present in the oscillated T2K FHC flux. The distributions show the nominal MC prediction of the T2K model before any event selections. The oscillation probabilities are computed using the parameters listed in Table 6.3.

1.635×10^{21} POT in RHC mode. Compared to the previous T2K model, the present model includes twice as much data in FHC mode, an additional sample in FHC mode, and, for the first time, a description of two anti-neutrino-enhanced samples in RHC mode.

The T2K model re-weights the existing SK atmospheric neutrino MC events to produce T2K MC events distributed according to T2K's flux and nominal cross section models. In the final analysis, the T2K model MC, together with binned T2K data, are added as extra samples in the fit alongside the SK atmospheric neutrino samples.

6.3.1 Flux Re-weighting

To use the atmospheric neutrino MC as a prediction for T2K events, the T2K model re-weights each atmospheric neutrino MC using the predicted flux ratio between the

Parameter	Value
$\sin^2\theta_{12}$	0.304
$\sin^2\theta_{13}$	0.0212
$\sin^2\theta_{23}$	0.528
Δm^2_{21} ($10^{-5}\,\mathrm{eV}^2$)	7.53
Δm^2_{32} ($10^{-3}\,\mathrm{eV}^2$)	2.509
δ_{CP}	4.682
Ordering	Normal

Table 6.3: Nominal oscillation parameters used by the T2K model. The values are the same as in Table III from [144].

T2K flux and the Honda atmospheric neutrino flux. While the T2K flux is a 1D function of energy, the Honda flux is expressed as a function of both the zenith angle, θ_z and the azimuthal angle, ϕ. The corresponding weight for each atmospheric neutrino MC event is:

$$w_\alpha(E_\nu, \theta_z, \phi) \propto \frac{\Phi_{\mathrm{T2K},\beta}(E_\nu)}{\Phi_{\mathrm{Honda},\alpha}(E_\nu, \theta_z, \phi)}, \tag{6.6}$$

where α and β indicate neutrino flavors. For muon neutrino events, $\alpha = \beta = \nu_\mu$, while for electron neutrino events, the weights are computed both for intrinsic, $\alpha = \beta = \nu_e$, and appearance, $\alpha = \nu_e, \beta = \nu_\mu$, oscillation channels. Each electron neutrino MC event is arbitrarily assigned to either the intrinsic or appearance channel, and the relative contribution of each is corrected in the next step. Because the T2K flux of electron neutrinos is small relative to that of muon neutrinos, $\nu_e \to \nu_\mu$ oscillations are a negligible contribution and are not considered. Flux weights are computed for all atmospheric neutrino MC events with energies from 0.1 GeV to 10 GeV.

An example re-weighting from the Honda flux to the T2K flux is shown in Figure 6·9. The figure shows events generated at a fixed direction according to the Honda flux, which typically has a falling-exponential shape, while the T2K flux has a peaked shape near $E_\nu \approx 600\,\mathrm{MeV}$. The weights change the relative frequency of the events

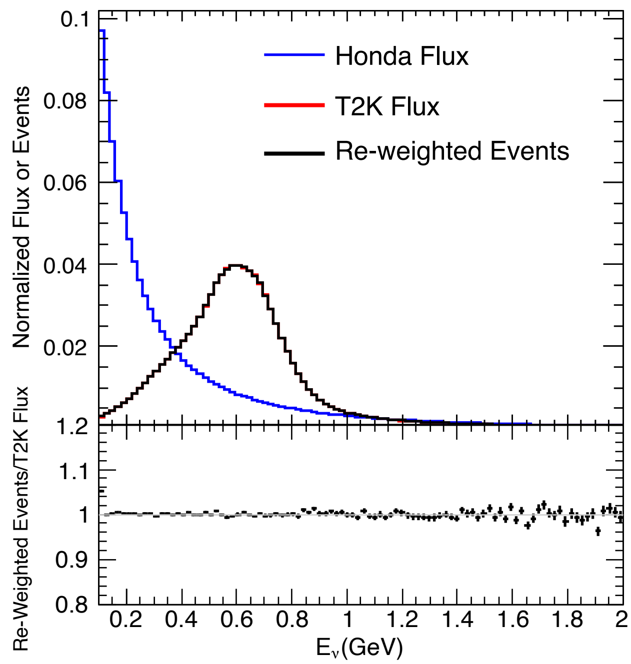

Figure 6·9: T2K model flux re-weighting demonstration, using atmospheric neutrino MC events generated according to the Honda flux at a fixed direction. The lower panel shows the ratio between the re-weighted events and the T2K flux distribution.

generated according to the Honda flux to match the T2K flux. Note that because the MC events were generated according to the Honda flux, the MC statistics decrease with increasing energy.

6.3.2 Normalization

As described in Chapter 4, 500 years of atmospheric neutrino MC is generated for the SK analysis. To re-weight the atmospheric neutrino MC to meaningful units for T2K, the T2K model applies a normalization to each oscillation channel. The normalizations are calculated by dividing the expected event rate of neutrinos with energies between 0.1 GeV to 10 GeV by the total number of T2K flux-weighted MC

Flux	Cross Section	Events/22.5 kt/10^{21} POT	
		FHC	RHC
Φ_{ν_μ}	σ_{ν_μ}	1480.45	210.24
Φ_{ν_μ}	σ_{ν_e}	1562.20	216.80
Φ_{ν_e}	σ_{ν_e}	28.90	8.90
$\Phi_{\bar{\nu}_\mu}$	$\sigma_{\bar{\nu}_\mu}$	45.15	344.94
$\Phi_{\bar{\nu}_\mu}$	$\sigma_{\bar{\nu}_e}$	46.71	362.87
$\Phi_{\bar{\nu}_e}$	$\sigma_{\bar{\nu}_e}$	2.54	6.25

Table 6.4: Un-oscillated event rates at SK, used by the T2K model for normalizing the SK MC, following Equation 6.7. The T2K fluxes are from [144], and the total cross sections are computed using the NEUT version 5.4.0 default configuration.

events in a fixed volume, i.e., the flux-weighted events are normalized to

$$N_x \propto \int_{0.1\,\mathrm{GeV}}^{10\,\mathrm{GeV}} \sigma_\alpha(E_\nu) \times \Phi_\beta(E_\nu) dE_\nu \tag{6.7}$$

where $\sigma_\alpha(E_\nu)$ is the total interaction cross section for neutrino flavor α, and $\Phi_\beta(E_\nu)$ is the T2K flux for neutrino flavor β. For the $\nu_\mu \to \nu_\mu$ and $\nu_e \to \nu_e$ channels, $\alpha = \beta$, while for the $\nu_\mu \to \nu_e$ channels, the cross section index $\alpha = \nu_e$, and the flux index $\beta = \nu_\mu$. The conventional 22.5 kt fiducial volume, computed as Avogadro's number multiplied by NEUT's cross section units and the fiducial volume mass, $6.022 \times 10^{23} \cdot 10^{-38} \cdot 22.5 \times 10^9$, sets the proportionality. The expected event rates for each oscillation channel are listed in Table 6.4. The event rates were calculated using the T2K fluxes from [144] and the total cross sections of the default NEUT 5.4.0 configuration.

After the normalization, the near detector constraints on the T2K flux are applied as an additional scaling. The constraint changes the normalization of each flavor in fixed energy ranges of the FHC and RHC fluxes. The values applied as part of the T2K model are listed in Table 6.9.

6.3.3 Cross Section Re-weighting

Following the flux re-weighting and normalization, the remaining differences between the T2K model MC events and the nominal MC prediction of the T2K Runs 1–9 analysis are due to differences in the neutrino interaction cross section models, discussed below.

1p1h: For the nominal simulation of 1p1h interactions, the T2K analysis uses an RFG model with $M_A^{\mathrm{QE}} = 1.13\,\mathrm{GeV/c^2}$ and Fermi momentum $p_F = 205\,\mathrm{MeV/c}$, while the SK analysis uses an LFG model (see Section 4.2.1). The T2K model implements a scheme to resolve the differences between the RFG and LFG models, as well as other features of the T2K nominal 1p1h simulation. This is a crucial step of reproducing the T2K MC because the distribution of lepton kinematics from 1p1h interactions has the largest impact on the predicted distribution of $E_\nu^{\mathrm{Rec.}}$ for T2K events.

The T2K model 1p1h re-weighting method is similar to the method used to calculate shifts in M_A^{QE} for the purposes of evaluating systematic uncertainties (see Section 5.2.2). The weight is calculated as the ratio of the double-differential cross sections, $d^2\sigma/dE_{\mathrm{Lep}}d\cos\theta_{\mathrm{Lep}}$, between the T2K nominal RFG model and the SK nominal LFG model, for each event's lepton kinematics and neutrino energy. However, this is an imperfect approach: There are some combinations of lepton angles and energies which have non-zero cross sections in one model but are zero, or very small in the other. Attempting to calculate the cross section ratio for these combinations can lead to large or undefined weights. Further, the NEUT implementation of the LFG model relies on a random number generator to calculate the double-differential cross section; the cross section is calculated for neutrino interactions at multiple, randomly selected radii within the nucleus, and averaged. The randomization leads to variations in the calculated double-differential cross section which should not be taken literally.

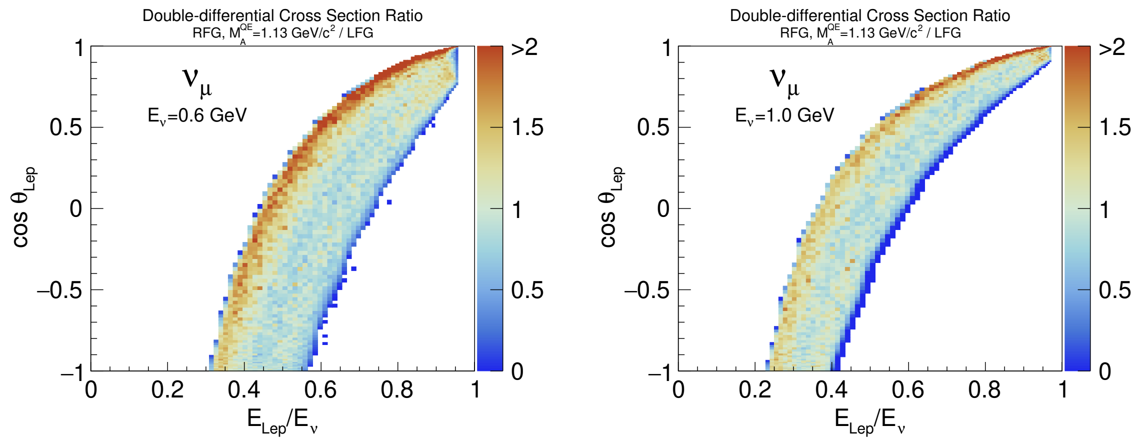

Figure 6·10: Ratios of double-differential 1p1h cross sections computed using the T2K nominal RFG model and the NEUT default LFG model. The color scale indicates the weight, and weights above 2 are not differentiated. No smoothing or averaging has been applied. Cross sections are for muon neutrinos. **Left**: $E_\nu = 600\,\mathrm{MeV}$. **Right**: $E_\nu = 1\,\mathrm{GeV}$.

Example 1p1h double-differential cross section ratios are shown for fixed neutrino energies in Figure 6·10. The figure shows the double-differential cross section ratios in the areas of phase space where the RFG and LFG models overlap. The x-axis of each panel shows the fraction of the neutrino energy carried by the outgoing lepton, and the y-axis shows the cosine of the lepton direction with respect to the true neutrino direction. The T2K nominal RFG model predicts smaller energy fractions for the outgoing lepton, as can be seen by the large weights on the left-hand edges and small weights on the right-hand edges of either panel. The T2K nominal RFG model also predicts leptons more aligned with the direction of the neutrino compared to the LFG model, indicated by the large weights near $\cos\theta_{\mathrm{Lep}} \gtrsim 0.5$. The double-differential cross section ratios are not smooth due to the random number generator used in computing the LFG cross sections.

To stabilize the RFG-LFG re-weighting, the T2K model implements the following corrections when computing the weights: (i) a cutoff weight is defined, such that weights above a certain threshold are set to 0. (ii) The double-differential cross sections are averaged over nearby regions of phase space before taking the ratio. (iii) The double-differential cross section in regions of non-overlapping phase space is integrated, and applied as an overall correction to preserve the total cross section after re-weighting. The corrections from (iii) are $\sim 1\,\%$.

A demonstration of the 1p1h re-weighting is shown as a function of the total neutrino cross section for muon neutrinos in Figure 6·11. The left panel shows the "out-of-the-box" agreement between the total T2K RFG cross section model after re-weighting LFG events by the double-differential cross section ratio computed by NEUT with no further corrections[1]. The right panel shows the result after the T2K model corrections are applied. The level of agreement before the corrections is poor at several energies, while, for the T2K model, the level of agreement in the total cross section is within a few percent for energies relevant to T2K.

The T2K nominal 1p1h model also includes RPA corrections which modify the cross section as a function of q^2. In the T2K analysis, the default NEUT RPA corrections from the Nieves model are replaced with an effective function based on Bernstein polynomials, referred to as "BeRPA". The function is given in [144] as

$$f(x) = \begin{cases} A(1-x')^3 + 3B(1-x')^2 x' + 3p_1(1-x')x'^2 + Cx'^3, & x < U \\ 1 + p_2 \exp(-D(x-U)), & x \geq U \end{cases} \tag{6.8}$$

where $x \equiv q^2$ and $x' = q^2/U$. The coefficients p_1 and p_2 are set to enforce continuity

[1]In NEUT 5.4.0, a software bug results in the LFG total cross section being shifted by 50 MeV in neutrino energy, cf. the `N1p1h::IntegralCrossSection` function included in NEUT. This also needs to be corrected as part of the re-weighting if events are generated according to this function, and so it is partially responsible for the poor agreement at low energies in the left panel of Figure 6·11. The bug has been fixed in more recent versions of NEUT, and never affected the double-differential cross sections.

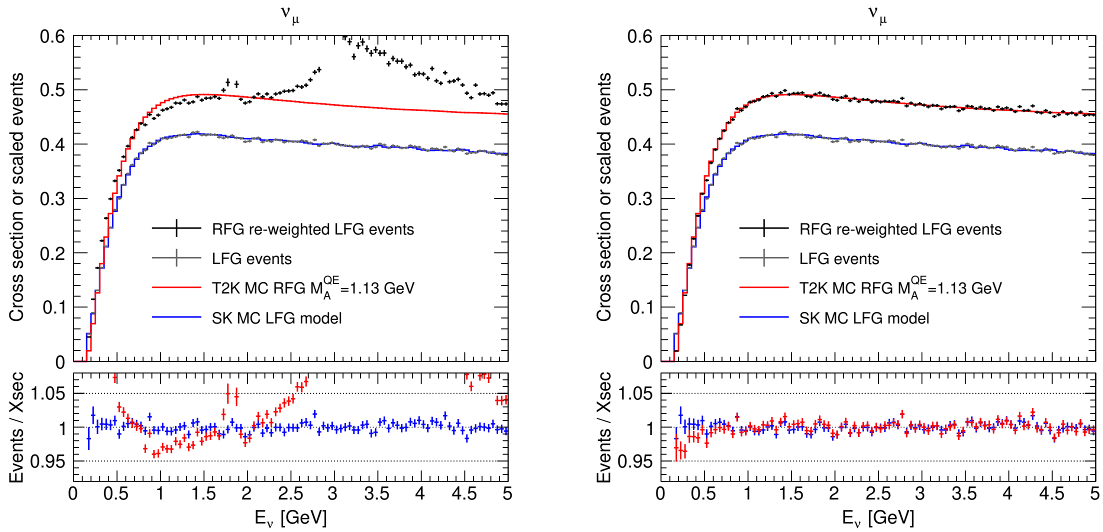

Figure 6·11: LFG to RFG re-weighting demonstration from the T2K model. Neutrino interactions (grey points) are generated according to the LFG model (blue line), then re-weighted by the ratio of the double-differential cross sections between the T2K RFG model and the LFG model. The black data points show the events after re-weighting. The red line shows the total cross section for the T2K RFG model. The lower panels show the ratio of events to the predicted total cross section before re-weighting (blue points) and after re-weighting (red points). **Left**: The result of the re-weighting using the raw values from NEUT. Large weights cause irregularities for some events. **Right**: The level of agreement in the total cross section with corrections applied by the T2K model.

for changes in the other parameters,

$$p_1 = C + \frac{UD(C-1)}{3}, \tag{6.9}$$

$$p_2 = C - 1. \tag{6.10}$$

The parameters A, B, C, D, and U are set to nominal values in the T2K analysis, then constrained by the fit to the near detector data[2]. This function is implemented

[2]The BeRPA values are listed for "A", "B", "D", "E", and "U" in Table XXV of [144]. The "D" value corresponds to the "C" parameter, and the "E" value corresponds to the "D" parameter in Equation 6.8.

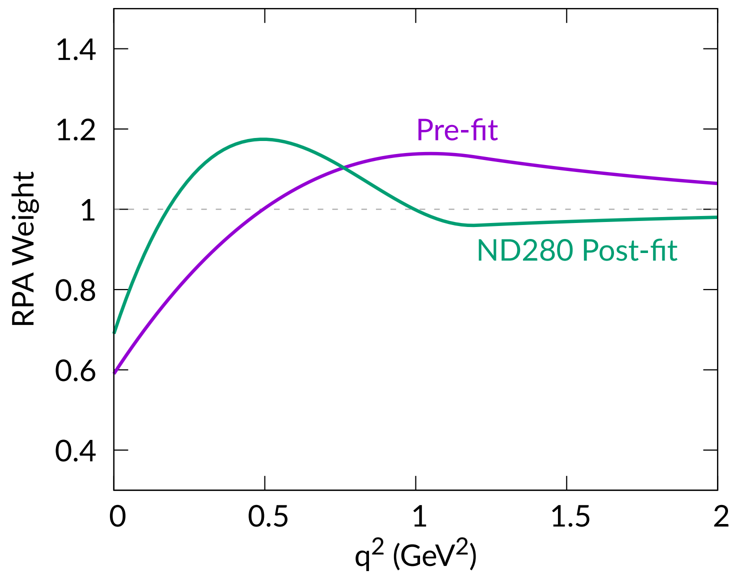

Figure 6·12: The "BeRPA" parametrization of the RPA correction used in the T2K analysis and re-implemented as part of the T2K model. The x-axis is the four-momentum transfer, q^2, and the y-axis shows the correction factor applied to bound-nucleon CCQE MC events.

within the T2K model, and it is applied as a correction to CCQE interactions with bound nucleons. The function is shown for the pre-fit and ND280 post-fit values from the T2K analysis in Figure 6·12.

2p2h: Both the T2K analysis and the SK analysis use the same 2p2h model, discussed in Section 4.2.1. However, the T2K analysis introduces an extra parameter to control the relative amount of the quasi-elastic and Δ-baryon-like resonance components of the 2p2h model. The parameter is then fit in the T2K analysis including the T2K near detector data. This parameter is not available in the default version of NEUT, and its implementation is not yet publicly available. Therefore, the T2K model does not re-weight 2p2h events.

Resonant pion production: Both the SK and T2K analyses use the same resonant single pion production models, although there are differences in the nominal values of

M_A^{Res}, C_A^5, and $I_{\frac{1}{2}}$. The T2K model re-weights the atmospheric neutrino MC events using the double-differential cross section ratio between the two sets of parameters. This is the same method used to computing the shift in neutrino event weights due to uncertainties in the resonant pion production parameters, discussed in Section 5.2.

Coherent pion production: The T2K analysis and the SK analysis use the same coherent pion production models. The T2K analysis also implements relative normalization parameters for the CC and NC coherent pion production processes. The T2K model implements these parameters by scaling the weight of these processes.

DIS: At T2K energies, DIS events are only a small fraction of the total event rate, so these are not re-weighted, despite slightly different treatment between SK and T2K.

Event Selection

The T2K oscillation analysis includes five single-ring samples: FHC e-like, FHC μ-like, FHC CC 1π-like, RHC e-like, and RHC μ-like. The FHC and RHC e-like and μ-like samples target CCQE interactions by selecting a events with a single, e-like ring with no decay electrons, or a single μ-like ring with zero or one decay electrons. The FHC CC 1π-like sample selects single-ring e-like events with one decay electron. This is the expected final state for a neutrino CC interaction which produces a π^+ below Cherenkov threshold[3].

Events in all samples must pass quality cuts, analogous to the SK atmospheric neutrino reduction. The visible energy, E_{Vis}, must be larger than 30 MeV, and the maximum number of OD hits in a single OD cluster must be smaller than 15. Events must also be contained within a fiducial volume. While the SK fiducial volume is defined by a fixed, minimum vertex distance to the ID walls, the T2K fiducial volume

[3]In RHC mode, the equivalent anti-neutrino interaction produces a π^- which is likely to be absorbed before decaying.

Selection	1-ring μ-like	1-ring e-like 0 d.e.	CC 1π (FHC Only)
Dist. from wall (cm)	> 50	> 80	> 50
Dist. to wall (cm)	> 250	> 170	> 270
PID	$\Lambda^e_\mu < 0.2p_e$	$\Lambda^e_\mu > 0.2p_e$	
Momentum (MeV/c)	> 200	> 100	
Decay electrons	≤ 1	0	1
NC π Rejection	$\Lambda^{\pi^+}_\mu < 0.15p_\mu$	$\Lambda^{\pi^0}_e < 175 - 0.875m_{\gamma\gamma}$	
E^{Rec}_ν (MeV)	–	< 1250	

Table 6.5: Summary of reduction steps for the five single-ring samples in the T2K analysis. The μ-like and e-like with zero decay electron samples are identical in FHC and RHC mode. The definition of Λ^α_β is given in Equation 6.11. This table is reproduced from Table IV of [144].

is defined by both the vertex distance to the wall, "`dwall`," and the vertex distance to the wall along the fitted direction of the ring, "`towall`." The combination of `dwall` and `towall` allows events with vertices closer to the wall to be kept in cases where the Cherenkov ring is pointed away from the nearest wall. The chosen cut values for the fiducial volume are separately optimized for each sample, and are listed in Table 6.5. Events with multiple rings and two or more decay electrons are not used in the T2K Runs 1–9 analysis. The distribution of the number of rings, and the distribution of decay electrons, for events which pass the fiducial volume cuts are shown in Figure 6·13 and Figure 6·14, respectively.

The remaining single ring events are further separated based on their PID characteristics. The T2K analysis separates events using the likelihood ratio between the different particle hypotheses considered by FITQUN, expressed as

$$\Lambda^\alpha_\beta \equiv \log \frac{\mathcal{L}_\alpha}{\mathcal{L}_\beta} \tag{6.11}$$

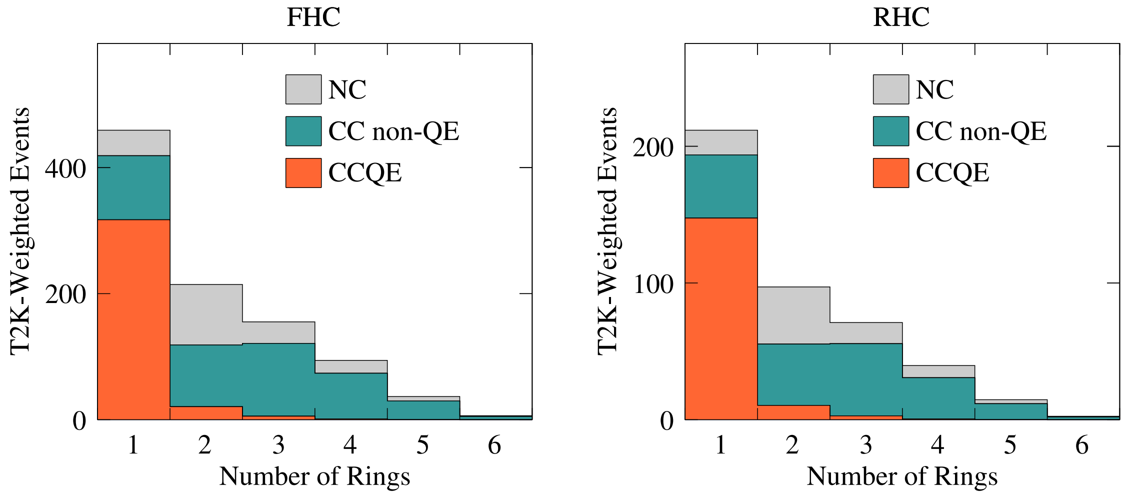

Figure 6·13: Number of rings distribution for T2K model MC events in **Left**: FHC and **Right**: RHC modes. Events with `dwall` > 80 cm and `towall` > 170 cm are shown. Oscillations are applied using the parameters listed in Table 6.3. The figures show the equivalent distributions to Figure 16 from [144].

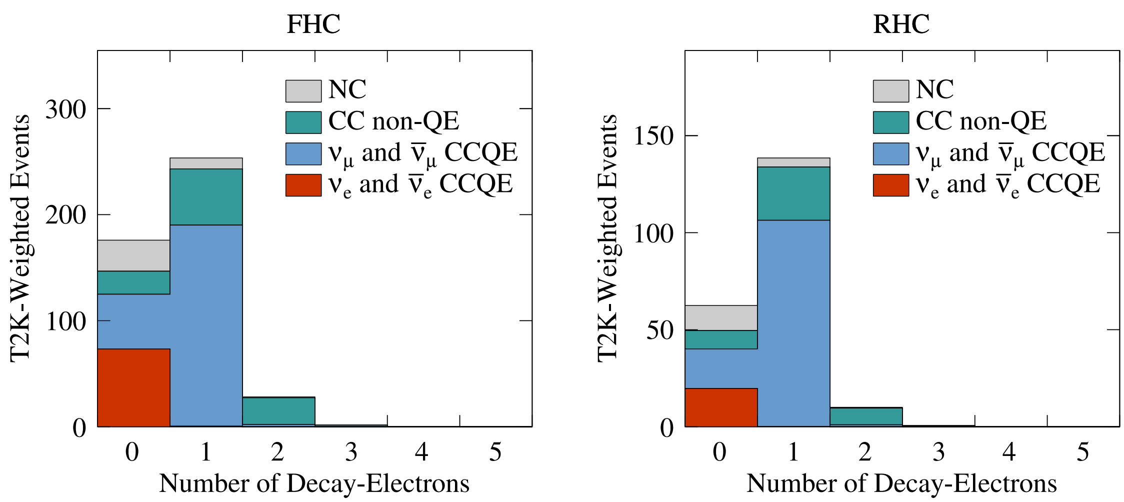

Figure 6·14: Number of decay electrons distribution for T2K model MC events in **Left**: FHC and **Right**: RHC modes. Events shown are the same as in Figure 6·13. The figures show the equivalent distributions to Figure 18 from [144].

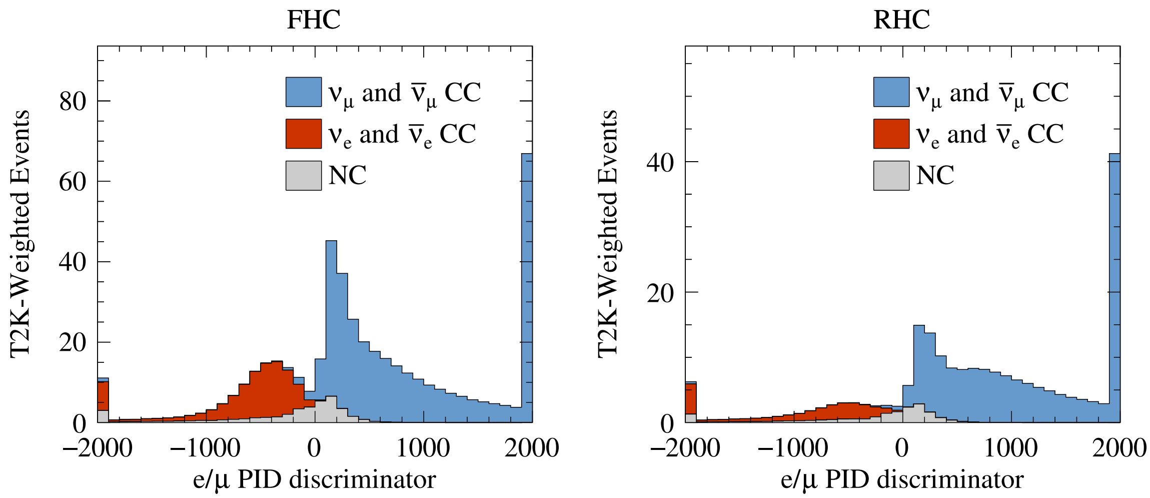

Figure 6·15: FITQUN e-μ discriminator distribution for T2K model MC events in **Left**: FHC and **Right**: RHC modes. Events with negative scores are considered e-like, while events with positive scores are considered μ-like. The events shown are the same as in Figure 6·13. The figures show the equivalent distributions to Figure 17 from [144].

where α and β are one of $e^{\pm}$, $\mu^{\pm}$, $\pi^{\pm}$ or π^0. T2K separates μ- and e-like rings using a momentum-dependent cut, $\Lambda^e_\mu - p_e/5\,\mathrm{MeV/c} > 0$ for e-like, and μ-like otherwise, where p_e is the FITQUN fitted momentum assuming the electron hypothesis. The e/μ separation condition is visualized in Figure 6·15. Selected μ-like events then must have a reconstructed momentum $p_\mu > 200\,\mathrm{MeV/c}$, while e-like events must have a reconstructed momentum $p_e > 100\,\mathrm{MeV/c}$.

The T2K analysis rejects NC backgrounds by separating μ-like events from charged pions, and e-like events from neutral pions. The separation conditions are based on the FITQUN likelihood ratios,

$$(\mu\text{-like}) \qquad \Lambda^{\pi^+}_\mu - 6p_\mu/40\,\mathrm{MeV/c} < 0 \tag{6.12}$$

$$(e\text{-like}) \qquad \Lambda^{\pi^0}_e - 175 + 35m_{\gamma\gamma}/40\,\mathrm{MeV/c^2} < 0 \tag{6.13}$$

where $m_{\gamma\gamma}$ is the reconstructed invariant mass of two photon rings, assuming a π^0 hypothesis. The distributions of the $\mu/\pi^{\pm}$ and e/π^0 discrimination variable are shown

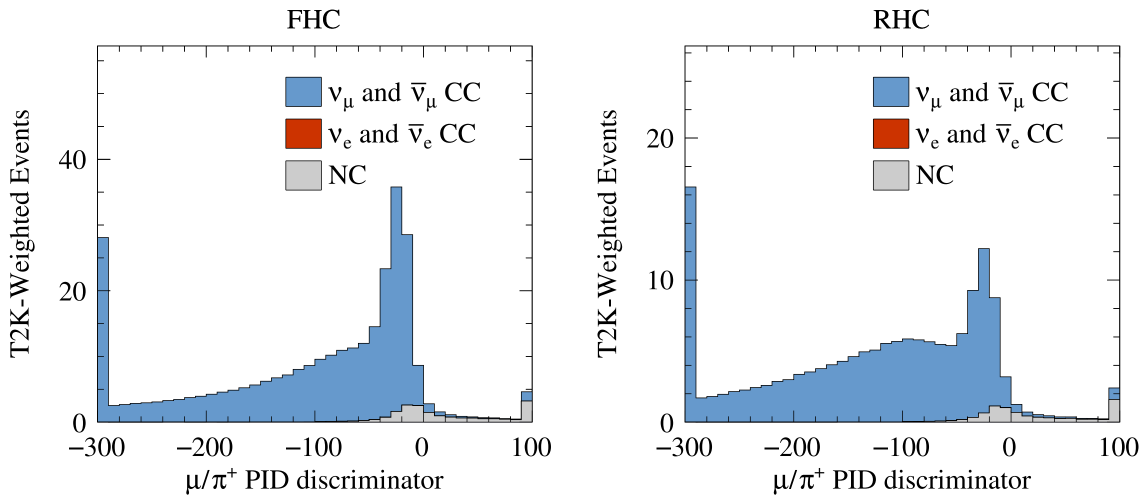

Figure 6·16: FITQUN μ-π^+ discriminator distribution for T2K model MC events in **Left**: FHC and **Right**: RHC modes. Events with scores < 0 are selected; events with positive scores are rejected as NC-like. Events shown have passed all other cuts of the μ-like reduction. The figures shows the equivalent distributions to Figure 21 from [144].

in Figure 6·16 and Figure 6·17, respectively.

The last selection requires that $E_\nu^{\text{Rec.}} < 1250\,\text{MeV}$ for the e-like samples. Electron neutrinos above this energy do not add sensitivity to the ν_e appearance signal. When computing $E_\nu^{\text{Rec.}}$ via Equation 6.5, T2K uses the proton and neutron masses, and an NRE value of 27 MeV, for the initial and final nucleon masses. For the CC 1π sample, since a resonant pion production process is assumed, T2K instead uses the mass of the Δ baryon for the nucleon masses and an NRE value of 0.

Tables 6.6–6.8 list the number of re-weighted atmospheric neutrino MC events remaining after each reduction step for each of the five T2K samples. The numbers in the penultimate row of each table show the accepted signal and background events remaining after all reduction steps. For comparison, the final row of each table lists the number of MC events from the T2K analysis in parentheses.

The final T2K model MC distributions of the five T2K samples are shown in Figure 6·18 and Figure 6·19. The three e-like samples are have 10 $E_\nu^{\text{Rec.}}$ bins each from

FHC e-like	$\nu_\mu + \bar{\nu}_\mu$ CC	$\nu_e + \bar{\nu}_e$ CC	$\nu + \bar{\nu}$ NC	$\nu_\mu \to \nu_e$ CC	$\bar{\nu}_\mu \to \bar{\nu}_e$ CC
FC and FV	643.69	40.73	199.14	80.72	0.75
Single particle	324.62	23.18	40.50	70.03	0.61
Electron like	6.72	23.12	22.19	69.79	0.61
$p_e > 100\,\mathrm{MeV/c}$	2.76	23.02	14.94	68.84	0.61
No decay-e	0.65	19.68	12.68	62.42	0.60
$E_{\mathrm{rec}} < 1250\,\mathrm{MeV}$	0.26	10.23	8.23	60.43	0.44
Not π^0	0.11	9.56	4.11	58.30	0.40
T2K	(0.27)	(8.79)	(4.21)	(58.53)	(0.38)
RHC e-like					
FC and FV	311.24	21.33	87.64	5.75	10.00
Single particle	168.00	12.08	18.06	4.40	8.94
Electron like	2.14	12.06	9.83	4.39	8.91
$p_e > 100\,\mathrm{MeV/c}$	1.14	12.03	6.74	4.35	8.88
No decay-e	0.27	10.80	5.73	3.81	8.83
$E_{\mathrm{rec}} < 1250\,\mathrm{MeV}$	0.11	4.73	3.70	3.17	8.30
Not π^0	0.05	4.35	1.71	3.00	7.81
T2K	(0.13)	(3.70)	(2.40)	(2.65)	(7.37)

Table 6.6: Nominal T2K model MC e-like event counts after each reduction step. The top and bottom portions of the table show the numbers in the FHC and RHC samples, respectively. Counts are shown with oscillations applied, calculated using the parameters listed in Table 6.3. The final row, labeled "T2K" shows the numbers from the T2K analysis, listed in Table V from [144].

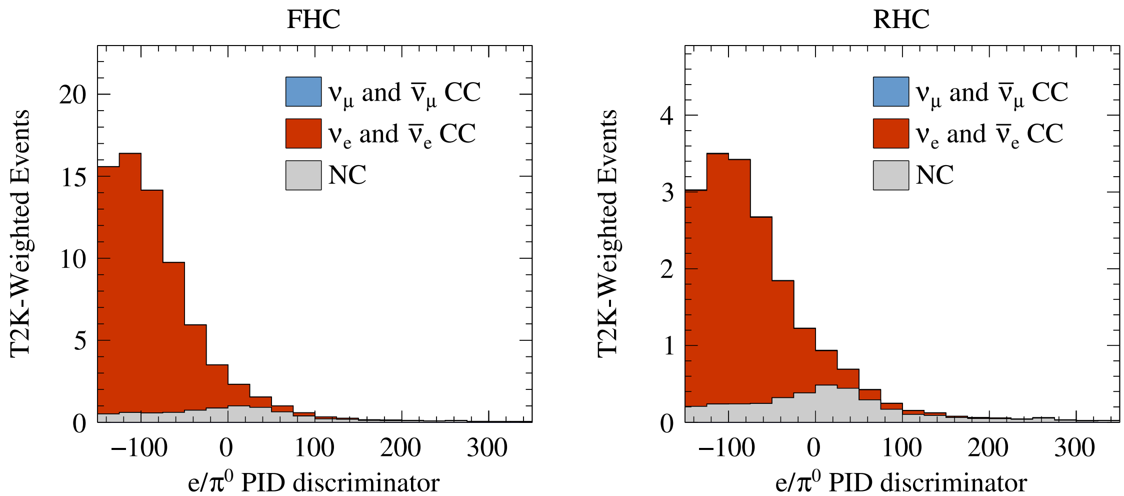

Figure 6·17: FITQUN e-π^0 discriminator distribution for T2K model MC events in **Left**: FHC and **Right**: RHC modes. Events with scores < 0 are selected; events with positive scores are rejected as NC-like. Events shown have passed all other cuts of the e-like reduction. The figures show the equivalent distributions to Figure 20 from [144].

FHC CC 1π-like	$\nu_\mu + \bar{\nu}_\mu$ CC	$\nu_e + \bar{\nu}_e$ CC	$\nu + \bar{\nu}$ NC	$\nu_\mu \to \nu_e$ CC	$\bar{\nu}_\mu \to \bar{\nu}_e$ CC
FC and FV	645.95	41.48	203.37	80.86	0.75
Single particle	320.52	23.33	40.61	69.91	0.61
Electron like	6.78	23.28	22.78	69.71	0.61
$p_e > 100\,\mathrm{MeV/c}$	2.74	23.17	15.18	68.71	0.61
1 decay-e	1.32	3.15	1.85	6.34	0.01
$E_{\mathrm{rec}} < 1250\,\mathrm{MeV}$	0.29	1.06	0.66	5.84	0.00
Not π^0	0.12	0.97	0.33	5.54	0.00
T2K	(0.16)	(0.93)	(0.38)	(5.64)	(0.01)

Table 6.7: Nominal T2K model MC CC 1π-like event counts after each reduction step. The counts are calculated using the oscillation parameters listed in Table 6.3. The final row, labeled "T2K" shows the numbers from the T2K analysis, listed in Table VI from [144].

FHC μ-like	$\nu_e + \bar{\nu}_e$ CC	$\nu + \bar{\nu}$ NC	$\nu_\mu + \bar{\nu}_\mu$ CC non-QE	ν_μ CCQE	$\bar{\nu}_\mu$ CCQE
FC and FV	116.84	194.59	349.91	241.05	15.18
Single particle	90.76	39.69	77.86	220.76	13.94
Muon like	0.27	18.30	73.73	217.62	13.87
$p_\mu > 200\,\mathrm{MeV/c}$	0.27	18.10	73.70	217.41	13.87
0 or 1 decay-e	0.27	17.65	48.77	215.41	13.79
Not π^+	0.26	8.43	46.87	212.47	13.58
T2K	(0.08)	(8.31)	(36.75)	(210.64)	(12.18)
RHC μ-like					
FC and FV	34.45	85.58	191.78	50.62	82.86
Single particle	24.25	17.68	45.53	43.97	78.26
Muon like	0.05	8.20	40.21	43.69	77.55
$p_\mu > 200\,\mathrm{MeV/c}$	0.05	8.12	40.17	43.68	77.52
0 or 1 decay-e	0.05	7.90	31.52	43.04	77.19
Not π^+	0.05	3.57	29.08	42.38	76.14
T2K	(0.02)	(3.89)	(24.71)	(35.36)	(65.00)

Table 6.8: Nominal T2K model MC μ-like event counts after each reduction step. The counts are calculated using the oscillation parameters listed in Table 6.3. The final row, labeled "T2K" shows the numbers from the T2K analysis, listed in Table VII from [144].

$[0, 1250]$ MeV, while the two μ-like samples have 30 $E_\nu^{\text{Rec.}}$ bins each from $[0, 3000]$ MeV. Combined, the five T2K samples add 90 bins to the fit. Events with $E_\nu^{\text{Rec.}} > 3000$ MeV in the μ-like samples are consolidated in the last bin. The figures also show the binned data counts from the T2K Runs 1–9 analysis, Figures 25-27 of [144].

6.3.4 Systematic Uncertainties

The T2K model implements several of the systematic uncertainties from [144]. For the combined analysis with the SK atmospheric neutrino samples and the T2K model samples, several of the systematic uncertainties described in Section 5.2 are replaced, and several new uncertainties are added.

Flux Uncertainties: The flux uncertainties in the T2K analysis consist of 25 parameters each for the FHC and RHC fluxes. These parameters change the normalization of the flux in different energy ranges and for each of the neutrino flavors present in the T2K beam. The T2K model implements a single flux uncertainty which varies all 50 of the flux parameters in each FHC and RHC mode from the T2K analysis by the 1σ uncertainties simultaneously. The $\pm 1\sigma$ variations in each of the flux parameters are listed in Table 6.9.

CCQE Uncertainties: The CCQE-related uncertainties described in Section 5.2.2 are replaced in favor of the equivalent uncertainties from the T2K analysis. The follow uncertainties from the SK analysis are *not* used: CCQE shape, CCQE normalizations (both Sub-GeV and Multi-GeV), CCQE neutirno ratios (both ν_e/ν_μ and $\bar{\nu}/\nu$). These are instead replaced by the T2K uncertainties on the RFG Fermi momentum, p_F, the BeRPA parameters, and uncertainties on the ν_e/ν_μ and $\bar{\nu}_e/\bar{\nu}_\mu$ ratios. In addition, the effect of a 1σ change in M_A^{QE} on CCQE MC events was re-computed using the T2K post-fit central value and uncertainty.

2p2h Uncertainties: The T2K analysis implements uncertainties on the normalization

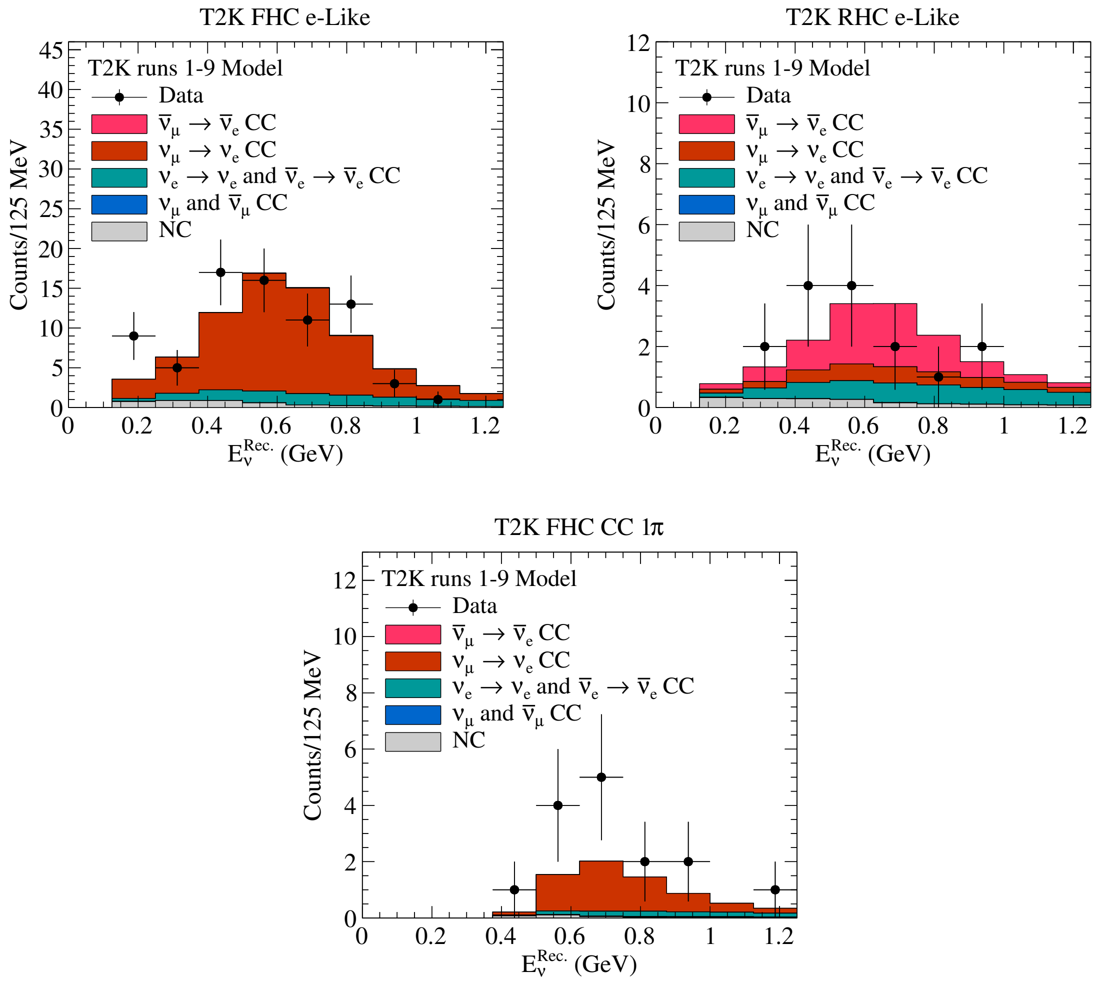

Figure 6·18: $E_\nu^{\text{Rec.}}$ distributions for the final T2K model e-like MC events, and corresponding T2K data counts. The MC includes the effect of oscillations, computed with the parameters listed in Table 6.3. The data are from [144] Figures 25 & 26. For the CC 1π sample, the definition of $E_\nu^{\text{Rec.}}$ uses the mass of the Δ baryon and no nucleon removal energy.

FHC Flux	Energy (GeV)	Value
ν_μ	[0.0 , 0.4]	1.01 ± 0.06
ν_μ	[0.4 , 0.5]	1.03 ± 0.05
ν_μ	[0.5 , 0.6]	1.02 ± 0.05
ν_μ	[0.6 , 0.7]	0.98 ± 0.04
ν_μ	[0.7 , 1.0]	0.93 ± 0.06
ν_μ	[1.0 , 1.5]	0.95 ± 0.05
ν_μ	[1.5 , 2.5]	1.02 ± 0.04
ν_μ	[2.5 , 3.5]	1.04 ± 0.05
ν_μ	[3.5 , 5.0]	1.03 ± 0.04
ν_μ	[5.0 , 7.0]	0.99 ± 0.04
ν_μ	[7.0 , ∞]	0.97 ± 0.05
$\bar{\nu}_\mu$	[0.0 , 0.7]	0.98 ± 0.08
$\bar{\nu}_\mu$	[0.7 , 1.0]	0.97 ± 0.05
$\bar{\nu}_\mu$	[1.0 , 1.5]	0.98 ± 0.06
$\bar{\nu}_\mu$	[1.5 , 2.5]	1.03 ± 0.06
$\bar{\nu}_\mu$	[2.5 , ∞]	1.10 ± 0.07
ν_e	[0.0 , 0.5]	1.02 ± 0.05
ν_e	[0.5 , 0.7]	1.02 ± 0.04
ν_e	[0.7 , 0.8]	1.02 ± 0.04
ν_e	[0.8 , 1.5]	1.01 ± 0.04
ν_e	[1.5 , 2.5]	1.03 ± 0.04
ν_e	[2.5 , 4.0]	1.03 ± 0.04
ν_e	[4.0 , ∞]	1.03 ± 0.06
$\bar{\nu}_e$	[0.0 , 2.5]	1.04 ± 0.06
$\bar{\nu}_e$	[2.5 , ∞]	1.08 ± 0.12

RHC Flux	Energy (GeV)	Value
$\bar{\nu}_\mu$	[0.0 , 0.4]	1.00 ± 0.07
$\bar{\nu}_\mu$	[0.4 , 0.5]	1.01 ± 0.05
$\bar{\nu}_\mu$	[0.5 , 0.6]	0.99 ± 0.05
$\bar{\nu}_\mu$	[0.6 , 0.7]	0.97 ± 0.04
$\bar{\nu}_\mu$	[0.7 , 1.0]	0.97 ± 0.05
$\bar{\nu}_\mu$	[1.0 , 1.5]	0.99 ± 0.05
$\bar{\nu}_\mu$	[1.5 , 2.5]	1.03 ± 0.04
$\bar{\nu}_\mu$	[2.5 , 3.5]	1.06 ± 0.05
$\bar{\nu}_\mu$	[3.5 , 5.0]	1.06 ± 0.07
$\bar{\nu}_\mu$	[5.0 , 7.0]	1.04 ± 0.06
$\bar{\nu}_\mu$	[7.0 , ∞]	1.00 ± 0.09
ν_μ	[0.0 , 0.7]	0.98 ± 0.07
ν_μ	[0.7 , 1.0]	0.99 ± 0.05
ν_μ	[1.0 , 1.5]	1.00 ± 0.05
ν_μ	[1.5 , 2.5]	1.05 ± 0.05
ν_μ	[2.5 , ∞]	1.04 ± 0.05
$\bar{\nu}_e$	[0.0 , 0.5]	1.01 ± 0.05
$\bar{\nu}_e$	[0.5 , 0.7]	1.00 ± 0.05
$\bar{\nu}_e$	[0.7 , 0.8]	1.00 ± 0.05
$\bar{\nu}_e$	[0.8 , 1.5]	1.01 ± 0.04
$\bar{\nu}_e$	[1.5 , 2.5]	1.04 ± 0.05
$\bar{\nu}_e$	[2.5 , 4.0]	1.04 ± 0.07
$\bar{\nu}_e$	[4.0 , ∞]	1.08 ± 0.13
ν_e	[0.0 , 2.5]	1.04 ± 0.05
ν_e	[2.5 , ∞]	1.04 ± 0.07

Table 6.9: List of T2K flux re-weighting and uncertainty parameters implemented in the T2K model. The values scale the flux normalization for each flavor in the given energy range. The values are from the "ND280 postfit" columns of Tables XIII-XIV in [144].

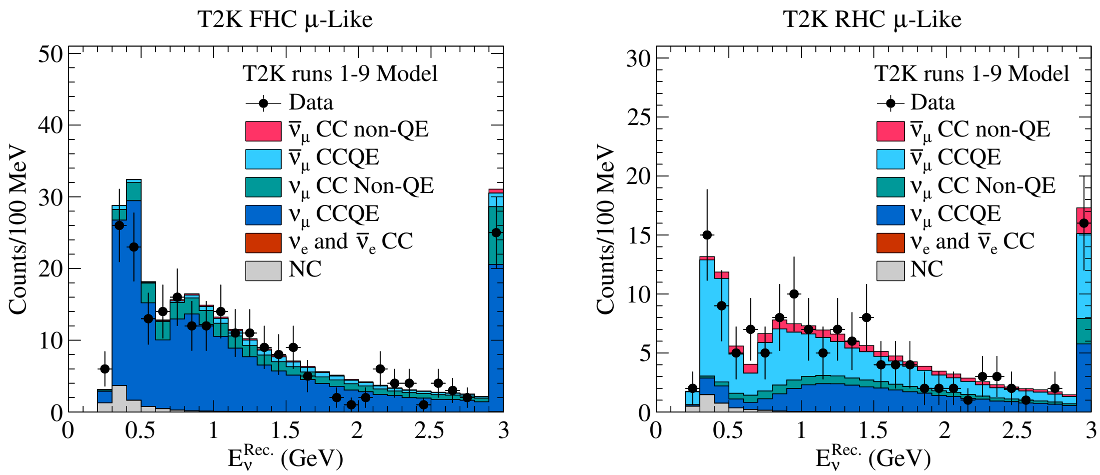

Figure 6·19: $E_\nu^{\text{Rec.}}$ distributions for the final T2K model μ-like MC events, and corresponding T2K data counts. The MC includes the effect of oscillations, computed with the parameters listed in Table 6.3. The data are from [144] Figure 27.

of neutrino and anti-neutrino 2p2h events, as well as a separate parameter on the Δ-baryon resonance component of 2p2h interactions. Since this final parameter is not implemented in the T2K model, the 100 % uncertainty on the normalization of 2p2h processes from the SK analysis is used instead, as a conservative estimate.

Single Pion Production Uncertainties: The effects of a 1σ change in M_A^{Res}, C_A^5, and the $I_{\frac{1}{2}}$ parameter on resonant single-pion MC events, and the normalizations of both CC and NC coherent pion MC events, were re-computed using the T2K post-fit central value and uncertainty.

The SK resonant pion uncertainty model includes separate uncertainties on the $\pi^{\pm}/\pi^0$ ratio and the $\bar{\nu}/\nu$ ratio from a comparison of single-pion production models. The T2K analysis does not include these uncertainties directly in the fit. Instead, the T2K analysis estimates the effect of using an alternative single-pion production model from [145] on fitted oscillation parameters directly with toy data studies. These the toy data studies involve simulations of both near and far detector data, and so are not reproducible using the T2K model. Due to this limitation, the original SK uncertainties are kept in the fit as a conservative estimate of the model differences.

FSI+SI Uncertainties: Both the T2K analysis and the SK analysis use the same models of FSI and SI processes implemented in NEUT, up to differences in the parameters, listed in Table 4.2 for the SK analysis. While it is possible to re-weight MC events to resolve the parameter differences, the FSI uncertainty treatment between SK and T2K is not compatible. For the T2K analysis, the FSI parameters are varied as part of the fit, while in the SK analysis, the largest effect due to variations of fixed parameter sets is used instead (see Section 5.2.2). In addition, the T2K fit treats the variations of the different FSI parameters as correlated, and the correlations are not published. As a result, the T2K model does not apply a re-weighting based on the FSI parameters, and the FSI uncertainties from the SK analysis are used as a conservative estimate.

NC Uncertainties: The T2K analysis places separate uncertainties on the normalization of NC processes, including an independent normalization uncertainty on NC processes producing a single photon, an important background to the ν_e appearance search. These uncertainties replace the NC/CC ratio uncertainty used by SK.

Table 6.10 lists the cross section parameter values and uncertainties implemented by the T2K model.

Reconstruction Uncertainties: The T2K analysis uses atmospheric neutrino events to estimate reconstruction performance. The estimation is performed similarly to the scale-and-shift procedure, described in Section 5.2.3. The T2K model implements reconstruction uncertainties on the e/μ discriminator distribution, the e/π^0 discriminator distribution, and the μ/π^+ discriminator distributions using the same scale-and-shift procedure from the atmospheric-only analysis. Additionally, the T2K

Parameter	Value
M_A^{QE} (GeV/c^2)	1.13 ± 0.08
p_F (MeV/c)	205 ± 15
BeRPA A	0.69 ± 0.06
BeRPA B	1.60 ± 0.12
BeRPA C	0.96 ± 0.13
BeRPA D	0.87 ± 0.35
BeRPA U	1.20 ± 0.10
C_A^5	0.98 ± 0.06
M_A^{Res} (GeV/c^2)	0.81 ± 0.04
$I_{\frac{1}{2}}$	1.31 ± 0.26
ν_e/ν_μ Ratio	1.00 ± 0.03
$\bar{\nu}_e/\bar{\nu}_\mu$ Ratio	1.00 ± 0.03
CC Coherent Norm.	0.87 ± 0.28
NC Coherent Norm.	0.94 ± 0.30
NC 1γ Norm.	1.00 ± 1.00
NC Other Norm.	1.00 ± 0.30

Table 6.10: Cross section parameter values used for re-weighting and calculating systematic uncertainties in the T2K model. The parameters are a subset of those listed in the "ND280 Postfit" columns of Table XXV from [144].

model performs the scale and shift procedure separately for events with zero, one, and two decay electrons, and in each of six fiducial volume regions, defined by combinations of `wall` and `towall`. The detector regions are visualized in Figure 30 of [144].

The energy scale uncertainty during the SK IV phase uses the same implementation as in the atmospheric analyses, described in Section 5.2.3. A 1σ change in the energy scale uncertainty for the SK IV phase simultaneously varies the reconstructed momentum values of SK IV atmospheric neutrino MC events and T2K model MC events in the combined fit.

The T2K analysis places an uncertainty on the NRE value used in the calculation of $E_\nu^{\text{Rec.}}$. However, this uncertainty is not part of the fit. Similarly to the alternative single pion production model uncertainty, T2K quantifies variations in NRE using a toy data study, which includes the propagation of its effects from the near detector data to the far detector data analysis. The result of the study showed that variations of the NRE value assumed could produce some bias in the fitted value of Δm^2_{32}. To account for the bias, the allowed range of Δm^2_{32} was smeared after the T2K oscillation fit. The smearing routine is not implemented within the T2K model, so the effects of NRE are neglected. The added uncertainty on Δm^2_{32} was reported as $0.041 \times 10^{-3}\,\text{eV}^2$.

ν_e Appearance Normalization Uncertainties: The T2K experiment's sensitivity to δ_{CP} and the neutrino mass ordering is driven by the total number of $\nu_\mu \to \nu_e$ and $\bar{\nu}_\mu \to \bar{\nu}_e$ events, i.e., largely independent of reconstructed neutrino energy and the other fitted oscillation parameters, $\sin^2\theta_{23}$ and Δm^2_{32}. An increase or decrease in the nominal MC prediction of these electron neutrino appearance events can bias the fit result to be more or less sensitive to δ_{CP}. Since the T2K model does not implement all features of the T2K analysis, differences in the nominal MC predictions are expected.

The difference in the total number of electron neutrino appearance events in the nominal MC predictions of T2K model and the T2K analysis was estimated by implementing two additional features from the T2K analysis. For this uncertainty estimation only, the ratios between the near detector-constrained and default NEUT values of the 2p2h normalization parameters and the FSI parameters were used to re-weight T2K model events. The differences in nominal MC prediction between the T2K model and T2K analysis after applying these weights is 5 % for the total number of $\nu_\mu \to \nu_e$ events, and 2 % for the total number of $\bar{\nu}_\mu \to \bar{\nu}_e$ events. These differences are taken as the 1σ effects of two additional systematic uncertainties which independently modify the normalization of electron and anti-electron neutrino appearance events in the T2K model MC.

6.3.5 T2K Model Performance & Limitations

The T2K model, fit to the binned 1D T2K Runs 1–9 data, and the T2K analysis, produce $\Delta\chi^2_{\mathrm{I.O.-N.O.}} \sim 3.6$. The T2K model finds a best fit in the normal ordering, with $\Delta m^2_{32} = 2.45 \times 10^{-3}\,\mathrm{eV}^2$, $\sin^2\theta_{23} = 0.55$, and $\delta_{\mathrm{CP}} = -1.74$. These are within the uncertainties of the fitted values from the T2K analysis, visualized as fractional differences from the T2K analysis values in Figure 6·20. Note that the smaller uncertainties on Δm^2_{32} measured by the T2K model do not include the additional post-fit uncertainty due to NRE added in the T2K analysis. Figure 6·21 shows the constraints on δ_{CP} in the two neutrino mass ordering scenarios from the T2K analysis, Figure 54 of [144], and the T2K model, fit using the SK method, cf. Equation 5.15.

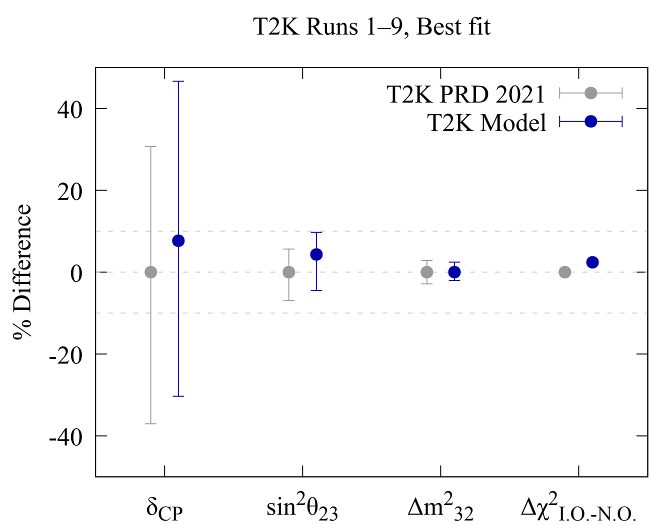

Figure 6·20: 1σ allowed oscillation parameter ranges from the T2K model and T2K analysis. The T2K PRD 2021 values are taken from the "NO" column of Table XV from [144].

While the T2K model successfully reproduces some aspects of the T2K analysis, it has three primary limitations:

1. Lack of near detector description

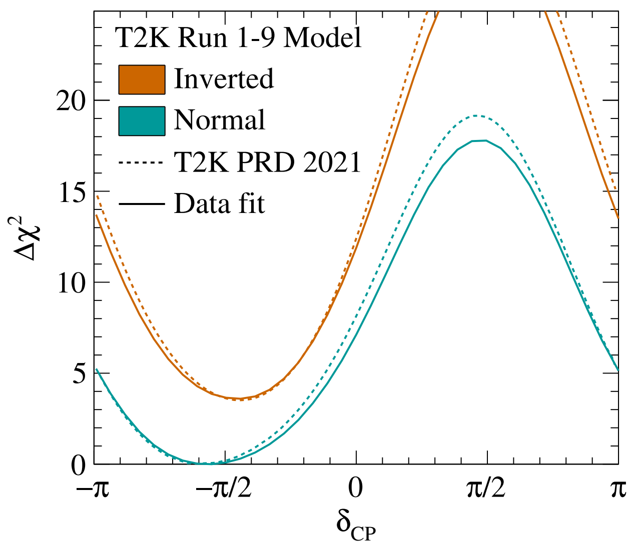

Figure 6·21: 1D $\Delta\chi^2$ profiles of δ_{CP} from the T2K model and T2K analysis. Both $\Delta\chi^2$ profiles are drawn with respect to the best-fit point in the normal ordering. The T2K PRD 2021 contours are taken from Figure 54 of [144].

2. Differences in uncertainty treatment

3. Reliance on re-weighting

Lack of near detector description: The near detector data set is integral to the T2K oscillation analysis, as it is jointly fit with the far detector samples to constrain the flux and cross section models. The T2K model does not describe the T2K near detector data. Without a near detector description, the T2K model is unable to reproduce the T2K toy data uncertainty studies, and cannot perform a simultaneous fit between the T2K near detector, T2K far detector, and SK atmospheric data samples. Such a simultaneous fit is desirable for a true joint analysis of all available data to assess the degree of agreement in cross section models between each data set. The T2K model assumes that the addition of SK atmospheric neutrino data would not significantly change the T2K near detector constraint. This assumption is based on the larger uncertainties in reconstructing the energies of atmospheric neutrino events, originating from the wider energy range of the atmospheric neutrino flux than for the T2K samples, and the unknown true neutrino direction. However, this assumption has not been quantified for the T2K model analysis.

Differences in uncertainty treatment: Although the T2K model implements similar uncertainties to those in the T2K analysis, the T2K analysis does not implement its uncertainties using the F_{ij} method of the SK analysis (see Section 5.3.2). In the SK method, all uncertainty sources are uncorrelated, and the response of the F_{ij}s is linear. In the T2K analysis, uncertainty sources are correlated, and several have non-linear responses in the fit. These differences create an interpretation issue when comparing results between the T2K model and the T2K analysis, i.e., even if the T2K model was able to perfectly reproduce the effect sizes of each systematic uncertainty, the differences in fit method could still produce different allowed regions of neutrino oscillation parameters.

Reliance on re-weighting: Re-weighting from a source distribution to a target distribution is only possible when the source distribution overlaps with the target distribution. In the case of re-weighting SK events to T2K events, the atmospheric neutrino flux overlaps the neutrino energy range of the T2K flux distribution, and the cross section models used by each collaboration have similar phase-spaces. However, as discussed in Section 6.3.3, the CCQE models do not have complete overlap, and so re-weighting will necessarily be inaccurate. Further, even if there is overlap between the source and target distributions, re-weighting events can lead to an undesirable dependence on MC statistics: If the original MC set has few events in a region where the target MC has many events, the weights may need to be large, amplifying any statistical fluctuations present in the original MC. This is visible in Figure 6·9: The re-weighted events have statistical MC uncertainties according to the Honda flux, despite being re-weighted on average to the T2K flux. The re-weighting issue is not severe for this version of the T2K model, but the method would not work in general to convert between other cross section and flux models.

The T2K and SK analyses also use different methods to draw allowed oscillation parameter ranges. This means that the $\Delta\chi^2$ contours are expected to differ, independent of the T2K model's ability to reproduce the T2K analysis' MC and systematic uncertainties. The T2K analysis uses the marginalization technique: The likelihood after fitting is integrated over all other parameters to draw the 1D projection. The SK analysis, on the other hand, uses the profiling technique: The likelihood is maximized over all other parameters, equivalent to taking the minimum $\Delta\chi^2$ value over all other parameters. As pointed out in [146], the marginalization and profiling procedures produce different contours when the fitted model has a non-linear dependence on the parameters, as is the case for neutrino oscillation analyses. Generally speaking, the profiling method, used to analyze results in this thesis, is more conservative.

Figure 6·21 shows the comparison of constraints on δ_{CP} from the T2K analysis, drawn with the marginalization technique, and the T2K model fit, drawn using the profiling technique used in the SK analysis. In the figure, the T2K model appears slightly conservative, indicated by the smaller values of $\Delta\chi^2$ for some values of δ_{CP}. Since the techniques used to draw the $\Delta\chi^2$ profiles differ, the conservative result of the T2K model fit compared to the T2K analysis cannot be entirely attributed to differences between the T2K analysis and the T2K model.

6.4 SK+T2K Model Results

In order to treat the cross section uncertainties as correlated between the T2K samples and the atmospheric neutrino samples in the analysis, all samples must use the same

Parameter	Min.	Max.	Steps
$\sin^2\theta_{23}$	0.3	0.725	35
Δm^2_{32} or Δm^2_{31} ($10^{-3}\,\mathrm{eV}^2$)	1.5	3.45	40
δ_{CP}	0	2π	37

Table 6.11: The oscillation point grid used for the SK+T2K model analysis with $\sin^2\theta_{13}$ constrained. Oscillation parameters are scanned in equally spaced steps, including the minimum and maximum points listed in the table. The grid is scanned twice, once for each mass ordering.

cross section models. Consequently, the cross section re-weighting aspects of the T2K model are also applied to the MC events used for the SK atmospheric neutrino samples, and the F_{ij}s are re-computed for the atmospheric neutrino bins using the nominal prediction after the cross section re-weighting.

The SK+T2K model analysis maintains the constraint on θ_{13}. The oscillation grid is also updated to increase the number of oscillation points scanned in a narrower range of Δm^2_{32} values, reflecting T2K's improved precision in this parameter. The oscillation parameter grid for the SK+T2K model analysis is listed in Table 6.11.

The 1D profiles of the fitted oscillation parameters are shown in Figure 6·22, and the allowed 1σ ranges for each of the parameters are listed in Table 6.12. Note that the χ^2 values are computed for 1020 bins, increased from 930 bins in the atmospheric analyses. The constraints on δ_{CP}, Δm^2_{32}, and $\sin^2\theta_{23}$ have all improved dramatically compared to the atmospheric-only analyses, reflecting both the excellent precision of the T2K experiment to measure these parameters, and the good complementarity of the SK data with the T2K data. The normal mass ordering preference is $\Delta\chi^2_{\mathrm{I.O.-N.O.}} = 8.54$, an increase of 2.85 compared to the atmospheric analysis with θ_{13} constrained. This increase is comparable to the T2K model's $\Delta\chi^2_{\mathrm{I.O.-N.O.}}$ value when fit alone, indicating very good agreement between the SK and T2K model preferences for the normal mass ordering. The T2K model prefers θ_{23} in the upper octant ($\sin^2\theta_{23} > 0.5$).

Ordering	$\Delta m^2_{32,31}$ $(10^{-3}\,\mathrm{eV}^2)$	$\sin^2\theta_{23}$	δ_{CP} $(-\pi,\pi)$	χ^2 1020 bins	χ^2 Syst.
Normal	$2.40^{+0.06}_{-0.02}$	$0.51^{+0.04}_{-0.04}$	$-1.75^{+0.41}_{-0.59}$	1111.41	56.07
Inverted	$2.40^{+0.02}_{-0.04}$	$0.53^{+0.03}_{-0.04}$	$-1.57^{+0.39}_{-0.43}$	1119.95	56.24

Table 6.12: Best-fit neutrino oscillation parameters in the combined SK+T2K model analysis with $\sin^2\theta_{13}$ constrained. The uncertainties on each oscillation parameter are the $\pm 1\sigma$ allowed regions assuming a χ^2 distribution with one degree of freedom.

This is in slight tension with the atmospheric results, but the T2K constraints are much stronger, bringing the SK+T2K model fitted value closer to the T2K model preferred value of $\sin^2\theta_{23}$.

6.5 Discussion

The SK atmospheric and T2K beam neutrino samples are largely in agreement: Both observe excess ν_e appearance, best explained by the normal ordering and values of δ_{CP} near $-\pi/2$. Like the atmospheric-only result, the T2K Runs 1–9 result from [144] also exceeds its sensitivity for preferring the normal mass ordering, $\Delta\chi^2_{\mathrm{I.O.-N.O.}} \approx 2$. This is consistent with T2K observing ν_e appearance in excess of the prediction from the best-case scenario, $\delta_{\mathrm{CP}} \sim -\pi/2$ with a further enhancement from matter effects in the normal ordering.

The $\Delta\chi^2_{\mathrm{I.O.-N.O.}}$ result indicates a strong preference for the normal mass ordering. Figure 6·23 shows the distribution of $\Delta\chi^2_{\mathrm{I.O.-N.O.}}$ values and corresponding p-values for the SK+T2K model fit, cf. Section 5.5. The data fit result is shown as a solid line at $\Delta\chi^2_{\mathrm{I.O.-N.O.}} = -8.54$, and corresponds to a p-value of $p = 5.5\times 10^{-3} \approx 2.54\,\sigma$ assuming the inverted ordering. In contrast, the p-value calculated from the measured $\Delta\chi^2_{\mathrm{I.O.-N.O.}}$ value assuming Wilks' Theorem is notably larger: $\sqrt{8.54} \approx 2.92\,\sigma$. The SK+T2K model CL_s value, following Equation 5.17, is $\mathrm{CL}_s = 0.021$. This value

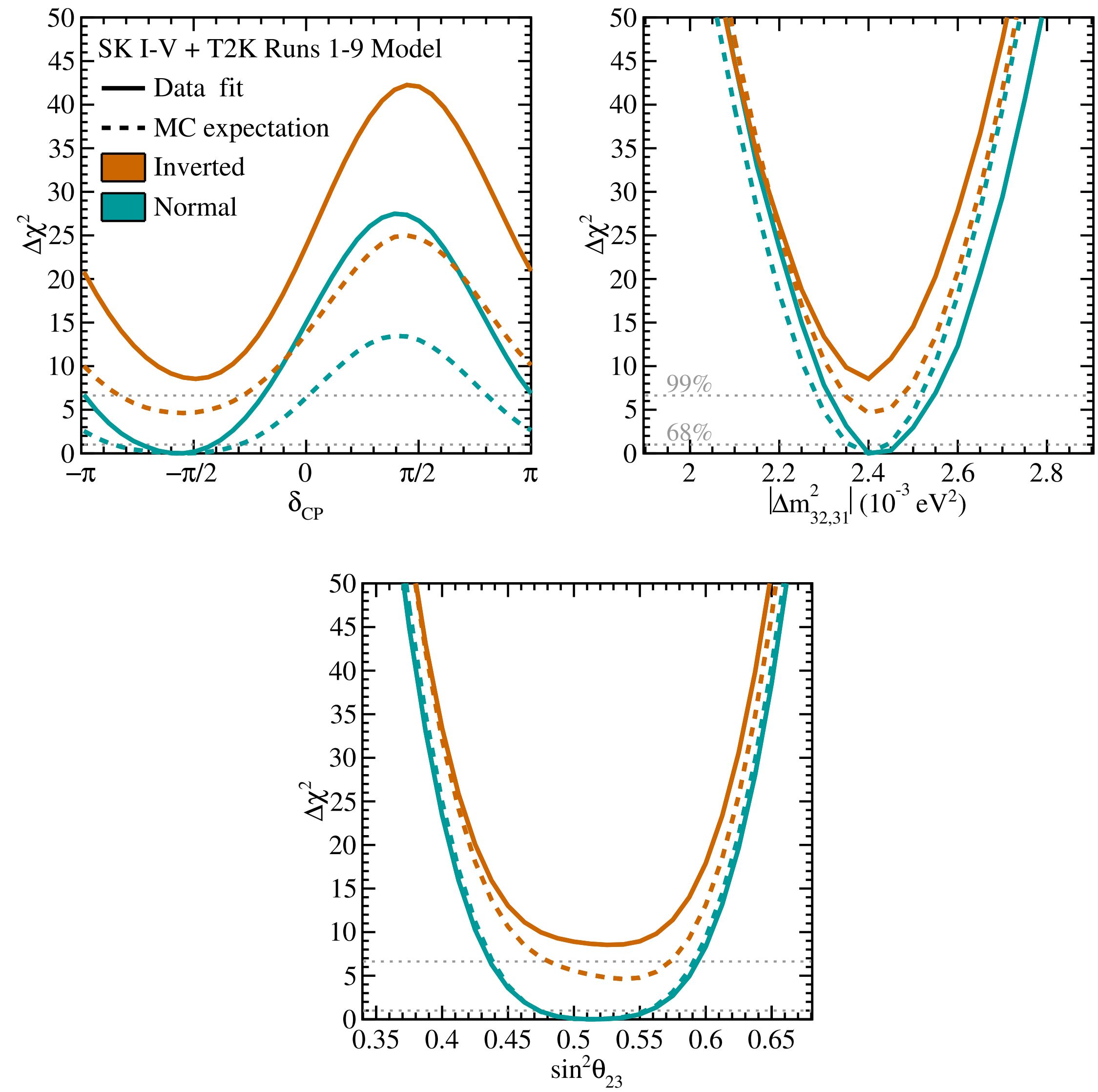

Figure 6·22: 1D $\Delta\chi^2$ profiles of the fitted oscillation parameters for the SK+T2K model analysis with $\sin^2\theta_{13}$ constrained. The $\Delta\chi^2$ values are taken with respect to the best-fit in the normal ordering, listed in Table 6.12. The meaning of the colors, solid and dashed curves, and dotted lines is the same as in Figure 5·14.

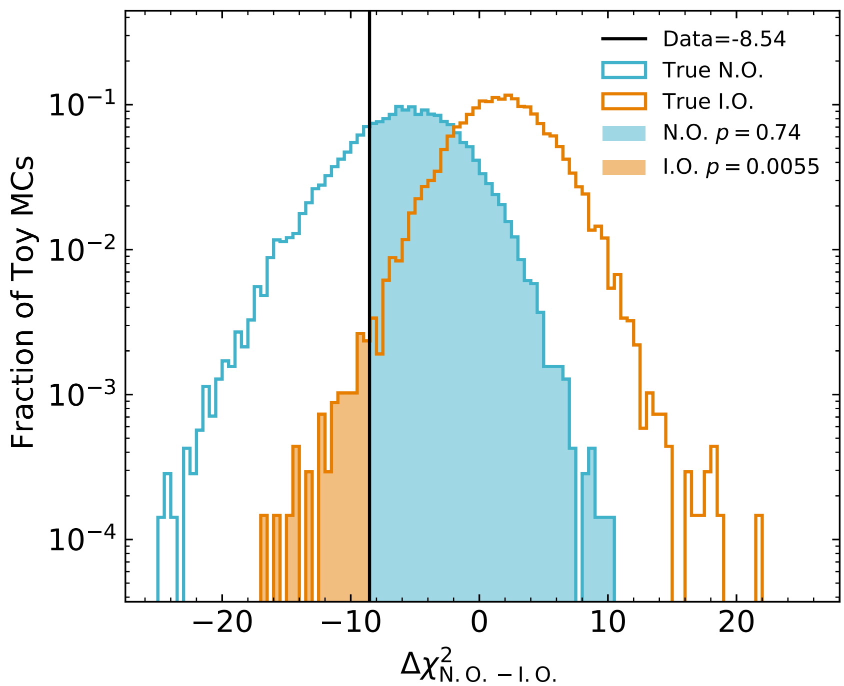

Figure 6·23: Distribution of $\Delta\chi^2_{\mathrm{I.O.}-\mathrm{N.O.}}$ from toy data sets and p-values in the SK+T2K model analysis with θ_{13} constrained. The meaning of the histograms is the same as in Figure 5·17.

corresponds to a rejection of the inverted mass ordering at $97.9\,\% \approx 2.03\,\sigma$.

The benefit of shared systematic uncertainty on the oscillation fit is shown in Figure 6·24. The figure compares the δ_{CP} $\Delta\chi^2$ profile from the SK+T2K model fit, i.e., the upper- left panel from Figure 6·22, with the sum of $\Delta\chi^2$ profiles from individual fits to the SK samples and the T2K samples. The combined analysis places stronger constraints on δ_{CP} than the sum, indicating an improvement due to the effect of shared systematic uncertainties.

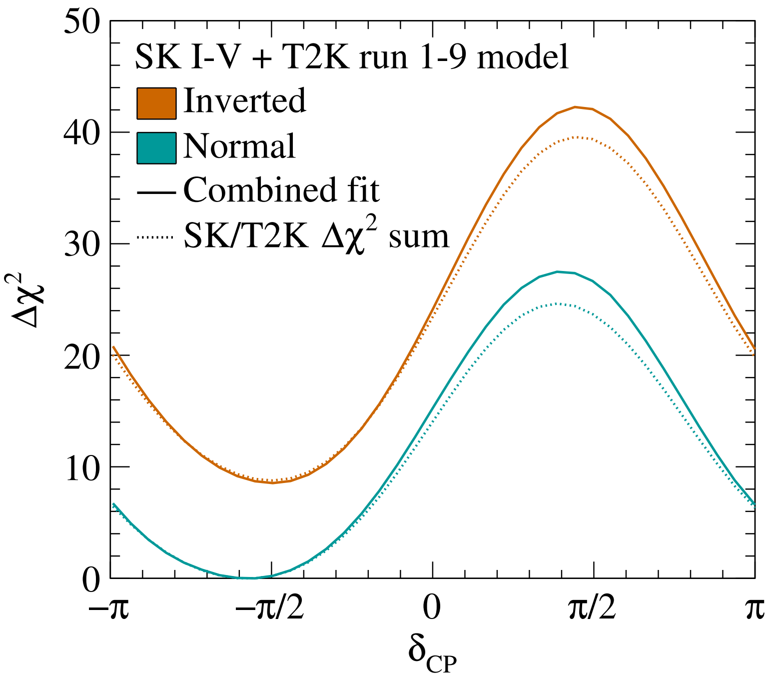

Figure 6·24: 1D $\Delta\chi^2$ profiles of δ_{CP} from the SK+T2K model analysis, fit as a combined data set and separately summed. The solid line is the same as in the upper-left panel of Figure 6·22.

Chapter 7

Conclusions

The neutrino mass ordering connects our understanding of fundamental neutrino properties to far-reaching areas of physics. Discerning the mass ordering would fix the neutrino's role in cosmology, further motivate searches for neutrino-less double beta decay experiments, and help us interpret the flux of neutrinos from supernova.

This thesis presented an analysis of the world's richest atmospheric neutrino data set for probing the mass ordering using neutrino oscillations. The Super-Kamiokande (SK) experiment's longevity, size, and detection technique make it uniquely well-suited to search for the mass ordering signature. At the same time, disentangling the signatures of the mass ordering from neutrino oscillations is complicated—the SK data tell the following story:

- We observe neutrino oscillations, well-described by the three-flavor PMNS paradigm, which are consistent with measurements from other sources of neutrinos.
- We observe an excess of upward-going electron neutrino-like events, with a few GeV of energy.
- We don't observe any excess of the equivalent anti-electron neutrino-like events.

The normal neutrino mass ordering scenario predicts this situation, while the inverted neutrino mass ordering does not. It appears the answer is at hand. Not so fast.

The neutrino mass ordering is unlike other measurements in physics: Instead of a mass or coupling, which could take a continuous range of possibilities, the mass ordering is a discrete choice between two options. When we ask our data to choose one or the other, unexpected results can happen. As this thesis showed, both the SK and T2K experiments exceed their sensitivity. These excesses should not necessarily be interpreted as stronger evidence for the normal ordering. Rather, the excesses result from unlikely scenarios which should instead motivate us to ask more questions.

At the same time, the analysis of atmospheric neutrino data with the T2K model demonstrated good agreement between the two data sets. This analysis observed maximum electron neutrino appearance in both the atmospheric samples and beam neutrino samples simultaneously, best explained by the combination of $\delta_{\mathrm{CP}} \approx -\pi/2$ and the normal mass ordering. This result is intriguing because it requires consensus between both naturally-produced atmospheric neutrinos and artificially-produced beam neutrinos which are subject to different systematic effects. It also showcases the benefits of performing the mass ordering analysis using atmospheric neutrino and beam neutrino data collected in a single detector. The planned Deep Underground Neutrino Experiment (DUNE) [147] and Hyper-Kamiokande experiments [148] will have the opportunity to perform single-detector combined atmospheric and beam neutrino analyses, and are recommended to do so!

While neither the atmospheric analysis nor the analysis including T2K constraints obtain a sufficient $5\,\sigma$ (or even $3\,\sigma$, depending on who you ask) statistical significance to claim a discovery of the mass ordering, the outlook for the neutrino mass ordering remains optimistic. If we are seeing hints of the normal mass ordering and values of $\delta_{\mathrm{CP}} \approx -\pi/2$, then nature has made our job easy: This scenario in particular predicts the largest electron neutrino appearance in neutrino oscillation experiments. Observing the electron anti-neutrino excesses expected in the inverted mass ordering would require much higher statistics, simply because anti-neutrinos interact less frequently. Similarly, other values of δ_{CP} lead to degeneracies in the predicted signal between the mass ordering and the other oscillation parameters.

The SK detector is currently operating with gadolinium in its water, which promises to increase its ability to detect neutrons. As this thesis demonstrated, SK does better at separating neutrinos and anti-neutrinos using neutrons. We expect further sensitivity improvements to the mass ordering beyond increased statistics in a future analysis using SK Gd data. There are also worldwide efforts to jointly analyze existing neutrino data now underway. While the T2K model analysis presented in this thesis is one such way of combining data sets, the SK, T2K, and NOvA collaborations are already sharing data and jointly developing analysis techniques. These joint analyses may bring us closer to a deeper understanding of neutrino oscillations and may even definitively reveal the neutrino mass ordering within the next decade.

Appendix A

Best-Fit Atmospheric Neutrino Samples

The following figures show the data and MC counts in the 930 atmospheric neutrino bins used in the analyses presented in this thesis. The data counts are identical for the atmospheric-only analysis, the atmospheric analysis with θ_{13} constrained, and the SK+T2K model analysis. The MC counts are shown with best-fit oscillation parameters and systematic uncertainty pulls (epsilons) from the atmospheric analysis with θ_{13} constrained, cf. Section 6.1. The MC counts are shown for both the normal ordering (blue line) and the inverted ordering (orange line). While the inverted ordering fit is drawn in every figure, it is only visible in bins where the MC prediction differs between the two orderings. Each figure also shows the 68 % variation of the MC prediction at the best-fit oscillation parameters from 1000 random throws of the systematic uncertainties, indicated by grey shaded regions.

Figures either show the zenith angle distribution in each momentum bin for each sample, or the momentum distribution for samples where there is only a single zenith angle bin. The Up-μ through-going samples only use a single momentum bin. The bin definitions are described in Section 5.1.4, and the momentum bin definitions are listed in Table 5.1.

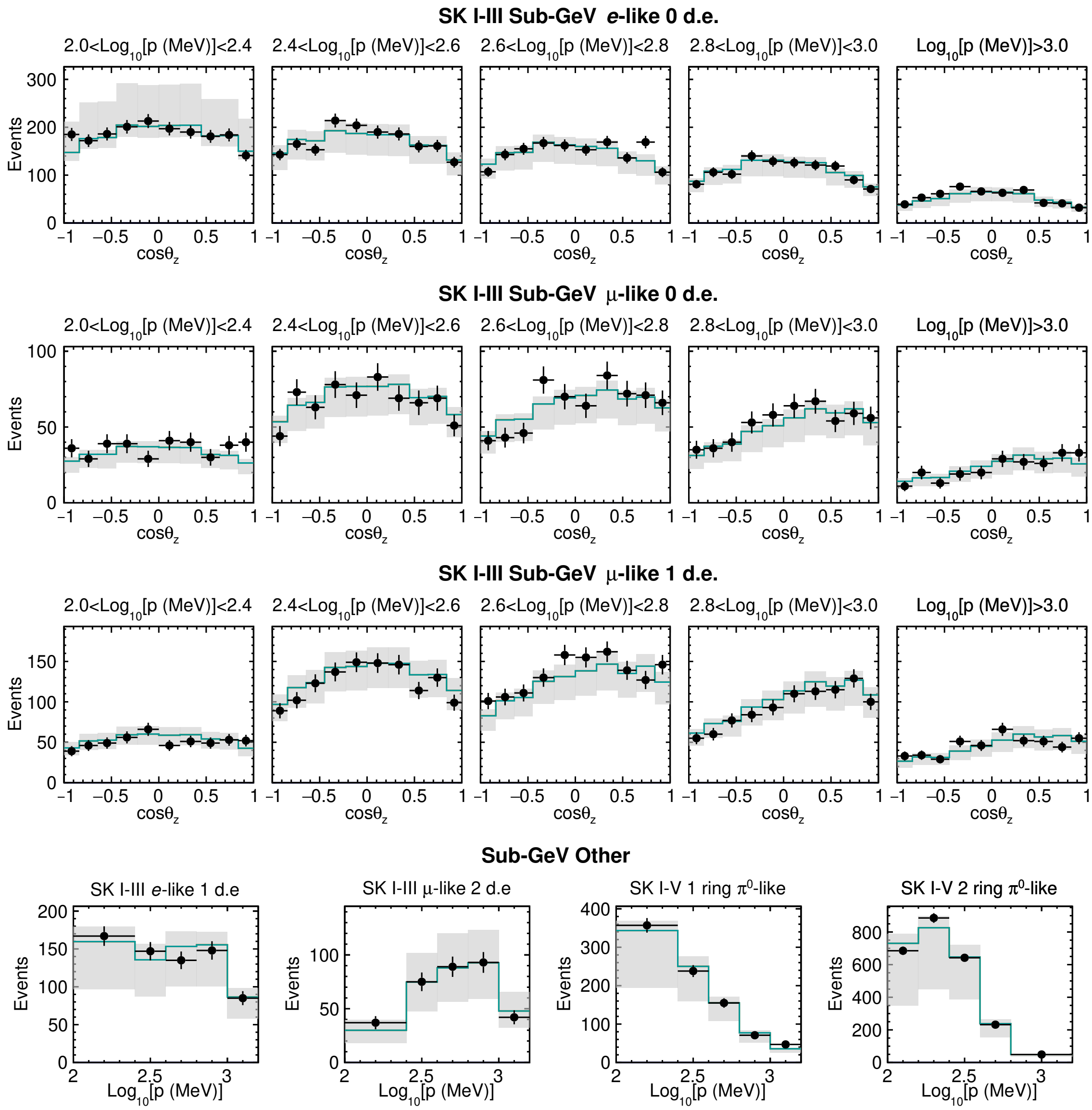

Figure A·1: SK I-III Sub-GeV single-ring samples, and Sub-GeV samples with only a single zenith angle bin.

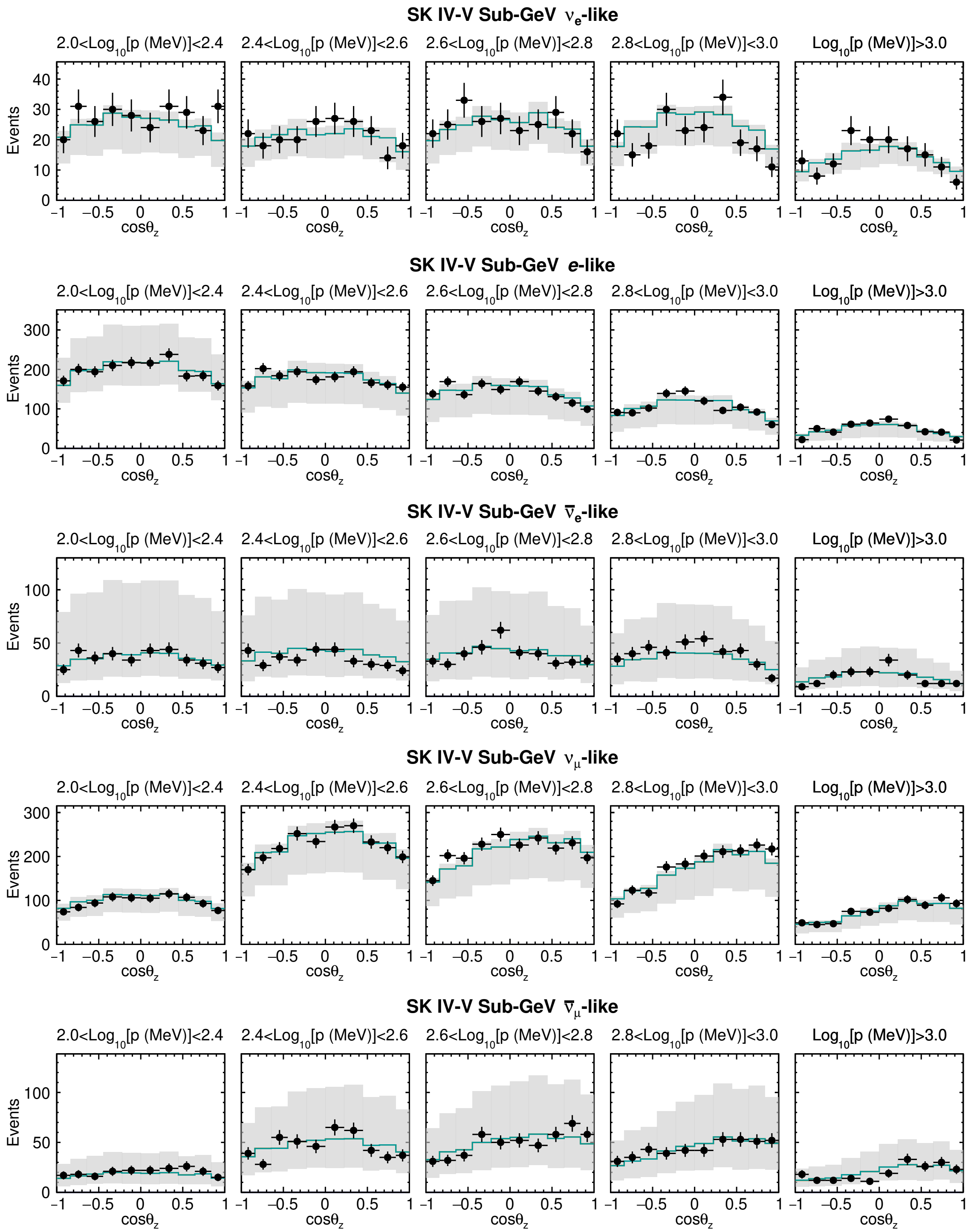

Figure A·2: SK IV-V Sub-GeV single-ring samples.

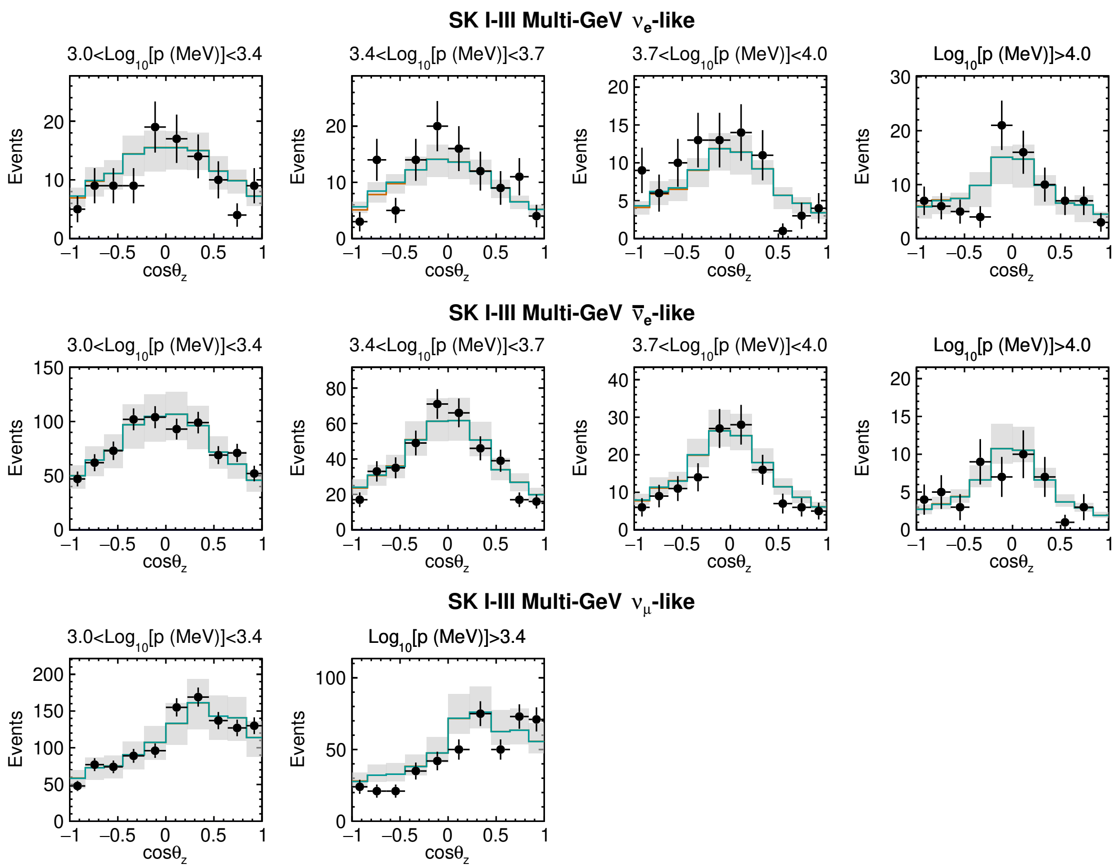

Figure A·3: SK I-III Multi-GeV single-ring samples.

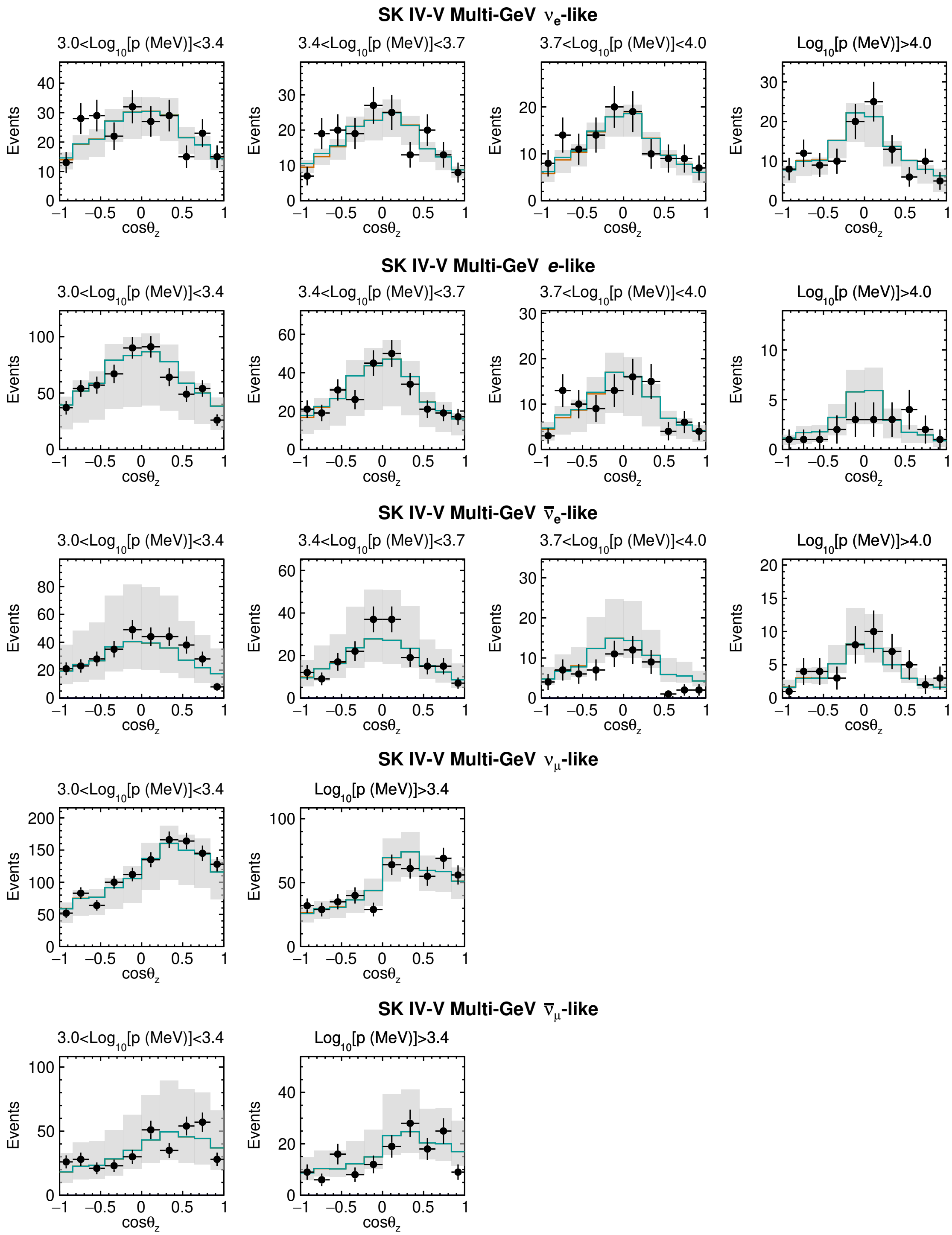

Figure A·4: SK IV-V Multi-GeV single-ring samples.

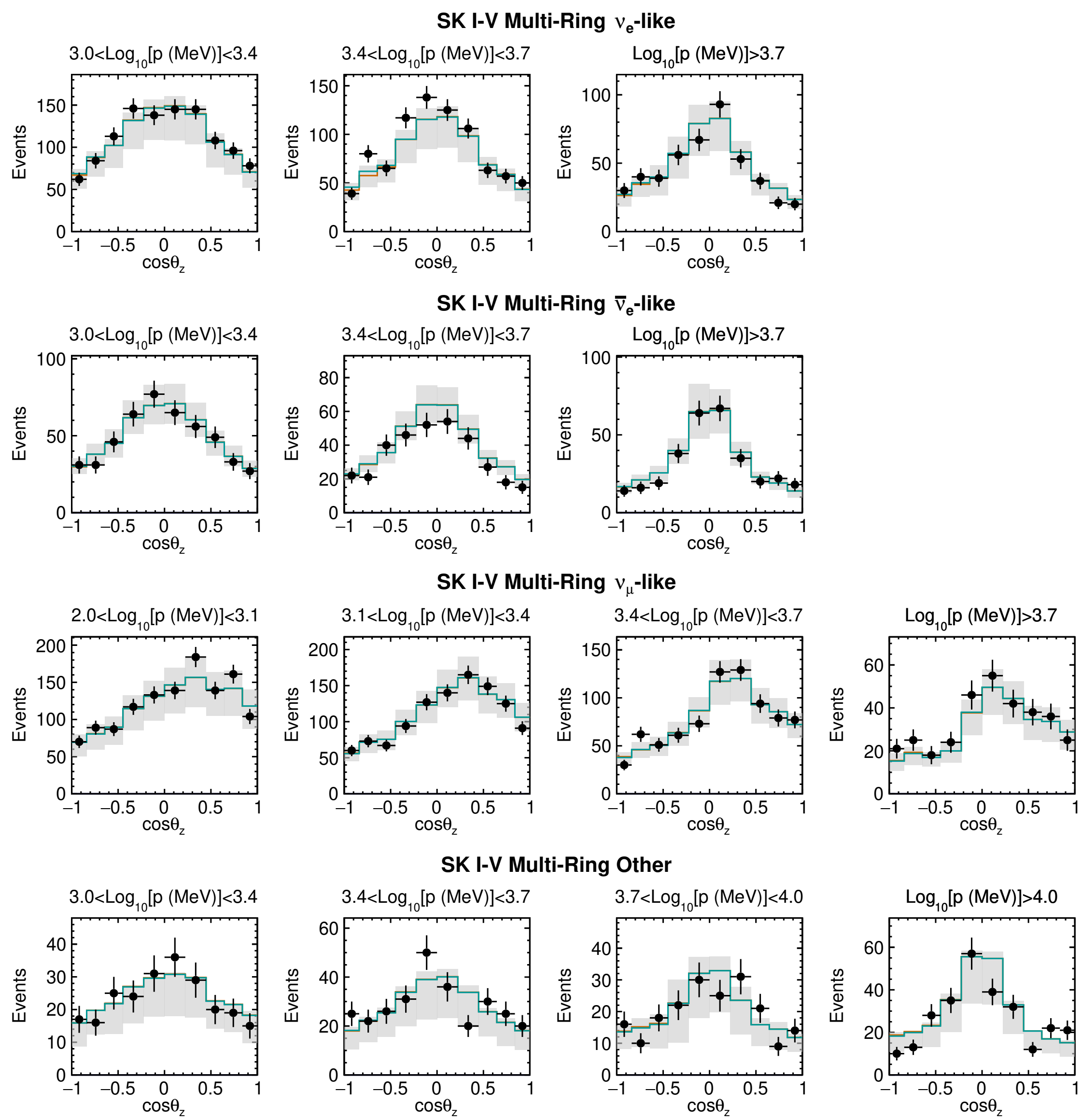

Figure A·5: SK I-V Multi-GeV multi-ring samples.

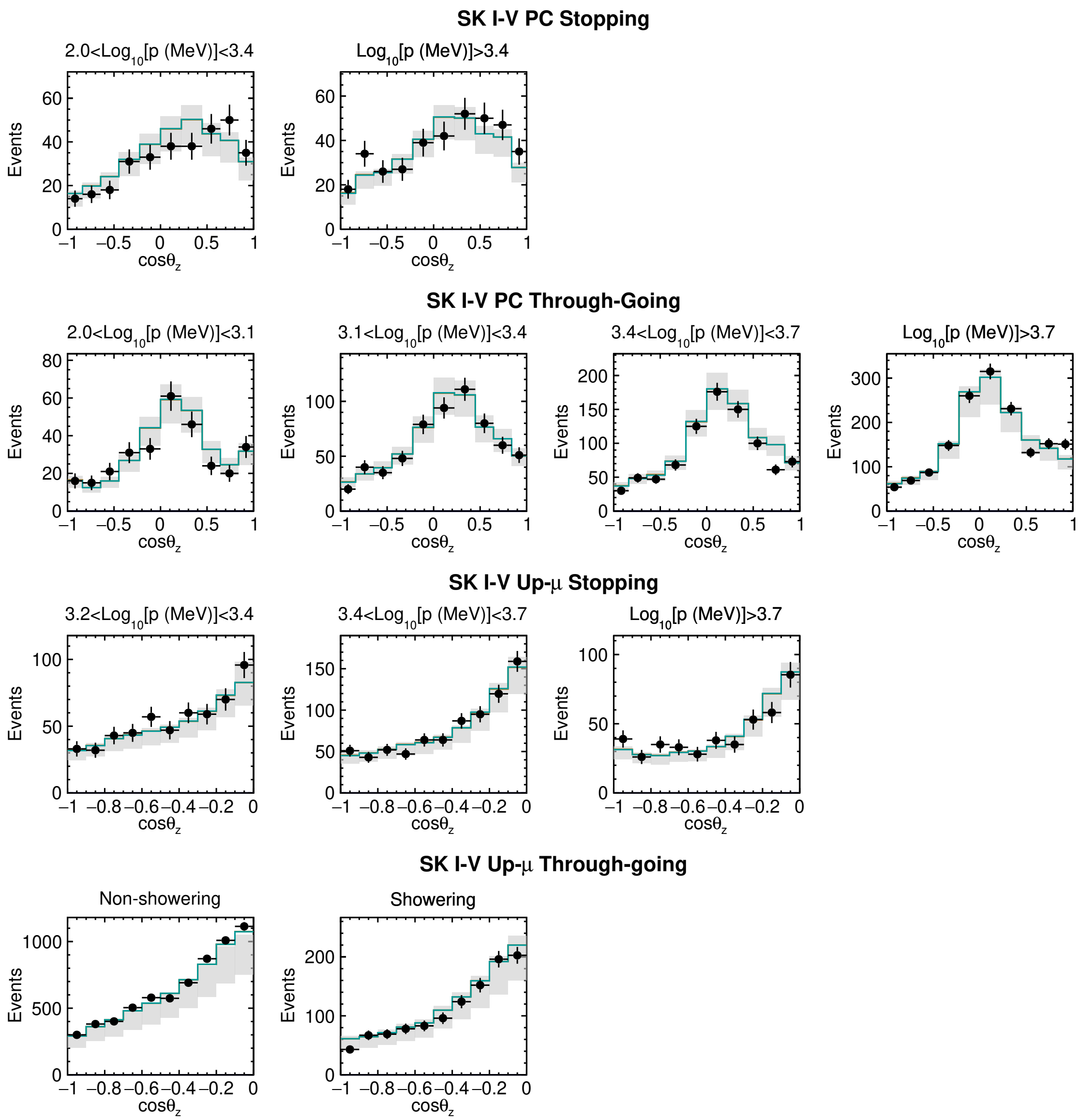

Figure A·6: SK I-V PC and Up-μ samples.

Appendix B

Best-Fit Systematic Uncertainties

This appendix provides listings of the fitted systematic error parameters (epsilons) at the best-fit oscillation points in the normal and inverted orderings for the analyses presented in this thesis, cf. Section 5.4, Section 6.1.1, and Section 6.4. Table B.1 lists the flux, cross section, and oscillation systematic uncertainties which are, with the exception of the solar activity uncertainty, common to all SK phases. Table B.2, Table B.3, and Table B.4 list the detector-related systematic uncertainties which are fit independently for each SK phase. Dashes indicate that a systematic uncertainty source is not used in a fit. In particular, the θ_{13} uncertainty is not used in the atmospheric neutrino fit with no external constraints, and several cross section uncertainties used in the SK atmospheric neutrino fits are replaced with alternative uncertainties in the fit with the T2K model. The SK IV absolute energy scale uncertainty simultaneously varies the atmospheric neutrino and T2K samples in the SK+T2K model fit.

Systematic Uncertainty	Fit Value(σ) SK Only Normal	SK Only Inverted	SK+θ_{13} Normal	SK+θ_{13} Inverted	SK+T2K Model Normal	SK+T2K Model Inverted
Atmospheric ν Flux						
Normalization						
$E_\nu < 1\,\mathrm{GeV}$	0.20	0.23	0.20	0.20	0.70	0.72
$E_\nu > 1\,\mathrm{GeV}$	1.32	1.33	1.32	1.31	1.50	1.51
$(\nu_\mu + \bar{\nu}_\mu)/(\nu_e + \bar{\nu}_e)$ ratio						
$E_\nu < 1\,\mathrm{GeV}$	0.46	0.44	0.44	0.44	0.27	0.16
$1\,\mathrm{GeV} < E_\nu < 10\,\mathrm{GeV}$	−0.27	−0.20	−0.28	−0.34	−0.05	−0.04
$E_\nu > 10\,\mathrm{GeV}$	0.82	0.80	0.82	0.83	0.61	0.61
$\nu_\mu/\bar{\nu}_\mu$ ratio						
$E_\nu < 1\,\mathrm{GeV}$	0.09	0.08	0.09	0.09	0.10	0.07
$E_\nu > 10\,\mathrm{GeV}$	−0.10	−0.11	−0.10	−0.12	−0.11	−0.11
$1\,\mathrm{GeV} < E_\nu < 10\,\mathrm{GeV}$	1.33	1.35	1.32	1.30	1.30	1.30
$\nu_e/\bar{\nu}_e$ ratio						
$E_\nu < 1\,\mathrm{GeV}$	0.22	0.26	0.24	0.22	0.54	0.64
$E_\nu > 10\,\mathrm{GeV}$	−0.38	−0.38	−0.38	−0.39	−0.30	−0.30
$1\,\mathrm{GeV} < E_\nu < 10\,\mathrm{GeV}$	−0.09	−0.12	−0.08	−0.02	−0.10	−0.09
K/π ratio	−1.08	−1.05	−1.09	−1.09	−0.99	−1.00
Up/Down Ratio	0.34	0.43	0.34	0.41	0.32	0.31
Horizontal/Vertical Ratio	−0.11	−0.12	−0.11	−0.19	0.05	0.06
Relative Normalization						
FC Multi-GeV	−1.33	−1.32	−1.33	−1.29	−1.64	−1.64
PC+UPMU Stopping	0.31	0.35	0.31	0.29	0.54	0.54
Solar Activity						
SK I	−0.33	−0.33	−0.33	−0.33	−0.27	−0.27
SK II	0.19	0.18	0.19	0.18	0.14	0.14
SK III	−0.23	−0.23	−0.23	−0.23	−0.24	−0.24
SK IV	0.13	0.14	0.14	0.14	0.12	0.12
SK V	−0.10	−0.10	−0.10	−0.10	−0.08	−0.07
Neutrino path length	−0.51	−0.44	−0.53	−0.42	−0.77	−0.81
CCQE						
M_A^{QE}	−0.44	−0.42	−0.45	−0.45	−0.82	−0.86
p_F	—	—	—	—	0.59	0.58
Shape	2.05	2.06	2.06	2.05	—	—
Norm., Sub-GeV	0.86	0.83	0.83	0.83	—	—
Norm., Multi-GeV	0.66	0.66	0.66	0.65	—	—
$\nu/\bar{\nu}$ Ratio	0.85	0.82	0.84	0.85	—	—

Continued on next page

Table B.1 – Continued from previous page

Systematic Uncertainty	Fit Value(σ)					
	SK Only		SK+θ_{13}		SK+T2K Model	
	Normal	Inverted	Normal	Inverted	Normal	Inverted
ν_μ/ν_e Ratio	0.74	0.77	0.74	0.73	0.41	0.40
2p2h Norm.	−0.38	−0.40	−0.38	−0.36	−0.97	−0.96
BeRPA A	—	—	—	—	0.44	0.43
BeRPA B	—	—	—	—	0.55	0.53
BeRPA D	—	—	—	—	0.62	0.61
BeRPA E	—	—	—	—	−0.02	−0.02
BeRPA U	—	—	—	—	−0.04	−0.03
Single Pion Production						
$\pi^0/\pi^\pm$ Ratio	−0.83	−0.84	−0.84	−0.84	−0.09	−0.09
$\bar{\nu}/\nu$ Ratio	0.13	0.17	0.14	0.13	0.69	0.70
$M_A^{\mathrm{Res.}}$	−1.55	−1.53	−1.55	−1.55	1.10	1.09
C_A^5	0.76	0.76	0.76	0.74	2.68	2.68
$I_{\frac{1}{2}}$	−0.91	−0.93	−0.91	−0.95	−0.94	−0.95
CC Coherent Norm.	−0.20	−0.21	−0.19	−0.20	−0.23	−0.23
NC Coherent Norm.	—	—	—	—	0.63	0.64
NC $\pi^\pm$ Contamination	0.16	0.14	0.16	0.15	0.06	0.01
DIS						
PDF Difference	1.13	1.13	1.14	1.17	0.82	0.83
World Average Difference	0.41	0.42	0.41	0.42	0.50	0.49
q^2, $W > 2\,\mathrm{GeV}$	−0.30	−0.29	−0.30	−0.28	−0.38	−0.39
q^2 (vec.), $W < 2\,\mathrm{GeV}$	0.75	0.74	0.75	0.73	1.02	1.02
q^2 (axi.), $W < 2\,\mathrm{GeV}$	−1.09	−1.11	−1.09	−1.08	−1.12	−1.11
q^2 Norm., $W < 2\,\mathrm{GeV}$	−0.41	−0.41	−0.41	−0.40	−0.55	−0.55
Hadron Multiplicity	0.36	0.37	0.36	0.35	0.23	0.24
Neutrons						
Multiplicity, Transverse p	−0.31	−0.31	−0.31	−0.31	−0.23	−0.23
Generator Comparison	0.40	0.40	0.40	0.40	0.45	0.45
Neutron Tagging	−0.22	−0.22	−0.22	−0.24	−0.42	−0.42
FSI						
FSI Max. Set	−0.06	−0.06	−0.06	−0.06	−0.10	−0.10
FSI Min. Set	−0.01	0.00	−0.01	−0.01	0.14	0.14
Other Xsec.						
NC/CC Ratio	1.83	1.81	1.83	1.85	—	—
NC 1γ Norm.	—	—	—	—	0.03	0.03
NC Other Norm.	—	—	—	—	1.25	1.23
CC ν_τ Cross Section	−0.07	0.03	−0.09	0.15	−0.18	−0.21

Continued on next page

Table B.1 – Continued from previous page

Systematic Uncertainty	Fit Value(σ)					
	SK Only		SK+θ_{13}		SK+T2K Model	
	Normal	Inverted	Normal	Inverted	Normal	Inverted
Oscillation						
Δm^2_{21}	−0.01	−0.01	−0.01	−0.01	0.01	0.01
$\sin^2\theta_{12}$	0.02	0.01	0.02	0.01	0.03	0.03
Matter effect	0.18	0.19	0.18	0.08	0.26	0.27
$\sin^2\theta_{13}$	—	—	0.01	0.03	0.25	0.22
T2K						
Post-ND280 Flux	—	—	—	—	−0.30	−0.33
ν_e Appearance Norm.	—	—	—	—	0.45	0.41
$\bar{\nu}_e$ Appearance Norm.	—	—	—	—	0.00	−0.01

Table B.1: Flux-, cross section-, and oscillation-related fitted systematic uncertainty parameters (epsilons) at the best-fit point for each of the three analyses presented in this thesis.

Systematic Uncertainty	Fit Value (σ) Normal					Inverted				
	I	II	III	IV	V	I	II	III	IV	V
Fiducial Volume	−0.45	−0.13	0.62	−0.42	−0.28	−0.46	−0.13	0.62	−0.43	−0.28
FC Reduction	−0.05	0.01	0.25	0.70	0.20	−0.05	0.01	0.25	0.71	0.20
PC Reduction	0.05	−0.53	0.00	−0.75	−0.25	0.05	−0.54	0.00	−0.76	−0.26
Up-μ Reduction	0.00	−0.11	0.23	0.12	0.01	0.00	−0.11	0.23	0.12	0.01
FC/PC Separation	−0.22	0.05	−0.10	0.02	0.00	−0.22	0.05	−0.10	0.02	0.00
PC Stop/Through Separation										
Top	0.39	−0.26	−0.28	−0.62	−0.28	0.39	−0.26	−0.27	−0.62	−0.27
Barrel	0.54	−0.35	−0.36	0.73	−0.60	0.54	−0.35	−0.35	0.74	−0.59
Bottom	−0.58	0.01	−0.03	−0.32	−0.44	−0.58	0.01	−0.03	−0.31	−0.44
Ring Counting	0.54	0.42	0.22	−0.40	−0.23	0.55	0.42	0.22	−0.40	−0.23
Single-Ring PID	−0.13	0.45	−0.74	1.02	0.15	−0.13	0.45	−0.74	1.03	0.15
Multi-Ring PID	−0.21	0.60	−0.21	−0.93	0.20	−0.21	0.60	−0.21	−0.93	0.20
Non-ν Background										
e-like	0.00	0.05	0.22	−0.03	−0.15	0.00	0.05	0.22	−0.03	−0.15
μ-like	0.53	0.32	0.19	−0.07	0.41	0.52	0.30	0.17	−0.11	0.39
Non-ν_e Background										
Single-Ring	0.10	−0.56	0.01	0.14	−0.04	0.10	−0.56	0.01	0.13	−0.04
Multi-Ring	0.24	0.21	−0.32	−0.23	0.03	0.24	0.20	−0.33	−0.23	0.02
Two-Ring π^0	−0.39	−0.02	0.00	0.57	−0.04	−0.39	−0.02	0.00	0.57	−0.04
Energy Scale										
Absolute	−0.12	−0.38	−0.05	−0.30	0.21	−0.12	−0.37	−0.04	−0.29	0.21
Up/Down	0.03	0.08	0.58	0.08	−0.27	0.06	0.10	0.59	0.12	−0.26
Decay-e Tagging	−0.63	−0.22	0.00	0.19	0.87	−0.64	−0.22	0.00	0.21	0.89
Multi-Ring BDT										
Efficiency	−0.18	1.25	−0.09	0.06	0.29	−0.18	1.24	−0.09	0.05	0.28
Migration	−0.10	0.16	0.10	0.39	0.08	−0.10	0.16	0.10	0.39	0.08
Up-μ										
Path Cut	−0.01	0.42	−0.34	−0.60	−0.37	−0.01	0.42	−0.34	−0.59	−0.37
Momentum Cut	0.01	0.04	0.48	−0.01	−0.10	0.00	0.04	0.49	0.00	−0.10
Separation										
Stop/Through	0.00	0.02	0.08	−0.09	−0.12	0.00	0.03	0.08	−0.09	−0.11
Non-showering Showering	1.65	−0.52	1.05	0.98	0.35	1.66	−0.52	1.05	0.98	0.36
Background Subtraction										
Stopping	0.75	−0.63	−0.26	−0.56	−0.39	0.74	−0.63	−0.27	−0.56	−0.39
Non-showering	−0.22	−0.24	0.05	0.18	−0.07	−0.22	−0.24	0.04	0.18	−0.08
Showering	−0.26	−1.87	0.16	−0.16	0.05	−0.26	−1.87	0.16	−0.16	0.05

Table B.2: Detector-related fitted systematic uncertainty parameters (epsilons) at the best-fit point for the atmospheric-only analysis.

Systematic Uncertainty	Fit Value (σ) Normal					Inverted				
	I	II	III	IV	V	I	II	III	IV	V
Fiducial Volume	−0.45	−0.13	0.62	−0.42	−0.28	−0.45	−0.13	0.62	−0.42	−0.28
FC Reduction	−0.05	0.01	0.25	0.70	0.20	−0.05	0.01	0.25	0.71	0.20
PC Reduction	0.06	−0.53	0.00	−0.75	−0.25	0.05	−0.54	0.00	−0.76	−0.26
Up-μ Reduction	−0.01	−0.11	0.23	0.12	0.01	0.00	−0.11	0.23	0.12	0.01
FC/PC Separation	−0.22	0.05	−0.10	0.02	0.00	−0.23	0.05	−0.10	0.02	0.00
PC Stop/Through Separation										
Top	0.39	−0.26	−0.27	−0.62	−0.28	0.37	−0.26	−0.29	−0.66	−0.29
Barrel	0.54	−0.35	−0.36	0.73	−0.60	0.54	−0.36	−0.36	0.73	−0.60
Bottom	−0.58	0.01	−0.03	−0.32	−0.44	−0.59	0.00	−0.03	−0.32	−0.44
Ring Counting	0.54	0.42	0.22	−0.40	−0.23	0.54	0.42	0.21	−0.41	−0.22
Single-Ring PID	−0.13	0.45	−0.74	1.01	0.15	−0.15	0.43	−0.73	1.00	0.15
Multi-Ring PID	−0.21	0.60	−0.21	−0.93	0.20	−0.19	0.62	−0.20	−0.87	0.20
Non-ν Background										
e-like	0.00	0.05	0.22	−0.03	−0.15	0.00	0.06	0.22	−0.02	−0.15
μ-like	0.53	0.32	0.19	−0.07	0.41	0.54	0.32	0.19	−0.07	0.41
Non-ν_e Background										
Single-Ring	0.10	−0.56	0.01	0.13	−0.04	0.11	−0.55	0.01	0.13	−0.04
Multi-Ring	0.24	0.21	−0.32	−0.22	0.03	0.24	0.20	−0.33	−0.24	0.03
Two-Ring π^0	−0.39	−0.02	0.00	0.57	−0.04	−0.39	−0.02	0.00	0.57	−0.04
Energy Scale										
Absolute	−0.12	−0.38	−0.05	−0.30	0.21	−0.11	−0.37	−0.04	−0.29	0.22
Up/Down	0.03	0.08	0.58	0.08	−0.27	0.04	0.09	0.59	0.09	−0.27
Decay-e Tagging	−0.64	−0.22	0.00	0.20	0.88	−0.63	−0.22	0.01	0.22	0.89
Multi-Ring BDT										
Efficiency	−0.18	1.25	−0.08	0.06	0.29	−0.18	1.23	−0.09	0.04	0.27
Migration	−0.10	0.16	0.10	0.39	0.08	−0.10	0.16	0.10	0.41	0.08
Up-μ										
Path Cut	−0.01	0.42	−0.34	−0.60	−0.37	−0.01	0.42	−0.35	−0.60	−0.37
Momentum Cut	0.01	0.04	0.48	−0.01	−0.10	0.01	0.04	0.48	−0.01	−0.10
Separation										
Stop/Through	0.00	0.02	0.08	−0.09	−0.12	−0.01	0.02	0.08	−0.09	−0.12
Non-showering Showering	1.65	−0.52	1.05	0.97	0.35	1.66	−0.52	1.06	0.99	0.36
Background Subtraction										
Stopping	0.75	−0.63	−0.26	−0.56	−0.39	0.76	−0.62	−0.25	−0.55	−0.38
Non-showering	−0.22	−0.24	0.05	0.18	−0.07	−0.22	−0.24	0.05	0.18	−0.08
Showering	−0.26	−1.87	0.16	−0.16	0.05	−0.26	−1.87	0.16	−0.16	0.05

Table B.3: Detector-related fitted systematic uncertainty parameters (epsilons) at the best-fit point for the SK analysis with θ_{13} constrained.

Systematic Uncertainty	Fit Value (σ) Normal I	II	III	IV	V	Inverted I	II	III	IV	V
Fiducial Volume	−0.42	−0.08	0.64	−0.34	−0.25	−0.42	−0.08	0.64	−0.33	−0.25
FC Reduction	−0.04	0.02	0.27	0.80	0.22	−0.04	0.02	0.27	0.80	0.22
PC Reduction	0.03	−0.57	−0.01	−0.79	−0.26	0.03	−0.56	−0.01	−0.78	−0.26
Up-μ Reduction	0.01	−0.11	0.23	0.13	0.01	0.01	−0.11	0.23	0.13	0.01
FC/PC Separation	−0.18	0.07	−0.09	0.02	0.00	−0.18	0.07	−0.09	0.02	0.00
PC Stop/Through Separation										
Top	0.41	−0.23	−0.23	−0.57	−0.24	0.41	−0.23	−0.23	−0.56	−0.24
Barrel	0.58	−0.31	−0.34	0.79	−0.56	0.59	−0.31	−0.34	0.79	−0.56
Bottom	−0.55	0.01	−0.02	−0.27	−0.42	−0.55	0.01	−0.02	−0.27	−0.42
Ring Counting	0.69	0.38	0.23	−0.29	−0.17	0.71	0.38	0.23	−0.29	−0.17
Single-Ring PID	−0.09	0.51	−0.80	1.05	0.09	−0.09	0.51	−0.81	1.03	0.09
Multi-Ring PID	−0.21	0.59	−0.21	−0.99	0.10	−0.21	0.59	−0.21	−0.99	0.10
Non-ν Background										
e-like	−0.01	0.06	0.24	−0.03	−0.08	−0.01	0.06	0.24	−0.03	−0.08
μ-like	0.50	0.28	0.13	−0.13	0.37	0.50	0.28	0.13	−0.13	0.37
Non-ν_e Background										
Single-Ring	0.13	−0.55	0.01	0.24	−0.03	0.13	−0.55	0.01	0.23	−0.03
Multi-Ring	0.22	0.25	−0.35	−0.20	0.01	0.23	0.25	−0.34	−0.19	0.02
Two-Ring π^0	−0.19	0.09	0.05	0.89	0.04	−0.19	0.09	0.05	0.89	0.04
Energy Scale										
Absolute	−0.15	−0.38	−0.06	−0.40	0.20	−0.15	−0.37	−0.06	−0.40	0.20
Up/Down	0.02	0.06	0.57	−0.04	−0.25	0.03	0.06	0.57	−0.03	−0.25
Decay-e Tagging	−0.66	−0.17	0.05	0.24	0.94	−0.66	−0.17	0.04	0.25	0.95
Multi-Ring BDT										
Efficiency	−0.30	1.10	−0.19	−0.03	0.24	−0.30	1.11	−0.19	−0.03	0.24
Migration	−0.10	0.14	0.10	0.41	0.08	−0.10	0.14	0.10	0.40	0.08
Up-μ										
Path Cut	0.00	0.42	−0.33	−0.57	−0.35	0.00	0.42	−0.33	−0.57	−0.35
Momentum Cut	−0.01	0.02	0.49	0.06	−0.09	−0.01	0.02	0.49	0.06	−0.08
Separation										
Stop/Through	0.01	0.03	0.08	−0.06	−0.10	0.01	0.03	0.08	−0.06	−0.10
Non-showering Showering	1.59	−0.56	1.02	0.90	0.33	1.59	−0.57	1.02	0.90	0.33
Background Subtraction										
Stopping	0.73	−0.64	−0.28	−0.58	−0.39	0.73	−0.64	−0.28	−0.57	−0.39
Non-showering	−0.22	−0.24	0.04	0.18	−0.07	−0.22	−0.24	0.04	0.18	−0.07
Showering	−0.24	−1.85	0.17	−0.15	0.06	−0.24	−1.85	0.17	−0.15	0.06
fiTQun (T2K Model)										
Decay-e Tagging			0.00					0.00		
Ring Counting			0.30					0.29		
e/μ Separation			0.08					0.07		
e/π^0 Separation			−0.09					−0.07		
μ/π^+ Separation			0.00					0.00		

Table B.4: Detector-related fitted systematic uncertainty parameters (epsilons) in the SK+T2K model analysis.

List of Journal Abbreviations

AIP Conf. Proc. .... AIP Conference Proceedings

APJ .... American Journal of Physics

Adv. Space Res. .... Advances in Space Research

Ann. Math. Stat. .... The Annals of Mathematical Statistics

Ann. Phys. .... Annals of Physics

Annu. Rev. Nucl. Part. Sci. .... Annual Review of Nuclear and Particle Science

Astron. Astrophys. .... Astronomy and Astrophysics

Astropart. Phys. .... Astroparticle Physics

Astrophys. J. .... The Astrophysical Journal

Comput. Phys. Commun. .... Computer Physics Communications

Eur. Phys. J. .... The European Physical Journal

Front. Astron. Space Sci. .... Frontiers in Astronomy and Space Science

Front. Phys. .... Frontiers in Physics

IEEE Trans. Nucl. Sci. .... IEEE Transactions on Nuclear Science

J. Geophys. Res. Space Phys. .... Journal of Geophysical Research: Space Physics

J. Phys. G Nucl. Partc. .... Journal of Physics G: Nuclear and Particle Physics

JHEP .... Journal of High Energy Physics

JINST .... Journal of Instrumentation

Nucl. Instrum. Meth. .... Nuclear Instruments and Methods in Physics Research

Nucl. Phys. Proc. Suppl. .... Nuclear Physics - Proceedings Supplements

Nucl. Phys. .... Nuclear Physics

Nuovo Cimento .... Il Nuovo Cimento

PTEP	Progress of Theoretical and Experimental Physics
Phys. Earth Planet. Inter.	Physics of the Earth and Planetary Interiors
Phys. Lett.	Physics Letters
Phys. Rept.	Physics Reports
Phys. Rev. Lett.	Physical Review Letters
Phys. Rev.	Physical Review
Phys. Today	Physics Today
Prog. Part. Nucl. Phys.	Progress in Particle and Nuclear Physics
Prog. Theor. Phys.	Progress of Theoretical Physics
Rept. Prog. Phys.	Reports on Progress in Physics
Rev. Mod. Phys.	Reviews of Modern Physics
Sov. J. Nucl. Phys.	Soviet Journal of Nuclear Physics
Sov. Phys. JETP	Soviet Physics Journal of Experimental and Theoretical Physics

Bibliography

[1] P. B. Denton, M. Friend, M. D. Messier, H. A. Tanaka, S. Böser, J. A. B. Coelho, M. Perrin-Terrin, and T. Stuttard, *Snowmass Neutrino Frontier: NF01 Topical Group Report on Three-Flavor Neutrino Oscillations*, 2022, arXiv:2212.00809 [hep-ph].

[2] M. A. Acero et al. (NOvA Collaboration), Phys. Rev. D **106**, 032004 (2022).

[3] L. M. Brown, Phys. Today **31**, 23 (1978).

[4] N. Bohr, in *Foundations of Quantum Physics I (1926–1932)*, Vol. 6, edited by J. Kalckar, Niels Bohr Collected Works (Elsevier, 1985), pp. 371–408.

[5] F. L. Wilson, APJ **36**, 1150 (1968).

[6] H. Bethe and R. Peierls, Nature **133**, 689 (1934).

[7] C. L. Cowan, F. Reines, F. B. Harrison, H. W. Kruse, and A. D. McGuire, Science **124**, 103 (1956).

[8] G. T. Danby, J.-M. Gaillard, K. A. Goulianos, L. M. Lederman, N. B. Mistry, M. Schwartz, and J. M. Steinberger, Phys. Rev. Lett. **9**, 36 (1962).

[9] K. Kodama et al. (DONuT Collaboration), Phys. Lett. B **504**, 218 (2001).

[10] S. L. Glashow, Nucl. Phys. **22**, 579 (1961).

[11] S. Weinberg, Phys. Rev. Lett. **19**, 1264 (1967).

[12] M. Aker et al. (KATRIN Collaboration), Nature Physics **18**, 160 (2022).

[13] Aghanim, N. et al. (Planck Collaboration), Astron. Astrophys. **641**, A6 (2020).

[14] B. Pontecorvo, Sov. Phys. JETP **26**, 984 (1962).

[15] Z. Maki, M. Nakagawa, and S. Sakata, Prog. Theor. Phys. **28**, 870 (1962).

[16] C. Giunti and C. W. Kim, *Fundamentals of Neutrino Physics and Astrophysics* (Oxford University Press, Mar. 2007).

[17] R. Davis, Phys. Rev. Lett. **12**, 303 (1964).

[18] J. N. Bahcall, M. H. Pinsonneault, and S. Basu, Astrophys. J. **555**, 990 (2001).

[19] J. N. Bahcall and M. H. Pinsonneault, Phys. Rev. Lett. **92**, 121301 (2004).

[20] N. Vinyoles, A. M. Serenelli, F. L. Villante, S. Basu, J. Bergström, M. C. Gonzalez-Garcia, M. Maltoni, C. Peña-Garay, and N. Song, Astrophys. J. **835**, 202 (2017).

[21] J. N. Bahcall, Phys. Rev. Lett. **12**, 300 (1964).

[22] R. J. Davis, in Proceedings of the 11th International Conference on Cosmic Rays, Vol. 29, International Conference on Cosmic Rays (Oct. 1970).

[23] J. N. Abdurashitov et al. (SAGE Collaboration), Phys. Rev. C **60**, 055801 (1999).

[24] M. Cribier et al., Nucl. Phys. B - Proceedings Supplements **70**, Proceedings of the Fifth International Workshop on topics in Astroparticle and Underground Physics, 284 (1999).

[25] Q. R. Ahmad et al. (SNO Collaboration), Phys. Rev. Lett. **87**, 071301 (2001).

[26] Q. R. Ahmad et al. (SNO Collaboration), Phys. Rev. Lett. **89**, 011302 (2002).

[27] L. Wolfenstein, Phys. Rev. D **17**, 2369 (1978).

[28] S. P. Mikheev and A. Y. Smirnov, Sov. J. Nucl. Phys. (Engl. Transl.); (United States) **42:6** (1985).

[29] M. Agostini et al. (BOREXINO Collaboration), Nature **562**, 505 (2018).

[30] M. Maltoni and A. Yu. Smirnov, Eur. Phys. J. A **52**, 87 (2016).

[31] K. Eguchi et al. (KamLAND Collaboration), Phys. Rev. Lett. **90**, 021802 (2003).

[32] M. Apollonio et al., Eur. Phys. J. C - Particles and Fields **27**, 331 (2003).

[33] F. Boehm et al., Phys. Rev. D **62**, 072002 (2000).

[34] J. K. Ahn et al. (RENO Collaboration), Phys. Rev. Lett. **108**, 191802 (2012).

[35] F. P. An et al., Phys. Rev. Lett. **108**, 171803 (2012).

[36] Y. Abe et al. (Double Chooz Collaboration), Phys. Rev. Lett. **108**, 131801 (2012).

[37] L. Zhan, Y. Wang, J. Cao, and L. Wen, Phys. Rev. D **78**, 111103 (2008).

[38] K. Abe et al. (Super-Kamiokande Collaboration), Phys. Rev. D **97**, 072001 (2018).

[39] F. Reines, M. F. Crouch, T. L. Jenkins, W. R. Kropp, H. S. Gurr, G. R. Smith, J. P. F. Sellschop, and B. Meyer, Phys. Rev. Lett. **15**, 429 (1965).

[40] C. Achar et al., Phys. Lett. **18**, 196 (1965).

[41] T. J. Haines et al., Phys. Rev. Lett. **57**, 1986 (1986).

[42] K. Hirata et al., Phys. Lett. B **205**, 416 (1988).

[43] Y. Fukuda et al. (Super-Kamiokande Collaboration), Phys. Rev. Lett. **81**, 1562 (1998).

[44] A. M. Dziewonski and D. L. Anderson, Phys. Earth Planet. Inter. **25**, 297 (1981).

[45] M. H. Ahn et al., Phys. Rev. Lett. **90**, 041801 (2003).

[46] P. Adamson et al. (MINOS+ Collaboration), Phys. Rev. Lett. **125**, 131802 (2020).

[47] H. Nunokawa, S. J. Parke, and J. W. F. Valle, Prog. Part. Nucl. Phys. **60**, 338 (2007).

[48] D. Beavis, A. Carroll, and I. Chiang (E889 Collaboration), *Long baseline neutrino oscillation experiment at the AGS. Physics design report*, Apr. 1995.

[49] K. Abe et al. (T2K Collaboration), Phys. Rev. Lett. **107**, 041801 (2011).

[50] P. Adamson et al. (NOvA Collaboration), Phys. Rev. Lett. **116**, 151806 (2016).

[51] R. L. Workman et al. (Particle Data Group), PTEP **2022**, 083C01 (2022).

[52] Z.-Z. Xing and Z.-H. Zhao, Rept. Prog. Phys. **79**, 076201 (2016).

[53] A. D. Sakharov, Soviet Physics Uspekhi **34**, 392 (1991).

[54] J. H. Christenson, J. W. Cronin, V. L. Fitch, and R. Turlay, Phys. Rev. Lett. **13**, 138 (1964).

[55] K. Abe et al. (T2K Collaboration), Nature **580**, 339 (2020).

[56] M. A. Acero et al. (NOvA Collaboration), Phys. Rev. D **106**, 032004 (2022).

[57] M. Gerbino and M. Lattanzi, Front. Phys. **5**, `10.3389/fphy.2017.00070` (2018).

[58] P. F. de Salas, S. Gariazzo, O. Mena, C. A. Ternes, and M. Tórtola, Front. Astron. Space Sci. (2018).

[59] K. Scholberg, J. Phys. G Nucl. Partc. **45**, 014002 (2017).

[60] T. Adam et al., *JUNO Conceptual Design Report*, 2015, arXiv:`1508.07166 [physics.ins-det]`.

[61] S. Fukuda et al., Nucl. Instrum. Meth. A **501**, 418 (2003).

[62] Y. Totsuka, Nucl. Phys. B - Proceedings Supplements **48**, Proceedings of the Fourth International Workshop on Theoretical and Phenomenological Aspects of Underground Physics, 547 (1996).

[63] W. Allison and P. Wright, "The Physics of Charged Particle Identification: dE/dx, Cerenkov and Transition Radiation", in *Experimental Techniques in High-Energy Nuclear and Particle Physics* (1991), pp. 371–417.

[64] K. Abe et al., Nucl. Instrum. Meth. A **1027**, 166248 (2022).

[65] M. D. Messier, "Evidence for neutrino mass from observations of atmospheric neutrinos with super-kamiokande", PhD thesis (Boston University, 1999).

[66] H. Nishino et al., Nucl. Instrum. Meth. A **610**, 710 (2009).

[67] S. Yamada et al., IEEE Trans. Nucl. Sci. **57**, 428 (2010).

[68] J. Zoll, R. Brun, J. Shiers, S. Banerjee, O. Schaile, and B. Holl, *ZEBRA: Overview of the ZEBRA System*, CERN Program Library Long Writeups (1995).

[69] R. Brun and F. F. Rademakers, Nucl. Instrum. Meth. A **389**, 81 (1997).

[70] K. Abe et al., Nucl. Instrum. Meth. A **737**, 253 (2014).

[71] L. K. Pik, "Study of the neutrino mass hierarchy with the atmospheric neutrino data observed in Super-Kamiokande", PhD thesis (University of Tokyo, 2012).

[72] T. F. Mclachlan, "Study of the Oscillation of Neutrinos and Anti-Neutrinos and of Non-Standard Neutrino Interactions with the Atmospheric Data in Super-Kamiokande", PhD thesis (University of Tokyo, 2015).

[73] F. M. Dufour, "Precise study of the atmospheric neutrino oscillation pattern using Super-Kamiokande I and II", PhD thesis (Boston University, 2009).

[74] S. Desai, "High Energy Neutrino Astrophysics with Super-Kamiokande", PhD thesis (Boston University, 2004).

[75] C. Kachulis, "Boosted Dark Matter and Atmospheric Neutrino Earth Matter Effects at Super-Kamiokande", PhD thesis (Boston University, 2018).

[76] M. Shiozawa, Nucl. Instrum. Meth. A **433**, 240 (1999).

[77] M. Jiang et al. (Super-Kamiokande Collaboration), PTEP **2019**, 053F01, `10.1093/ptep/ptz015` (2019).

[78] *Machine Analysis of Bubble Chamber Pictures*, Vol. 590914, International Conference on High Energy Accelerators and Instrumentation (1958), pp. 554–558.

[79] M. Ishitsuka, "L/E Analysis of the Atmospheric Neutrino Data from Super-Kamiokande", PhD thesis (University of Tokyo, 2004).

[80] Y. Okajima, "Development of Neutrino Energy Reconstruction Algorithm for Neutrino Mass Hierarchy Determination", PhD thesis (Tokyo Institute of Technology, 2020).

[81] K. Abe et al. (Super-Kamiokande Collaboration), JINST **17**, P10029 (2022).

[82] M. Smy, in Proceedings of the 30th International Cosmic Ray Conference, Vol. 5, International Cosmic Ray Conference (Jan. 2008), pp. 1279–1282.

[83] M. Honda, T. Kajita, K. Kasahara, and S. Midorikawa, Phys. Rev. D **83**, `10.1103/physrevd.83.123001` (2011).

[84] Y. Hayato, Nucl. Phys. B - Proceedings Supplements **112**, 171 (2002).

[85] T. K. Gaisser and M. Honda, Annu. Rev. Nucl. Part. Sci. **52**, 153 (2002).

[86] S. Haino et al., Phys. Lett. B **594**, 35 (2004).

[87] J. Alcaraz et al., Phys. Lett. B **472**, 215 (2000).

[88] M. Catanesi et al., Astropart. Phys. **29**, 257 (2008).

[89] T. H. Johnson, Phys. Rev. **43**, 834 (1933).

[90] M. Potgieter, Adv. Space Res. **19**, The Heliosphere at Solar Minimum and Beyond, 883 (1997).

[91] J. A. Simpson, Phys. Rev. **73**, 1389 (1948).

[92] *Newark/Swarthmore, USA/Bartol Neutron Monitor Database*, `http://www01.nmdb.eu/station/newk/`, Accessed: 2023-02-20.

[93] J. Nieves, I. R. Simo, and M. J. V. Vacas, Phys. Rev. C **83**, 045501 (2011).

[94] N. J. Baker, A. M. Cnops, P. L. Connolly, S. A. Kahn, H. G. Kirk, M. J. Murtagh, R. B. Palmer, N. P. Samios, and M. Tanaka, Phys. Rev. D **23**, 2499 (1981).

[95] M. Martini, M. Ericson, G. Chanfray, and J. Marteau, Phys. Rev. C **80**, 065501 (2009).

[96] C. Llewellyn Smith, Phys. Rept. **3**, 261 (1972).

[97] N. C. Mukhopadhyay, H. C. Chiang, S. K. Singh, and E. Oset, Phys. Lett. B **434**, 7 (1998).

[98] R. Bradford, A. Bodek, H. Budd, and J. Arrington, Nucl. Phys. B - Proceedings Supplements **159**, Proceedings of the 4th International Workshop on Neutrino-Nucleus Interactions in the Few-GeV Region, 127 (2006).

[99] R. Gran, J. Nieves, F. Sanchez, and M. J. V. Vacas, Phys. Rev. D **88**, 113007 (2013).

[100] D. Rein and L. M. Sehgal, Ann. Phys. **133**, 79 (1981).

[101] C. Berger and L. M. Sehgal, Phys. Rev. D **76**, 113004 (2007).

[102] A. Higuera et al. (MINERvA Collaboration), Phys. Rev. Lett. **113**, 261802 (2014).

[103] C. Albright and C. Jarlskog, Nucl. Phys. B **84**, 467 (1975).

[104] M. Derrick et al., Phys. Rev. D **17**, 1 (1978).

[105] B. Jongejans et al., Nuovo Cimento A **101**, 435 (1989).

[106] T. Sjöstrand, Comput. Phys. Commun. **82**, 74 (1994).

[107] M. Glück, E. Reya, and A. Vogt, Eur. Phys. J. C **5**, 461 (1998).

[108] A. Bodek and U. K. Yang, AIP Conf. Proc. **1222**, 233 (2010).

[109] E. S. P. Guerra et al., Phys. Rev. D **99**, 052007 (2019).

[110] E. S. Pinzon Guerra et al. (DUET Collaboration), Phys. Rev. C **95**, 045203 (2017).

[111] R. Brun, F. Bruyant, F. Carminati, S. Giani, A. McPherson, G. Patrick, and L. Urban, *GEANT: Detector Description and Simulation Tool*, CERN Program Library (1993).

[112] C. Zeitnitz and T. Gabriel, Nucl. Instrum. Meth. A **349**, 106 (1994).

[113] Y. Nakano, "^{8}B solar neutrino spectrum measurement using Super-Kamiokande IV", PhD thesis (University of Tokyo, 2016).

[114] J. Hosaka et al. (Super-Kamiokande Collaboration), Phys. Rev. D **74**, 032002 (2006).

[115] R. Wendell et al. (Super-Kamiokande Collaboration), Phys. Rev. D **81**, 092004 (2010).

[116] M. Jiang, "Study of the neutrino mass hierarchy with the atmospheric neutrino data collected in Super-Kamiokande IV", PhD thesis (Kyoto University, 2019).

[117] R. Matsumoto, "Development of an atmospheric event classification method for Super-Kamiokande", Japanese, MA thesis (Tokyo University of Science, 2020).

[118] A. Takenaka et al. (Super-Kamiokande Collaboration), Phys. Rev. D **102**, 112011 (2020).

[119] M. Honda, T. Kajita, K. Kasahara, S. Midorikawa, and T. Sanuki, Phys. Rev. D **75**, 043006 (2007).

[120] G. Battistoni, A. Ferrari, T. Montaruli, and P. Sala, Astropart. Phys. **19**, 269 (2003); Corrected in, Astropart. Phys. **19**, 291 (2003).

[121] G. D. Barr, T. K. Gaisser, P. Lipari, S. Robbins, and T. Stanev, Phys. Rev. D **70**, 023006 (2004).

[122] A. E. Hedin, J. Geophys. Res. Space Phys. **92**, 4649 (1987), eprint: `https://agupubs.onlinelibrary.wiley.com/doi/pdf/10.1029/JA092iA05p04649`.

[123] *U.S. Standard Atmosphere, 1976*, `https://ntrs.nasa.gov/citations/19770009539`, Accessed: 2023-03-24.

[124] E. Hernández, J. Nieves, and M. Valverde, Phys. Rev. D **76**, 033005 (2007).

[125] A. Capella, A. Kaidalov, C. Merino, and J. Tran Thanh Van, Phys. Lett. B **337**, 358 (1994).

[126] A. Bodek and U. K. Yang, *Axial and Vector Structure Functions for Electron- and Neutrino- Nucleon Scattering Cross Sections at all Q^2 using Effective Leading order Parton Distribution Functions*, 2010, arXiv:`1011.6592`.

[127] C. Andreopoulos et al., Nucl. Instrum. Meth. A **614**, 87 (2010).

[128] R. Akutsu, "A Study of Neutrons Associated with Neutrino and Antineutrino Interactions on the Water Target at the T2K Far Detector", PhD thesis (University of Tokyo, 2020).

[129] Z. Li et al. (Super-Kamiokande Collaboration), Phys. Rev. D **98**, 052006 (2018).

[130] J. E. Kim, P. Langacker, M. Levine, and H. H. Williams, Rev. Mod. Phys. **53**, 211 (1981).

[131] V. Barger, K. Whisnant, S. Pakvasa, and R. J. N. Phillips, Phys. Rev. D **22**, 2718 (1980); A sign error in Eq. 21 was noted in P. Langacker, J. P. Leveille, and J. Sheiman, Phys. Rev. D **27**, 1228 (1983).

[132] R. A. Wendell, "Three flavor oscillation analysis of atmospheric neutrinos in Super-Kamiokande", PhD thesis (Duke University, 2008).

[133] G. L. Fogli, E. Lisi, A. Marrone, D. Montanino, and A. Palazzo, Phys. Rev. D **66**, 053010 (2002).

[134] S. S. Wilks, Ann. Math. Stat. **9**, 60 (1938).

[135] S. Kirkpatrick, C. D. Gelatt, and M. P. Vecchi, Science **220**, 671 (1983), eprint: `https://www.science.org/doi/pdf/10.1126/science.220.4598.671`.

[136] A. L. Read, J. Phys. G Nucl. Partc. **28**, 2693 (2002).

[137] D. Adey et al. (Daya Bay Collaboration), Phys. Rev. Lett. **121**, `10.1103/physrevlett.121.241805` (2018).

[138] C. D. Shin et al. (RENO Collaboration), JHEP **2020**, `10.1007/jhep04(2020)029` (2020).

[139] H. de Kerret et al. (Double Chooz Collaboration), Nature Physics **16**, 558 (2020).

[140] M. G. Aartsen et al. (IceCube Collaboration), *Three-year high-statistics neutrino oscillation samples*, 2019.

[141] A. Himmel, *New Oscillation Results from the NOvA Experiment*, Neutrino 2020 Conference, July 2020.

[142] C. Bronner, *Accelerator Neutrino I: Recent results from T2K*, Neutrino 2022 Conference, June 2022.

[143] K. Abe et al., Nucl. Instrum. Meth. A **659**, 106 (2011).

[144] K. Abe et al. (T2K Collaboration), Phys. Rev. D **103**, 112008 (2021).

[145] M. Kabirnezhad, Phys. Rev. D **97**, 013002 (2018).

[146] K. Abe et al. (T2K Collaboration), Phys. Rev. D **91**, 072010 (2015).

[147] B. Abi et al. (DUNE Collaboration), JINST **15**, T08008 (2020).

[148] K. Abe et al. (Hyper-Kamiokande Collaboration), *Hyper-Kamiokande Design Report*, 2018, arXiv:`1805.04163 [physics.ins-det]`.

Biography

Thomas Benjamin Wester was born in Chicago, Illinois to Drs. William and Barbara Wester in July, 1995. Thomas' proximity to Fermi National Accelerator Laboratory (Fermilab) proved fortuitous. In the summer of 2012, Thomas worked with the liquid argon R&D group at Fermilab where his interest in computer programming quickly transferred to dark matter detectors. Thomas spent the following summer at Gran Sasso National Laboratory, where he helped with the commissioning of the DarkSide-50 detector. Thomas continued working with dark matter detectors as an undergraduate at the University of Chicago with Professor Luca Grandi. During Thomas' time at UC, the Grandi group deployed and operated a small-scale liquid xenon detector, which would become the subject of Thomas' undergraduate thesis. Thomas spent UC's summer breaks back at Fermilab, where he worked on the MicroBooNE neutrino experiment as part of Professor Janet Conrad's group. After graduating UC, Thomas moved to Boston and continued work with the Conrad group, now on the ion source demonstrator for the upcoming IsoDAR neutrino experiment. By this point, Thomas had decided to pursue neutrino physics, and happily accepted the opportunity to enroll as a graduate student at Boston University in 2018. He joined the Super-Kamiokande collaboration before starting his first semester of classes, and the timing could not have been better: The SK tank was opened that summer for the first time in 12 years, giving Thomas first-hand experience with the detector. Throughout his Ph.D., Thomas worked under the supervision of Professors Ed Kearns and Roger Wendell to develop improvements for the SK atmospheric neutrino oscillation analysis. Upon graduating from BU, Thomas will return to the University of Chicago, his alma mater, as a McCormick postdoctoral fellow.